Modelling the outer retina utilising ex vivo tissue and stem cells to optimise complement gene therapy

Sarah Bassim Hamid Hammadi

A thesis submitted to Newcastle University for the degree of Doctor of Philosophy (PhD)

Biosciences Institute
Faculty of Medical Sciences
Newcastle University, U.K.

May 2025

Abstract

Age-related macular degeneration is a leading cause of blindness worldwide. However, a gap remains due to no available model with a truly representative Bruch's membrane (BrM), which is key to realistically model the disease and evaluate therapies. This study addressed this gap by attempting to recreate the human RPE/BrM/choroid complex by recellularising decellularised ex-vivo human retina. Firstly, an optimal decellularisation protocol for BrM-choroidal complex was selected, ensuring cellular removal while preserving ECM proteins. Second, the ability of iPSC-RPE to form a functional monolayer on decellularised BrM (dBrM) was assessed. Lastly, apical transduction capabilities of AAV2 vs AAV8 GFP and AAV2 sCR1 CCP1-11 Flag His tag (truncated sCR1) vectors were evaluated.

Human donor eyes were dissected and decellularised using three protocols: Chirco K *et al.* (CP), and two shortened protocols (SP1 and SP2). iPSC-RPE cells were cultured on dBrM or Matrigel, and evaluated with proteomics, imaging, functional assays (VEGF and PEDF secretion) and phagocytosis of photoreceptor outer segments. Transduction of cells on Matrigel at day 3 vs 23 with AAV2 and AAV8 GFP was performed and quantified by flow cytometry for optimisation. Final transduction of day 23 cells on dBrM with AAV2 truncated sCR1 was followed by FLAG ELISA and fluid-phase co-factor assay.

CP was the most effective decellularisation protocol with the least DNA persistence. Proteomic analysis confirmed nuclear protein removal and ECM retention, particularly laminin and collagen. From day 21, iPSC-RPE on dBrM formed a ZO1-positive monolayer with higher basal VEGF and apical PEDF. Imaging revealed representative RPE morphology, while proteomics identified known RPE cell markers. GFP transduction at day 23 showed AAV2 outperformed AAV8. Finally, 6-, 13- and 22-days post AAV2 truncated sCR1 transduction, iPSC-RPE cells released functional truncated sCR1.

These results showed successful decellularisation of the human BrM/choroidal complex, recellularisation with iPSC-RPE and efficient AAV2 truncated sCR1 transduction secreting functional protein.

In the name of God, the Most Gracious, the Most Merciful

"Read in the name of your Lord who created."
(The Quran; Surah Al-Alaq, 96:1)

Acknowledgement

First and foremost, I thank God for His endless grace, guidance, and strength, which have carried me through this journey. Without Him, none of this would have been possible.

I would like to express my heartfelt gratitude to my supervisors, David Steel, Majlinda Lako and Claire Harris. Your guidance and support throughout my project have been instrumental in shaping me into the researcher I am today. Your passion for research has been a constant source of inspiration, and your insight and encouragement have made this journey both enriching and fulfilling.

This project wouldn't be possible without the support from my funding body, Gyroscope Therapeutics, a Novartis Company and Newcastle University. Thank you for giving me the opportunity to build on my passion for research. I would also like to thank my industrial supervisors, Magali Saint-Geniez, Katharina Lo, Ingrid Porpino Meschede, Scott Sharp, and Marlene Rosa Do Carmo, for all their guidance and support.

Throughout my project, I am thankful for the help from Erin Cocks, Ross Laws and Tracey Davey from Newcastle University Electron Microscopy Research Services for processing samples for transmission electron microscopy. I would also like to thank Pawel Palmowski and Andrew Porter from Newcastle University Protein and Proteome Analysis for processing the Proteomic samples. For all the countless help with microscopy and imaging, I would like to thank Veronika Boczonadi from Newcastle University Bio-imaging Unit. To both my panel members, Marzena Kurzawa-Akanbi and Kevin Marchbank, thank you for your guidance and advice. Your support has helped me grow personally and professionally. The modelling in this project would not have been successful without the help from Michael Wilkes from the School of Engineering at Newcastle University, thank you.

During my PhD journey, I had the privilege of meeting incredible friends whose support and encouragement uplifted me every step of the way. A massive thank you to Maria Georgiou, Sally Harwood, Avril Watson, Eldo Galo, Robert Atkinson, Marina Moya-Molina, Maria Elia, Konstantina Kyriakou and Giulia Carozza. Thank you for always being there for me, listening with an open heart, and hearing me when I need to be heard. I truly appreciate all of you, you showed me what true friendship looks like through the highest highs and the lowest lows. I would also like to thank the members of the Linda Lako Stem Cell Group and the Newcastle Complement Research Group for all their support.

Thank you to all my friends all around, who have always been there for me, supporting me throughout this journey. Thank you for always believing in me when I doubted myself.

Last but certainly not least, my foundation, my strength, and the reason I stand tall today - my dad, mom, and sister. You are the vision, and I am merely the eyes. For what are eyes without vision? Dad, thank you for being my unwavering guide and steadfast protector. Mom, your warmth, love, and boundless support have been my safe haven. And to my sister, my best friend and my heart - you are my greatest gift; you always clap so hard I would never hear who doesn't. Dear lovely family, thank you for your support, pushing me to be the best version of myself, for providing for me and ensuring I'm always happy and safe. Thank you for allowing me to spread my wings and fly, even if it meant that I would be away from you. Distance has been very hard but in every step, you are always in my heart.

Being away from home and navigating the ups and downs of a PhD journey has been an experience filled with both laughter and tears. As I stand at this significant milestone of completing my PhD thesis, I feel an overwhelming sense of pride. This achievement is not just personal but a tribute to the remarkable lineage of women in my family who have pursued the highest levels of education, inspiring me every step of the way.

Contents

List of Figures

List of tables

List of Abbreviations

AAV	Adeno-associated viruses
AGE	Advanced glycation end product
AMD	Age-related macular degeneration
Ang1	Angiopoietin-1
Ap	Apical
apoE	apolipoprotein E
ATP	Adenosine triphosphate
AV	Adenovirus
Ba	Basal
BCA	Bicinchoninic acid
BCE	Bovine corneal endothelial cell
BCVA	Best corrected visual acuity
bGH pA	Bovine Growth Hormone polyadenylation signal
BLamD	Basal laminar deposits
BLinD	Basal linear deposits
BMSF	Bombyx mori silk fibroin
BP	Biological process
BrM	Bruch's membrane
BSA	Bovine serum albumin
C2	Complement component 2
CAG	Chicken beta-actin promoter
CC	Cellular component
CCP	Complement control protein repeat units
CEC	Choroidal endothelial cell
CEL	Central elastic layer
CMV	Cytomegalovirus
CNV	Choroidal neovascularisation
COLIV	Collagen IV
CO_2	Carbon dioxide
CP	Chirco K *et al* protocol
CR1	Complement receptor 1
CRP	C-reactive protein

DAF	Decay accelerating factor
dBrM	Decellularised Bruch's membrane
dH2O	De-ionised water
DNA	Deoxyribonucleic acid
EC	Endothelial cells
ECFC	Endothelial colony forming cells
ECM	Extracellular matrix
EDTA	Ethylenediaminetetraacetic acid
ELISA	Enzyme linked immunosorbent assay
FB	Factor B
FBS	Fetal bovine serum
FCS	Flow cytometry standard
FDA	Food and Drug Administration
FGF	fibroblastic growth factor
FH	Factor H
FHL	Factor H like
FI	Factor I
FITC	Fluorescein-isothiocyanate
fRPE	fetal retinal pigment epithelium
GA	Geographic atrophy
GFP	Green fluorescent protein
GO	Gene ontology
GWAS	Genome-wide association studies
HAMP	human amniotic membrane powder
HDL	High-density lipoprotein
hRPE	Human retinal pigment epithelium
HSPGs	Heparan sulphate proteoglycans
HUVEC	Human umbilical vein endothelial cells
H_2O_2	Hydrogen peroxide
ICL	Inner collagenous layer
IFN	Interferon
IgG	Immunoglobulin G
IHC	Immunohistochemistry
INT	2-(4-iodophenyl)-3-(4-nitrophenyl)-5-phenyl-2H-tetrazolium chloride

iPSC	Induced pluripotent stem cell
LAMA	Laminin subunit alpha
LAMB	Laminin subunit beta
LAMC	Laminin subunit gamma
LDH	Lactate dehydrogenase
LHR	Long homologous repeat domains
MAC	Membrane attack complex
MASP	Mannose binding lectin -associated serine proteases
MBL	Mannose binding lectin
MCP	Membrane cofactor protein
mEGFP	Enhanced green fluorescent protein
MEM	Minimum Essential Medium
MF	Molecular function
MFI	Mean fluorescence intensity
MMP	Matrix metalloproteinases
MOI	Multiplicities of infection
MOPS	3-(N-morpholino)propane sulfonic acid
mRNA	Messenger ribonucleic acid
MSC	Mesenchyme stem cells
MSD	Mesoscale discovery
NaCl	Sodium chloride
NAD	Nicotinamide adenine dinucleotide
NADH	Reduced nicotinamide adenine dinucleotide
NCT	National clinical trial
NHS	National health service
oBRB	Outer blood-retinal barrier
OCL	Outer collagenous layer
OCT	Optimum cutting temperature
PAMP	Pathogen-associated molecular pattern
PANi	Polyaniline
PBS	Phosphate-buffered saline
PCL	Polycaprolactone
PDMS	Poly(dimethylsiloxane)
PEDF	Pigment epithelium-derived factor

PEG-NB	Poly(ethylene glycol) norbornene
PenStrep	Penicillin-Streptomycin
PET	Polyethylene terephthalate
PFA	Paraformaldehyde
PFK	Phosphorylated focal adhesion kinase
PG	Protein-coding genes
PLG	Poly(latic-co-glycolod acid)
PLVAP	Plasmalemma vesicle-associated protein
POS	Photoreceptor outer segment
PVDF	Polyvinylidene difluoride
R3-IGF-1	Long R3 insulin-like growth factor 1
RCA	Regulators of complement activation’
RGD	Arginine-glycine-aspartic acid
RNA	Ribonucleic acid
ROCK	Rho-associated coiled-coil containing kinases
RPE	Retinal pigment epithelium
rssP	REcombinant spider silk proteins
sCR1	Soluble complement receptor 1
SDS	Sodium dodecyl sulfate
SEM	Long R3 insulin-like growth factor 1
SLS	Scientific Laboratory Supplies
SP1	Shortened protocol 1
SP2	Shortened protocol 2
ssDNA	Single-stranded deoxyribonucleic acid
T3	Triiodo-L-thyronine
TBS	Tris-buffered saline
TCP	Tissue culture plastic
TEER	Transepithelial electrical resistance
TEM	Transmission electron microscopy
TIMP	Tissue inhibitor metalloproteinases
TMB	3,3′,5,5′-Tetramethylbenzidine
TNF	Tumor necrosis factor
UV	Ultraviolet
VEGF	Vascular endothelial growth factor

VLDL	Very low-density lipoproteins
WPRE	Woodchuck Hepatitis Virus Posttranscriptional Regulatory Element
ZO1	Zonula Occludens-1

Chapter 1 Introduction

1.1 The human eye

The human eye serves as the primary point through which individuals perceive the world around them. The eye possesses immune privilege, allowing it to tolerate some antigen activation without always eliciting an inflammatory immune response (Horai et al., 2013). This is essential to maintain the delicate tissue structure in the eye. The eye is enclosed posteriorly by three tissue layers, from outermost to innermost: sclera, uvea (iris, ciliary body, and choroid) and retina (**Figure 1- 1**). The outermost layer is known as the sclera; it is made of a network of variably orientated collagen fibres to form a strong outer wall, which anteriorly merges into the cornea, a specialised, transparent tissue that allows light to enter the eye. The uvea consists of the iris, the ciliary body, and the choroid. The iris is the coloured region in the eye which contains the sphincter muscle fibre, that contracts or relaxes to control pupil size. This controls the amount of light entering the eye towards the retina to ensure optimal vision in different lighting conditions. The ciliary body encircles the lens and contains the ciliary muscle to adjust the refractive power of the lens, which is essential in accommodation. This allows an individual to focus on objects at different distances. When an individual focuses on a near object, the ciliary muscles contract, causing the zonule fibres to relax and vice versa when focusing on a far object. The posterior chamber located near the ciliary body plays an important role in changes in volume and pressure of the aqueous humour that affects the shape and position of the lens as it undergoes fluid exchange with the aqueous chamber. The vitreous humour is a gel-like substance that fills the space between the lens and the retina (innermost layer), which helps maintain the shape of the eye by maintaining the intraocular pressure.

1.1.1 The human retina

The retina is the innermost layer, located posteriorly in the eye. Nutrients are supplied via the retinal vasculature and the choriocapillaris. The choriocapillaris are located in the choroid, and they comprise a network of capillaries separated from the retina via a thin extracellular matrix (ECM) layer known as Bruch's membrane (BrM). BrM is a modified basement membrane of the retinal pigment epithelium (RPE) cells and choroidal endothelial cells (CECs). The choriocapillaris supply the outer retina, while the retina vasculature supplies the inner retina. The layers of the retina from the inner to the outermost consist of the ganglion cell layer, inner plexiform layer, inner nuclear layer, outer plexiform layer, outer nuclear layer, photoreceptor

outer segment (POS) and the RPE cells (**Figure 1- 1**). The photoreceptor cells and the neuronal network send signals to the brain via the ganglion cells. The RPE cells are a polarised monolayer of pigmented epithelial cells that play a crucial role in maintaining retinal homeostasis. They help regulate nutrient and oxygen uptake from the choroid to the photoreceptors and are essential for the phagocytosis of POS as part of the visual cycle (Bok, 1993). They also secrete growth factors, provide structural support, and protect the retina from oxidative stress via the presence of melanosomes, which absorb excess light (Bhutto & Lutty, 2012). The macula, 5 mm in diameter, is the central region of the retina (Kolb et al., 1995). The central region of the macula, known as the fovea, contains the foveola at its centre, a cone-rich area that, like the fovea, relies on the choriocapillaris for its blood supply. The macula lutea, which is yellowish in colour due to the presence of lutein and zeaxanthin pigments, is a 3 mm diameter circle centred on the fovea. The fovea contains a high density of cones, while the parafovea includes a high density of rods (Armento et al., 2021; Curcio et al., 1996). Rods and cones are photoreceptors, with the rods having a low spatial resolution but sensitive to light, while the cones have a high spatial resolution and are less sensitive to light. These photoreceptors are known as photosensitive cells, converting photons of light into a neural signal through a biochemical pathway called phototransduction. These signals are then transferred to bipolar cells, which synapse with ganglion cells, that transmit signals from the eye to the brain via the optic nerve to allow vision.

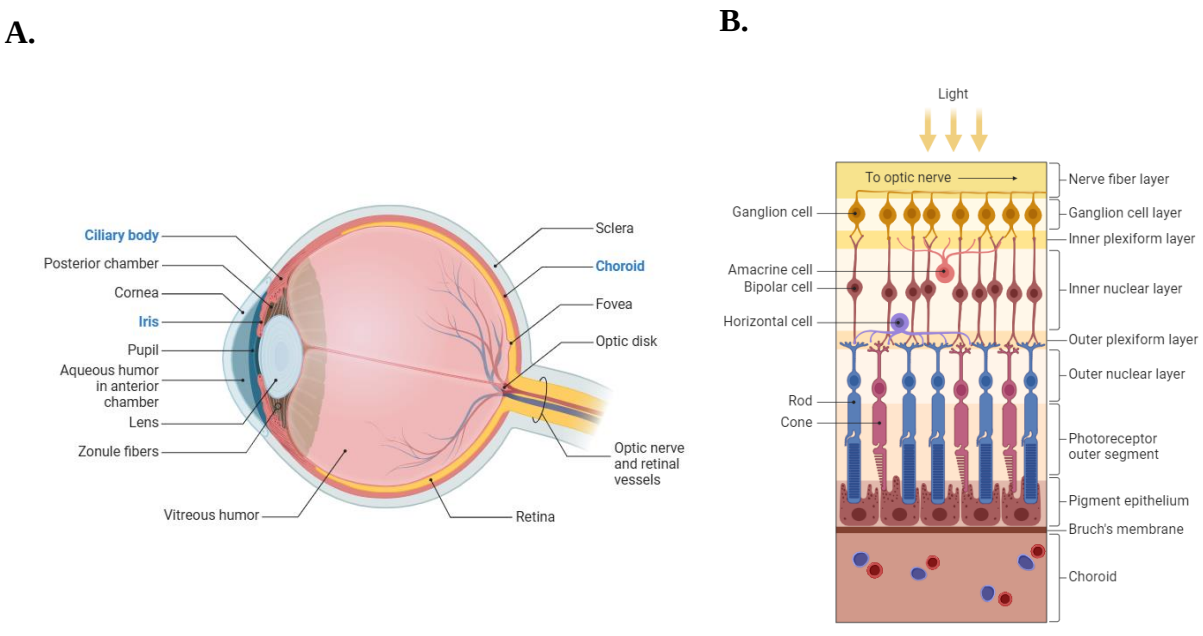

Figure 1- 1. Schematic of the human eye. (A) The eye mainly comprises three layers: the sclera, uvea (in blue bold: Iris, ciliary body and choroid), and retina. **(B)** The layers of the retina, from the innermost, are the nerve fibre layer, ganglion cell layer, inner plexiform layer, inner nuclear layer, outer plexiform layer, outer nuclear layer, photoreceptor outer segment, pigment epithelium, BrM, and choroid. Figures were made using Bio-render.

1.1.2 The human choroid

The human choroid is located posteriorly between the retina and sclera and comprises a large vascular connective tissue. At birth, it is around 200 µm thick and reduces to around 80 µm by the age of 90 (Ramrattan et al., n.d.). The choroid holds crucial functions as it has one of the highest blood flow rates per gram of any tissue in the human body which is crucial to provide at least 85% of the retinal oxygen supply (Reiner et al., 2018). Besides that, the choroid is involved in light absorption and modulation of the intraocular pressure via the uveoscleral pathway (Nickla & Wallman, 2010). The choroid appears pigmented due to the presence of melanocytes that are distributed throughout the stroma except in the choriocapillaris (Edwards & Lutty, 2021).

From the inner (retinal side) toward the outer layer (sclera side), the choroid consists of five sublayers: BrM, choriocapillaris, Sattler's and Haller's layer and the suprachoroidal layer. The three-layer vasculature is firstly composed of the choriocapillaris, consisting of fenestrated capillaries, followed by Sattler's layer, which consists of medium-sized vessels of venules and arterioles, and lastly, Haller's layer consists of large diameter vessels of bigger than 100 µm (Branchini et al., 2013; Lejoyeux et al., 2022; Hasegawa et al., 2007). These vasculatures are apparent at the central submacular region with less dense choriocapillaris and larger blood vessels towards the periphery.

The choroidal blood is supplied by the short and long posterior ciliary arteries, with input from the anterior ciliary arteries (Kur et al., 2012) (**Figure 1- 2**). The short posterior ciliary arteries pass into the eye in a circular arrangement around the optic disc and are responsible for supplying blood to the posterior part of the eye, while the long posterior ciliary arteries pass into the eye in a triangular pattern from the posterior pole to the periphery and are responsible for supplying blood to the ciliary body and anterior part of the eye (Borrelli et al., 2018) (**Figure 1- 2**). The short posterior ciliary arteries penetrate the sclera around the optic nerve to contribute to the circle of Zinn. The circle of Zinn is a circular arterial structure around the optic nerve head that supplies blood to the optic nerve and adjacent parts of the choroid (**Figure 1- 2**). The venous drainage from the choroid is facilitated by four to eight vortex veins, which merge with the ophthalmic vein and eventually drain to the superior and inferior ophthalmic veins.

Besides blood vessels, the choroid contains elastic and collagenous connective tissue and other cell types such as CECs, fibroblast, melanocytes, pericytes, smooth muscle cells, neurons, and immune cells such as macrophages, mast cells and dendritic cells (McMenamin & Polla, 2013; Kezic & McMenamin, 2008; Chinnery et al., 2017; Brinks et al., 2022). Vascular endothelial growth factor (VEGF) plays a vital role in ensuring migration of CECs to the blood vessels and tubulogenesis during angiogenesis (Provis, 2001; PROVIS et al., 1997; Stalmans et al., 2002). Fibroblast growth factor (FGF) (Gerwins et al., 2000; Auguste et al., 2003; Javerzat et al., 2002) and angiopoietin-1 (Ang1) (Uemura et al., 2002), also help the tubulogenesis. Pericytes (Eilken et al., 2017; Darland et al., 2003) and RPE cells (Saint-Geniez et al., 2009a; Young et al., 2005; Pollreisz et al., 2013) have been shown to secrete VEGF which promotes CEC growth and regulates fenestration. Thus, this indicates that all these cells contribute to the homeostatic balance of the choroid and ensure the growth of CECs.

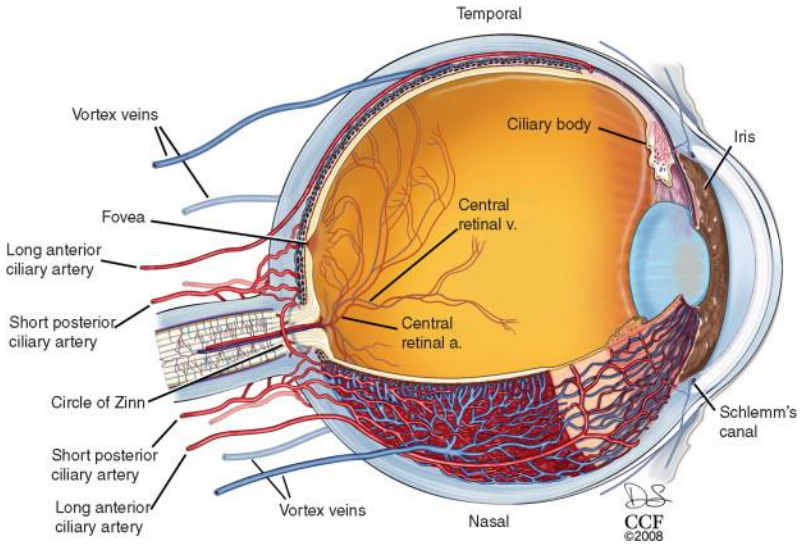

Figure 1- 2. Vascular composition of the human eye. The circle of Zin and short posterior artery supplies blood to the optic nerve and around the choroid while the long posterior artery supply blood to the ciliary body and the anterior part of the choroid. Figure adapted from Anand-Apte *et al* 2009.

1.2 Bruch's membrane

BrM is a 2–4 μm thick membrane with unique transmission properties, lying between the RPE and fenestrated choriocapillaris (Booij et al., 2010). It is a continuous membrane posterior to the ora serrata, deficient only at the point of optic nerve insertion (Nickla & Wallman, 2010). Besides that, it has a heterogenous thickness across the eye being thinner in the macula while thicker at the periphery mainly due to the difference in the thickness of the elastin and collagen layer (Chong et al., 2005). In 1971, Hogan outlined BrM as comprising five layers (Edwards & Lutty, 2021), arranged from innermost to outermost as follows:

- The RPE basement membrane measures approximately 0.15 μm in thickness and consists of collagen IV α1-5, collagen V, chondroitin sulphate, heparan sulphate, laminins 1, 5, 10, 11 and nindogen-1 (Guymer et al., 1999; Das, 1990; Chen, 2003; Call & Hollyfield, 1990; Booij et al., 2010; Beattie et al., 2010; Aisenbrey et al., 2006).

- The inner collagenous layer (ICL) measures approximately 1.4 μm thick consisting of crossed layers of collagen I, III, and V fibronectin, clusterin, apolipoprotein E (apoE), chondroitin sulphate, dermatan sulphate, heme, vitronectin and lipoproteins (Lin et al., 1992; Ruberti et al., 2003; Anderson et al., 2001; Tezel et al., 2009).

- The central elastic layer (CEL) measures approximately 0.8 μm thick, discontinuous in the macular region and contains elastin fibres contiguous with the ICL and outer collagenous layer (OCL). The CEL is essential for antiangiogenic barrier functions, biomechanical properties, and choroidal contractility (Chong et al., 2005).

- The OCL thickness varies within a range from 1 to 5 μm (Curcio & Johnson, 2013) and contains collagen I, III and V, fibronectin, fibulin-5, chondroitin sulphate, lipoproteins, dermatan sulphate, clusterin, apoE (Aisenbrey et al., 2006; Beattie et al., 2010; Tezel et al., 2009; Newsome et al., 1987; Ruberti et al., 2003; Wang et al., 2009).

- CEC basement membrane measures approximately 0.07 μm thick and consists of, heparan sulphate, collagen IV, α1, α2, V, VI, endostatin, laminin, and chondroitin sulphate. It is discontinuous due to choroidal inter-capillary pillars between choriocapillaris lumens (Booij et al., 2010; Beattie et al., 2010; Das, 1990; Chong et al., 2005; Bhutto, 2004; Mullins et al., 2007).

BrM functions as a physical support for the adhesion of RPE cells and as a selective barrier between the choroid and retina, allowing only specific proteins to diffuse (Clark et al., 2017) (**Figure 1- 3**). Changes in BrM composition, such as lipid deposition and heparan sulphate depletion with age, interfere with the homeostatic balance between the retina and choroid which in turn affects BrM diffusion properties.

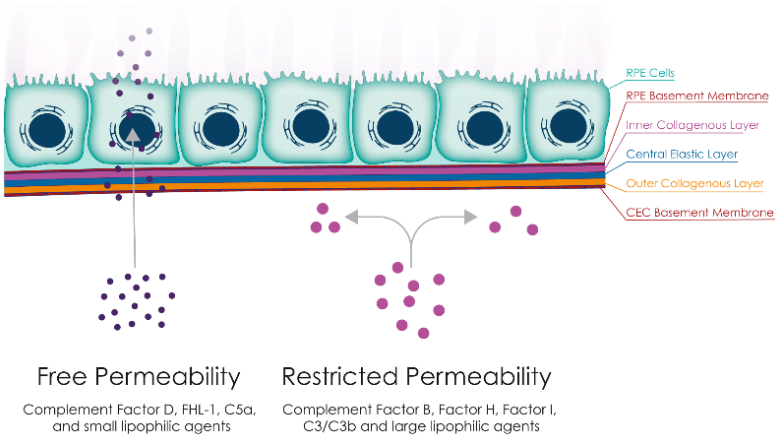

Figure 1- 3. BrM diffusion. BrM consists of five layers: the RPE basement membrane, inner collagenous layer, central elastic layer, outer collagenous layer, and CEC basement membrane. RPE: retinal pigment epithelium; CEC: choroidal endothelial cells. Figure adapted from Hammadi S *et al* 2023.

1.2.1 Development of retina and Bruch's membrane

Retinogenesis begins with the development of the eye field from the medial anterior neural plate (**Figure 1- 4**) ((Heavner & Pevny, 2012; O'Hara-Wright & Gonzalez-Cordero, 2020; Quinn & Wijnholds, 2019). Key transcription factors, such as *Pax6, Six3, Six6, Rax and Lhx2*, are responsible for specifying the eye field fate. (O'Hara-Wright & Gonzalez-Cordero, 2020). The eye field then undergoes a crucial step where it separates from the diencephalon, which is the caudal region of the forebrain. Within the neural folds, there is indentation, which generates the optic grooves. The optic grooves evaginate bilaterally from the diencephalon to form the optic vesicle. The optic vesicle then grows towards the surface ectoderm to form the lens placode. The optic stalk connects the optic vesicle to the forebrain and becomes the optic nerve at a later stage.

The optic vesicle undergoes the process whereby it folds inwards to form a pocket-like shape; the process is known as invagination. When it undergoes this process, it differentiates into two double-layer optic cups. At the surface of the ectoderm, the lens placode continues to develop into the lens vesicle. At the anterior of the optic cup, the iris and ciliary body begin to form, while the outer layer of the posterior cup becomes the RPE. Retinal progenitor cells proliferate within the inner layer of the posterior cup to form the sensory neurons crucial for phototransduction. The newly generated retinal progenitor cells continue to populate the retina to form diverse retinal neurons.

The outer RPE basal membrane incorporates into BrM. The exact formation of the ECM component is still unknown. However, RPE cells have been shown to synthesise the major components of BrM ECM, such as collagen, laminins, and fibronectins (Booij et al., 2009).

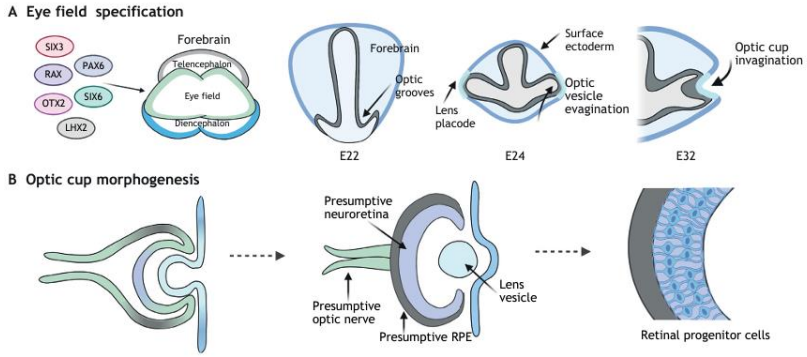

Figure 1- 4. Schematic of retinogenesis. (A) Eye field specification. The transcription factors are responsible for the presumptive eye field in the diencephalon of the developing forebrain. By embryonic day 22 (E22), the optic groove forms; by E24, it forms the optic vesicle. The optic vesicle invagination then occurs by E32. **(B)** The optic cup morphogenesis. The inner layer of the optic cup forms the presumptive neuroretina, while the outer layer specifies the presumptive RPE. The optic stalk connects the optic vesicle to the forebrain, which forms the optic nerve. The lens then pinches from the anterior of the surface ectoderm. In the presumptive neuroretina, retinal progenitor cells differentiate from the retinal cells. Figure adapted from O'Hara-Wright *et al* 2020.

1.2.2 Diffusion properties

BrM, as discussed previously, is a thin sheet of ECM that acts as a barrier between the RPE and choriocapillaris. It is highly negatively charged due to the glycosaminoglycans and contains pores approximately 2-3nm in diameter, depending on the age of BrM (Booij et al., 2010). The diffusion of substances across BrM depends not only on the properties of the diffusing substance but also on the charge characteristics of BrM itself. Oxygen, nutrients, electrolytes and cytokines required by the RPE, and photoreceptors can diffuse from the choroidal side via BrM to the RPE cells. Waste materials from the RPE cells can also diffuse back towards the choroid via the BrM. Diffusion through BrM occurs mainly by passive diffusion and is dependent on the molecular composition of BrM itself, which varies with both regional differences (macular vs peripheral regions) and ageing within the retina.

Earlier research looking at the relationship between BrM porosity and the diffusion of water confirmed that the EL, which has greater pore sizes, has the largest water conductivity (Moore & Clover, 2001) On the other hand, the ICL with the smallest pore has the lowest water conductivity (Moore & Clover, 2001). Besides that, diffusion through BrM also relies on

hydrostatic pressure on both sides of BrM and the concentration of the biomolecule or ions. Molecules from the choroid passing through BrM to reach RPE include lipids, nutrients, pigment precursors, vitamins, minerals, oxygen, antioxidants, and others that bind to BrM or are taken up by the RPE (Strauss, 2005; Bok, 1993). Molecules passing from RPE to choroid through BrM include water, CO_2, oxidised lipids, ions and other waste products from RPE. The waste products from the retina are from the RPE or photoreceptors, and they consist of the visual cycle, metabolic or electrophysiological waste and POS (WIMMERS et al., 2007; Strauss, 2005).

Besides that, Moore DJ *et al* showed that proteins up to 200kDa can pass across young BrM (Moore & Clover, 2001). They also showed that the transmission property of BrM reduces with age (Moore & Clover, 2001) . Molecular weight is not the only factor determining which proteins can pass as the hydrodynamic size, post-translational modification, and shape of each protein also determine their ability to pass through the BrM. It has been suggested that complement proteins FHL-1, FD, C5a and mini CR1 (CTx001) can pass through enriched BrM (RPE and choroid removed by gentle scraping) unidirectionally (Clark et al., 2014, 2017). When comparing why C5a can pass through the BrM and not C3a, although both have small molecular weights (C3a: 9kDa; C5a: 8.3kDa), it was shown that C3a has a significantly greater net positive charge at 9.2Q compared to C5a which is 5.2Q. BrM is highly negatively charged due to the glycosaminoglycans present (35, 36), so it could be that the C3a becomes bound on the surface; however, this is not yet proven true.

1.3 Age-related macular degeneration

Age-related macular degeneration (AMD) is a multifactorial degenerative disease of the macula which leads to irreversible blindness. Genetic and environmental factors, as well as complement overactivation being the main factors in pathogenesis and progression of the disease, with the major risk factor being age followed by genetic. **Figure 1- 5** shows how a person with AMD would see. Specifically, the region of macula lutea (high in lutein and zeaxanthin pigment) which is a 3 mm diameter circle centered on the fovea is the most vulnerable to AMD (Curcio et al., 2024). AMD is seen more in individuals above 60 years old, and so it is estimated that 300 million people will be affected by AMD by the year 2040 (Wong et al., 2014) . There are two types of advanced AMD, wet and dry AMD (**Figure 1- 6**). Both are initially characterised by drusen in BrM, followed by choroidal neovascularisation (CNV) in wet AMD and geographic atrophy (GA) in dry AMD. In CNV, the neovascularisation develops above or

below the RPE cell layer and these abnormal blood vessels often leak blood or serous fluid. This leaking results in haemorrhages and/or macular oedema, which can lead to rapid vision loss. In GA, the degeneration of RPE, choriocapillaris and photoreceptors usually starts within the macula and extends to the fovea. Roughly 16% of patients with bilateral GA are registered as severely sight impaired within 6 years (Chakravarthy et al., 2018).

Figure 1- 5. Representation of normal vision against vision with AMD. Image from: Neoretina Eyecare institute.

Both advanced AMD subtypes are preceded by the accumulation of extracellular materials, which leads to BrM thickening. Focal accumulations lead to drusen formation. Drusen can be divided into hard or soft types, which are visible as yellowish spots fundoscopically in the macula region. A defined shape characterises hard drusen, while soft drusen have less sharply demarcated edges (Bird et al., 1995). There is still uncertainty as to the main content of drusen, but known contents include lipids (esterified cholesterol, phosphatidylcholine) and proteins such as, complement factors, apoE, vitronectin and crystallin (Mullins et al., 2000; Crabb et al., 2002; Wang et al., 2010). Prior to drusen formation, diffuse lipoprotein depositions results in BrM thickening and are known as basal laminar deposits (BLamDs) and basal linear deposits (BLinDs). BLamDs and BLinDs are distinguished by their anatomical location, BLamDs are found above the RPE basement membrane, while BLinDs are found beneath RPE basement membrane (Sarks et al., 2007; Sura et al., 2020). BLamDs also have a striated histological appearance due to the long-spaced collagen. BLamD and BLinDs have similar lipid and protein constituents to drusen and are often confluent together (Sarks et al., 2007). Subretinal drusenoid deposits or reticular pseudodrusen, are characterised by being in the subretinal spaces between RPE and photoreceptors and are also seen in AMD (Rudolf et al., 2008; Zweifel et al., 2010).

Single-cell RNA sequencing has revealed transcriptional changes between a patient with intermediate AMD and an unaffected subject (Collin et al., 2023). Comparing the peripheral and macular regions, changes were seen in the macular region (Collin et al., 2023). In particular,

in the macular region, there were reduced RPE cells, increased cadherin 19 (CDH19) and reduced melanocytes in the intermediate AMD subjects compared to the unaffected subjects (Collin et al., 2023). Cadherins are calcium-dependent cell adhesion proteins, which are involved in the functional and structural organisation of cells. RPE cell integrity is partly maintained by adhesion junctions, composed of cadherin homodimers and α catenins, β catenins and p120 catenin linking to actin filaments.

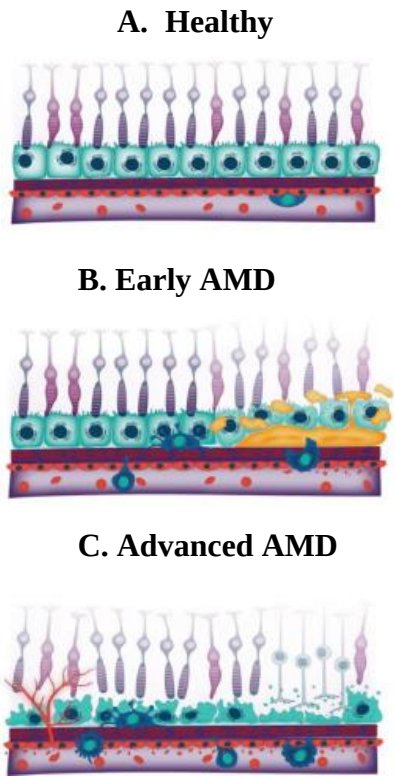

Figure 1- 6. Changes from healthy BrM to early and advanced AMD. (A) In healthy individuals, the tissues are in a state of metabolic equilibrium. **(B)** Early/intermediate AMD is characterised by the accumulation of extracellular deposits such as soft drusen/BLinDs beneath the RPE and subretinal drusenoid deposits above it. **(C)** In the advanced stages, GA and CNV form.

1.4 Complement system

The complement system plays a crucial role in the immune system, bridging innate and adaptive immunity while also playing a central role in the pathogenesis of AMD. Complement is one of the first lines of defence against infection, consisting of a cascade of proteins that protect the host from foreign pathogens. This proteolytic cascade generates opsonins and inflammatory mediators through enzymatic activity, facilitating the clearance of foreign cells by promoting phagocytosis (Epstein et al., 1986). Ultimately, the cascade culminates in the formation of the membrane attack complex (MAC), which can induce cell lysis or trigger inflammatory cell signalling. Complement is an inflammatory cascade, but there are mechanisms in place to prevent its over-activation. For example, it binds to apoptotic cells or immune complexes,

aiding in their removal from damaged tissue or the circulation (Davies et al., 1994; Mevorach et al., 1998). Complement proteins exist in plasma as inactive precursors known as zymogens and are primarily synthesised in the liver (Nesargikar et al., 2012). On cell surfaces, complement proteins function as receptors or regulators, facilitating binding interactions rather than enzymatic activity. However, serum does not get to all the sites where it is required, so some cells produce complement proteins locally (Lubbers et al., 2017). Some immune cells are known to secrete complement proteins including mast cells, monocytes, macrophages, dendritic cells, natural killer cells and B and T lymphocytes (Lubbers et al., 2017). As it is immune privileged, the retina relies on the retinal cells such as RPE, microglial and horizontal cells to secrete local complement proteins.

The human eye has its own local complement expression due to the inability of complement proteins to pass through the blood-retina barrier (Cunha-Vaz et al., 2011). RPE cells have been shown to express complement components such as C3, C5, C1q, factor D (FD) and FI are expressed (Schäfer et al., 2020). RPE cells also exhibit low expression of complement receptor 1 (CR1) on their surface, moderate expression of regulators SERPING1, FH, FI, and robust expression of clusterin (Zauhar et al., 2022; Simmons et al., 2020). Under normal conditions, complement activators are expressed in the retina, with FD and C3 produced by microglial cells and C7 by horizontal cells (Zauhar et al., 2022). In the choroid, EC express FI, while fibroblasts express C3, SERPING1, FH, and clusterin (Zauhar et al., 2022). Additionally, the retinal vasculature endothelium expressed membrane-bound complement regulators such as CD46, CD55, and CD59 (Zauhar et al., 2022).

Numerous studies looking at mouse or monkey complement protein expression in retinal cells allows good guidance (Sugita et al., 2018; Pauly et al., 2019). However, it is crucial to note species-specific differences (Zauhar et al., 2022). In humans, C3 is detected in all retinal cell types; however, in mouse models, only RPE and neurones express C3 (Zauhar et al., 2022). This is the same for FH, which is only detected in human RPE but present in all mice retinal cell types (Zauhar et al., 2022). Species-specific variations should be considered, especially when trying to target complement as a therapeutic target.

The complement system operates through three primary activation pathways: the classical, lectin, and alternative pathways (**Figure 1- 7**). Each pathway, with its unique activation mode, ends in the same common pathway of complement proteins and outcomes.

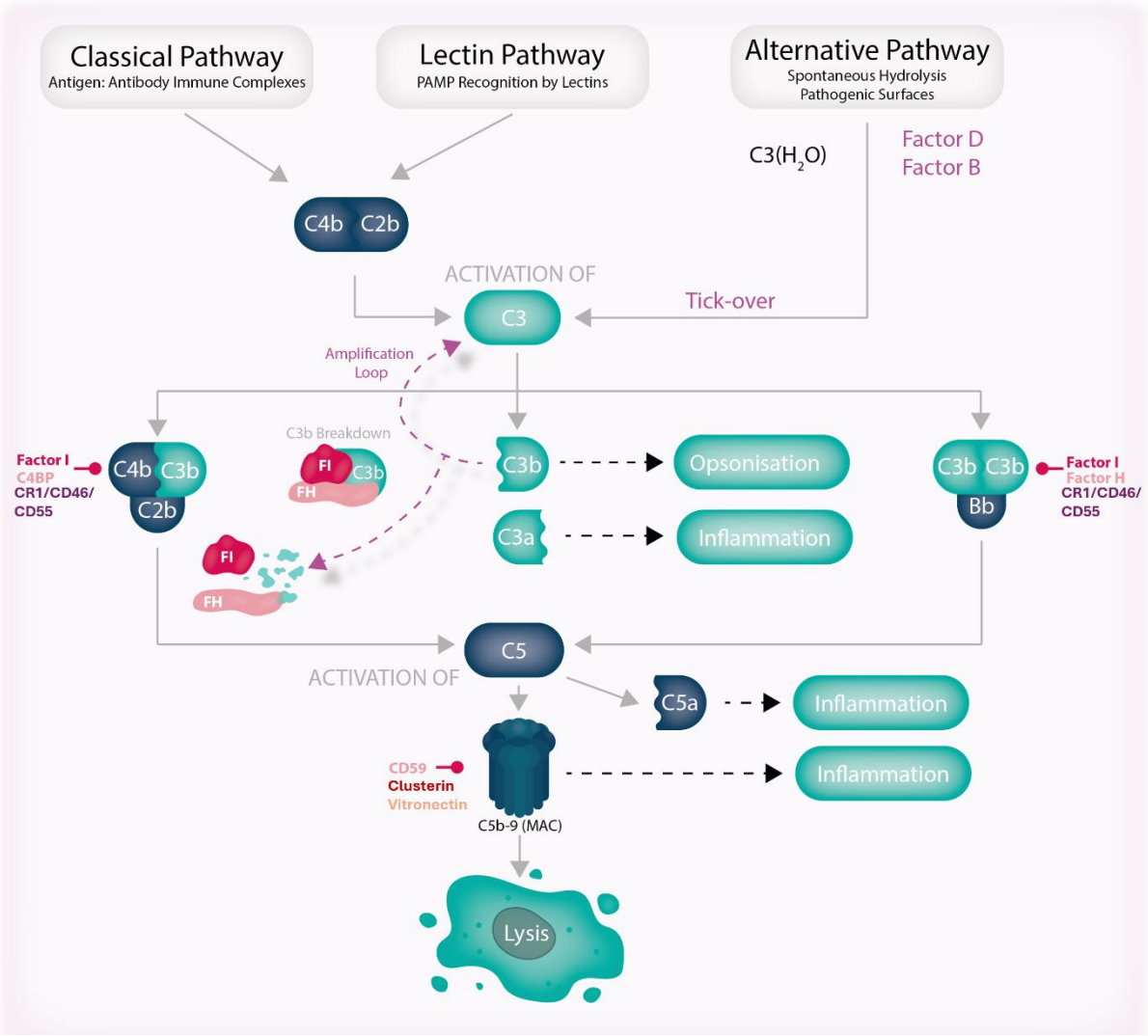

Figure 1- 7. The pathways in the complement system. The three pathways in the complement system are classical, lectin and alternative pathway. The classical pathway is activated via antigen-antibody immune complexes, the lectin pathway via pathogen associated molecular pattern (PAMP) recognition by lectins and the alternative pathway is constantly activated at low levels by the body. All three pathways form the same complement proteins, producing the same outcome and eventually leading to the formation of MAC. Figure adapted from Hammadi S *et al* 2023.

1.4.1 The classical pathway and lectin pathway

The classical pathway (Noris & Remuzzi, 201(N is antibody-dependent activation as it is initiated by binding of C1q to the Fc region of IgM or IgG antigen/antibody complexes (**Figure 1- 7**). The calcium-dependent C1 complex consists of C1q and two molecules each of the serine proteases, C1s and C1r. Upon binding to the antibody Fc region, C1q undergoes a conformational change, which activates C1r. Activated C1r then cleaves and activates C1s. The activation of C1s results in the cleavage of C4 into C4a and C4b, exposing a reactive internal thioester bond in C4b. This thioester bond can then react with hydroxyl groups on cell surfaces,

forming a covalent bond between C4b and the cell surface. This interaction facilitates the binding of C2 to C4b, forming the C3 convertase complex C4bC2a, and releasing C2b, with C2a being the smaller fragment and C2b being the larger fragment. Finally, C3 is cleaved by C3b, producing C3a and C3b, which further propagate the complement cascade.

The lectin pathway (Noris & Remuzzi, 2013) is activated through the binding of the collectin family of plasma proteins, such as ficolins and mannose-binding lectin (MBL), to carbohydrate ligands found on the surfaces of pathogens (**Figure 1- 7**). This binding leads to the activation of MBL-associated serine proteases (MASPs), such as MASP-1, MASP-2, and MASP-3. MASP-2 then cleaves C4 into C4a and C4b, allowing C4b to bind to the cell surfaces by the thioester group covalently. C2, in turn, is cleave into C2a and C2b. This allows the generation of a similar C3 convertase in the classical pathway, C4bC2a. These C3 convertases, which are stabilised by $Mg^{2+,}$ are then able to cleave C3 into C3a and C3b (Cooper & Müller-Eberhard, 1970). In both classical pathway and lectin pathway, the binding of C3b to the C3 convertase allows the formation of the C5 convertase (C4bC2aC3b).

1.4.2 The alternative pathway

This project centres on the alternative pathway (Noris & Remuzzi, 2013) which is constantly activated at a low level, known as the 'tick-over' mechanism (**Figure 1- 7**). The alternative pathway is initiated in the fluid phase via spontaneous hydrolysis of C3. However, productive amplification and complement activation require deposition and stabilisation of surface bound C3b. It begins with the initiated via spontaneous hydrolysis of the thioester bond within the C3 by nucleophilic attack of its thioester domain by a water molecule (Ricklin et al., 2016). This leads to a conformational change to the structure of the C3 which results in the formation of the hydrolysed C3, C3(H_2O). FB binds to C3(H_2O) and the bound FB becomes a substrate for a serine protease known as FD. FD cleaves FB, resulting in the production of Ba and Bb. Bb remains bound to C3(H_2O) to form the C3 convertase of the alternative pathway C3(H_2O)Bb. The C3 convertase can then cleave C3 into C3a and C3b. Properdin, a gamma globulin positive regulator protein binds to the C3 convertase in the alternative pathway to stabilise it.

Nascent C3b generated via fluid-phase activation can covalently attach to nearby surfaces. Surface-bound C3b then binds FB, which is cleaved by FD to form the surface-associated C3 convertase (C3bBb). This complex amplifies complement activation by cleaving additional C3, depositing more C3b on the surface known as the amplification loop. The accumulation of

surface-bound C3b allows for the formation of the C5 convertase (C3bBbC3b), initiating the terminal pathway and membrane attack complex (MAC) assembly.

1.4.3 The terminal pathway

The terminal pathway (25), which is the final phase of all three complement pathways, is initiated by the cleavage of C5 by C5 convertase into C5a and C5b (**Figure 1- 7**). The C5 convertase is formed by the binding of C3b to C3 convertase, this forms C3bBbC3b in the alternative pathway and C4bC2aC3b in the classical and lectin pathway. Properdin also binds to the C5 convertase (and C3 convertase) in the alternative pathway to stabilise it as it extends the half-life of these complexes (Medicus et al., 1976; Fearon & Austen, 1975). The C5 convertase can then cleave C5 into C5a and C5b. C5b binds to C6, forming the C5bC6 complex. C7 can then bind to C5bC6 to form a stable trimeric complex known as C5b-7. C5b-7 binds to cell membranes due to its exposed transient lipid binding site in the molecule. C8 binds to the complex and allows the polymerisation of 10 to 16 molecules of C9, forming the C5b-9, also known as the MAC. The MAC forms a cylindrical channel (10 nm diameter) which disrupts the integrity of target cell membrane. This occurs as the pore permits the uncontrolled flow of ions and water across the membrane, which causes osmotic imbalance, swelling and cell lysis.

1.5 Complement regulation

Complement regulatory proteins play a crucial role in maintaining balance within the complement system by preventing uncontrolled activation or insufficient response. These regulators can be negative, which inhibit overactivation, or positive, which enhance activation when needed. This is carried out by the fluid phase regulators present in the plasma or the membrane-bound regulators on cells. As C3 is the central protein of the complement pathways as it is activated in all three pathways, inactivating C3 is crucial to control complement activation. As C3 is cleaved into C3a and C3b, C3b can be further cleaved into its inactive form, iC3b (**Figure 1- 8**) (Lachmann, 2019). This is conducted in the presence of FI and its co-factor, either FH, CR1 or membrane cofactor protein (MCP). Despite iC3b being inactive, it still retains the ability to bind to CR3 and CR4 to trigger phagocytosis, sometimes allowing it to be a driver of disease pathogenesis (Lachmann, 2019). In the presence of FI and CR1 as the co-factor, iC3b can be converted to C3dg (and C3d), due to the binding affinity of CR1 being the greatest out of the other co-factors (Lachmann et al., 2018). **Table 1- 1**, **Table 1- 2** and **Table 1-**

3, summarises the complement regulators (Bajic et al., 2015; Noris & Remuzzi, 2013; Sándor et al., 2024).

Besides that, CR1, FH and DAF regulates the complement by binding to the ligands C3b and C4b as they share similar binding sites. CR1 competes with Factor Bb and C2a and displaces them from the C3 convertase (C4bC2a in classical pathway and lectin pathway and C3bBb in alternative pathway) and C5 convertase (C4bC2aC3b in classical pathway and lectin pathway and C3bBbC3b in AP). This is termed decay acceleration activity and blocks any further complement activation (Fearon, 1979; Iida & Nussenzweig, 1981).

CR1 acts as a receptor for phagocytosis as immune complexes coated with polymeric CR1 recognises and bind to C3b on deposited on surfaces of pathogens (Fearon et al., 1981; Abrahamson & Fearon, 1983). On immune cells, CR1 can work in conjunction with FC-gamma receptors, which recognise Fc portion of IgG antibodies on the surface of pathogens. These particles are then internalised and eliminated in the lysosome (Ehlenberger & Nussenzweig, 1977; Schorlemmer et al., 1984). CR1 is also involved in the regulation of B and T cell responses. In B cells (Józsi et al., 2002; Erdei et al., 2003; Kremlitzka et al., 2013), CR1 present on the surface controls the proliferation of B cells while in T cells (Török et al., 2015; Wagner et al., 2006), the CR1 present on CD4+ and CD8+ in immune regulation.

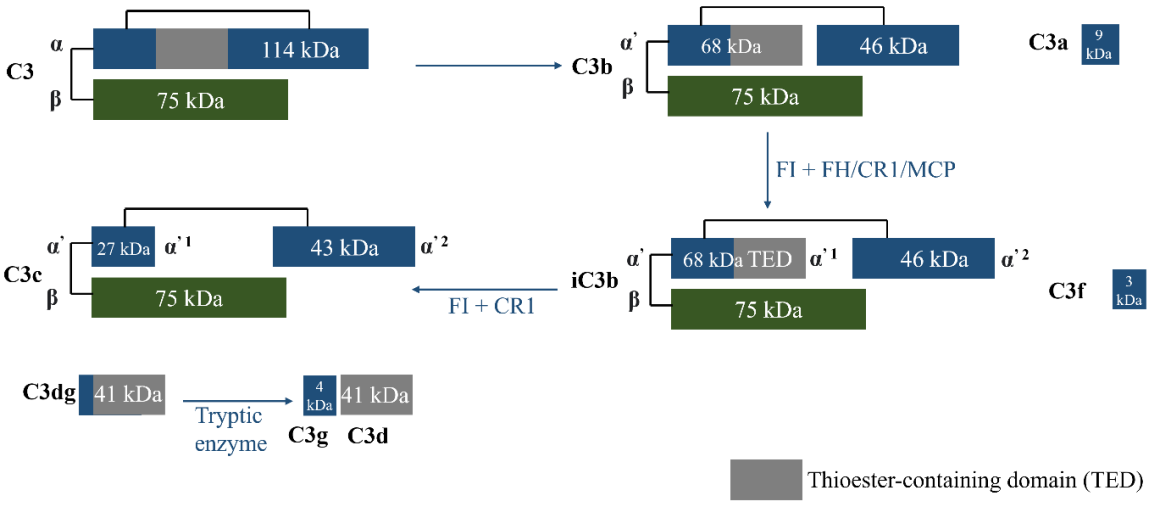

Figure 1- 8. Complement C3b inactivation. C3b forms iC3b by FI and cofactors (FH, CR1 and MCP). iC3b is then further cleaved into C3c and C3dg by FI using CR1 as the cofactor.

Fluid phase Regulator (soluble)	Targets	Function
Properdin	C3 and C5 convertases	Stabilises the C3 and C5 convertases of the alternative pathway

Table 1- 1. Fluid phase positive regulators.

Fluid phase Regulators (soluble)	Targets	Function
Factor H	C3b	Alternative pathway C3 convertase decay and co-factor activity for FI
FHL-1	C3b	Alternative pathway C3 convertase decay and co-factor activity for FI
CFHR1	C3b and C5	Binds to C3b to compete with FH to increase comoplement activation and bind to C5 to inhibit its cleavage and reduce MAC formation
CFHR2	AP C3 convertase	Inhibition of AP C3 convertase by binding to C3b
CFHR3	C3b	Competes with FH
CFHR4	C3b	Enhances AP C3 convertase decay by stabilising the convertase
CFHR5	C3b	Competes with FH, inhibition of C5 convertase
Factor I	Co-factor for FH	Degrades C3b, iC3b, C4b, and iC4b
C4b binding protein (C4BP)	C4b and FI	Binds to C4b to form Classical and lectin pathway C3 convertase and accelerates the decay. C4BP acts as a cofactor for FI.
C1 inhibitor (C1-INH)	C1r, C1s, MASPs	Serine protease inhibitor produced by SERPING1 gene
Vitronectin	C5b-C7 and MAC	Inhibits MAC formation
Clusterin	C2b, C4b and MAC	Inhibits MAC formation
MaP19	MBL and ficolins	Competes with MASP-2 in vitro
MaP44	MBL and ficolins	Blocks MASP transactivation

Table 1- 2. Fluid phase negative regulators.

Membrane-bound regulators	Targets	Function
Complement receptor 1 (CR1)	C3b, C3 and C5 convertase (Classical, lectin and alternative pathway)	Co-factor for FI and decay accelerator for C3 and C5 convertase
Membrane co-factor protein (MCP/CD46)	C3b, C4b	Co-factor for FI
Decay accelerating factor (DAF)	C3b, C4b, AP and CP C3 convertase	Classical, alternative and lectin pathway C3 convertase decay
CD59	C8 in the forming MAC	Inhibits MAC formation

Table 1- 3. Membrane-bound negative regulators.

1.5.1 Complement receptor 1

CR1, or CD35, is a cell surface-bound protein expressed on erythrocytes and immune cells such as macrophages, monocytes, neutrophils, eosinophils, and certain T and B cells (Ross & Lambris, 1982; Fearon, 1980; Ahearn & Fearon, 1989). CR1 also exist as a soluble protein at low levels (50 ng/ml) by the proteolytic cleavage of the extracellular domain from the membrane. The CR1 gene is located on chromosome 1 at locus 1q23 (Weis et al., 1987; Karthikeyan et al., 2007). The dominant allelic variant of CR1 in humans is a 2039 amino-acid protein with a 41 amino acid signalling peptide, a 1930 amino acid extracellular domain, and a 68 amino acid cytoplasmic tail (Krych-Goldberg & Atkinson, 2001; Weisman et al., 1990; HAMER et al., 1998) (**Figure 1- 9**). The extracellular domain is comprised of 30 complement control protein repeat units (CCP) (Krych-Goldberg & Atkinson, 2001; Klickstein et al., 1987) (**Figure 1- 9**). The CCP are arranged into four long homologous repeat domains (LHR), which are LHR-A, LHR-B, LHR-C and LHR-D. Each LHR is composed of seven CCP. There is a 99% homology between CCP within CR1, such as between CCP 8-10 and CCP 15-17 and between CCP 1-3 and CCP 24-26 (Krych-Goldberg & Atkinson, 2001) (**Figure 1- 9**). CR1 is highly glycosylated, and the glycans are exclusively N-linked (Lublin et al., 1986).

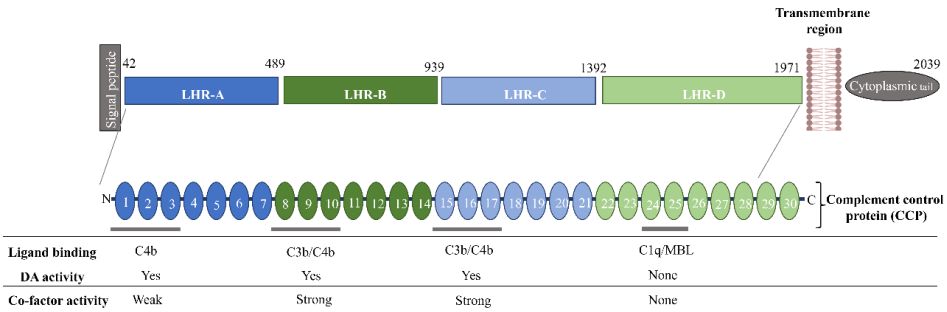

Figure 1- 9. The structure of human CR1. The schematic of human CR1 is composed of an N terminal extracellular domain, a short cytoplasmic tail, and a transmembrane region. The signalling peptide assists in the trafficking of mRNA to the endoplasmic reticulum for protein synthesis. The extracellular domain contains four long homologous repeats (LHR), which are LHR-A, LHR-B, LHR-C and LHR-D.

There are four main CR1 length variant polymorphism, they are distinguished by how many LHRs they have. The variants are CR1*1 (A) with 4 LHRs, followed by CR1*2 (B) with 5 LHRs and the two rare forms, CR1*3 (C) with 3 LHRs and CR1*4 (D) with 6 LHRs, with molecular weights of 190kDa, 220kDa, 160kDa, and 250kDa, respectively (Dykman et al., 1985). Hence, the longer isoforms have an extra LHR-B which contains additional C3b/C4b binding sites (**Figure 1- 10**) (Kisserli et al., 2017). Isoform CR1*2, the longest isoform has been shown to be associated with Alzheimer's disease (Kisserli et al., 2017). However, more functional studies on understanding the impact of CR1 length isoforms are needed to understand the disease risk and progression.

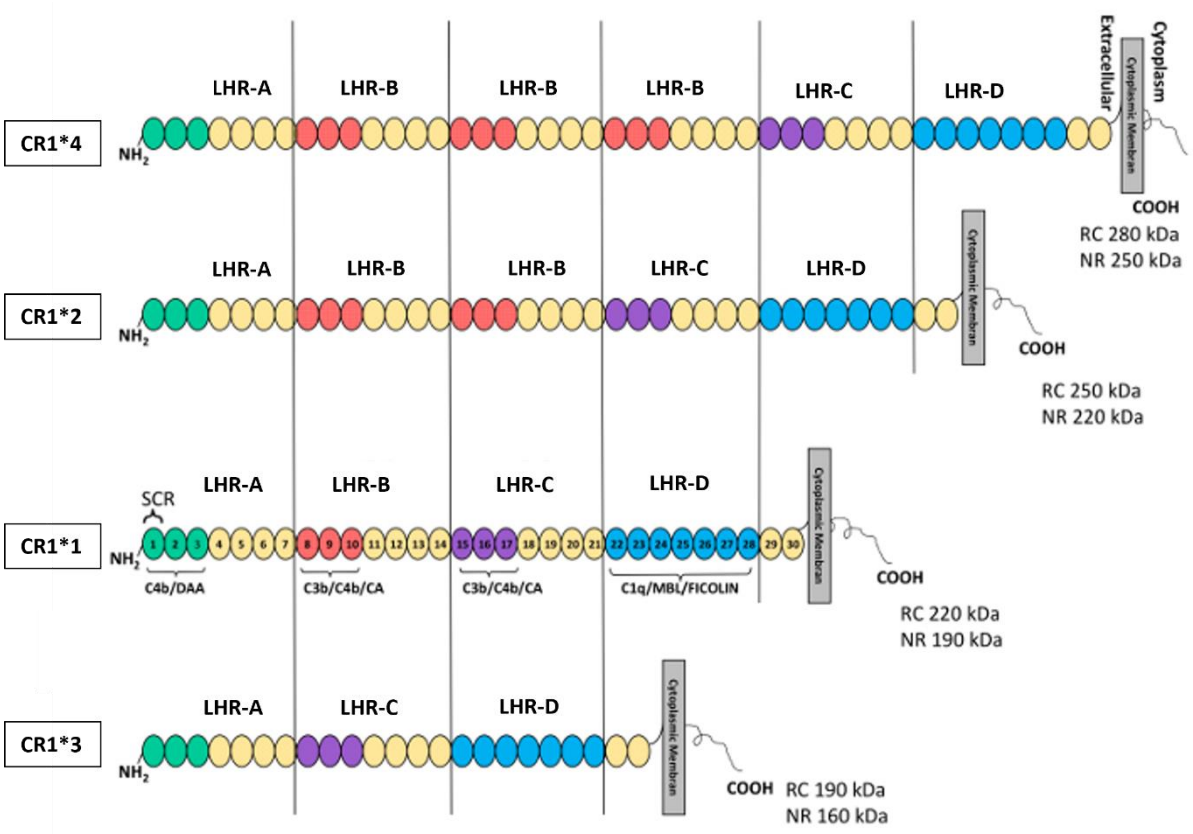

Figure 1- 10. Schematic overview of CR1 length isoforms. From the longest isoform, CR1*4 followed by CR1*2, CR1*1 and CR1*3. Figure adapted from Kisserli *et al* 2017.

1.6 Risk factors for age related macular degeneration

1.6.1 Genetic risk factors

Gene variants that increase the risk of AMD have been identified by genome-wide association studies (GWAS) in two significant loci on chromosomes 1 and 10. The first locus, identified in

2005 within chromosome 1 (1q31), involves the 'regulators of complement activation' (RCA) cluster, with C*FH* and its related genes (Fritsche L, 2013; Klein et al., 2005). The common Y402H polymorphism in FH, in which tyrosine is replaced by histidine at position 402, has consistently been identified as a major risk factor for AMD (Day et al., 1988). Within chromosome 10 (10q26), the major risk loci involve the open reading frame on the gene for age-related maculopathy susceptibility 2 (*ARMS2*), which is an ECM protein of unknown function (Fritsche L, 2013; Iyengar et al., 2004; Kortvely et al., 2010) and high-temperature requirement 1 (*HTRA1*), which is a serine protease that processes ECM proteins (Yang et al., 2010; DeWan et al., 2006). GWAS studies have also identified 63 other discrete loci involved in AMD (Fritsche et al., 2016; He et al., 2024). These include genes involved in extracellular remodelling, such as tissue inhibitor metalloproteinases 3 (*TIMP3)* and collagen type VIII alpha 1 chain (*COL8A1*), other complement system proteins (*CFB, CFI, C2, C3, C9*), cholesteryl ester transfer protein (*CETP*), genes involved in the metabolism of cholesterol, such as adenosine triphosphate (ATP)-binding cassette transporter (*ABCA1*), apolipoprotein E (*APOE*), and lipase C and lastly, genes in less defined pathways, such as rho GTPase activating protein 21 (*ARHGAP21*) and beta 3-glucosyl-transferase (*B3GALTL*) (de Breuk et al., 2021; Fritsche et al., 2016).

1.6.2 Environmental risk factors

Smoking, as we know, is harmful to the body. It has been shown to increases the probability of developing AMD by 10-15% (Chen et al., 2010). Smoking also increases the oxidative stress and inflammation of RPE cells, further exacerbating the chances of vasoconstriction and abnormal blood vessel growth of choriocapillaris (Roth et al., 2004).

Besides that, diet also poses a risk as a higher intake of fats in diet, such as vegetable fats, polyunsaturated fats and monounsaturated fats and linoleic acid is associated with greater risk of advanced AMD (Seddon, 2001). Diets high in omega-3 fatty acids are inversely associated with AMD when intake of linoleic acid is low (Seddon, 2001). The AMD risk variant 402H has been associated with the accumulation of lipoproteins such as B48 and A1 in the RPE/choroid of aged mice fed with high cholesterol diet (Landowski et al., 2019). Studies on the serum or plasma samples of AMD patients have revealed a strong correlation between increased large and extra-large high-density lipoprotein (HDL) levels and decrease in very low-density lipoproteins (VLDL) and amino acids level (Acar et al., 2020). These were all associated with increased complement activation and independent of AMD status. Other studies have shown

the presence of FH in large HDL particles indicating FH could be getting trapped preventing their protective function (Zhang et al., 2019).

1.6.3 Complement in age-related macular degeneration

There have been numerous studies exhibiting a strong association between the complement system and AMD (Clark et al., 2010, 2014). Complement overactivation is thought to initiate in the choriocapillaris layer in people with early AMD (Whitmore et al., 2015; Mullins et al., 2014; Keenan et al., 2015). Precisely, the overactivation of the alternative pathway, where most of the genetic risk variants have been discovered, is thought to be the main contributor to the pathogenesis of AMD. In early AMD, CEC loss is seen, and as GA develops, more intense CEC loss is observed (Mullins et al., 2011; Sohn et al., 2019). FH is present in drusen and BLamD deposits, which may contribute to its reduced levels in retinal region of AMD compared to controls. While plasma-derived FH is abundant, local factors—such as extracellular deposits, increased consumption due to complement activation, or impaired local production—may reduce its availability in the choroid. Notably, C-reactive protein (CRP) levels are increased in early and wet AMD but decrease alongside FH in atrophic regions of GA (Bhutto et al., 2011; Fett et al., 2012). A study revealed that FH was significantly lower in AMD patients when compared to the control patients (Bhutto et al., 2011).

Local complement production of FH in the choroid plays an important role in AMD. In a model of AMD iPSC-derived human CEC, it was shown that the overexpression of FH protects the CECs against damage by MAC deposition (Mulfaul et al., 2022). FH in the choroid is either produced locally or derived systemically, as FH is produced by the liver and is circulated into the choroid, including the choriocapillaris via short posterior ciliary arteries (Hayreh, 2004). In liver transplant patients with discordant donor and recipient genotypes, the AMD risk is associated with the recipient genotype. This suggests that the local production of FH plays a more prominent role than the systemic FH (Khandhadia et al., 2013). As FH is a cofactor for FI, the lack of FH may decrease inactivation of C3b.

The other cofactor for FI, CR1, which is membrane-bound, is not well expressed on RPE cells (Simmons et al., 2020). Hence overexpression of CR1 on ARPE19 cells with a plasmid containing CR1 was successful in inhibiting the deposition of C3b and C6, providing promising results for complement inhibition as a therapeutic strategy (Simmons et al., 2020).

Interestingly, individuals carrying rare genetic variants of FI have low systemic levels of FI, and these variants are strongly associated with an increased risk of AMD (Hallam et al., 2020). This worsens the development of AMD because FI, which is secreted by CECs and RPE cells, does not diffuse through BrM (Clark et al., 2017). As a result, it is unable to regulate overactivation of the complement system both in the choroidal side and in the sub-RPE space between the BrM and the RPE, contributing to AMD progression.

Besides that, blocking C5 activation protects the retina as it prevents the formation of C5a and C5b (Rossi et al., 2014). Targeting C5 preserves C3 function, allowing for a balance between complement inhibition and activation. Specifically, blocking at the level of C5 ensures that C3 is not inhibited, enabling surfaces and bacteria to be opsonised with C3b. This approach avoids the complete blockage of the complement system, which could otherwise increase the risk of infection.

In AMD, studies have shown other genetic association with systemic factors as a risk factor for AMD as an increase in the plasma or serum concentration of tumor necrosis factor (TNF-α, TNFII, CRP, CXCL10, IL-6, IL-17and IL-22 is detected in AMD patients (Faber et al., 2015; Krogh Nielsen et al., 2019; Liu et al., 2011; Cousins, 2004). Pre-exposure of primary RPE and ARPE19 cells to TNF-α and interferon gamma (IFN-γ) was shown to promote the alternative pathway of the complement system with MAC deposition (Udsen et al., 2022). In addition to this, oxidative stress in AMD has also been shown to induce complement protein production or activation. ARPE19 cells grown as polarised monolayer exposed to hydrogen peroxide (H_2O_2) have shown an increase in the gene expression and the accumulation of C3, CR3, C5, C5aR1, properdin, cathepsin B, cathepsin L (Trakkides et al., 2019).

Similarly, the supernatant from the culture of human fetal RPE (hfRPE) cells grown on BrM from AMD patients showed an increase in matrix metalloproteinases 2 (MMP-2) levels, indicating ECM turnover is impaired and had increased levels of C3a when compared to control (Fernandez-Godino et al., 2018).

These studies suggest that the complement system is overactivated in AMD, which could be due to low FI systemically, insufficient FH, increased drivers of complement activation (such as drusen), or another co-factor (Bakri et al., 2023; Heesterbeek et al., 2020; Simmons et al., 2020; Hallam et al., 2020). Hence, targeting complement seems promising in allowing the activity of complement to be restored to prevent overactivation.

1.7 Age-related changes to Bruch's membrane

BrM undergoes significant changes with age. These changes affect the permeability of molecules that diffuse through BrM. Due to the imbalance of diffusing substances, these changes may lead to an increased rate of inflammation or infection. The anatomical, biomechanical, and permeability changes with age are discussed below (**Figure 1- 11** and **Table 1- 4**).

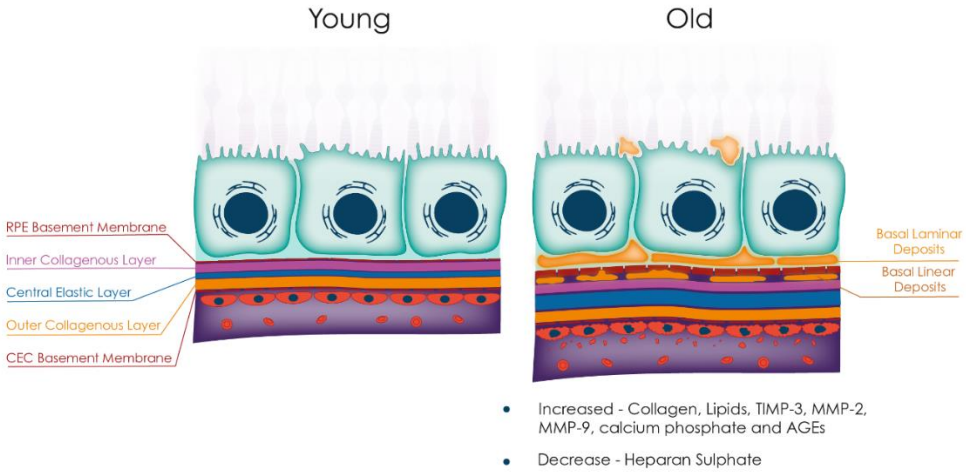

Figure 1- 11. Schematic showing age-related changes to layers of BrM. In the older retina, BrM thickens with basal laminar and basal linear deposits, increased depositions of collagen, lipids, TIMP and MMPs with decrease in heparan sulphate. Figure adapted from Hammadi S *et al* 2023.

1.7.1 Anatomical and biomechanical changes

The anatomical and biomechanical changes that occur to BrM with ageing include an increase in calcification of elastin fibres, collagen fibres and turnover of glycosaminoglycans (Ramrattan et al., 1994) with the accumulation of advanced glycation end product (AGE) and lipids in the deeper layer of BrM (Glenn et al., 2009; Curcio et al., 2001; Huang et al., 2008). These changes would affect the charge of BrM, thereby altering its diffusion capabilities. In turn, AGEs, such as carboxymethyl lysine and pentosides, cause inflammation via the activation of AGE receptors on RPE and immune cell (Pietkiewicz et al., 2008). Due to the heterogeneous distribution of BrM, as mentioned earlier, the thickening appears first at the periphery and progressively towards the macular region (Chong et al., 2005; Newsome et al., 1987). This increase in thickness leads to a reduction in flexibility, elasticity, and permeability (Moore & Clover, 2001). BLamDs and BlinDs are observed with age, with BLamDs present more than BlinDs.

Laminin and proteoglycans are essential for BrM structural properties and for RPE attachment, which changes with age. RPE cells synthesise laminin 1 (α1ß1γ1), 5 (α3ß3γ2), and 10/11 (α5ß1/2γ1), to facilitate its adhesion to BrM via integrin-mediated mechanism (Aisenbrey et al., 2006). Heparan sulphate proteoglycans (HSPGs), which are a key binder for FH during complement regulation, are seen to decrease with age (Keenan et al., 2014), and hence, this may lead to an increase in complement activation and inflammation (Clark et al., 2006; Prosser et al., 2007). This could worsen the impact of the FH Y402H polymorphism, a significant genetic risk factor for AMD, as it has been suggested that the variant protein exhibits weaker binding to HSPGs compared to the wild-type protein (Clark et al., 2006; Prosser et al., 2007).

With age, BrM remodelling accumulates minerals such as zinc and calcium within the interstitial matrix (He et al., 2007). The MMPs and TIMPs at this level are active to ensure ECM turnover (Cabral-Pacheco et al., 2020). MMPs and TIMPs play a crucial role in regulating ECM. However, the presence of these minerals affects the activity of these enzymes, which in turn leads to an effect on the equilibrium causing ECM turnover (Chong et al., 2005). Specifically, changes in matrix molecules such as an increase in MMPs 2 and 9 and TIMP-3, their inhibitor may also contribute to BrM thickening (Guo et al., 1999; Kamei & Hollyfield, 1999; Handa et al., 1999a).

Functional changes	Anatomical changes
Decrease in elasticity	Accumulation of lipids, TIMP-3, MMP-2 and 9, calcium, zinc and AGEs
Decrease in water permeability	BrM thickening
Decrease in protein permeability	Reduced in heparan sulphate
Decrease in complement control protein permeability	Increase in complement activation

Table 1- 4. Functional and anatomical changes to BrM with age.

1.7.2 Permeability changes

The diffusion of water across BrM, measured with Ussing chamber, shows it decreases with age (Moore et al., 1995; Starita et al., 1996, 1997; Hillenkamp, 2004). This diffusion loss is seen the most in the ICL surrounding the macular area (Starita et al., 1997). Besides that, protein transport decreases with age. A study conducted by Moore DJ *et al* showed a 10-fold reduction in the permeability of serum proteins from the first to the ninth decade of life with a decrease from 3.5 10^{-6} to 0.2x10^{-6} cm/s (Moore & Clover, 2001). As water permeability decreases with age, this disrupts the osmotic pressure of diffusion molecules, affecting the ability of molecules

to diffuse. This study also observed that in the younger donors, BrM was permeable to serum proteins with molecular weights greater than 200kDa, while in the elderly donor, it decreased to 100kDa (Moore & Clover, 2001). However, recent research shows that complement proteins with molecular weight less than 100kDa could not diffuse through BrM (Clark et al., 2017). This shows that other mechanisms could influence this diffusion and that these models do not capture the complex changes of human physiology occurring with age. With age, the permeability of fluorescein-isothiocyanate-labelled (FITC) dextran (21.2kDa) across BrM in the macular region declines significantly (Hussain et al., 2010). By the time a person reaches their ninth decade (around 80-90 years old), the permeability drops to about 6.5% of what it was in the first decade of life (Hussain et al., 2010). In comparison, the peripheral region retains about 44% of its initial permeability over the same period. Similarly, FITC-albumin (65 kDa) exhibits an age-related reduction in diffusion (Lee et al., 2015).

1.8 Stem cells

Stem cells are characterised by infinite self-renewal capability and their ability to differentiate into different specialised cells. There are various types of stem cells with different potency to differentiate into specialised cells (Bindu A & B, 2011):

- Pluripotent stem cells – These are cells that give rise to almost any cell type with the limitation of forming an entire organism. Examples are human embryonic stem cells (hESCs) and human induced pluripotent stem cells (hiPSCs). hiPSCs are induced and reprogrammed to form pluripotent from non-pluripotent cells, such as fibroblasts.
- Multipotent stem cells—These are specialised cells that give rise to a limited range of cell types, such as hematopoietic stem cells (HSCs), which become red blood cells, platelets, or white blood cells.
- Totipotent stem cells- These are the most versatile type as they can differentiate into all cell types, such as the zygote, which undergoes cell division to reproduce the whole organism.
- Unipotent stem cells – These are cells with limited potential to differentiate as they can only produce of cell type with limited potential to self-renew. Example is muscle stem cells (satellite cells) that can only become muscle cells.

Pluripotent stem cells are unspecialised cells that can differentiate into any cell type of the three embryonic germ layers (endoderm, mesoderm, and ectoderm). These cells are capable of self-renewal and can be cultured for an indefinite period *in vitro*. The two subcategories of pluripotent stem cells are hESCs and hiPSCs. For years, researchers have explored the potential

of pluripotent stem cells, leveraging their self-renewing nature, high proliferative capacity, and ability to generate specialised cell types. However, it was not until 2006 that the breakthrough eased the use of pluripotent stem cells (Takahashi & Yamanaka, 2006a). This alternative method involves reprogramming somatic cells to produce hiPSC, which circumvents many of the complex ethical issues associated with hESCs (Takahashi & Yamanaka, 2006a).

hESC are derived from the inner cell mass of the blastocytes. Ethical controversies surrounding the derivation of hESCs and the limited supply of human embryos have paved a new way forward, offering an alternative without ethical constraints: the use of hiPSC. hiPSC RPE is derived from various somatic cells, such as fibroblasts, using multiple reprogramming techniques. Both ESCs and hiPSCs are similar in terms of morphology and surface markers (Takahashi et al., 2007; Yu et al., 2007a). However, there have been reports of variability in their *in vitro* differentiation potential between the two cell types as they differ in several key aspects, including their epigenetic memory, transcriptional profiles, and efficiency in generating specific cell types (Narsinh et al., 2011). iPSCs often retain residual epigenetic marks from their somatic cell of origin, which can influence their differentiation bias compared to ESCs. Additionally, transcriptional differences between iPSCs and ESCs may contribute to variability in differentiation outcomes, highlighting the need for tailored approaches depending on the application.

The advantage of iPSC-derived models is that their human origin makes them more physiologically relevant to human conditions compared to animal models. This allows modelling by utilising iPSC to serve as a foundation for drug trials and disease modelling, decreasing the need for animal models. An example of this is the modelling of the retinal organoids. Retinal organoids are lab grown miniature full thickness neurosensory retinas derived from pluripotent stem cells, including light sensitive photoreceptors and are currently revolutionising research in all fields (Hallam et al., 2018; Mellough et al., 2019; Chichagova et al., 2019; Dorgau et al., 2022; Cora et al., 2019; Zhong et al., 2014; Capowski et al., 2018; Fernando et al., 2022; Saha et al., 2022; Wahlin et al., 2017). These 3D cellular structures hold immense potential, offering a promising future for retinal disease treatment. While *in vivo* tissue contains the vasculature that retinal organoids lack, recent breakthroughs show significant success towards the direction of vascularised organoids (Volker Busskamp; Kritika Sharma, 2023). Some limitations to the use of retinal organoids are the limited immune system influence, as they currently only incorporate microglia short term (Kurzawa-Akanbi et al., 2024). Besides that, the lack of the presence of BrM, which plays a crucial role in understanding the diffusion property (Kurzawa-Akanbi et al., 2024).

1.9 Modelling the outer retina

To understand the pathology of a disease or potential therapies, it is crucial to have a model with as high a resemblance to human disease as possible. A model that mimics natural physiology will significantly benefit and ensure the best outcome. When looking at models of the retina, RPE cells cultured on transwells are the default most accessible 2D models to replicate. Several types of RPE cells are commonly used; these are fRPE, ARPE 19 and iPSC derived RPE cells. In our research, we utilise iPSC-RPE cells. The somatic cells used to generate iPSCs are reprogrammed into a pluripotent state using Yamanaka factors, namely *Oct4, Sox2, Klf4* or *c-Myc* or *OCT4, SOX2, NANOG and LIN28* (Takahashi & Yamanaka, 2006b; Yu et al., 2007b). Once they reach pluripotent state, they undergo differentiation, which takes about six weeks using RPE maintenance medium into iPSC-RPE cells. The resulting iPSC-RPE cells exhibit the features of native RPE, including pigmented monolayer with tight junction, phagocytosis of POS and RPE gene and protein expression (Geng et al., 2017; Miyagishima et al., 2017; Westenskow et al., 2012).

Besides that, fRPE are primary cells harvested directly from the retinal tissue of foetuses between 10 to 16 weeks gestational age. ARPE-19 is an immortalised human RPE cell line originally derived from the retina of a 19-year-old human donor. ARPE-19 have been adapted to endure continuous culture, allowing them to be passaged many times. iPSC-RPE, from the name, are cell lines derived from stem cells and are fully differentiated and perform the RPE function. When modelling, it is crucial to maintain the type of cells used to maintain consistency for achieving reproducible results. Here, two main approaches of modelling the outer retina are discussed. Those utilising human derived BrM and RPE cells and those utilising a synthetic BrM and RPE cells (**Figure 1- 12**).

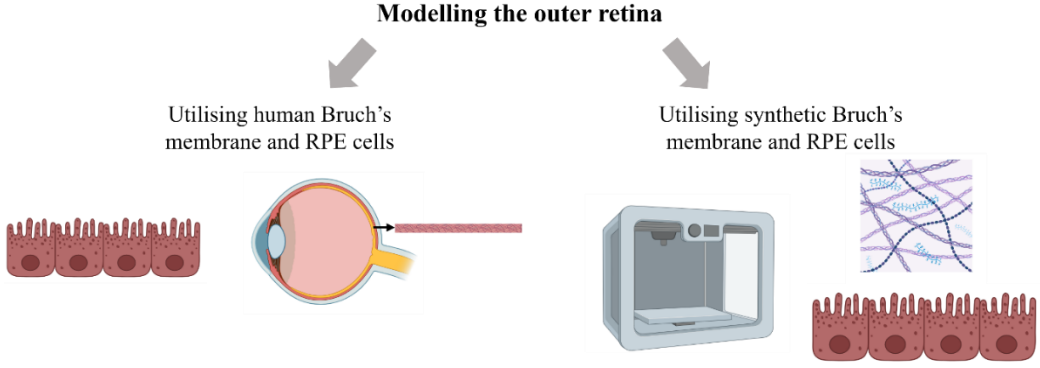

Figure 1- 12. Approach to modelling the outer retina. Researchers are currently investigating two approaches: the first uses human BrM and RPE cells, and the second uses synthetic BrM and RPE cells, such as 3D printing and synthetic culture surfaces. Figure was made using Bio-render.

Firstly, when modelling the outer retina, it is crucial to understand the synergetic relationship between RPE, BrM mimic and CECs. Sakamoto *et al* demonstrated that RPE cells play a dual role in promoting and inhibiting CECs growth and development (Sakamoto, 1995). When RPE cells were introduced at the start of the culture, it promoted angiogenesis and when introduced at day 14 (a later stage), it inhibited the growth of pre-existing endothelial tubes. RPE also secrete VEGF towards the CEC to promote their growth (Saint-Geniez et al., 2009b; Blaauwgeers et al., 1999).

Besides that, Hamilton *et al* demonstrated that co-culturing human umbilical vein endothelial cells (HUVECs) with ARPE-19 on the opposite side of an amnion membrane resulted in the induction of a fenestrated EC phenotype (Hamilton et al., 2007). Co-culturing RPE with HUVECs have also enhanced RPE barrier properties and increased the expression of RPE genes such as RPE-65 (Peng et al., 2013).

The physical property of the ECM, in particular collagen stiffness, plays a role in RPE maturation (Benedicto et al., 2017). Stiff collagen anchor points in the ECM promoted the formation of tight junctions in RPE cells through B1-integrin signalling (Benedicto et al., 2017). This activates Rac1 and PhoA/ROCK pathways, which regulate the assembly of tight junctions in RPE cells (Benedicto et al., 2017). These findings demonstrate that the type of ECM used to culture RPE cells plays a crucial role in the maturation of RPE cells. These findings also suggest the importance of RPE, a suitable BrM mimic, and EC, which are essential to model the outer retina.

1.9.1 Modelling by utilising RPE and *ex vivo* Bruch's membrane

Recently, several studies have attempted to use *ex vivo* BrM, with RPE cells to model the outer retina. Some have also shown success in creating vascularised models with an added element of the choriocapillaris (Song et al., 2023). Studies as early as 1998 (Castellarin et al., 1998) showed the successful integration of fRPE on human cadaver BrM. The human cadaver BrM used was debrided to remove RPE cells before the addition of fRPE, which were incubated for 24 hours. This study successfully showed that the RPE cells could attach with their intact cellular morphology. Pre-coating BrM with vitronectin, laminin or fibronectin increased the RPE cells' attachment rate. Studies have also shown that RPE cells' reattachment to BrM was highest on the inner aspect of BrM and decreased as the deeper layers of BrM were exposed,

indicating that gently handling BrM is essential in ensuring RPE cell attachment (Ho & Del Priore, 1997).

The success of culturing iPSC-RPE cells onto human BrM has been shown more recently. The native RPE cells on the human BrM were removed by 0.02 M ammonium hydroxide for 20 minutes at room temperature before the addition of the iPSC-RPE cells (Cai et al., 2018). However, it was not shown definitively whether adding ammonium hydroxide for 20 minutes was sufficient to remove the remaining cellular material, which is crucial to ensure the success of the re-culture with iPSC-RPE cells. Chirco K *et al* utilised four protocols to decellularise BrM before re-cellularising with monkey CECs (Chirco et al., 2017). The study identified the best of the 4 decellularisation protocols tested for removing the most cellular material while maintaining ECM components crucial for re-cellularisation. In this thesis, the best decellularistaion protocol is describes as Chirco K *et al* protocol (CP).

Numerous earlier studies have aimed to reverse the AMD phenotype by transplanting RPE cells onto diseased BrM. To improve the success of transplantation researchers studied the culture of RPE cells onto *ex vivo* BrM, particularly the group of M Zarbin. In 2002 (Tsukahara et al., 2002), they examined the attachment of RPE cells harvested from aged donors (hRPE) to *ex vivo* BrM with either preserved or removed basement membranes. Their findings showed that primary hRPE cells attached at higher rates to BrM with an intact membrane than an exposed inner collagenous layer. However, many cells began dying after 1 hour, suggesting that modification of BrM or RPE cells was required to enhance cell attachment and survival.

Their research progressed over several years, all focusing on the challenges of RPE adhesion to aged debribed submacular BrM. Their earlier research looked at identifying why uncultured primary hRPE cells do not grow on aged debrided submacular human BrM after 24 hours in culture (Zarbin, 2003). Uncultured hRPE cells were defined as those directly taken from a donor without prior maintenance in a culture environment. Their purpose was to understand if culturing alters hRPE cell integrin expression, thus allowing them to grow on aged BrM. Their study revealed that uncultured aged hRPE and fRPE had low levels of integrin (α1-5 mRNA and α3 and β5 mRNA respectively) subunits which were crucial to form receptors for laminin, collagen and fibronectin. Their study suggested that culturing RPE increases integrin expression, potentially improving their adhesion to BrM.

Building on their findings, their study progressed into understanding if the culture surface may be improved to allow better RPE cells attachment and coverage. In 2005 (Gullapalli et al., 2005) they looked at human fRPE culture onto aged debribed submacular human debrided BrM. BrM is debribed to expose the native RPE basement membrane and the inner collagenous layer, allowing the transplanted RPE cells to attach. To promote better adhesion, BrM was pre-treated with bovine corneal endothelial cell-extracellular matrix (BCE-ECM). Their study revealed that the cells seeded on the BCE-ECM had better RPE cell coverage and morphology. In 2010 (Sugino et al., 2011), the group studied whether resurfacing debrided submacular human BrM with cell-deposited ECM would improve RPE cell attachment and survival. BCE were cultured on the ICL of debrided submacular human BrM to allow ECM deposition to occur. The BCE were then removed to expose the deposited ECM and fRPE cells were cultured on for 1, 14 and 21 days. The BCE treated cultures showed significantly higher RPE nuclear density than the controls (without BCE cells). The RPE also expressed more differentiated features on the BCE-ECM treated membranes however, they had less mRNA for bestrophin or RPE65.

Since integrins have been shown to play a role in improving RPE adhesion (Zarbin, 2003) they further studied changes in integrin expression in primary adult hRPE cells after culture to further understand the role of integrins in RPE adhesion to aged debrided submacular human BrM (Gullapalli et al., 2008). The hRPE cells were cultured on BCE-ECM and compared to uncultured hRPE. Cultured hRPE showed an increase in the expression of α1-5 whilst the levels of the α2, 3 and 5 subunits in particular were low in uncultured adult hRPE. The α1-3 subunits were shown to co-localise with phosphorylated focal adhesion kinase (PFK) at focal adhesion points in hRPE spread on laminin. Subunits α 2 and α3 co-localised with phosphorylated FAK at the focal adhesion points of RPE cells on collagen 1. This study showed that blocking the α1 subunit alone or blocking with α2 and/or α3 significantly reduced hRPE cell adhesion to laminin. When compared to the control, less hRPE cells spread on aged debrided subacular human BrM when α1-5 subunits were blocked. They concluded that α1-5 subunits were upregulated by culturing hRPE cells on BCE-ECM and were essential for hRPE cell attachment on submacular debrided human BrM.

These studies, in summary, suggested that culturing donor RPE cells prior to adding them onto debrided BrM improved the cells' adhesion and survival rate. Furthermore, the culture surface plays a role in the adhesion of RPE, where ECM on BrM and integrins on RPE cells promoted and improved adhesion.

1.9.2 Modelling by utilising Synthetic Bruch's membrane

Many studies have focused on using a variety of synthetic and naturally occurring BrM biomimics instead of utilising *ex vivo* BrM for *in vitro* models. Palanisamy K *et al* (Palanisamy et al., 2019), isolated primary hRPE and hCEC from donor's eyes, cultured on a polyester transwell membrane. The transwell was coated with fibronectin, and hCECs were seeded on the apical side with hRPE on the basal side. The model mimicked some features of human disease e.g., administration of VEGF increased the permeability to FITC dextran (20 kDa) through the RPE monolayer. Chen L *et al* (Chen et al., 2017), used a microfluidic device with an upper layer, followed by a porous membrane and a lower layer. The porous membrane was fabricated from a 2:1 mixture of poly(dimethylsiloxane) (PDMS) and hexane into a thickness of 6.5 µm and the pore diameter of 10 µm. ARPE-19 cells and HUVEC were co-cultured in the microfluidic device.

To mimic BrM, Manian K *et al*, (Manian et al., 2021) developed a hydrogel-based extracellular matrix (6 mm diameter and 2 mm thickness) as the BrM. The hydrogel was synthesised using an 8-arm poly(ethylene glycol) norbornene (PEG-NB) polymer, which are crosslinked with MMP-sensitive peptide and arginine-glycine-aspartic acid (RGD) peptide to help cells adhere. This mixture is photopolymerised to form the hydrogel. They then integrated iPSC-derived ECs, RPE, and mesenchyme stem cells (MSCs) from human donors onto the hydrogel-based ECM. This model has allowed the replication of key features for healthy and diseased eyes. Human iPSCs-derived MSCs were cultured, followed by adding the hydrogel, hiPSC-ECs, RGD adhesive peptides, and, lastly, the hiPSC RPE cells were cultured as a monolayer on the apical surface. EC fenestration typical of CEC was demonstrated in the model by positive staining for plasmalemma vesicle-associated protein (PLVAP).

Similarly, Kim J *et al* (Kim et al., 2021) developed a model using a 3D printed BrM-derived porcine ECM (BM-ECM) to mimic BrM which allowed high attachment of ARPE-19. BM-ECM was prepared by treating the porcine BrM with 1% sodium dodecyl sulfate (SDS) and 3% pepsin in acetic acid for 72 hours. Next, 3D printing technology was also utilised with the BM-ECM to produce fibrillar structures resembling natural BrM. The ARPE-19 on the ECM showed a variety of key functions, such as the phagocytosis of POS, expression of phototransduction enzymes, and secretion of anti-angiogenic factors.

Galloway C *et al* (Galloway et al., 2018) cultured hiPSC-RPE monolayer onto a bombyx mori silk fibroin (BMSF) scaffold. BMSF was used to replicate BrM when the isolated fibroin protein is dissolved in a solution and cast as a film; once dried, it results in a strong and flexible transparent film with customisable thickness, permeability, and ECM components (Shadforth et al., 2012, 2015). The BMSF were produced by dissolving fibroin in aqueous solution to form a 3 μm thick membrane which were used to either coat tissue culture plastic (TCP) or on its own within a custom design Teflon chamber. However, BMSF membranes have shown an increase permeability to dextran when compared with native-aged BrM (Shadforth et al., 2012). As controls, laminin-coated TCP or laminin-coated polyethylene terephthalate (PET) transwell inserts were used.

Other studies have co-cultured ARPE-19 and HUVECs on amnion membranes but did not show phagocytosis activity, secretion of pigment epithelium-derived factor (PEDF) or RPE65 formation (Hamilton et al., 2007). Another study used commercial equine collagen type I membranes, 7 μm thickness to culture ARPE-19 and showed phagocytosis and the presence of RPE65 (Thumann et al., 2009).

Further advancements in BrM modeling utilized various innovative techniques. The study by Kim J *et al* (Kim et al., 2022) modelled the outer blood-retinal barrier (oBRB) using hybrid membrane printing to mimic BrM. RPE-BrM were obtained from porcine eyes before being isolated, purified and digested to form the collagen biolink. ARPE-19 formed a polarised monolayer on the biolink, showing the success of this model. Smoke-induced damage was measured, and ARPE-19 function was found to be damaged due to oxidative stress. Building on efforts to mimic BrM,

Several other studies explored innovative approaches to mimic BrM such as by Harris *et al* utilised recombinant spider silk proteins (rSSP) to mimic BrM (Harris et al., 2019), while Wang S *et al* developed a nanofibrous membrane rich in integrin binding peptide to mimic BrM (Wang et al., 2022). In another approach, Liu *et al* utilised ultrathin scaffold using an electrohydrodynamic jet printing method (Liu et al., 2022).

Electrospinning which is widely used for fabricating nanofibrous scaffolds that resembles ECM was used by three different studies to mimic BrM. Firstly, by Majidnia E *et al* where they utilised an electrospinning technique with human amniotic membrane powder (HAMP)/polycaprolactone (PCL) to mimic BrM (Majidnia et al., 2022). The ARPE-10 cells

showed high adhesion on the BrM mimic (Majidnia et al., 2022). Next, by Khodamoradi M *et al* where they utilised a hybrid scaffold containing laminated and conductive hydrogel/fibre by electrospinning (Khodamoradi et al., 2021). Lastly, by Warnke P *et al* where they utilised electrospinning to form the nanofibrous membrane from collagen 1 and poly(latic-co-glycolod acid) PLG (Warnke et al., 2013).

Recently, a highly accurate BrM mimic incorporating choriocapillaris fenestration successfully demonstrated success in reproducing the disease phenotype of dry and wet AMD (Song et al., 2023). The model utilised by Song M *et al* (Song et al., 2023) engineered a 3D oBRB by incorporating a biodegradable scaffold as BrM. On the basal side, iPSC-EC, primary fetal fibroblast, and human pericyte were bio-printed, while iPSC-RPE cells formed a monolayer on the apical side. choriocapillaris fenestration was successfully demonstrated in this model, and features of dry and wet AMD phenotype, were reproduced. The dry AMD phenotype that was successfully reproduced were drusen deposits, RPE atrophy with loss of barrier function and capillary degeneration, while wet AMD was induced via chemical and genetic approaches, leading to CNV-like responses. This model was shown to be a successful one, mimicking the outer retina as closely as possible despite not containing BrM. However, more experiments are required to determine how similar this is to the *in vivo* situation. This could be conducted by looking at the permeability across this model and comparing it to what we know (Clark et al., 2014, 2017).

A key limitation of all these models is that the diffusion properties of the BrM model have not been systematically investigated. The unique diffusion properties of native BrM are critical to accurately model the disease process of AMD and evaluate new therapies *in vitro*. Utilising decellularised *ex vivo* BrM to model the outer retina and AMD offers significant potential for accurately replicating the disease, providing novel insights into its pathogenesis and paving the way for innovative therapies. Complement protein diffusion in particular is important. Clark S *et al* (Clark et al., 2017, 2014) studied complement protein diffusion across isolated BrM with key findings but this was without RPE or EC co-culture. Besides that, no studies have examined iPSC-RPE cell culture on optimally decellularised BrM with removal of all cellular material whilst preserving ECM. Co-culture with EC has also not been studied. The discussed models are all utilising different synthetic substance to mimic BrM, this brings large variability especially with the difference in thickness and pores, which would allow free permeability. These models are summarised in **Table 1- 5**.

Authors	Material	Type of BrM	Tissue treatment method	Thickness	Elastic modulus	Permeability	Cell Cultured			Outcome
							RPE	EC	Other	
Castellarin A *et al* (1998)	Macular Human BrM	Native	RPE cell debrided	-	-	-	Fetal human RPE cells	-	-	RPE cells morphology appeared after 6 hours
Tsukahara I *et al* (2002)	Human BrM	Native	RPE cell debrided	-	-	-	RPE cells from aged donors	-	-	RPE cells died after 1 hour
Gullapalli V *et al* (2005)	Aged submacular Human BrM	Native	RPE cell debrided				Fetal human RPE cells	-	-	Variable; some survived up to 14 days and some had poor cellular morphology
Sugino Ilene *et al* (2010)	Submacular Human BrM + cell deposited ECM	Native	RPE cell debrided	-	-	-	Fetal human RPE cells	BCE	-	BrM treated with BCE allowed RPE cell to

										adhere better
Majidnia E *et al* (2012)	PCL/collagen based human amniotic membrane	Synthetic	Decellularisation/electrospinning	-	25-40kPa	-	ARPE-19	-	-	Cells survived
Warnke P *et a*l (2013)	Poly(lactide-co-glycolide)-collagen	Synthetic	Electrospinning/casting	14µm	PLG: 131.9 ± 13.3 MPa	-	Poly(lactide-co-glycolide)-collagen	Synthetic	-	14um
Chen L *et al* (2017)	Porous membrane	Synthetic	-	6.5µm		Up to 70 kDA FITC dextran	ARPE-19	HUVEC	-	Cells survived
Chirco K *et al* (2017)	Human BrM	Native	Decellularised	-	-	-	-	Monkey EC	-	Cells survived
Cai H *et al* (2018)	Human BrM (aged and younger donor)	Native	0.02 M ammonium hydroxide in PBS to remove RPE cells	-	-	-	iPSC-RPE cells	-	-	Cells survived
Galloway C *et al* (2018)	Silk fibroin	Synthetic	Casting	3µm	-	Upto 70kDa dextran	ARPE-19	-	-	Cells survived
Palanisamy K *et al* (2019)	Fibronectin	Synthetic	-	-	-	-	Human primary RPE cells	Human Primary CEC		

Harris T *et al* (2019)	Spider silk	Synthetic	Spin coat	3-10µm	12-20MPa	Upto 10kDa FITC - dextran	ARPE-19			Cells survived
Manian K *et al* (2021)	Hydrogel (PEG-NB, MMP, RGD)	Synthetic	Photopolymerisation	2mm	1.7 ± 0.4 kPa	-	iPSC-RPE cells	iPSC-EC	iPSC-MSC	Cell survived
Khodamoradi M *et al* (2021)	Polyaniline (PANi) + gelatine	Synthetic	Electrospinning/casting	2-5µm	2.66 ± 0.33 MPa	-	hRPE	-	-	Cells survived
Wang S *et al* (2022)	PCL	Synthetic	Electrospinning	2.16 ± 0.78 µm	-	-	ARPE-19	-	-	Cells survived
Kim J *et a*l (2021, 2022)	porcine BrM	Natural	Decellularization/Bioprinting	1mm	0.02-0.03MPa	-	ARPE-19	-	-	Cells survived
Liu H *et al* (2022)	PCL	Synthetic	Electrohydrodynamic jet printing	7.88 - 7.96 µm	9-45MPa	Upto 40kDa FITC-dextran	ARPE-19	-	-	Cells survived
Song M *et al* (2023)	PLG	Synthetic	Bioprinting	4-10 µm	-		iPSC-RPE cells	iCell EC, Primary human retinal microvascular EC	Primary fetal choroidal fibroblast, human microvascular pericyte	Cell survived

Table 1- 5. Materials used to fabricate BrM to model the outer retina.

1.10 Current available treatments for age-related macular degeneration

As discussed previously, AMD is a multifactorial disease, and hence, developing a therapeutic treatment possesses many challenges. There are currently two Food and Drug Administration (FDA) approved intravitreal treatments for the slowing of progression of GA (**Table 1- 6**). Pegcetacoplan (Trade name: Syfovre; Apellis Pharmaceutical), first approved in February 2023, inhibits complement protein C3. Two phase 3 trials, OAKS and DERBY evaluated the efficiency and safety of pegcetacoplan in patients over 60 years and older with GA secondary to AMD. In OAKS, pegcetacoplan monthly and every other month reduced GA growth by 21% and 16%, respectively, at 12 months (Heier et al., 2023). In DERBY, pegcetacoplan monthly and every other month reduced GA growth by 12% and 11% at 12 months (Heier et al., 2023). However, the American Society of Retinal Specialists (ASRS) reported intraocular inflammation and retinal vasculitis following the first injection of Syfovre (Witkin et al., 2024). The second approved treatment is avacincaptad pegol (Trade name: Zimura; Iveric Bio), which was approved in August 2023 to inhibit complement protein C5 (Jaffe et al., 2021). Two trials, GATHER 1 which is a phase 2/3 and GATHER 2 which is a phase 3 evaluated avacinaptad pegol for GA secondary to AMD. GATHER1 study showed a 28% reduction in GA over 18 months in the 2 mg cohort and 30% in the 4 mg cohort (Patel et al., 2023). Meanwhile, GATHER2 study showed a 14% reduction in GA over 12 months in the 2mg cohort (Khanani et al., 2023).

Drug name	Indication	Target against	Delivery method
Pegcetacoplan	GA	C3	Intravitreal injection
Avacincaptad pegol	GA	C5	Intravitreal injection

Table 1- 6. Summary of licensed cell therapy for advanced dry AMD.

The treatment for CNV (wet AMD) is predominantly with anti-VEGF drugs. There are 6 anti-VEGF drugs available, aflibercept (Eylea), ranibizumab (Lucentis), brolucizumab (Beovu), faricimab (Vabysmo), bevacizumab (Avastin) and bevacizumab gamma (Lytenava). There are now also two ranibizumab biosimilars, ranibizumab-eqrn (Cimerli) and ranibizumab-uuna (Byooviz) (Rosenfeld et al., 2005). The agents are highly effective in treating CNV however, recent studies have suggested associations with retinal thinning, stroke, myocardial infarction and elevated blood pressure (Zhou et al., 2023; Ziemssen et al., 2020).

Faricimab targets both VEGF and angiopoietin-Tie 2 systems allowing potentially increased durability of effect as the angiopoietin-Tie 2 is known to complement the function of VEGF (Panos et al., 2023; Wong et al., 2025). The Tie-2 tyrosine kinase receptor is a key regulator of adult vascular homeostasis as it is part of the angiopoietin Tie-2 system, activation by Ang1 leads to vascular stabilisation. Ang1 has been shown to counteract VEGF inflammation (Kim et al., 2001).

1.11 Gene therapy

Gene therapy involves introducing genetic material into a host to treat disease. There are two main types of delivery methods: viral vectors, which have been extensively studied, and non-viral vectors, which have been less extensively studied. Examples of viral vectors are adenovirus (AV), adeno-associated viruses (AAVs), retrovirus, and lentivirus. Non-viral vectors include delivering naked DNA, niosomes, and liposomes. The delivery method for eye disease can be via intravitreal, subretinal or suprachoroidal routes (**Figure 1- 13**).

In December 2017, the first gene therapy for a retinal disease was approved (Novartis Pharmaceuticals Canada Inc., 2021). Voretigene neparvovec (Trade name: Luxturna; Spark Therapeutics Inc.) was approved as a subretinal injection for the treatment of retinal dystrophy caused by biallelic RPE65 mutations. The therapy utilizes an AAV serotype 2 (AAV2) vector to deliver the RPE65 transgene at a dose of 1.5×10^{11} viral genomes (vg) per eye.

Relevant to this project is the investigation by Complement Therapeutics currently in the pre-clinical phase investigating CTx001, an AAV2 carrying mini CR1 (Keefe D et al., 2023). Mini CR1 refers to a truncated form of CR1, though the exact CCP composition of the construct has not been disclosed to the public. They showed when hRPE cells were transduced *in vitro* with CRx001 and the mini CR1 co-factor activity was successful in the proteolysis of C3b to the inactive form, C3dg, preventing MAC formation (Keefe D et al.,2023). In an *ex vivo* Ussing chamber model, mini CR1 was reported to cross human BrM (enriched from human donor eyes) while maintaining its co-factor activity (Keefe D et al., 2023). Subretinal injection of CTx001 in murine eyes reduced MAC formation following laser-induced CNV by 69% when compared to null vector (Keefe D et al.,2023). Complementary research is currently investigating GA in the natural history study i-GAIN (investigating geographic atrophy insight) (NCT05797896) (Complement Therapeutics, n.d.). This study aims to understand the relationship between

genetics, blood biomarkers, and phenotypic changes in the eye with GA to support the clinical development of CTx001.

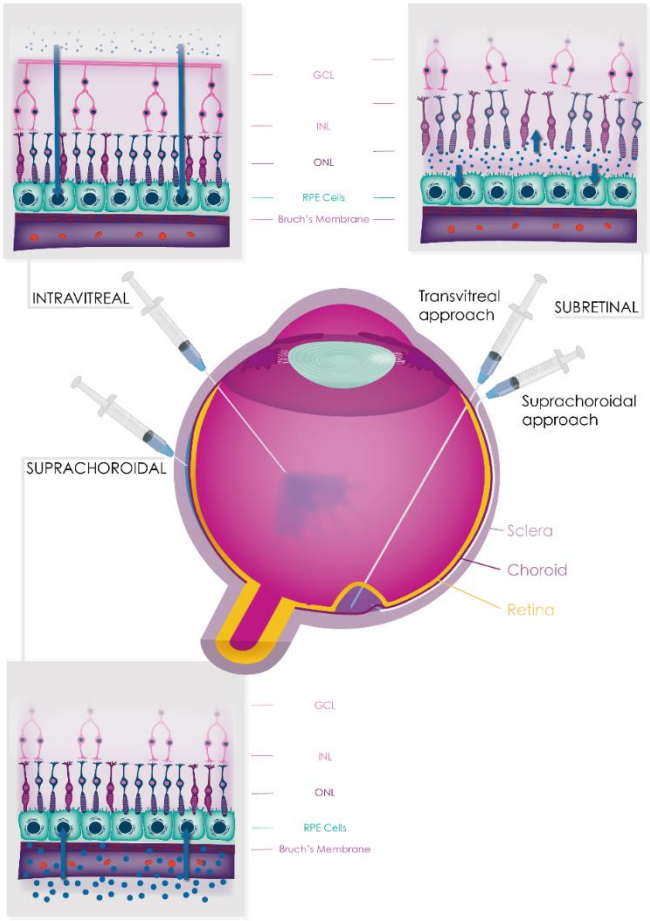

Figure 1- 13. Methods and routes of drug delivery in the human eye. Intravitreal injections are commonly conducted to administer therapeutic agents into the eye, besides subretinal and suprachoroidal injections. Subretinal agents are administered by a cannula through the suprachoroidal space or transliterally. Figure adapted from Hammadi S *et al* 2023.

There are currently 26 active clinical trials investigating gene therapy for AMD, either CNV or GA (**Figure 1- 14** and **Table 1- 7**) (HuidaGene Therapeutics Co., 2025; Shanghai BDgene Co., 2025; Adverum Biotechnologies, 2023; Chengdu Kanghong Pharmaceutical Group Co., 2024a; Ke et al., 2023; Frontera Therapeutics, 2023; Innostellar Biotherapeutics Co., 2024a, 2024b; Skyline Therapeutics, 2025; Peking Union Medical College Hospital, 2025; L. Janssen Research & Development, 2025b; Exegenesis Bio, 2025; Oxford BioMedica, 2017; Neuracle Genetics, 2025; Chengdu Kanghong Pharmaceutical Group Co., 2024b; REGENXBIO Inc., 2023; AbbVie, 2024c, 2024b, 2024a; Shanghai Refreshgene Technology Co., 2024; Adverum Biotechnologies, 2025; AbbVie, 2025; 4D Molecular Therapeutics, 2024; Lions Eye Institute,

2017; Sanofi, 2018; L. Janssen Research & Development, 2025a). This can be divided into two gene therapy groups, one not targeting VEGF and one targeting VEGF (**Figure 1- 14**). For treating wet AMD, FT003 (NCT05611424), NG101 (NCT05984927), KH658 (NCT06458595), RRG001 (NCT06141460) are currently recruiting in clinical trials. However, there is no publicly available information as to what the therapeutic agents target. On the other hand, Retinostat (NCT01301443) targets angiostatin and endostatin. Currently in phase 1 are FT003 and Retinostat while in phase 2 are NG101, KH858 and RG001 (**Figure 1- 14** and **Table 1- 7**)

There are several gene therapy trials specifically targeting the treatment of CNV with anti-VEGF agents (**Figure 1- 14**) namely: HG202 (NCT06031727), BD311 (NCT05099094), ADVM-022 (NCT03748784), KH631 (NCT05657301), LX102 (NCT06198413) (NCT06196840), SKG0106 (NCT06213038), AAVCAGsCD59 (NCT03585556) AAV2 sFLT01(NCT01024998) (NCT01494805), EXG102-031 (NCT05903794), KH631 (NCT05672121), RGX-314 (NCT03066258) (NCT04832724) (NCT04514653) (NCT04704921) (NCT05407636), SKG0106 (NCT05986864), 4D-150 (NCT05197270), ADVM-022 (NCT05536973).

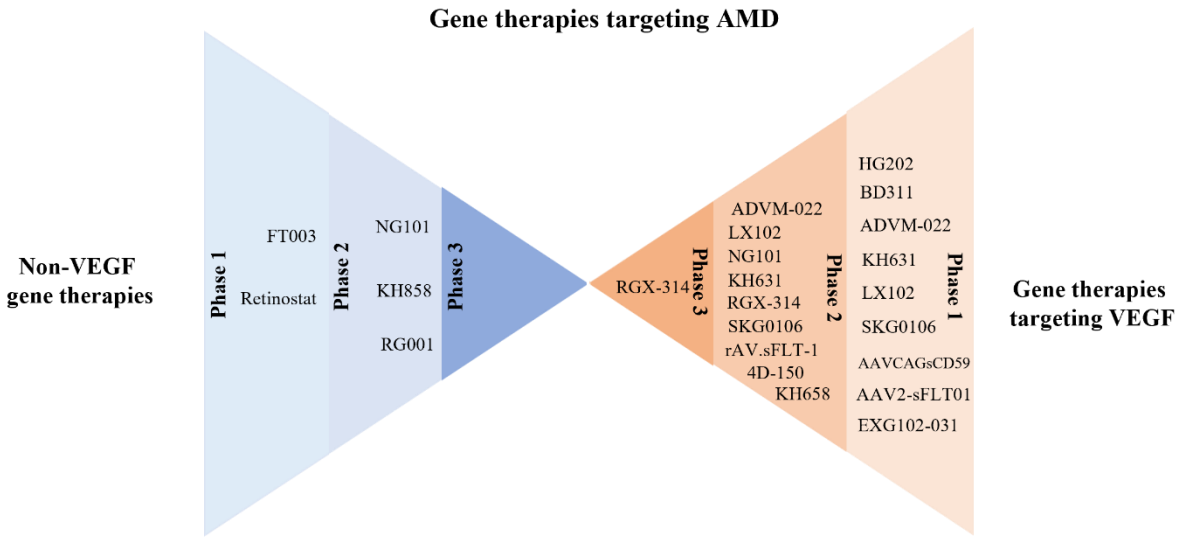

Figure 1- 14. Current phases of gene therapies targeting neovascular AMD. There are two approaches: either targeting VEGF or not. Looking at non-VEGF gene therapies, in phase 1 are FT003 and Retinostat. In phase 2, are NG101, KH858 and RG001. None are currently in phase 3. Gene therapy targeting VEGF, in phase 1 are HG202, BD311, ADVM-002, KH631, KX102, SKG0106, AAVCAGsCD59, AAV2-sFLT01 and EXG102-031. In phase 2 are, ADVM-002, LX103, NG101, KH631, RGX-314, SKG0106, rAAV.sFLT-1 4D-150 and KG658. In phase 3 is RGX-314.

NCT Number	Conditions	Phases	Study Status	Sponsor	Therapy	Delivered method	Concentration (vg/eye)
NCT06031727	Wet AMD	Early, Phase 1	Recruiting	HuidaGene Therapeutics Co., Ltd.	HG202 – AAV2 gene therapy targeting RNA against VEGF	Subretinal injection	Unknown
NCT05099094	Wet AMD	Early, Phase 1	Recruiting	Shanghai BDgene Co., Ltd.	BD311 – targeting VEGFA	Subretinal injection	Unknown
NCT03748784	Wet AMD	Phase 1	Completed, data unpublished.	Adverum Biotechnologies, Inc.	ADVM-022- AAV.7m8-aflibercept gene therapy against VEGFA	Intraviteral injection	$6x10^{11}$, $2x10^{11}$
NCT05657301	AMD	Phase 1	Recruiting	Chengdu Origen Biotechnology Co., Ltd.	KH631-AAV8 gene therapy against anti-VEGF	Intraocular injection	Unknown
NCT05611424	Wet AMD	Phase 1	Not yet recruiting	Frontera Therapeutics	FT-003 – AAV gene therapy with unknown composition	Intravitreal injection	Unknown
NCT06198413	Wet AMD	Phase 1	Recruiting	Innostellar Biotherapeutics Co.,Ltd	LX102 - AAV gene therapy against VEGF	Subretinal injection	$2x10^{10}$, $1.25x10^{11}$
NCT06213038	Wet AMD	Phase 1	Recruiting	Youxin Chen	SKG0106 - AAV gene therapy against VEGF	Intraocular injection	Unknown
NCT03585556	Wet AMD	Phase 1	Completed. Four patients did not require treatment after 6 months of therapy.	Janssen Research & Development, LLC	HMR-1002-AAV gene therapy against CD59	Intravitreal injection	$3.56x10^{11,}$ $1.071x10^{12}$
NCT03144999	Dry AMD	Phase 1	Completed. Showed decline in GA area.	Janssen Research &	HMR-1001-AAV gene therapy against CD59	Intravitreal injection	$3.56x10^{10}$, $1.071x10^{11}$, $3.56x10^{11}$

				Development, LLC			
NCT01024998	AMD	Phase 1	Completed. Five of the patients receiving the highest dose showed measurable levels of sFLT01 (VEGF neutralising protein) in aqueous humor.	Genzyme, a Sanofi Company	AAV gene therapy against sFLT01(soluble Flt1 receptor to neutralise VEGF)	Intravitreal injection	$2x10^8$, $2x10^9$, $6x10^9$, $2x10^{10}$
NCT05903794	Wet AMD	Phase 1	Recruiting	Exegenesis Bio	EXG102-031 – AAV gene therapy with transgene angiopoietin domain and VEGF receptor	Subretinal injection	Unknown
NCT01301443	Wet AMD	Phase 1	Completed. The mean levels of endostatin and angiostatin were the highest between 12 and 24 weeks after the injection at $2.4\ X10^5$ vg/eye or $8.0X10^5$ vg/eye , with endostatin levels at 57–81 ng/mL and 15–27 ng/mL for angiostatin.	Oxford BioMedica	RetinoStat - lentivirus	Subretinal injection	$2.4x10^4$, $2.4x10^5$, $8.0x10^5$

			Their levels remained stable and were well expressed after 2.5 years in 8 subjects and 4 years in 2 subjects.				
NCT05984927	AMD	Phase 1, Phase 2	Recruiting	Neuracle Genetics, Inc	NG101 -AAV8 gene therapy with unknown composition	Subretinal injection	$1x10^9$, $3x10^9$, $8x10^9$
NCT06458595	AMD	Phase 1, Phase 2	Not yet recruiting	Chengdu Origen Biotechnology Co., Ltd.	KH658- AAV gene therapy with unknown composition	Suprachoroidal injection	Unknown
NCT05672121	AMD	Phase 1, Phase 2	Recruiting	Chengdu Origen Biotechnology Co., Ltd.	KH631 – AAV 8 gene therapy against VEGF	Subretinal injection	Unknown
NCT03066258	Wet AMD	Phase 1, Phase 2	Completed. The best dose that resulted in prolonged concentration in aqueous humour was $6X10^{10}$ vg/eye.	REGENXBIO Inc.	RGX-314 - AAV 8 gene therapy against VEGFA	Subretinal injection	$3x10^9$, $1x10^{10}$, $6x10^{10}$, $1.6x10^{11}$, $2.5x10^{11}$
NCT05986864	Wet AMD	Phase 1, Phase 2	Recruiting	Skyline Therapeutics (US) Inc.	SKG0106 AAV gene therapy against VEGF	Intravitreal injection	Unknown
NCT06141460	Wet AMD	Phase 1, Phase 2	Recruiting	Shanghai Refreshgene Technology Co., Ltd.	RRG001 – AAV gene therapy with unknown composition	Subretinal injection	Unknown
NCT01494805	Wet AMD	Phase 1, Phase 2	Completed. Visual acuity	Lions Eye Institute, Perth,	AAAV gene therapy against sFLT01(soluble	Subretinal injection	$1x10^{10}$, $1x10^{11}$

			was maintained in patients over 52 weeks post-delivery. Compared to the control group (ranibizumab), the gene therapy-treated group had fewer ranibizumab re-treatments.	Western Australia	Flt1 receptor to neutralise VEGF)		
NCT05197270	Wet AMD	Phase 1, Phase 2	Recruiting	4D Molecular Therapeutics	4D-150 - AAV gene therapy targeting VEGF-C and codon-optimized sequence encoding aflibercept	Intravitreal injection	$3x10^{10,}$ $1x10^{10}$, $6x10^{9}$
NCT04832724	Wet AMD	Phase 2	Completed. Results unavailable to the public.	AbbVie	RGX-314 - AAV 8 gene therapy against VEGFA	Subretinal injection	Unknown
NCT06196840	Wet AMD	Phase 2	Recruiting	Innostellar Biotherapeutics Co.,Ltd	LX102 - AAV gene therapy encoding VEGF-trap	Subretinal injection	$2x10^{10}$
NCT04514653	Wet AMD	Phase 2	Recruiting	AbbVie	RGX-314 - AAV 8 gene therapy against VEGFA	Suprachoroidal injection	Unknown
NCT05536973	Wet AMD	Phase 2	Active not recruiting	Adverum Biotechnologies, Inc.	ADVM-022 - AAV.7m8-aflibercept, gene therapy combination with 1 or 4 corticosteroid treatments	Intravitreal injection	$2x10^{11}$, $6x10^{10}$
NCT04704921	Wet AMD	Phase 2, Phase 3	Recruiting	AbbVie	RGX-314 - AAV 8 gene therapy against VEGFA	Intravitreal injection	Unknown

NCT05407636	Wet AMD	Phase 3	Recruiting	AbbVie	RGX-314 - AAV 8 gene therapy against VEGFA	Intravitreal injection	Unknown
NCT04645212	Wet AMD		Active not recruiting	Adverum Biotechnologies, Inc.	Follow up with ADVM-002 (OPTIC-EXT)	-	-
NCT05481827	AMD	Phase 2	Enrolling by invitation	Gyroscope Therapeutics Limited	Follow up on patients who received GT005 (AAV 2 FI)	-	-
NCT03999801	Wet AMD	Phase 2	Enrolling by invitation	AbbVie	Follow up on patients who received RGX-314 (AAV 8 transgene VEGFA)	-	-

Table 1- 7. Summary of the registered clinical trial in AMD for gene therapy.

1.12 Complement therapies in age-related macular degeneration

Numerous studies are looking at targeting complement by inhibiting its activity or supplementing regulators to control overactivation (AbbVie, 2025, 2024a; Campochiaro et al., 2024). **Figure 1- 15** and **Table 1- 8** summarises several completed, terminated and ongoing investigations into complement therapies in AMD.

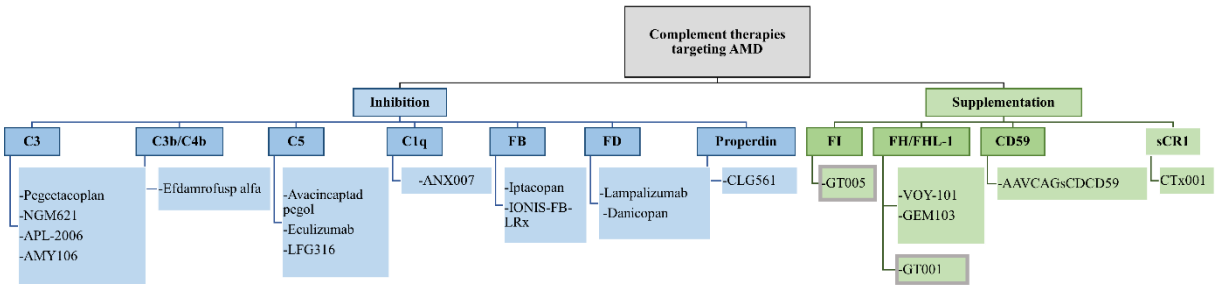

Figure 1- 15. Complement therapies targeting AMD. There are two main approaches. One to inhibit and one to supplement. In the inhibition of complement therapies, currently inhibition of C3b, C3b/C4b, C5, C1q, FB. FD and properdin are being investigated. In the supplementation of complement therapies, supplementation of FI, FH/FHL-1 and CD59 are being investigated. Grey border boxes indicate discontinued studies.

Complement C3 inhibition						
Agent	**Drug type**	**Delivery method**	**Condition**	**Sponsor**	**Clinical trial**	**Outcome**
Pegcetacoplan (Syfovre)	Peptide inhibitor	Intravitreal injection	GA	Apellis	**Phase I** NCT03777332	Completed; data not published
					Phase II NCT02503332(FILLY)	Completed. Reduction in GA lesion growth 6 months post-treatment.
					Phase III 1.NCT03525600 (DERBY) 2.NCT03525613 (OAKS) 3.NCT04770545(GALE extension study)	1. Completed. Reduction in GA lesion growth 24 months post-treatment. 2. Completed. Reduction in GA lesion growth 24 months post-treatment. 3. Active
NGM621	Humanised IgG1 monoclonal antibody	Intravitreal injection	GA	NGMBio	**Phase I** NCT04014777	Completed. The GA lesion area and mean visual acuity were stable throughout, with

						no antibody against the drug detected in the serum
					Phase II NCT04465955(CATALINA)	Completed. No increase in CNV conversions. However, the efficacy endpoint of the significance rate in the GF lesion area change in NGM621 vs sham was not met
APL-2006	Bispecific fusion protein	Intravitreal injection	GA and wet AMD	Apellis	None to date	NA
AMY106	Compstatin analogue	Intravitreal injection	GA and wet AMD	Amyndas	None to date	NA
Complement C3b/C4b inhibition						
Efdamrofusp alfa (IBI302)	Bispecific fusion protein	Intravitreal injection	Wet AMD	Innovent Biologics	**Phase I** NCT04370379	Completed. Achieved a mean change in the baseline in best corrected visual acuity (BCVA) of 9 letters after 20 weeks.
					Phase II 1.NCT04820452 2.NCT05403749	1. Unknown status. 2. Completed, data not published

Complement C5 inhibition						
Avacincaptad pegol (Zimura)	Aptamer-based inhibitor	Intravitreal injection	Wet AMD, GA	Iveric Bio	**Wet AMD**	
					Phase I NCT00709527	Completed, data not published
					Phase II NCT03362190	Completed. BCVA indicates visual improvements 6 months post-treatment
					Phase IIa NCT05571267	Terminated
					GA	
					Phase I NCT00950638	Completed, data not published
					Phase II/III NCT02686658	Completed, showed less GA progression and BCVA indicate visual improvements 6 months post-treatment
					Phase III 1**.** NCT04435366(GATHER2) 2. NCT05536297(open-label extension)	1. Completed. GA progression and BCVA indicate visual

						improvements and delayed persistent vision loss 24 months post-treatment 2. Active
Eculizumab	Humanised monoclonal antibody	IV infusion	GA	Alexion	**Phase II** NCT00935883(COMPLETE)	Completed. Minimal difference in GA growth rate, decreased drusen formation and improved visual acuity 6 months post-treatment
LFG316	Antibody	Intravitreal injection	GA	Alcon/Novartis	**Phase II** NCT01527500	Completed. Minimal difference in GA, improved visual acuity and more frequent serious adverse side effect 16 months post-treatment
Complement C1q inhibition						
ANX007	Antibody	Intravitreal injection	GA	Annexon Inc	**Phase II** NCT04656561(ARCHER)	Completed. No ANX007-treated patients with less advanced disease lost 15 letters,

						compared to sham patients. ANX007 reduced EZ loss in patients with less EZ loss at baseline compared to sham.
Complement FB inhibition						
Iptacopan (LNP023)	Small molecule	Oral	Early and intermediate AMD	Novartis	**Phase II** NCT05230537	Recruiting
IONIS-FB-LRx (RG6299)	siRNA	Subcutaneous injection	GA	Ionis Pharmaceuticals in partnership with Roche	**Phase II** NCT03815825(GOLDEN)	Completed, data not published
Complement factor D inhibition						
Lampalizumab (FCD4514S)	Antibody Fab fragment	Intravitreal injection	Dry AMD	Genentech/Roche	**Phase II** 1.NCT01229215(MAHALO) 2.NCT02288559	1. Completed, data not published 2. Completed. Improved GA lesion area and increase in drug serum concentration 6 months post-treatment.

					Phase III NCT02247479(CHROMA) NCT02247531(SPECTRI) NCT02745119 (long-term extension)	Terminated Terminated Terminated
Danicopan	Small molecule	Oral	Dry AMD	Alexion Pharmaceuticals	**Phase II** NCT05019521	Active
Properdin inhibition						
CLG561(alone and in combination with LFG316)	Monoclonal antibody	Intravitreal injection	Dry AMD	Alcon/Novartis	**Phase II** NCT02515942	Completed. No differences in GA lesion area 6 months post-treatment.
Complement factor I supplementation						
GT005	AAV gene therapy	Single subretinal injection	Dry AMD	Gyroscope Therapeutics, a Novartis Company	**Phase II** NCT03846193, NCT04437368	Terminated Terminated
Complement factor H and factor-H like 1 supplementation						
VOY-101	AAV gene therapy	Single intravitreal injection	Dry AMD	Perceive Biotherapeutics	**PhaseI/IIa** NCT05380492	Active

GEM103	Full-length protein	Intravitreal injection	Dry AMD	Gemini Therapeutics	**PhaseII** NCT04643886(REGATTA) NCT04684394	 Terminated Terminated
GT011	AAV gene therapy	Unknown	Dry AMD	Gyroscope Therapeutics, a Novartis Company	NA	Terminated
Complement CD59 supplementation						
AAVCAGsCDCD59/ JNJ81201887	AAV gene therapy	Single intravitreal Injection	GA, Wet AMD	Janssen Research & Development (formerly Hemera Biosciences)	**GA**	
					Phase I NCT03144999	Completed, data not published
					Phase II NCT04358471 NCT05811351	 Withdrawn Active
					CNV	
					Phase I NCT03585556	Completed, data not published

Table 1- 8. Complement inhibition and supplementation drugs in clinical trial.

1.13 Project aims

The research in this project aims to:

1. Compare native vs decellularised BrM (dBrM), ensuring that decellularisation preserves ECM proteins, effectively removes cellular component and maintains the structural integrity of BrM
2. Model the outer retina by growing iPSC-RPE cells on dBrM and evaluate the functionality and morphology of these iPSC-RPE cells.
3. Assess the efficiency of AAV transduction in iPSC-RPE cultured on Matrigel vs dBrM, using AAV 2 and AAV 8 vectors encoding enhanced green fluorescent protein (mEGFP) and sCR1 CCP1-11 Flag His tag (truncated sCR1).

Chapter 2 Materials and Methods

2.1 General chemical reagents

The chemical reagents used for the methodology were purchased from Sigma-Aldrich, VWR chemicals, or Thermofisher Scientific. General lab plastics, such as falcon tubes and Eppendorf, were purchased from Grenier Bio-One and Fisher Scientific. Cell culture dishes, media bottles, and strippets were purchased from Starlab, Grenier Bio-one, Helena Biosciences, and Scientific Laboratory Supplies (SLS).

2.2 Preparation of decellularised Bruch's membrane

2.2.1 Human donor eye tissues

The human donor eyes were obtained from the Tissue and Eye Service (NHS Blood and Transplant) after corneal transplantation. The eyes were received as posterior eye cups after corneal removal for transplant purposes. Ethical approval was obtained from the Research Ethics Committee (21/NE/0068). **Table 2- 1** shows the details of each donor to date with other eye diseases excluded besides AMD based on experiments in each chapter (CH).

Num	Donor ID	Age	Gender	AMD status	Hours postmortem	Experiment
1	G170022301246U	82	F	No	70	Modelling (CH4)
2	G170022301327s	59	F	No	55	Proteomic dBrM (CH3)
3	G170022301560a	63	F	No	52	BrM DNA quantification (CH3) & Modelling (CH4)
4	G170022302139K	77	F	No	81	RPE culture (CH4)
5	G1700223021698	51	M	No	71	Modelling (CH4)
6	G170022302831H	56	F	No	51	BrM DNA quantification (CH3) & Modelling (CH4)

7	G170023306010A	59	M	No	66	Modelling (CH4)
8	G170023305921M	42	M	No	57	Modelling (CH4)
9	G170223501708H	62	M	No	55	Proteomic of dBrM (CH3) & RPE culture (CH4)
10	G170023306186*	78	M	No	52	Proteomic of dBrM (CH3) & RPE culture (CH4)
11	G1700233061755	43	F	No	66	RPE culture (CH4)
12	G170023306516W	81	M	No	54	dBrM via 3 protocols (CH3)
13	G170023306471Q	62	F	No	48	dBrM via 3 protocols (CH3) & RPE culture (CH4)
14	G1700233082680	61	F	No	70	ECFC culture & modelling (CH4)
15	G170023308393R	54	F	No	69	Complement protein diffusion (CH4)
16	G170023308896I	69	F	No	59	RPE culture (CH4)
17	G170024311112T	49	M	No	51	ECFC culture (CH4)
18	G170024311198M	83	F	No	52	BrM DNA quantification (CH3)
19	G170024311972F	59	M	No	86	RPE culture (CH5)
20	G170024312492V	72	M	No	66	RPE Culture (CH5)
21	G170024312648N	77	F	No	63	RPE Culture (CH5)
22	G170024312602E	80	M	No	71	RPE Culture (CH5)
23	G170022300777T	84	F	No	108	Modelling (CH4)

Table 2- 1. The details of each BrM donor. M: male, F: female and CH: chapter.

2.2.2 Eye tissue preparation

All tissue preparation steps needed for tissue culture were conducted under the microscope (Nikon SMZ645 Stereo Microscope 08x - 5x). The images of the dissection tools can be found at **Figure 2- 1**. The eye cup was held, and the vitreous and neurosensory retinal were removed (**Figure 2- 2**). The sclera was cut using long cuvet scissors (2801267, covertus) to flatten the eye cup (**Figure 2- 2**). The RPE/BrM complex was then separated from the sclera by gently dissecting it using a crescent knife (MCU26SK, Altomed). Once isolated, the BrM/Choroid tissue was washed multiple times with 1% Penicillin-Streptomycin (PenStrep) (ThermoFisher; 15140148) in deionised water (dH_2O). The decellularisation process was then carried out. Dissection tools were sterilised after each use with 100% ethanol.

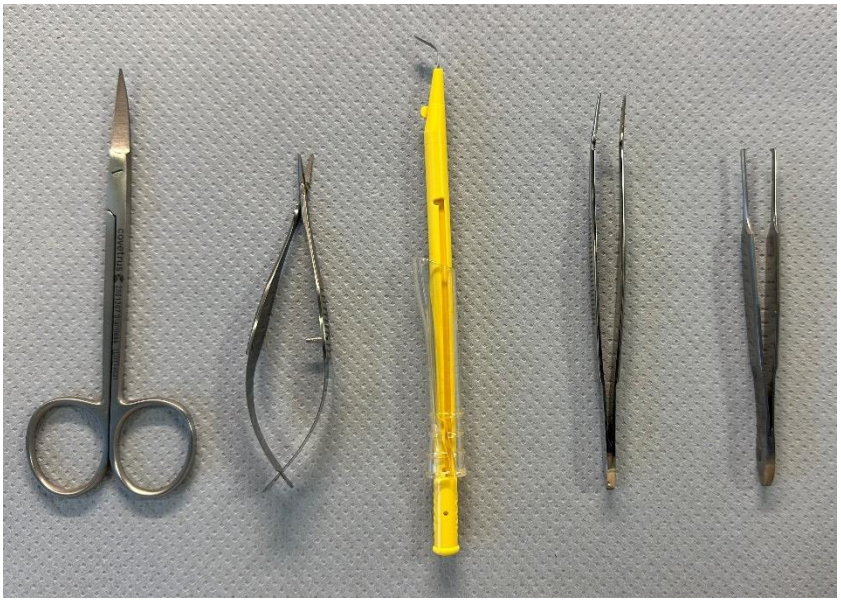

Figure 2- 1. The Dissection tools. From left to right: cvet scissors iris curved (2801267, covertus), world precision instrument student vannas scissors (15433612, Fisher Scientific), crescent knife (MCU26SK, Altomed), Bochem™ stainless steel bent tip forceps (10623462, Fisher Scientific) Bochem™ stainless steel tissue forceps (10098140, Fisher Scientific).

A. **B.** **C.** **D.**

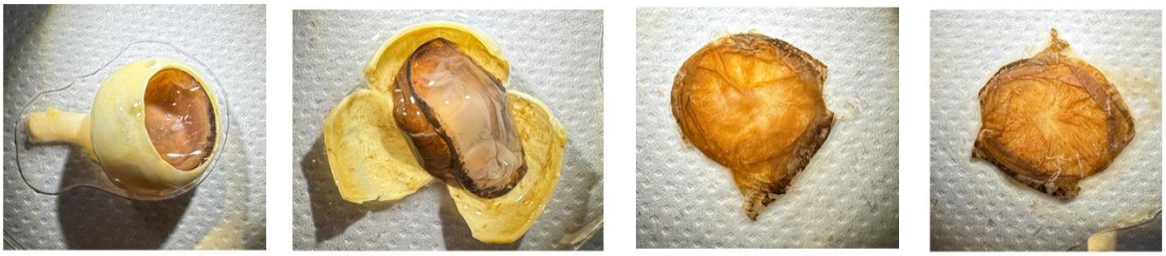

Figure 2- 2. Images of the dissection process. (A) Represents the eye cup with the cornea removed. **(B)** The sclera is cut open to flatten the eye cup. **(C)** RPE/Bruch's membrane/choroidal complex after vitreous and retina removal shown RPE side facing up. **(D)** Choroidal side up, as streaks of choriocapillaris are visible. Donor globe in image = g170023306516W.

2.2.3 Bruch's membrane decellularisation protocols

The RPE/BrM complex tissue was cut into two or three parts, each covering a well in a 24-well plate (Corning incorporated; 3524). Three protocols of decellularisation were carried out as below and summarised in a schematic diagram (**Figure 2- 3**). Once decellularised, BrM is referred to as dBrM.

1) **Chirco K *et al* protocol (CP)**: dH_2O was applied for 1.5 hours followed by 1% Triton X-100 (215682500, Thermo Scientific Acros) in phosphate buffered saline (PBS) (10010023, ThermoFisher Scientific) for 3 hours, PBS for 15 minutes, 1% Triton X-100 for 18 hours, PBS for 15 minutes, 0.1% SDS + 0.1M ethylenediaminetetraacetic acid (EDTA)for 3 hours, PBS for 15 minutes, 10U/ml DNase I solution (EN0521, Thermo Fisher Scientific) for 1 hour at 37^{o}C, PBS for 15 minutes and lastly dH_2O for 1.5 hours. The plate was left on the plate shaker (Eppendorf ThermoMixer C Plate shaker) at 350 rpm.

2) **Shortened protocol 1 (SP1)**: 1% Triton X-100 in PBS was applied for 30 minutes, followed by a wash with 1% Penstrep twice. The tissue was then treated with 1% Triton X-100 for 1 hour, followed by another two washes with 1% Penstrep. This step was repeated once more. For all steps with 1% Triton X-100, the plate was left on the plate shaker at 350 rpm.

3) **Shortened protocol 2 (SP2)**: The tissue was first treated with 1% Triton X-100 for 30 minutes, followed by a 15-minute wash with 1% Penstrep. This was followed by an incubation in 1% Triton X-100 for 1 hour, after which the tissue was washed again with 1% Penstrep for

15 minutes. The treatment with 1% Triton X-100 for 1 hour and the subsequent Penstrep wash were repeated once more. Next, the tissue was incubated in a 10 U/mL DNase I solution at 37°C for 1 hour. Finally, a last 15-minute wash with 1% Penstrep was performed to complete the process. For all steps with 1% triton X-100, the plate was left on the plate shaker at 350rpm.

2.3 DNA extraction and quantification

2.3.1 DNA Extraction from Bruch's membrane

DNA was extracted from BrM via the QIAamp DNA micro kit (56304, Qiagen). The tissue samples used were less than 10mg. All steps were per manufacturer protocol (Qiagen., 2025). Briefly, 180µl of buffer ATL was added and allowed to equilibrate to room temperature before adding 20µl of proteinase K and pulse vertexing for 15 seconds. The samples were then left overnight at 56ºC. The remaining protocol followed manufacturer instructions, and the DNA was eluted with 20µl buffer AE.

2.3.2 DNA quantification

DNA quantification was conducted using a Qubit 1X high-sensitivity assay kit (Q33230, Invitrogen), as the quantitation range is between 0.1 and 120 ng. The steps were carried out per the manufacturer's protocol (ThermoFisher Scientific. Qubit., 2025). Prism (GraphPad, USA) was used to plot the graphs. One-way ANOVA with Tukey's multiple comparisons test was performed to determine significance. Results were considered significant when $P < 0.05$.

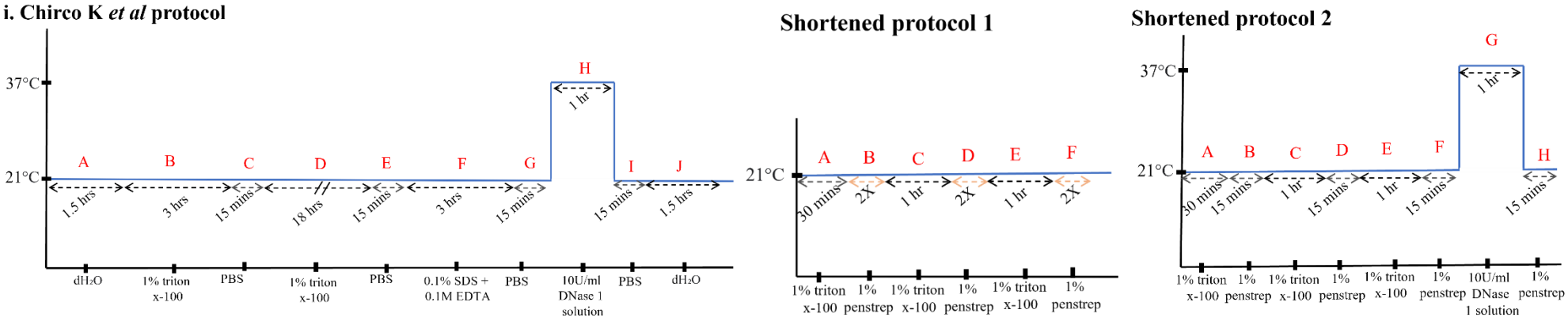

Figure 2- 3. Schematic of the three protocols of decellularisation. The y-axis represents the temperature, while the x-axis represents the chemicals used. CP was a 10-step protocol (A-J), SP1 was a 6-step protocol (A-F), and SP2 was an 8-step protocol (A-H). CP is the most extended protocol, followed by SP2, then SP1. SP1 and SP2 are similar, except for the washing steps (SP1 washing step is twice with 1% penstrep while in SP2 it is left for 15 minutes) and SP2 has the addition of DNase I. hrs= hours; mins= minutes; dH_2O= deionised water; PBS= Phosphate-buffered saline; SDS= Sodium dodecyl sulfate; EDTA= Ethylenediaminetetraacetic acid.

2.4 Proteomic analysis

2.4.1 Mass spectrometry

Mass spectrometry was conducted by the Proteomic and Proteome Analysis Group at Newcastle University. It was performed to identify relative proteomic differences in native BrM, dBrM and iPSC-RPE co-cultured on dBrM (with or without Matrigel coated). Pierce BCA protein assay (23250, Thermo Fisher Scientific) was performed per manufacturer protocol to determine the total protein concentration. The data was analysed using Microsoft Excel, and R Studio was used to generate the volcano and bubble plots.

2.4.2 Analysis of proteomic results

The data obtained from the proteomic team at Newcastle University were processed for statistical analysis and were Log_2 transformed. Z score of Log(Fold change of sample/Control) was then obtained with the $-Log_{10}$ P required as below:

- To compare dBrM and native BrM, a volcano plot was generated with $-Log_{10}$ P (y-axis) against Z score of Log(Fold change dBrM/Native BrM) (x-axis). The significance cut-off for the Z score was 2, and the P value was 0.05.
- To compare iPSC-RPE cells co-culture on dBrM to native BrM and to dBrM, a volcano plot was generated with $-Log_{10}$ P against Z score of Log(Fold change iPSC-RPE cells co-culture on dBrM/Native BrM) and Log(Fold change iPSC-RPE cells co-culture on dBrM/dBrM). The significance cut-off for the Z score was 2, and the P value was 0.05.

The Z score formula used was consistent across all comparisons, which is as below =

$$\text{Z score} = \frac{[\text{Log(Fold change of x / y)}] - \text{Mean}}{\text{Standard deviation}}$$

2.4.3 Gene enrichment functional analysis

Gene ontology (GO) enrichment of the protein group genes was conducted, and the top 10 significantly retained and removed processes were plotted. This analysis included the GO terms for biological processes, cellular components, and molecular functions using Fisher's exact test

for null hypothesis testing and the Benjamin-Hochberg procedure to adjust for multiple testing (**Table 2- 2**).

GO processes	Definitions
Molecular function (MF)	Describes the specific activities performed by the gene products at the molecular level.
Cellular component (CC)	Identifies the locations within the cellular compartments and structures where the gene products are active. This includes two main categories: cellular anatomical entities (where gene products carry out functions) and stable macromolecular complexes (of which gene products are part).
Biological process (BP)	Describes processes accomplished by multiple molecular activities.

Table 2- 2. GO process and definitions. The definitions for molecular function, cellular component and biological process.

2.5 Mounting Bruch's membrane on Ussing chamber

Sectioned dBrM was mounted in a Ussing Chamber (1306, Scientific Instruments), and silicon grease (SGPGT90, Silverhook) was applied to the Ussing chamber to enhance the sealant. Next, 2.5 ml PBS was added to each side of the chamber.

2.6 Mounting Bruch's membrane on models

2.6.1 Cell Crowns

The first mounting model tested was called cell crowns. There are three sizes of the cell crowns with different diameters for BrM attachment; these were 96, 48, and 24 well cell crowns (**Figure 2- 3**, **Table 2- 4**, and **Table 2- 5**). Briefly, for the 48- and 24-well cell crowns, dBrM was placed on the body, and the ring was clipped on to secure dBrM (**Figure 2- 4**). For the 96-well cell crown, dBrM was placed on the cup, and the cusp was clicked onto the cup (**Figure 2- 4**).

Cell crown / Dimensions	24 well crown inserts
Inner diameter of the body	10 mm
Outer diameter of the body	12 mm
Height of the body	12 mm
Inner surface area	0.79 cm^2
Inner diameter of the ring	12.5 mm
Height of the ring	2.5 mm
Suitable sample sizes in diameter	0.05-0.3 mm

Table 2- 3. The dimensions of the 24 well cell crown inserts.

Cell crown / Dimensions	48 well crown inserts
Inner diameter of the body	7 mm
Outer diameter of the body	8 mm
Height of the body	12 mm
Inner surface area	0.38 cm^2
Inner diameter of the ring	8.5 mm
Height of the ring	2.5 mm
Suitable sample sizes in diameter	> 10 mm

Table 2- 4. The dimensions of the 48 well crown inserts.

Cell crown / Dimensions	96 well crown inserts
Inner diameter of the cup	3.0 mm
Outer diameter of the cup	6.0 mm
Height of the combined inserts	10.2 mm
Inner surface area	0.071 cm2
Inner diameter of the cusp	2.7 mm
Height of the cusp	5.5 mm
Suitable sample sizes in diameter	Thin sample: > 5mm Thick sample: 3 - 4.5 mm

Table 2- 5. The dimensions of the 96 well crown inserts.

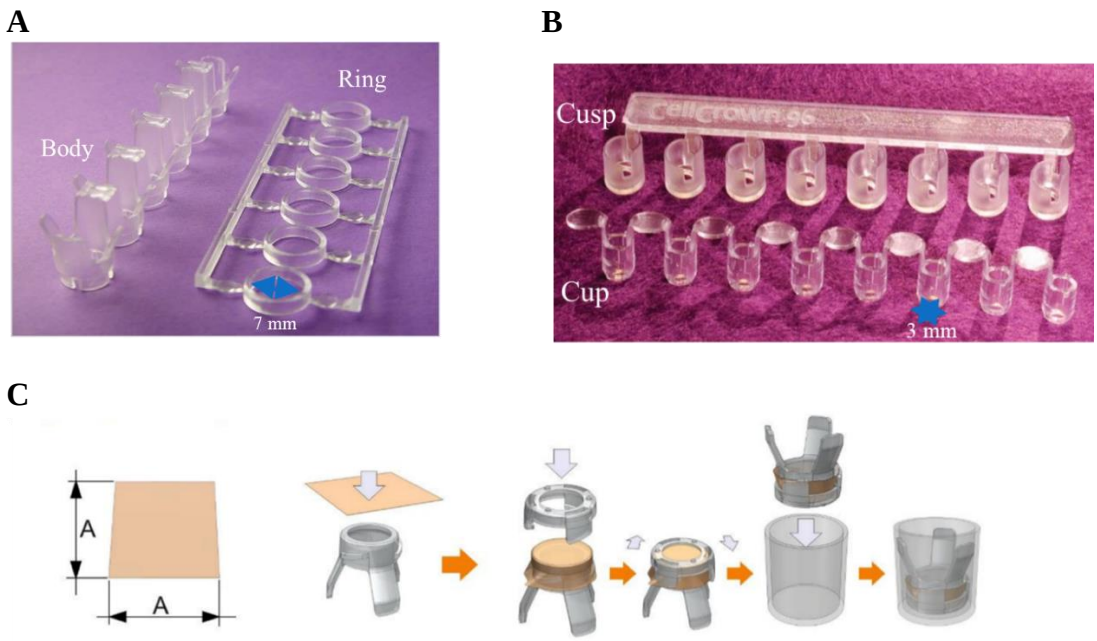

Figure 2- 4. Cell crowns used. (A) Image of the 24 well cell crown and **(B)** 96 well cell crown**. (C)** Shows the attachment of tissue on the 24 or 48-well cell crown.

2.6.2 Model 1: 12 well transwell and O-ring (Newoutset)

Model 1 used a 12 well transwell (665641, Grenier Bio-One) and nitrile rubber O-ring (Newoutset). To mount dBrM, it was placed on the transwell, and the O-ring was placed on top of dBrM to secure it and attempt to create a seal so that nothing could pass via the edges (**Figure 2- 5**). The basal volume was 2 ml and apical volume 0.5ml.

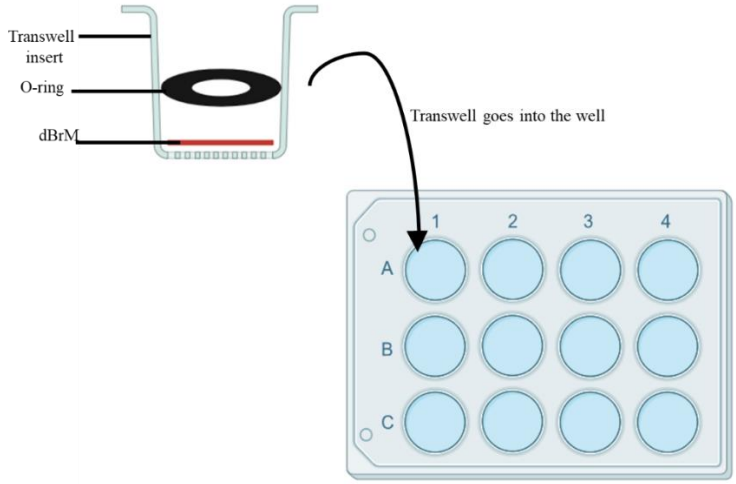

Figure 2- 5. Schematic diagram of the transwell insert assembly with dBrM and O-ring.

2.6.3 Model 2: 12 well transwell and O-ring (Accu)

Model 2 used a 12 well transwell (665641, Grenier Bio-One) and nitrile rubber O-rings (Accu) (**Figure 2- 6**). The assembly method was as described previously in model 1 (**Section 2.6.2**). The basal volume was 2 ml and apical volume 0.5ml.

A **B**

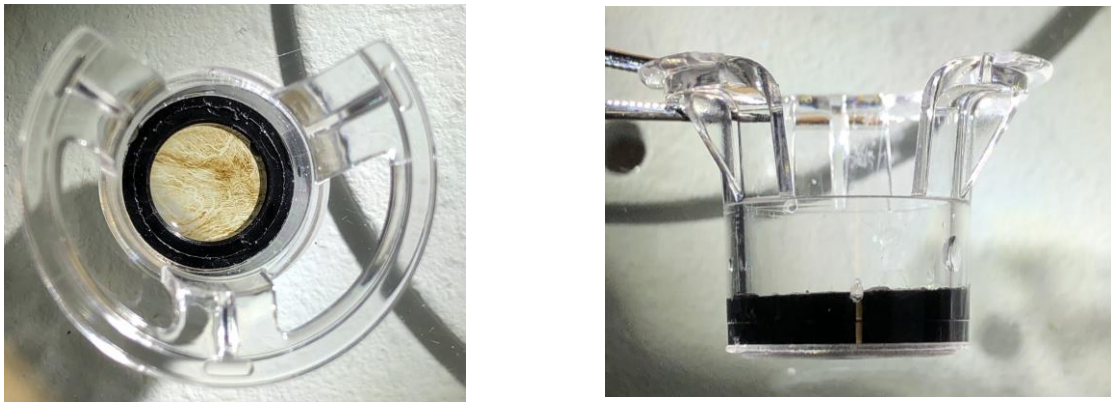

Figure 2- 6. Model 2. The **(A)** Top of the transwell with dBrM and **(B)** side image of the transwell with dBrM and O-ring insert.

2.6.4 Model 3: 12 well transwell with the membrane removed and O-ring (Accu) model inserted within (top 1 O-ring followed by Bruch's membrane and two o-rings)

Model 3, used a 12 well transwell (665641, Grenier Bio-One) with the membrane removed and O-ring (Accu) model inserted within (top 1 O-ring followed by dBrM and two O-rings). The assembly method is presented in **Figure 2- 7**. The basal volume was 2 ml and the apical volume 0.15 ml.

A

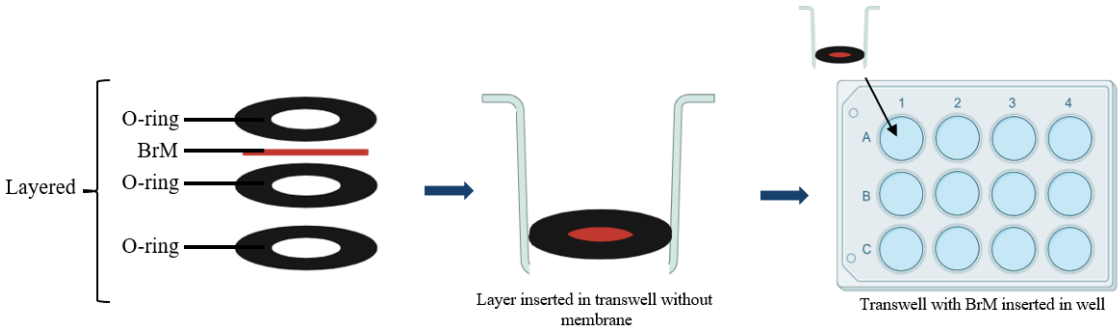

B

Figure 2- 7. Model 3. (A) Illustration of model 3 set up in the transwell. **(B)** Model 3 set up.

2.6.5 Model 4: 2 O-rings (Accu) followed by Bruch's membrane, and two O-rings (Accu)

Model 4 used 2 O-rings (Accu) followed by dBrM, and two O-rings. The model was not sturdy enough to hold the apical or basal volume and was leaking liquid – it was therefore not formally tested (**Figure 2- 8**).

A **B** **C**

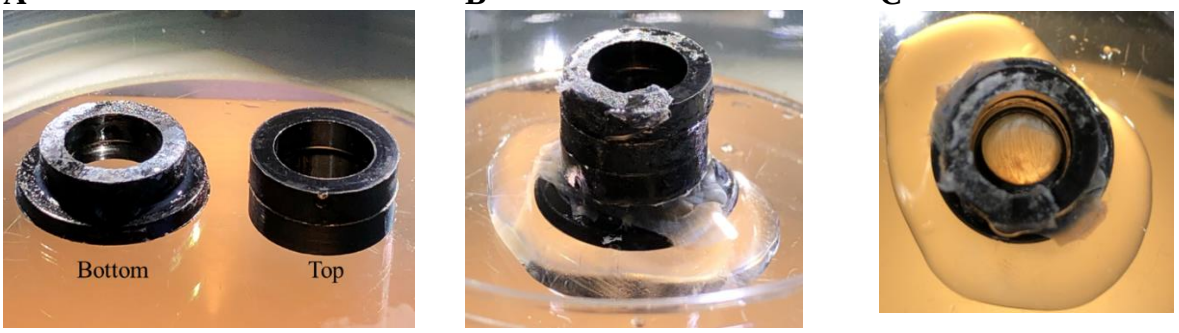

Figure 2- 8. Model 4. (A) Set up for model 4. Leaking observed in model 4. From **(B)** side and **(C)** top view.

2.6.6 Model 5: Custom made model fabicated using clear acrylic

Model 5, was custom made to my design and machined from clear acrylic by Michael Wilkes from the School of Engineering at Newcastle University (**Figure 2- 9**). The model consisted of a base, into which was inserted a two-piece acrylic membrane held together. The basal volume was 2.5ml and apical volume 0.15ml (**Figure 2- 9**).

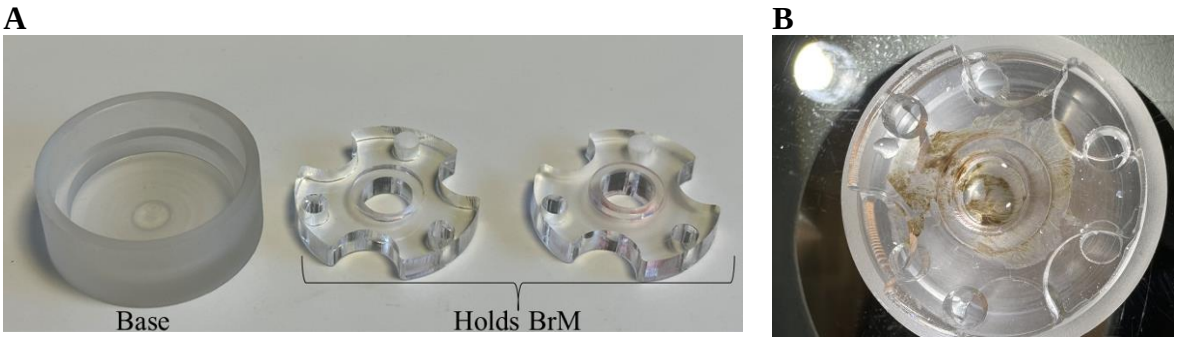

Figure 2- 9. Model 5. (A) An image of the parts of model 5. **(B)** Top view of the model with the dBrM attached.

2.6.7 Model 6: 3D printed model in clear resin

Model 6 was a 3D printed model in clear resin made with the help of Michael Wilkes from the School of Engineering at Newcastle University (**Figure 2- 10**). Again, it consisted of a two-parts to hold BrM (**Figure 2- 10**). As model 5 previously had a large basal volume, the volume of model 6 was reduced. The apical compartment had a 0.3ml volume, while the basal compartment held 0.4ml.

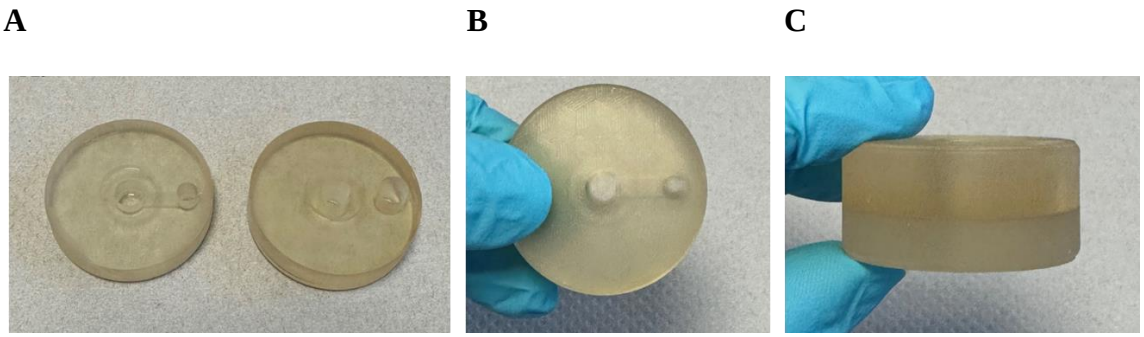

Figure 2- 10. Model 6. (A) The top and bottom compartments of the mode. **(B)** Top view of the model. **(C)** Side view of the model.

2.6.8 Model 7: Model machined on a lathe and milling machine from clear acrylic bar

Model 7 was like model 5, machined from clear acrylic by Michael Wilkes from the School of Engineering at Newcastle University. The model contains two top compartments that hold dBrM (**Figure 2- 11 A -** label 1 and 2) and a bottom compartment (**Figure 2- 11 A**—label 3). The basal compartment holds 1 ml, and the apical holds 0.25 ml.

A

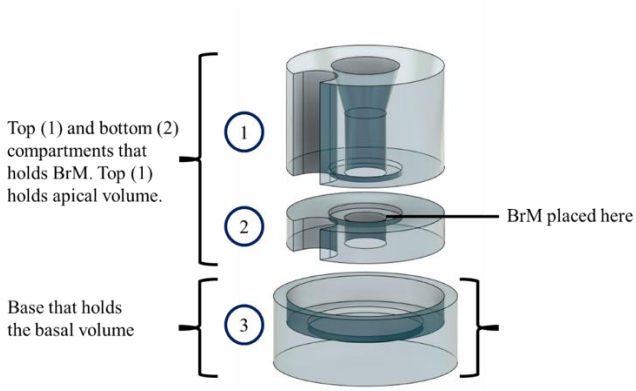

B

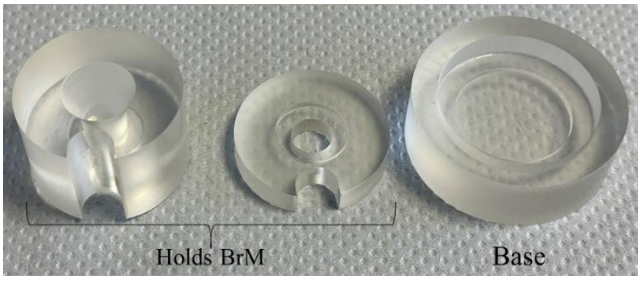

C

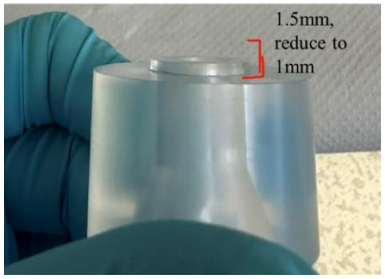

Figure 2- 11. Model 7. (A) Illustration of model 7. **(B)** The top and bottom compartments of the model. **(C)** The top compartment of the model shows a 1.5mm zone that acts to clip the two compartment together and that was subsequently reduced to 1mm.

2.7 Diffusion experiment

In the diffusion experiments, the dBrMs used did not show the presence of AMD or any other macular pathology (based on patient information and gross morphology) and were decellularised via CP as in **section 2.2.3**. When looking at the diffusion on Ussing chamber, on the sample chamber, purified complement proteins (C5a, C3a, FD, FH and sCR1 CCP1-11 Flag His tag (hereafter known as truncated sCR1), FITC-IgG and glucose were diluted with 0.2% BSA (A9418, Sigma-Aldrich) in PBS (**Table 2- 6**). The concentration of the complement proteins, glucose and FITC-IgG was 10 µg/ml except for FH at 5 µg/ml. The diffusate chamber was filled with 2.5ml 0.2% BSA in PBS. About 200 µl of the sample dilution mixture was left alongside the Ussing chamber as a control for comparison of the concentration of the proteins (known as pre-chamber). It was left for 24 hours on a magnetic stirrer (HS120549, Sigma-Aldrich). This was the same for diffusion experiment of FITC-IgG and glucose across dBrM in Model 1,2,3 ,5 , 6 and 7 (**Section 2.6**).

Proteins and molecules	Cat code	Source
CFI	A138	Hycult Biotech
FD	A136	Comptech
C3a	A118	Comptech
C5a	A144	Comptech
sCR1 CCP1 – 11 Flag His tag	NA	In-house (Gyroscope Therapeutics, a Novartis Company)
FITC-IgG	F9636	Sigma
D-Glucose	G7528	Sigma

Table 2- 6. The proteins used during the diffusion experiment. The proteins, catalogue number and source.

2.7.1 Mesoscale discovery analysis

R-Plex mesoscale discovery (MSD) analysis was conducted to determine the percentage of diffusion of complement proteins CFI, FD, C3a and C5a (**Table 2- 6**). MSD Gold 96-well small spot streptavidin plates (Cat L45SA-1, MSD) were coated with CFI, FD, C3a and C5a biotinylated antibodies diluted in 1% BSA in PBS (**Table 2- 7**). The MSD plates were then incubated on a plate shaker (EP5384000012, Merck) at 750 rpm at room temperature for 1 hour. MSD plates were then washed three times with MSD wash buffer (R61AA-1, Meso Scale Discovery) before adding the standards (**Table 2- 6**) and samples, which were diluted in 1% BSA 10mM EDTA. MSD plates were incubated at 850 rpm at room temperature for 1 hour. The washing step was repeated before adding the detection antibodies (**Table 2- 8**) and left to incubate at 850 rpm at room temperature for 1 hour. MSD plates were then washed before adding the MSD Gold read buffer, and the plate was analysed on MESO QuickPlex SQ120.

Assay	Cat code and source	Required concentration
CFI	A247, Quidel	1.50 µg/ml
FD	MSD, C213E-3 (R-plex)	1:17.5
C3a	MSD, C21V0-3 (R-plex)	1:17.5
C5a	NBP2-23498, Biotechne	1.00 µg/ml

Table 2- 7. Coating antibodies. The coating antibodies used for each MSD assay.

Assay	Cat code and source	Required concentration
CFI	Quidel, A231	0.5 µg/ml
FD	MSD, D213E-3	1:1000
C3a	MSD, D21V0-3	1:1000
C5a	Biotechne, MAB20371	2 µg/ml

Table 2- 8. Detection antibodies. The detection antibodies used for each MSD assay.

2.7.2 Jess automated western blot

JESS Simple Western™ was conducted to assess the diffusion of truncated sCR1 (**Table 2- 6**) across the dBrM. The truncated sCR1 was used to plot the standard curve. Samples and the positive control were diluted in 1x fluorescent master mix (EZ standard pack I – PS-ST01EZ-8; ProteinSimple®). Each well was added with 3 µL samples. The primary antibody, rabbit anti-DYKDDDDK (MAB8529) was used at 1:50, diluting in antibody diluent 2 (042-203, Proteinsimple) and 10µl were added per well. The secondary antibody (Anti-Rabbit-HRP) was added to each well at 10µl, while the luminol and peroxide solution (DM-001) were used as instructed with 15µl at each well. The capillary cartridges and plates were from the 12-120 kDa separation module (ProteinSimple®, SM-W004-1). Compass for Simple Western was used to analyse the results.

2.7.3 Glucose analysis

Glucose colorimetric assay (10009582, Cayman Chemical) was performed to assess the diffusion of glucose (**Table 2- 6**) across dBrM. The percentage of glucose diffused was as per the manufacturer's instructions (Cayman Chemical. Glucose assay., 2025). Briefly, the sample and diluted assay buffer, at a ratio of 3:17, respectively, were mixed. The reaction was then initiated by adding enzyme mixture at a ratio of 1:1 and allowing the plate to incubate for 10 minutes at 37ºC. The absorbance was then measured at 520 nm using a Varioskan Lux multimode microplate reader (ThermoFisher Scientific). The formula to measure the percentage of diffusion was [(Apical absorbance)/(Apical + basal absorbance)*100%].

2.7.4 IgG analysis

The percentage of FITC-IgG (**Table 2- 6**) diffuse across dBrM was measured by measuring the sample's fluorescence at excitation 495 nm and emission 525nm using a Varioskan Lux multimode microplate reader (ThermoFisher Scientific). The formula to measure the percentage of diffusion was [(Apical absorbance)/(Apical + basal absorbance)*100%].

2.8 iPSC-RPE cell culture

2.8.1 iPSC-RPE cells culture and seeding

The iPSC-RPE cells were pobtained from Fujifilm, Cellular Dynamics (R1113). These are known as iCell RPE cells, comprising a highly pure population of research-grade RPE cells derived from human iPSCs. These cells were handled in a Class II biosafety cabinet laminar airflow tissue culture hood (KS12 Herasafe, Heraeus). The iPSC-RPE cells were cultured on a transparent transwell with a pore diameter of 0.4µm (665641 or 662641, Grenier bio-one). The coating surface was covered with 2mg Matrigel (354230, Corning) and left for 1 hour at room temperature before being removed for cell seeding. The cryovials of iPSC-RPE cells were obtained from the liquid nitrogen. The cryovials were allowed to thaw for 3 minutes at room temperature, then spun at 1000 rpm for 5 minutes before resuspending with the prepared media. Cells were seeded based on their required densities **(Table 2- 9)**. Media changes occurred three times a week. The media recipe is shown below. Cells were maintained until desired time points in a humidified environment at 37^{o}C and 5% CO_2 (HERAcell 150, Heraeus).

Transwell name	Transwell culture diameter (cm)	Transwell culture area (cm^2)	Manufacturer and catalogue number	Cell seeding density (cells)	Apical volume (ml)	Basal volume (ml)
12-well transwell	1.38	1.13	Grenier bio-one, 665641	175 000	0.4	1.0
24 well transwell	0.84	0.33	Grenier bio-one, 662641	51 107	0.25	0.50

Table 2- 9. Cell density required for culture area.

2.8.2 iPSC-RPE cells media

The media used to culture these iPSC-RPE cells were prepared to the final concentration as in **Table 2- 10**. During transduction experiments, Opti-MEM media (31985070, ThermoFisher Scientific) was utilised as a serum free media.

Components	Manufacturer and catalogue number	Final concentrations
Minimum essential medium (MEM) alpha	ThermoFisher Scientific, 12571-062	91.3%
Heat-inactivated fetal bovine serum (FBS)	ThermoFisher Scientific, 10500064	5%
N-2 supplement	ThermoFisher Scientific, 17502-048	1%
Hydrocortisone	Sigma, H6909	55 nM
Taurine	Sigma, T0625	250 µg/ml
Triiodo-L-thyronine (T_3)	Sigma, T5516	14 pg/ml
Gentamicin	ThermoFisher Scientific, 15750-060	25 µg/ml

Table 2- 10. Media preparation for iPSC-RPE cells. Components, manufacturer and catalogue number, and final concentration required.

2.8.3 Transepithelial electrical resistance measurement

Transepithelial electrical resistance (TEER) measures the transepithelial resistance or barrier function giving insights into RPE cell maturity. The TEER values were measured in OHMs (Ω) using Millicell ERS-2 Voltohmeter (MERS00002, Milipore), with two electrodes (a short and a long electrode). To measure the TEER, the short electrode tip is inserted on the side of the transwell insert, while the long electrode tip is inserted on the side of the well (**Figure 2- 12**). A blank transwell measurement was taken from transwells that contained the MEM alpha medium alone. The readings were then obtained for the rest of the transwells. The reading of the blank transwell was subtracted from the reading of the transwells with iPSC-RPE cells. The formula was applied: Unit area resistance = resistance (Ω) x effective membrane area (cm^2). TEER measurements were taken at different day points.

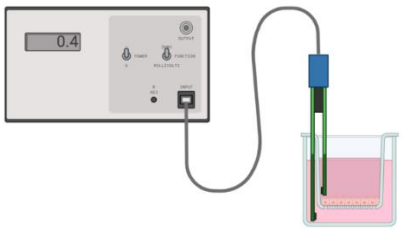

Figure 2- 12. Schematic of TEER measurement. It shows the position of the electrodes, with the shorter one on one side of the transwell and the longer one in the well.

2.8.4 VEGF ELISA

Secreted VEGF from iPSC-RPE cells was measured with a human VEGF enzyme linked immunosorbent assay (ELISA) Kit (DY293B, Biotechne Europe Ltd) as per manufacturer's instruction (Bio-techne., 2025). Briefly, plates were coated with 1 µg/ml coating antibody overnight at 4^{o}C. The plates were washed with 0.05% Tween 20 in PBS three times before blocking with 1% BSA in PBS for 1 hour at room temperature, followed by the washing step. The standards and samples were incubated for 2 hours at room temperature before the washing step. The detecting antibody at 100 ng/ml was allowed to incubate for 2 hours at room temperature. Washes were performed before adding strep-HRP for 20 minutes. A final washing was performed before adding substrate solution for 20 minutes, followed by a stop solution. The absorbance was then measured at 450 nm using a Varioskan Lux multimode microplate reader (ThermoFisher Scientific).

2.8.5 PEDF ELISA

Secreted PEDF from iPSC-RPE cells was measured with a human Serpin F1 ELISA Kit (EH415RB, ThermoFisher Scientific) as per manufacturer's instruction (ThermoFisher Schientific, 2025). Briefly, pre-coated plates were blocked with 1% BSA in PBS for 1 hour at room temperature, followed by the washing step as in **section 2.8.4**. The standards and samples were incubated for 2.5 hours at room temperature before the washing step. The biotin conjugate was then incubated on for 1 hour at room temperature followed by washing step. Next, Streptavidin-HRP was incubated for 45 minutes followed by washing step. Lastly, incubation with TMB for 30 minutes at room temperature in the dark followed by a stop solution. The absorbance was then measured at 450 nm using a Varioskan Lux multimode microplate reader (ThermoFisher Scientific).

2.8.6 Phagocytosis assay

Labelled bovine POS were obtained from InVision BioResources. These were centrifuged for 4 minutes at 2600 rcf, and the supernatant was aspirated. The POS pellet was resuspended in 10 ml RPE maintenance media supplemented with 0.4 mg/ml FITC (46950, Sigma). Next, the mixture was left on a shaker for one hour, protected from light. The mixture was then centrifuged for 4 minutes at 2600 rpm, and the supernatant was aspirated. Following this,

washes were performed by resuspending the pellet with PBS. This was performed twice. After the last wash with PBS, FITC-POS were counted using a haemocytometer. FITC-POS were resuspended and stored in 2.5% sucrose in PBS at -80^{o}C.

iPSC-RPE cells cultured on Matrigel or dBrM were treated with 20 POS per cell and incubated for 4 hours at 37^{o}C. Two controls were performed alongside this; the first control, iPSC-RPE cells, were challenged with the same number of non-stained POS and incubated for 4 hours at 37^{o}C. The second control, iPSC-RPE cells, were challenged with the same number of FITC-POS and incubated for 4 hours at 4^{o}C as phagocytosis does not take place at low temperatures.

After the incubation, cells were washed with PBS and detached using 10X trypleE^{TM} Select Enzyme (A1217707, ThermoFisher Scientific) for 12-15 minutes. The cells were resuspended with flow buffer containing 5% FBS in PBS and 5mM DRAQ5 (424101, Biolegend) to label the cell nucleus. After 5 minutes, cells were centrifuged at 1000 rpm for 3 minutes and treated with 0.2% trypan blue to quench the fluorescence of extracellular FITC-POS for 10 minutes. Next, the cells were washed three times and resuspended in the flow buffer. Samples were analysed using LSR Fortessa flow cytometry, and the events were set to 10,000 events. Analysis was performed on FCS Express 7.

2.9 Endothelial colony forming cells cell culture

2.9.1 Endothelial colony forming cells culture and seeding

The endothelial colony forming cells (ECFC) were obtained from Dr Reinhold Medina's lab at Queen University Belfast. Briefly, mononuclear cells were obtained from fresh human peripheral blood by density gradient fractionation. The mononuclear cells were then resuspended with EGM-2 MV (Lonza) media supplemented with 10% FBS and seeded on a precoated well with rat tail collagen type 1 (15250061 ThermoFisher Scientific). ECFC handling was performed in a Class II biosafety cabinet laminar airflow tissue culture hood (KS12 Herasafe, Heraeus). The ECFCs were cultured on a 6-well plate (CC7682-7506, Starlab). The wells were coated with rat tail collagen type 1 and left to incubate for 1 hour before being removed for cell seeding. The ECFCs in the cryovials were taken from liquid nitrogen and were allowed to thaw for 3 minutes at room temperature, then spun at 1000 RPM for 5 minutes before being resuspended with the prepared media. Cells were seeded based on their required densities of 10 000 cells/cm^{2}. Media changes occurred three times a week, and the media is shown below.

Cells were maintained until desired time points in a humidified environment at 37ºC and 5% CO_2 (HERAcell 150, Heraeus).

2.9.2 ECFC media

The media used to culture these ECFCs were EBM-2 basal medium (CC-3156, Lonza) supplemented with EGM SingleQuots Supplement Pack (FBS, hydrocortisone, human fibroblastic growth factor (hFGF), VEGF, long R3 insulin-like growth factor 1 (R3-IGF-1), ascorbic acid. hEGF, GA-1000 and heparin) (CC-4176, Lonza). Components were mixed together, and additional FBS (10500064, ThermoFisher Scientific) were added to the final media mixture at a 1:5 ratio before being filtered using a 0.22 µm filter (99150T, Helena Bioscience).

2.10 iPSC-EC cell culture

2.10.1 iPSC-EC culture and seeding

The iPSC-ECs were primary cells obtained from Fujifilm, Cellular Dynamics (01434). These cells were handled in a Class II biosafety cabinet laminar airflow tissue culture hood (KS12 Herasafe, Heraeus). The iPSC-EC cells were cultured on a transparent transwell with a pore diameter of 0.4µm (665641 or 662641, Grenier bio-one). The coating surface was covered with 2 mg Matrigel (354230, Corning) and left for 1 hour at room temperature before being removed for cell seeding. The cryovials of iPSC-EC cells were obtained from the liquid nitrogen. The cryovials were allowed to thaw for 3 minutes at room temperature, then spun at 1000 RPM for 5 minutes before resuspending with the prepared media. Cells were seeded based on their required densities at 15, 000 cells/cm^2. Media changes occurred three times a week, and the media is discussed below. Cells were maintained until desired time points in a humidified environment at 37ºC and 5% CO_2 (HERAcell 150, Heraeus).

2.10.2 iPSC-EC media

The media used to culture these iPSC-ECs was similar to ECFC media, EBM-2 basal medium (CC-3156, Lonza). This is described in the **section 2.9.2** .

2.11 Co-culturing of iPS- RPE cells and iPSC-EC on decellularised Bruch's membrane

All steps were conducted under a class II biosafety cabinet laminar airflow tissue culture hood (KS12 Herasafe, Heraeus).

2.11.1 Culturing iPSC-RPE cells on the RPE side of decellularised Bruch's membrane

iPSC-RPE cells were cultured on Matrigel coated dBrM or dBrM alone. The model of dBrM attachment was either Model 2 or Model 7 (**Section 2.6.3** and **section 2.6.8**). To coat the dBrM with Matrigel, the coating surface was covered with 2 mg Matrigel (354230, Corning), which was left for 1 hour at room temperature before being removed for cell seeding. Cells were seeded as described previously (**Section 2.8.1**) at the seeding densities as in **Table 2- 11**.

Model	Model culture diameter (cm)	Model culture area (cm^2)	Manufacturer and catalogue number	Cell seeding density (cells)	Apical volume (ml)	Basal volume (ml)
Model 2	0.8	0.50	Grenier bio-one, 665641	77 500	0.4	1.0
Model 7	0.6	0.23	Grenier bio-one, 662641	36 000	0.2	1.0

Table 2- 11. The seeding cell densities. The seeding density of iPSC-RPE cells on model 2 and 7.

2.11.2 Culturing ECFC or iPSC-EC on decellularised Bruch's membrane

The ECFCs passage 15 were cultured on dBrM coated with rat tail collagen type 1 or 2 mg Matrigel on model 2 at a seeding density of 10 000 cells/cm^2. The maintenance medium was as described in **section 2.9.2**, and the cells were left for 5 days.

iPSC-ECs passage 1 were cultured on the basal side of dBrM with day 21 iPSC-RPE cells on the apical side at 15, 000 cells/cm^2 in model 2. The maintenance medium was described in **section 2.9.2** and the cells were left for 7 days.

2.12 Histology analysis

2.12.1 Fixing of iPSC-RPE cells, ECFCs and Bruch's membrane

iPSC-RPE cells or ECFCs on transwells were fixed with 4% paraformaldehyde (PFA) for 30 minutes at room temperature, followed by three washes with PBS for 5 minutes each. ECFCs were then ready for staining, while the iPSC-RPE cells in the transwell were cut and placed on glass slides (J1800AMNZ, Epredia) for staining.

Native BrM, dBrM, or co-cultured dBrM were all fixed similarly. The tissue was incubated with 4% PFA at room temperature for 1 hour, followed by three washes with PBS for 5 minutes. Dehydration was achieved by incubating the tissue with 30% sucrose for 1 hour at room temperature, followed by three washes with PBS for 5 minutes. Tissue sections were then ready for sectioning.

2.12.2 Sectioning of tissue

Tissue sections were embedded in moulds (HIS0221, Wolf Laboratories Ltd) using optimum cutting temperature (OCT) medium (KMA-0100-00A, CellPath) on dry ice for 10 minutes. The sample blocks were sectioned into slices of 10µm on a cryostat (CM1860, Leica), and sections were placed on a glass slide (J1800AMNZ, Epredia). Slides were stored at -20^{o}C until needed.

2.12.3 Immunofluorescence analysis

Sections on the glass slide were separated using a hydrophobic pen, ImmEdge® hydrophobic barrier pen (H-4000, Vector laboratories) and allowed to air dry for 10 minutes at room temperature. Sections were incubated with blocking solution (10% horse serum in PBS for tissue and 10% horse serum 5% BSA in PBS for cells) for 1 hour at room temperature. Sections were then incubated with primary antibodies (**Table 2- 12**) overnight at 4^{o}C. Sections were washed with PBS three times for 10 minutes each before adding the secondary antibody (**Table 2- 13**) and nuclear stain, Hoechst (hoe) (B2261, Sigma) for 1 hour at room temperature. Sections

were washed three times with PBS for 10 minutes each time before adding Vectashield (H-1000, VectorLabs). The glass slides were then sealed with a cover slip (10083957, Fisher Scientific). The glass slides were kept at 4°C until required for microscopy. Three sections from each sample were stained.

Antibody	Cat num and source	Host	Target	Dilution
ZO1	61-7300, ThermoFisher	Rabbit	Cell membrane	1:50
Laminin	2E8, Development studies hybridoma bank antibodies (DSHB)	Mouse	ECM	1:50
Collagen IV	Ab6586, Abcam	Rabbit	ECM	1:50
CD31	GA61061-2, Agilent Dako	Mouse	Surface of ECs	Neat (pre diluted)

Table 2- 12. List of primary antibodies. The list of primary antibodies, cat num, source, host, target and dilution used in immunofluorescence.

Antibody	Cat num and source	Host	Against	Dilution
AlexaFluor 546 donkey anti-rabbit	A10040, Invitrogen	Donkey	Rabbit	1:400
AlexaFluor 488 donkey anti-mouse	A21202, Invitrogen	Donkey	Mouse	1:400

Table 2- 13. List of secondary antibodies. The list of secondary antibodies, cat number, source, host, target and dilution used in immunofluorescence.

2.12.4 Microscopy and image analysis

Fluorescence images and brightfields of tissue or cells on glass slides were analysed and captured using an Axio Imager 4 microscope with apotome (Zeiss, Germany). Analysis was carried out using Zeiss Zen blue software.

2.13 Transmission electron microscopy

Tissue and cell sections required for transmission electron microscopy (TEM) were fixed with 2% glutaraldehyde in 0.1M sodium cacodylate buffer and stored at 4°C. The samples were then processed by Newcastle University electron microscopy facility. Briefly, 1% of osmium tetroxide was further used to fix the samples before they were dehydrated and embedded using gradient acetone and epoxy resin. Ultrathin sections of 70 nm were then stained with heavy

metals such as uranyl acetate and lead citrate on copper grids. Images were taken using Philips CM100 TEM.

2.14 Transduction of iPSC-RPE cells

2.14.1 Transduction of iPSC-RPE cells with AAV 2 or 8 GFP

iPSC-RPE cells were apically transduced with AAV2 GFP and AAV8 GFP obtained from Gyroscope Therapeutics, a Novartis Company (**Figure 2- 13 A**) to determine the most optimal AAV. AAV-2 and AAV-8 null were used as controls as they carry the random stuffer sequence (**Figure 2- 13 B**). The conditions tested are as below and summarised in **Figure 2- 14**:

1. Comparing AAV 2 and AAV 8 GFP when transduced on day 3 and day 21 iPSC-RPE cell at five different multiplicities of infection (MOI). MOI is the number of AAV particles that are added per cell (**Table 2- 14**).

2. Comparing the difference between MEM alpha medium and Opti-MEM during the transduction period. Opti-MEM differs from MEM alpha as serum free.

3. Comparing at 500 000 MOI but different concentrations of AAV2 GFP, 5.63E+10 vg/ml, 9.00E+10 vg/ml and 2.25E+11 vg/ml.

4. Once the optimum AAV, MOI and concentration were determined, iPSC-RPE cells cultured on dBrM were transduced with AAV 2 GFP at 500 000 MOI and 1.56E+11 vg/ml.

The concentration of each AAVs stock is as follow:

AAV2 GFP stock concentration: 4.32E+12 vg/ml

AAV8 GFP stock concentration: 1.48E+13 vg/ml

AAV2 null stock concentration: 2.90E+12 vg/ml

AAV8 null stock concentration: 1.18E+13 vg/ml

A.

B.

Figure 2- 13. Vector scheme for AAV 2/8 mEGFP and Null. (A) Represents the mEGFP schematic, while **(B)** represents the null schematic. ITR: Inverted Terminal Repeat. CMV: Cytomegalovirus promoter. CBAP: Chicken beta actin promoter. mEGFP: monomeric enhanced green fluorescent protein, bGH pA: Bovine Growth Hormone polyadenylation signal.

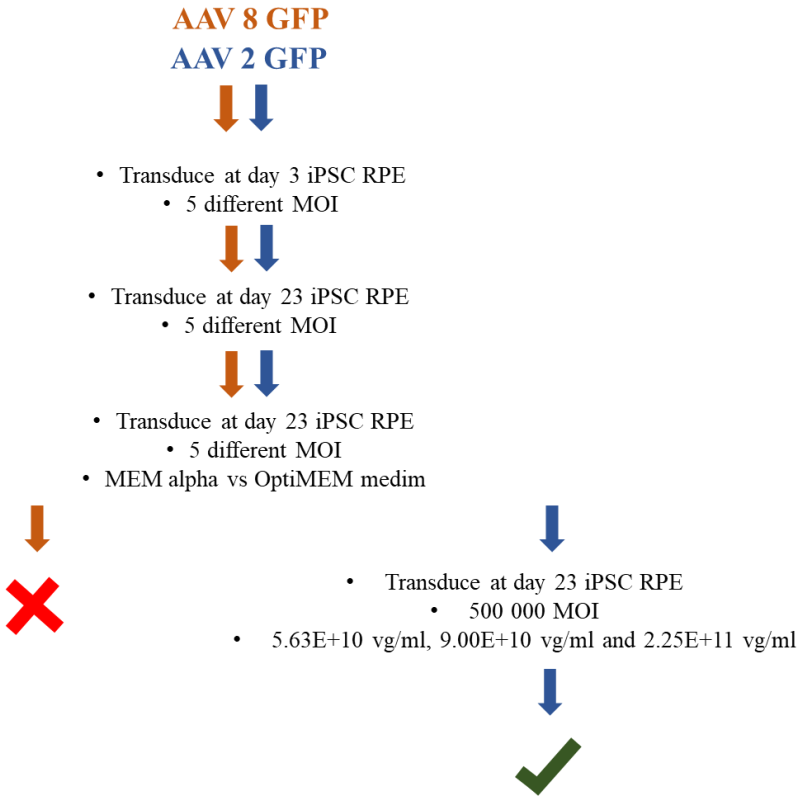

Figure 2- 14. The flow summary of the optimisation of transduction experiment. Initially, both AAV 8 GFP and AAV 2 GFP were added at day 3 iPSC-RPE cell with 5 different MOI. Next, AAV 8 GFP and AAV 2 GFP were added on day 23 iPSC-RPE cells with 5 different MOI. Then, AAV 8 GFP and AAV 2 GFP were added at day 23 iPSC-RPE cells with 5 different MOI. During the addition of AAV, the medium was compared between MEM alpha and Opti-MEM. Lastly, AAV 8 GFP was decided not to be taken forward, and AAV 2 GFP were transduced on day 23 iPSC-RPE cells on Matrigel, at 500,000 MOI and 3 different AAV concentrations (5.63E+10 vg/ml, 9.00E+10 vg/ml and 2.25E+11 vg/ml).

MOI (vg/ml)	Cell density (cells)	AAV particles (vg)	AAV concentration (vg/ml)
0	45 000	0	0
1 000	45 000	4.50E+07	9.00E+07
10 000	45 000	4.50E+08	9.00E+08
100 000	45 000	4.50E+09	9.00E+09
1 000 000	45 000	4.50E+10	9.00E+10

Table 2- 14. The MOI, cell density, AAV particles and AAV concentration. These were the values for AAV 2 / 8 GFP and null.

2.14.2 Transduction of iPSC-RPE cells with AAV2 truncated sCR1

The iPSC -RPE cells cultured on dBrM or Matrigel were then transduced with AAV2 truncated sCR1 (**Figure 2- 15**). Gyroscope Therapeutics, a Novartis Company, produced AAV2 CR1 CCP1-11 HIS FLAG. As a control, iPSC-RPE cells cultured on dBrM or Matrigel were transduced with AAV2 Null (**Figure 2- 13 B**). The concentration used to transduce was 4.88E+10 vg/ml for iPSC-RPE cells cultured on dBrM and 4.50E+10 vg/ml for iPSC-RPE cultured on Matrigel.

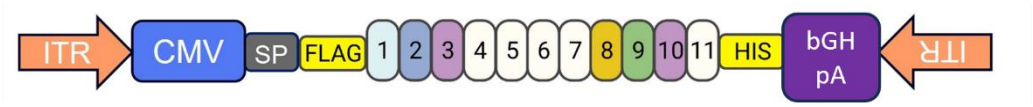

Figure 2- 15. Vector scheme for AAV2 sCR1 CCP1-11 Flag His tag (truncated sCR1). ITR: Inverted Terminal Repeat. CMV: Cytomegalovirus promoter. SP: Signal Peptide. bGH pA: Bovine Growth Hormone polyadenylation signal.

2.14.3 Analysis of GFP positive cells via flow cytometry

To measure the percentage of GFP-positive iPSC-RPE cells was performed using a Special-Order BD LSRFortessa^{TM} Cell Analyzer. The iPSC-RPE cells were washed with PBS before dissociated using 10X trypleE^{TM} Select Enzyme (A1217707, ThermoFIsher Scientific) for 12-15 minutes. The cells were resuspended with flow buffer containing 5% FBS in PBS and washed twice by centrifuging at 1000 RPM for 3 minutes. Samples were resuspended with flow buffer and analysed using LSR Fortessa flow cytometry, and the events were set to 10,000 events. Analysis was performed on FCS Express 7.

2.14.4 Analysis of GFP positive cells via Incucyte imaging

The GFP-positive cells were imaged on the IncuCyte at 20X magnification. Analysis was conducted on Incucyte software.

2.14.5 Measuring cell cytotoxicity

Cell cytotoxicity was determined by two methods: TEER measurements and lactate dehydrogenase (LDH) assay. TEER was carried out as described in **Section 2.8.3**. To perform the LDH assay, the kit CyQUANT^{TM} LDH Cytotoxicity Assay Kit (C20300, Invitogen) was used. The samples were prepared as follows:

- Maximum LDH activity: 20 µl of triton X-100 was added to one well and gently mixed by pipetting. The obtained values corresponded to a completely disrupted cell sample.
- Spontaneous LDH activity: dH_2O was added to the cells. The obtained values were to measure normal LDH activity.
- AAV-treated LDH activity: The supernatant of AAV treated cells.

The protocol was as per the manufacturer's instructions (Invitrogen. CyQUANTTM LDH Cytotoxicity Assay Kit., 2025). Briefly, 50 µl of the reaction mixture (provided in the kit) was mixed with the sample wells. The plate was then incubated for 30 minutes at room temperature (light protected) before adding 50 µl of stop solution. The absorbance was measured at 490 nm and 680 nm using a VarioskanTM LUX multimode microplate reader.

2.14.6 Western blot fluid phase co-factor assay

The fluid phase co-factor assay determined the efficacy of truncated sCR1 in terms of its co-factor activity with FI. This is conducted by incubating the supernatant of the cell after transduction with AAV2 truncated sCR1with 1µg C3b (A114, Comptech) and 100ng FI (A138, Comptech). As a positive control, supernatant from the untreated cultures were incubated with 1µg C3b, 100ng FI and 1.3 µg truncated sCR1 (Gyroscope Therapeutics) were diluted in PBS. For the negative control, the supernatant of AAV2 null treated was incubated with 1µg C3b and 100ng FI was diluted in PBS. Some experiments were performed without the addition of FI to test if FI released from the cells can form this breakdown. Samples and control were left for 1 hour at 37ºC. To stop the reaction, an equal volume of 2X Laemlli buffer (J60015, Life

Technologies) with 50 mM dithiothreitol (DTT) (R0862, ThermoFisher Scientific) was added to the samples and incubated for 2 minutes at 99^{o}C.

The samples and control proteins were separated using a NuPAGE, 4 to 12% Bis-Tris 1.0-mm mini gel (NP0322BOX, ThermoFisher Scientific) at 100V for 1 hour. Additionally, 5 µl of molecular weight protein marker, PageRuler Plus prestained protein ladder (26619, ThermoFisher Scientific) was loaded while 15µl pf the samples were loaded. The running buffer was MOPS (3-(N-morpholino)propane sulfonic acid) (NP0001, Invitrogen).

Proteins were transferred onto a polyvinylidene difluoride (PVDF) membrane (IB24001, Invitrogen) using an iBlot 2 (IB24002, ThermoFisher Scientific) at 20V for 7 minutes. The PVDF membranes were blocked with 5% milk in tris-buffered saline (TBS) solution substituted with 0.05% Tween (TBS-T) for 1 hour at room temperature. The membranes were incubated overnight with the primary antibody, Polyclonal rabbit anti-human C3d complement (A006302-2, Agilent) at 1 in 1000 dilution at 4^{o}C overnight. Thereafter, the membranes were washed three times with TBS-T for 10 minutes before adding the secondary antibody, Peroxidase-conjugated AffiniPure donkey anti-rabbit IgG (H+L) (711-035-152-JIR, Stratech) at 1 in 50 000 dilutions for 1 hour at room temperature. The washing step was repeated before detecting the protein band by adding SuperSignal West Femto Maximum Sensitivity Substrate (ThermoFisher, 34095). The signal was developed using the Syngene Gbox Chemi XX6.

2.14.7 FLAG Tag ELISA

An ELISA (DYKDDDDK-Tag Detection ELISA Kit 501560, Cayman Chemical) was performed to detect any Flag-bound truncated sCR1 was conducted on supernatant from iPSC-RPE cells cultured on media or dBrM. This was performed as per manufacturer's instructions (Cayman Chemical. DYKDDDDK-Tag Detection ELISA Kit., 2025). Briefly, samples and standards were incubated on the precoated plate for 90 minutes, followed by 5 washes with the wash buffer. TMB substrate solution was then added and incubated for 30 minutes at room temperature. The reaction was stopped by adding the HRP stop solution, and the plate was read at 450nm using a Varioskan Lux multimode microplate reader (ThermoFisher Scientific).

2.15 Data analysis

Statistical analysis was performed using Prism (GraphPad, USA). To compare variables and statistical significance, t-test or ANOVA was used. Multiple comparison tests such as Tukey's and Sidak's tests with Bonferroni correction were also used. Information is all indicated in the figure legend.

Chapter 3 Comparing three Bruch's membrane decellularisation protocols to native Bruch's membrane

3.1 Introduction

Tissue decellularisation has been applied to various ocular tissues, with each tissue requiring a tailored approach due to differences in ECM composition, thickness, and structural properties. A critical aspect of any decellularisation process is preserving the integrity of the ECM, which is fundamental to subsequent cell survival and attachment during recellularisation process. This chapter focuses on the decellularisation of BrM, detailing methods involving detergents and enzymes.

In most decellularisation regimes, detergents such as Triton X-100 or SDS are key agents. SDS which is an anionic detergent, is known to be more effective than Triton X-100, a non-ionic detergent. Non-ionic detergents disrupt the hydrophobic interactions within lipid bilayers, allowing the detergent to insert itself into the cell membrane, disrupting the lipid-lipid and lipid-protein interactions (Pizzirusso et al., 2017). Anionic detergents interact with the hydrophobic region of proteins and membranes, with their negative charge crucial to their denaturing abilities (Owoyomi et al., 2005). Interestingly, when used together, the interactions allow for more efficient solubilisation compared to using each alone (Owoyomi et al., 2005) . Other key agents used in decellularisation are such as ammonium hydroxide, hypertonic sodium chloride (NaCl) solution and DNase. Ammonium hydroxide, a mildly basic compound, disrupts the cell membrane while disrupting hydrogen bonds to induce cell lysis (Moffat et al., 2022). Decellularisation via hypertonic NaCl, a neutral salt removes cellular content through osmotic stress (L. H. W. Y. Luo H & Zhang M, 2013). While DNase is used as a treatment step useful for removing nucleotides from ECM (Moffat et al., 2022). During washing steps, streptomycin or penicillin are usually added to prevent bacterial contamination (Moffat et al., 2022). Other methods of decellularisation include physically removing cells from the tissue using a cell scraper, which may cause tears, variability between samples, and ECM disruption (McHarg et al., 2015).

The success of decellularisation can be assessed through brightfield imaging, immunofluorescence, DNA quantification, and proteomic analysis. Brightfield and immunofluorescence imaging allow the visualisation of components such as pigmentation (indicating cellular presence) or ECM markers like collagen IV and laminin. DNA quantification measures residual cellular content post-decellularisation, while proteomic

analysis provides a deeper understanding of protein retention and removal, as well as the biological processes they are involved in. Preserving the ECM is crucial to maintaining its structural framework, essential for studies aiming to model the disease. Laminin and collagen are the proteins that play an important role in the ECM component of BrM (Chirco et al., 2017). Laminin has three main subunits: alpha (LAMA1-5), beta (LAMB 1-4) and gamma (LAMC1-3) (Sicari et al., 2023). Laminin is a crucial ECM that facilitates the adhesion of RPE cells to BrM via the integrin–laminin interaction (Aisenbrey et al., 2006). Both integrin α3β1 and α6β1 on the RPE cell surface bind to several laminins on BrM, including Laminin 1 (α1β1γ1), Laminin 5 (α3β3γ2), and Laminin 10 (α5β1γ1) (Aisenbrey et al., 2006). Lastly, there are 28 types of collagens, with collagens I, III, IV and V being the primary ones found in BrM (Chirco et al., 2017).

A number of previous studies have explored the decellularisation of human BrM, followed by its recellularisation for disease modelling. The earliest study of BrM decellularisation was by Tezel T *et al*, where decellularisation of BrM was performed, followed by attachment of fetal hRPE and ARPE-19 reattachment (Tezel et al., 1999, 2004). During the decellularisation, they utilised 0.02N ammonium hydroxide in PBS for 20 minutes, followed by three washes with PBS (Tezel et al., 2004, 1999). Lastly, BrM was treated with 0.1% Triton X-100 and 0.1% sodium citrate solution for 20 minutes at 4°C (Tezel et al., 2004, 1999). The use of Triton X-100 successfully ensured the membranous debris from BrM was extracted while preserving the anionic glycosaminoglycan bridges between collagen fibrils and native collagen structures while dissolving membranous POS without disrupting the ultrastructure of the matrix (Tezel et al., 2004, 1999; Pauleikhoff et al., 1994; Scott & Thomlison, 1998). Besides that, sodium citrate successfully facilitated the solubilisation of lipid debris and facilitated the breakdown of age-related pentosidine cross-link between collagen fibres (Tezel et al., 2004, 1999; Handa et al., 1999b).

Another study by Cai H *et al* decellularised BrM from young (20-49 years) vs old (50-89 years) donors and observed the ability of primary RPE cells attachment and survival, assessed by apoptosis and proliferation rates, phagocytosis of POS, cell polarity and gene expression (Cai et al., 2018). The decellularisation process consisted of incubating BrM in 0.02 M ammonium hydroxide in PBS for 20 minutes at room temperature and then washing it three times with PBS. BrM was then covered basal side down in solidified agarose gel to stabilise the complex.

A key study used in this thesis was by Chirco K *et al* where four different BrM decellularisation protocols were assessed for best cellular material removal and ECM preservation (Chirco et al., 2017). Once the best protocol was established and confirmed by DNA quantification, proteomic

analysis and fluorescence imaging, attempted dBrM recellularisation with monkey CEC was assessed (Chirco et al., 2017). Their protocol 4 (hereafter referred to as Chirco K *et al* protocol (CP)) removed the most cellular material while preserving the ECM. The protocol began with cell lysis and disruption of DNA-protein interaction by changing the osmolarity of the tissue by incubating BrM with dH_2O for 1.5 hours. Next, 1% Triton X-100 was applied for 3 hours to disrupt DNA-protein, lipid-protein and lipid-lipid interactions. The washing step with PBS was then applied for 15 minutes. To ensure complete disruption of the molecular bonds, the tissue was then incubated for 18 hours in 1% Triton X-100 before being washed with PBS. Solubilisation of cellular and nuclear membranes to remove cellular material and disrupt their adhesion to ECM was then carried out with the addition of 0.1% SDS + 0.1M EDTA for 3 hours. Washes with PBS were conducted before incubation at 37^{o}C with 10U/mL DNAse I to remove any remaining DNA. The final PBS washes was conducted before dH_2O was applied for 1.5 hours as a final rinse.

Other studies have investigated tissue types beyond the retina, including those of porcine origin, such as the study by Luo H *et al,* where the decellularisation of porcine cornea was used for corneal graft (Luo H., 2013) and by Zhao H *et al* , for the decellularisation of porcine conjunctiva for tissue engineering studies (Zhao et al., 2014). However, it is important to note that the structures and ECM composition of the animal models' eye tissue differ from humans, particularly in the retina (Volland et al., 2015a; Dong et al., 2019). As a result, the decellularisation processes may vary. Focusing on retinal tissue decellularisation, studies in bovine models looking at decellularisation of the retina for the production of retinal progenitor cell culture utilising SDS and pepsin (Kundu et al., 2016) and in mouse and porcine retina decellularisation to allow recellularisation with RPE (Maqueda et al., 2021) have been conducted. Although these decellularisation protocols are not specific to BrM, they are summarised in **Table 3- 1**.

Publication	Tissue origin	Tissue type	Purpose of decellularisation	Method of decellularisation
Tezel T *et al* (1999, 2004)	Human	BrM	Recellularise with fetal human RPE cells and ARPE-19 cells	• 0.02 N ammonium hydroxide in PBS for 20 minutes at room temperature. • PBS wash 3 times. • 0.1% Triton X-100 and 0.1% sodium citrate solution for 20 minutes at 4°C.

Luo H *et al* (2013)	Porcine	Cornea	Recellularise with amniotic epithelial cells	• dH_2O for 12 hours. • 2M NaCl for 30 minutes. • dH_2O for 30 minutes. • Repeat NaCl and dH_2O steps three times. • 0.2% Triton X-100 for 6 hours. • PBS wash.
Zhao H *et al* (2014)	Porcine	Conjunctiva	Recellularise with corneal epithelial cells	• PBS containing 100 U/mL penicillin and 100 mg/mL streptomycin, treated with 0.1% SDS for 12 hours at 37°C • PBS wash 3 times. • Air-dried.
Kundu J *et al* (2016)	Bovine	Retina	Forming decellularised retina films to culture human retinal progenitor cells	• 1% SDS at room temperature for 3 hours • Centrifuged at 10,000 rpm for 15 minutes at 25°C, and resuspended in dH_2O. • Wash with dH_2O 48 hours.
Chirco k *et al* (2017)	Human	BrM	Recellularise with monkey CEC	• dH_2O for 1.5 hours. • 1% Triton X-100 for 3 hours. • PBS wash for 15 minutes. • 1% Triton X-100 overnight (18 hours). • PBS wash for 15 minutes. • 0.1% SDS + 0.1M EDTA for 3 hours. • PBS wash for 15 minutes. • 10 U/μL DNase I at 37°C. • Wash with dH_2O for 1.5 hours.
Cai H *et al* (2018)	Human	BrM	Recellularise with primary RPE cells	• 0.02 M ammonium hydroxide in PBS for 20 minutes at room temperature. • PBS wash three times.

Maqueda M *et al* (2021)	Mouse and porcine	Retina	Recellularise with hiPSC-RPE and ocular progenitor cells	• Decellularisation at room temperature with agitation (50 rpm) using a stepwise protocol:
				  ○ dH_2O with Turbo DNase I for 2 hours.
				  ○ 0.5% Triton X-100 in water overnight.
				  ○ 0.1% SDS in water for 2 hours.
				• Washes with dH_2O (2 × 30 minutes) and PBS with penicillin/streptomycin for 24 hours.

Table 3- 1. The different methods of decellularisation of different tissue types.

Despite the various decellularisation methods available, the CP protocol remains limited due to its lengthy duration, making it time consuming for research. Establishing a standardised protocol for BrM would improve consistency across studies and ensure the preservation of key ECM structures necessary for its function. Therefore, refining the protocol to optimise efficiency while maintaining ECM integrity is essential for advancing research in this field.

3.2 Aims

This chapter aimed to identify a decellularisation protocol that most optimally preserved ECM proteins and removed cellular components in a time efficient manor. Bright-field imaging, immunofluorescence, DNA quantification, and proteomic analysis were conducted on native BrM as a control, and BrM decellularised via three different protocols (CP, SP1, and SP2). **Figure 3- 1** summarises the experimental aims of this chapter.

As described previously, CP is published and shows successful ECM preservation and removal of cellular material. A shortened protocol (SP1) had been adopted by Scott Scarp, who previously worked at Gyroscope Therapeutics, a Novartis company. Scott used SP1 as it was shorter than CP, allowing diffusion experiments on BrM to be carried out in a 3-day windows. Further modifications were made to SP1 to produce SP2, with the addition of DNase to assess its effect on cellular content. **Table 3- 2** describes the three protocols.

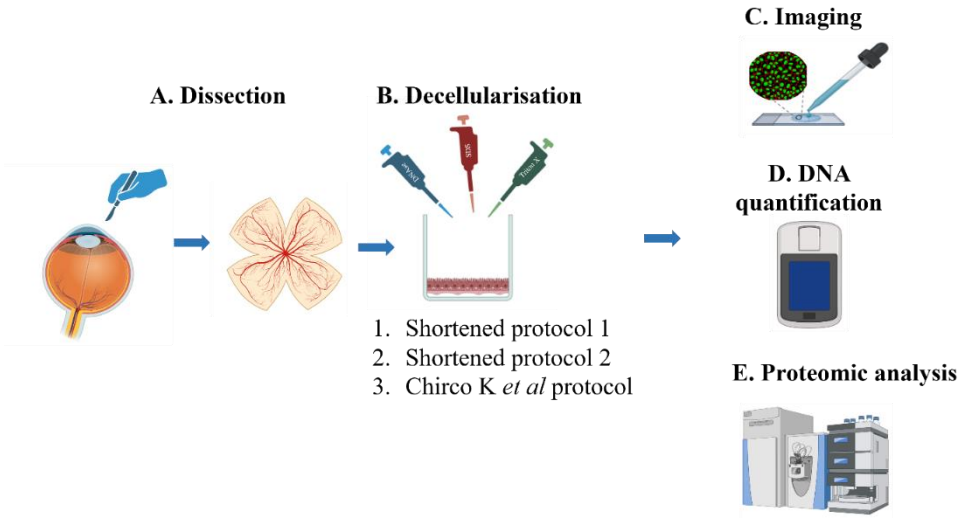

Figure 3- 1. Graphical overview of the chapter. (A) Dissection of the donor globes was conducted, followed by **(B)** decellularisation of BrM using three different protocols: **(C)** Imaging, **(D)** DNA quantification and **(E)** proteomic analysis. Images were created using BioRender.

CP	SP1	SP2
• dH_2O for 1.5 hours. • 1% Triton X-100 for 3 hours. • PBS wash for 15 minutes. • 1% Triton X-100 for 18 hours. • PBS wash for 15 minutes. • 0.1% SDS + 0.1M EDTA for 3 hours. • PBS wash for 15 minutes. • 10 U/μL DNase I at 37°C. • Wash with dH_2O for 1.5 hours.	• 1% triton X-100 for 30 minutes. • Wash 1% penstrep twice. • 1% triton X-100 for 1 hour. • Wash 1% penstrep twice. • 1% triton X-100 for 1 hour. • Wash 1% penstrep twice.	• 1% triton X-100 for 30 minutes. • Wash 1% penstrep for 15 minutes. • 1% triton X-100 for 1 hour. • Wash 1% penstrep for 15 minutes. • 1% triton X-100 for 1 hour. • Wash 1% penstrep for 15 minutes. • 10U/mL DNase 1 solution at 37°C for 1 hour. • Wash 1% penstrep for 15 minutes.

Table 3- 2. **The decellularisation protocols.** The decellularisation protocols used in this chapter, namely CP, SP1 and SP2.

3.3 Results

3.3.1 Imaging of the choroidal and RPE surface after decellularisation

The dBrM and native BrM were observed by capturing bright field images. This was to observe any cellular content that remained after decellularisation, such as pigmented RPE cells. Images were taken facing the choroidal and RPE sides. BrM decellularised via CP, SP1, and SP2 showed transparent blood vessels, indicating the decellularisation protocol successfully cleared residual blood cells as seen in the native BrM choroidal side up (**Figure 3- 2**). All three decellularisation protocols showed no visible RPE cells compared to the native BrM, which appeared as a hexagonal and pigmented cell sheet (**Figure 3- 2**). However, some irregular non descript pigmentation was present on the RPE side of BrM decellularised via SP1, and to a lesser extent after SP2 (**Figure 3- 2**). Overall, these results show effective decellularisation in removing residual blood cells, with some pigmentation seen in SP1 and SP2.

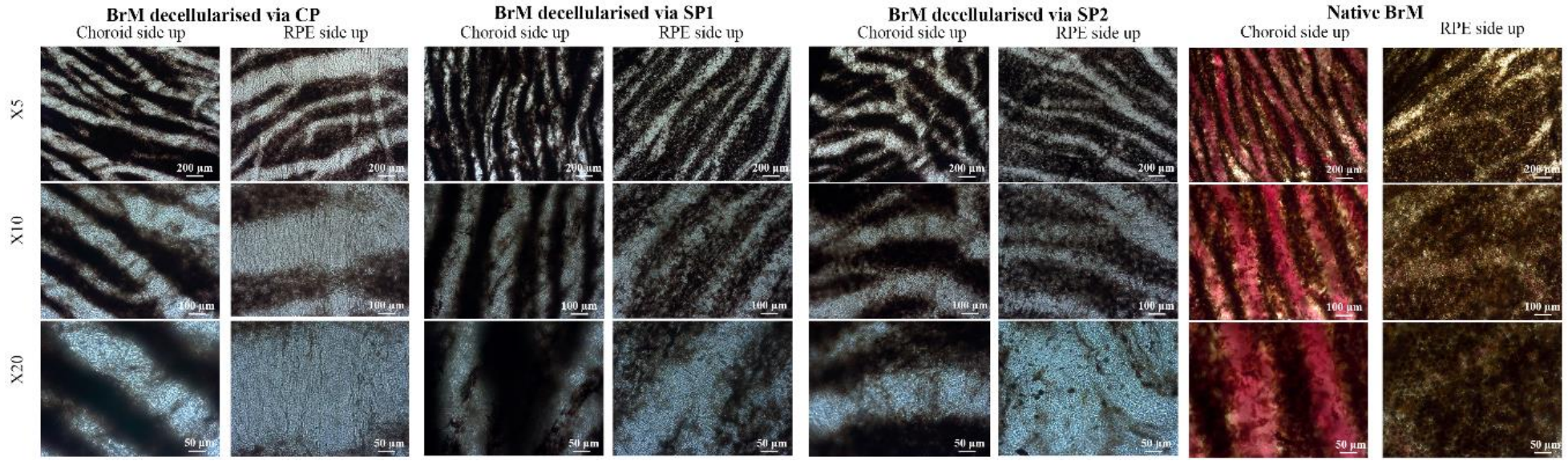

Figure 3- 2. Bright-field images of choroidal and RPE side up of decellularised BrM via three protocols and native BrM. From left to right, BrM decellularised via CP, SP1, SP2 and native BrM. Images are choroidal and RPE side up at x5, x10 and x20 magnification. CP: Chirco K et al protocol ; SP1: Shortened protocol 1 ; SP2: Shortened protocol 2.

3.3.2 Immunofluorescence detection of ECM markers and cellular material after decellularisation

Immunofluorescence staining was conducted to allow anatomical preservation to be assessed. Cellular materials were detected by positive nuclear stain (Hoechst (Hoe)) and CD31 (CEC marker). The markers used for ECM were collagen IV and pan-laminin (hereafter referred to as laminin.

BrM decellularised via CP shows no pigmentation in the bright field images (**Figure 3- 3 A**) Collagen IV and laminin were detected in the dBrM via CP, while CD31 was not (**Figure 3- 3 B-D**). Some pigmentation was detected in the dBrM via SP2 in the bright field images (**Figure 3- 3 I**). In decellularisation via SP2, laminin was seen much less compared to CP, SP1 and native BrM, with collagen IV detected while CD31 was not (**Figure 3- 3 B, F, J, K** and **N**). In contrast, BrM decellularised via SP1 displayed noticeable pigmentation in bright-field images (**Figure 3- 3 E**). Hoechst and minimal CD31 staining were present (**Figure 3- 3 F-G**), indicating incomplete removal of cellular components. However, collagen IV and laminin were retained (**Figure 3- 3 F**).

The native BrM (**Figure 3- 3 M-P**) served as a reference, showing the expected intact ECM with collagen IV and laminin distribution and the presence of cellular markers such as CD31 and Hoechst. Compared to native tissue, the decellularised samples displayed varying degrees of visible ECM preservation and cellular removal, underscoring differences in protocol effectiveness. The results indicate that both CP and SP2 achieved effective cellular removal while preserving ECM, whereas SP1 exhibited some residual cellular material.

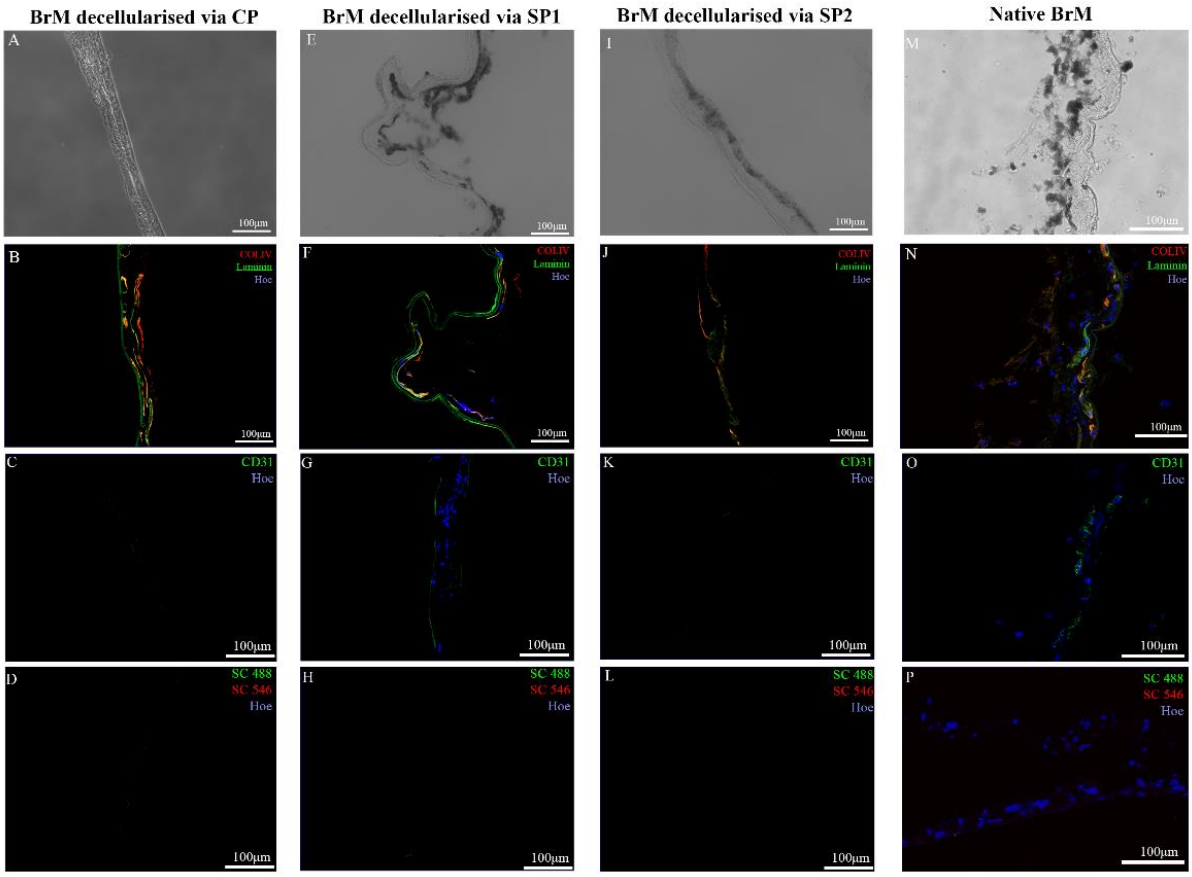

Figure 3- 3. Immunofluorescence images of BrM decellularised via CP, SP1, SP2 and native BrM. (A, E, I and M) the bright field images of BrM decellularised via CP, SP1, SP2 and native BrM, respectively. **(B, F, J and N)** collagen IV (red), laminin (green) and Hoechst (hoe) (blue) immunofluorescence images of BrM decellularised via CP, SP1, SP2 and native BrM, respectively. **(C, G, K and O)** CD31 (green) and hoe (blue) immunofluorescence images of BrM decellularised via CP, SP1, SP2 and native BrM, respectively. **(D, H, L and P)** the secondary control (No primary antibody added) immunofluorescence images of BrM decellularised via CP, SP1, SP2 and native BrM, respectively.

3.3.3 Quantification of remaining DNA after decellularisation

DNA quantification was performed on BrM decellularised via CP, SP1, SP2 and native BrM to determine any residual cellular material. The DNA concentration in BrM decellularised via CP was 0.63±0.37 ng/µl, via SP1 4.34±0.61 ng/µl, via SP2 0.72±0.37 ng/µl and in native BrM 4.81±1.20 ng/µl (**Figure 3- 4**). There was a significant difference between the DNA concentration in CP and SP2 when compared to native BrM ($p = 0.014$and $p = 0.016$, respectively) (**Figure 3- 4**). There was also a significant difference between CP and SP1 ($p=0.026$) and SP1 and SP2 ($p=0.030$) (**Figure 3- 4**). In contrast, the DNA concentration in SP1 was not significantly different from native BrM ($p = 0.966$) (**Figure 3- 4**). As well as between

CP and SP2 (p=0.999) (**Figure 3- 4**). Overall, these results indicate that decellularisation via CP and SP2 resulted in significantly less DNA than SP1, suggesting that CP and SP2 decellularisation was efficient.

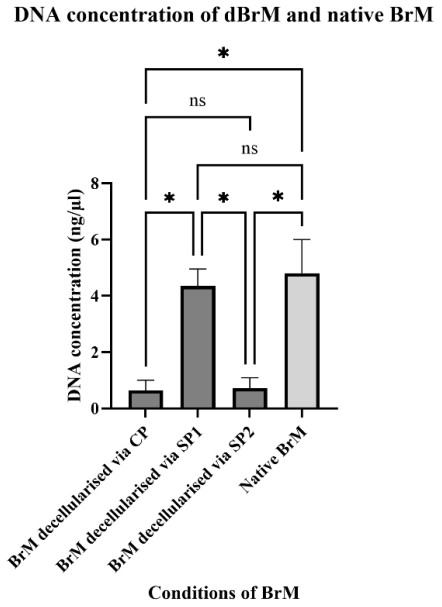

Figure 3- 4. The DNA concentration in dBrM. The DNA concentration (ng/µl) of dBrM and native BrM. Data shows mean ± SEM (n = 3 tissue sections per condition). One-way ANOVA with Tukey's multiple comparisons test was conducted to determine significance. Values with $p \leq 0.05$ were considered statistically significant ($*p \leq 0.03$).

3.3.4 Identifying ECM protein retention and cellular protein removal after decellularisation

Proteomic analysis was conducted to assess protein-coding genes (PG genes), which correspond to the identified protein groups that remained after decellularisation; these were compared to native BrM. The volcano plot was performed to visualise the proteins that were removed or retained after decellularisation (n=3). The analysis was performed on decellularised tissue (CP, SP1, or SP2) against native BrM, where their Z scores of fold changes were obtained (**Figure 3- 5 A-C**). The volcano plot visualised -Log10 P (y-axis) against Z score (Fold change dBrM/Native BrM) (x-axis), revealing significance based on a p-value of -Log10 P greater than 1.3, with Z score values less than -2 or greater than 2 considered significant (red plots) (**Figure 3- 5 A-C**). Values that fall within the Z score range are represented as green plots, p-value ranges as blue dots, and non-significant values as grey dots (**Figure 3- 5 A-C**).

The proteins that represent the ECM that were labelled in the volcano plot (**Figure 3- 5 A-C**) were fibronectin 1 (FN1), laminin subunits such as LAMA2, LAMA3, LAMA4, LAMA5,

LAMB2, LAMC1, LAMC3 and collagen type IV alpha 2 chain (COL4A2). Conversely, the proteins that were selected in the volcano plot (**Figure 3- 5 A-C**) to represent cellular material were histones and nucleoporins such as H2A Clustered Histone 6 (H2AC6), H2AC21, linker histones such as H1-2, H1-3, H1-4, H1-5 and H4 cluster histone 1 (H4C1), nucleoporin 43 (NUP43), NUP188, NUP54, NUP37.

A.

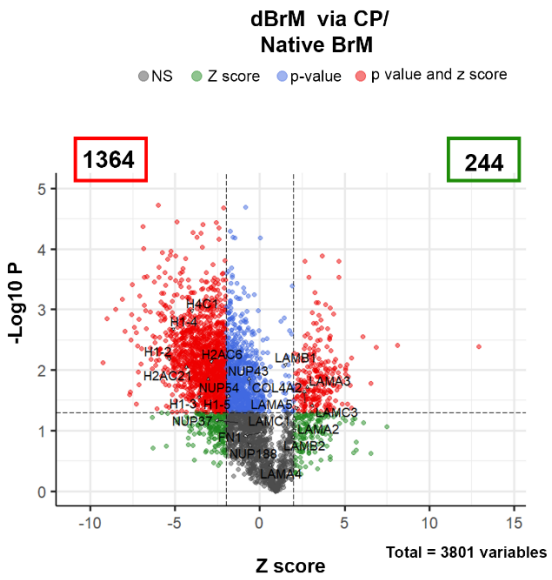

B.

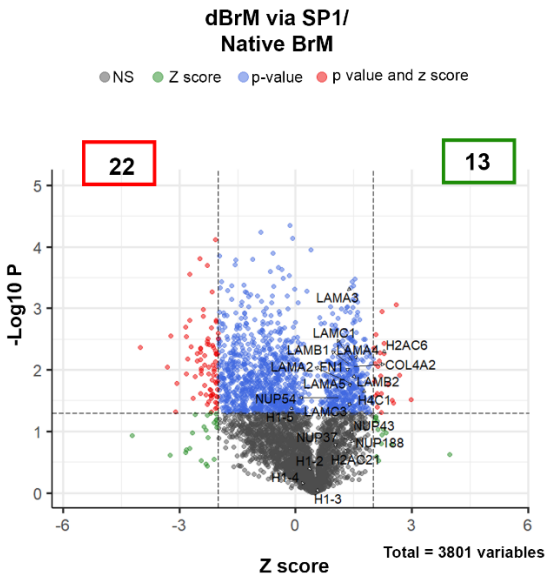

C.

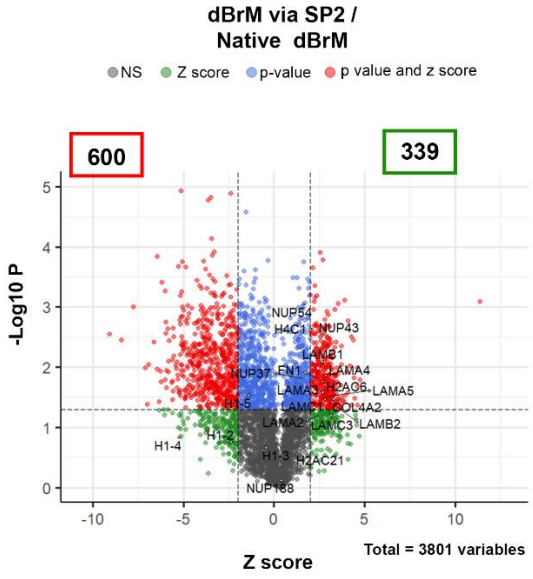

Figure 3- 5. Proteomic analysis of BrM decellularised via CP, SP1, SP2 and CP compared to native BrM. (A,B,C) Log10 P against Z score volcano plots for all the proteins that are detected in the decellularised and native BrM. The volcano plots of **(A)** CP/native, **(B)** SP1/native and **(C)** SP2/native. The area in red highlights proteins within the Z score and p-value; hence, they are significant. The area in blue highlights proteins within the p-value range, the green area shows the proteins within the z-score range, and the grey area shows the proteins in the non-significant range. n = 3.

In the analysis, a total of 3801 PG genes were detected. When comparing BrM decellularised via CP, to native BrM, 1364 proteins were significantly removed (red plots on the left), and 244 proteins were significantly retained (red plots on the right) (**Figure 3- 5 A**) in dBrM via CP. Histones and nucleoporins were significantly removed compared to native BrM, as indicated by the red plots on the left for H4C1, H2AC21, H2AC6, H1-2, H1-3, H1-4, and NUP54. In contrast, key ECM markers such as LAMC3, LAMA3, LAMA5, and COL4A2 were significantly retained after decellularisation, as shown by the red plots on the right (**Figure 3- 5 A**). Although some nucleoporins and histone, such NUP43, NUP188, NUP37, and H1-5 were not significantly removed, they still appeared on the left side of the graph, suggesting they were removed relative to the native BrM, including LAMA4 as indicated by the blue, grey and green plots on the left . Other ECM markers FN1, LAMA2, LAMC1, LAMB1, and LAMB2, were located towards the right side of the graph, indicating they were largely retained as shown by the blue, grey and green plots on the right .

Next, the decellularisation of BrM via SP1 compared to native BrM , 22 proteins were significantly removed (red plots on the left), and 13 proteins were significantly retained (red plots on the right) (**Figure 3- 5 B**). The majority of ECM, histones, and nucleoproteins were retained as they fell towards the right side of the volcano plot shown by the blue, grey and green plots on the right except H1-4 and H1-5 (**Figure 3- 5 B**). H2AC6 was significantly retained compared to native BrM as indicated by the red plots on the right (**Figure 3- 5 B**).

In BrM decellularised via SP2, compared to native BrM 600 proteins were significantly removed (red plots on the left), and 339 proteins were significantly retained (red plots on the right) (**Figure 3- 5 C**). ECM proteins such as LAMB1, LAMB2, LAMA3, LAMA4, LAMA5, LAMC1, LAMC3, and COL4A2, along with the nucleoporin NUP43, were significantly retained, as indicated by their positions on the right side of the volcano plot by the red plots (**Figure 3- 5 C**). Additional proteins that were retained, also appearing on the right side of the graph, were represented by blue, grey, and green plots, including NUP37, NUP54, NUP188, H1-3, H4C1, H2AC21, and FN1 (**Figure 3- 5 C)**. Conversely, proteins removed during the decellularisation process were located on the left side of the graph, as shown by blue, grey, and green plots. These included H1-2, H1-3, H1-4, and H1-5 (**Figure 3- 5 C)**.

To understand the roles of the differentially expressed proteins (DEPs) in dBrM compared to BrM, an analysis of the top BP, CC, and MF associated with these proteins was performed using GO terms. GO provides a structured framework for categorising genes based on their BP, MF,

and CC. The significantly retained and removed PG genes from the volcano plots (**Figure 3- 6 A-B**) were analysed using GO enrichment analysis (Gene ontology GO enrichment analysis), and bubble plots were generated for the GO categories that were significantly retained (**Figure 3- 6 A**) and removed (**Figure 3- 6 B**). In the plots (**Figure 3- 6 A-B**), fold enrichment analysis provided quantitative insights into the preservation of specific molecules and functions. Enrichment values above 1 indicated an increased relative abundance of molecules or activities, likely due to retention during decellularisation. Conversely, a fold enrichment of less than 1 suggested a reduction in abundance, potentially reflecting removal (or partial degradation) of specific proteins. Significant GO categories that were retained or removed were determined by the categories with the lowest p-values.

A.

Processes significantly retained

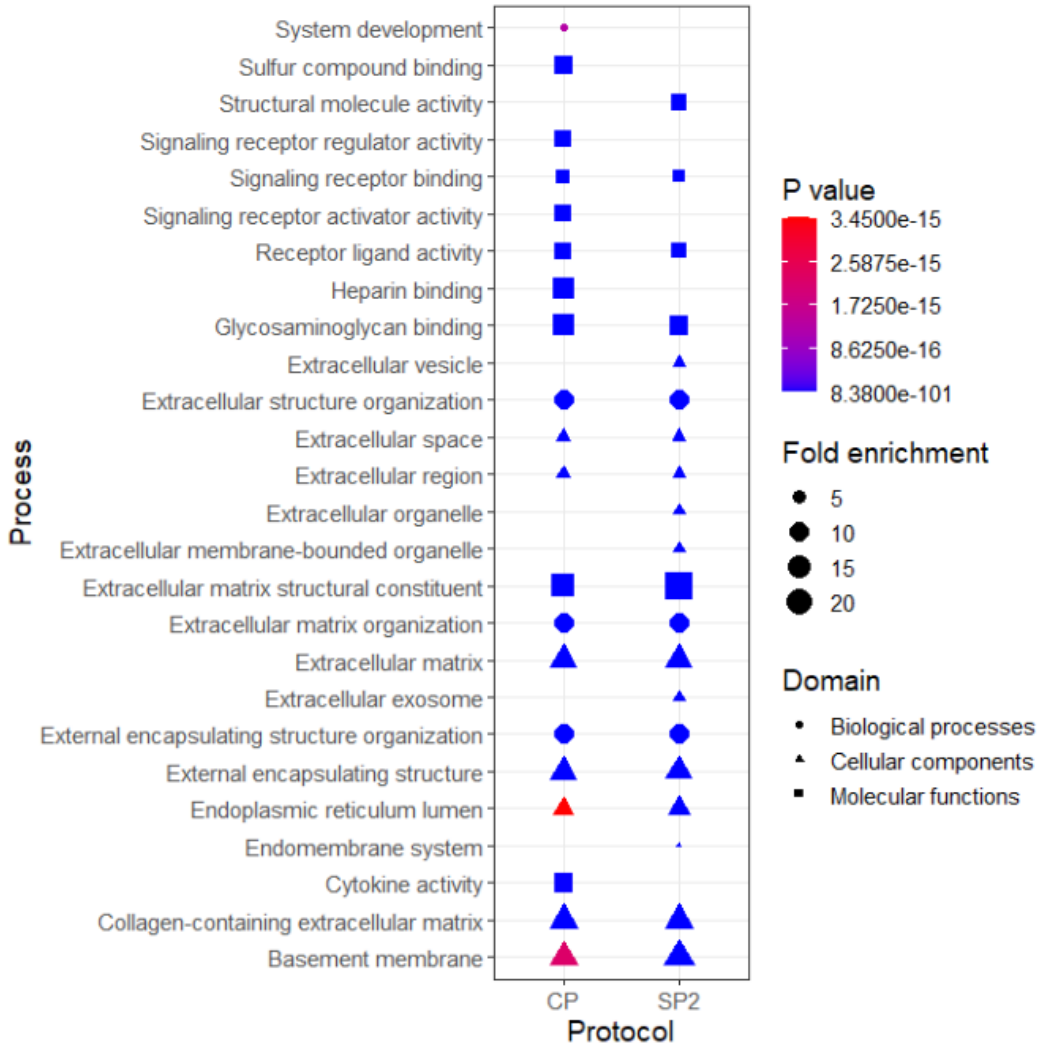

B.

Processes significantly removed

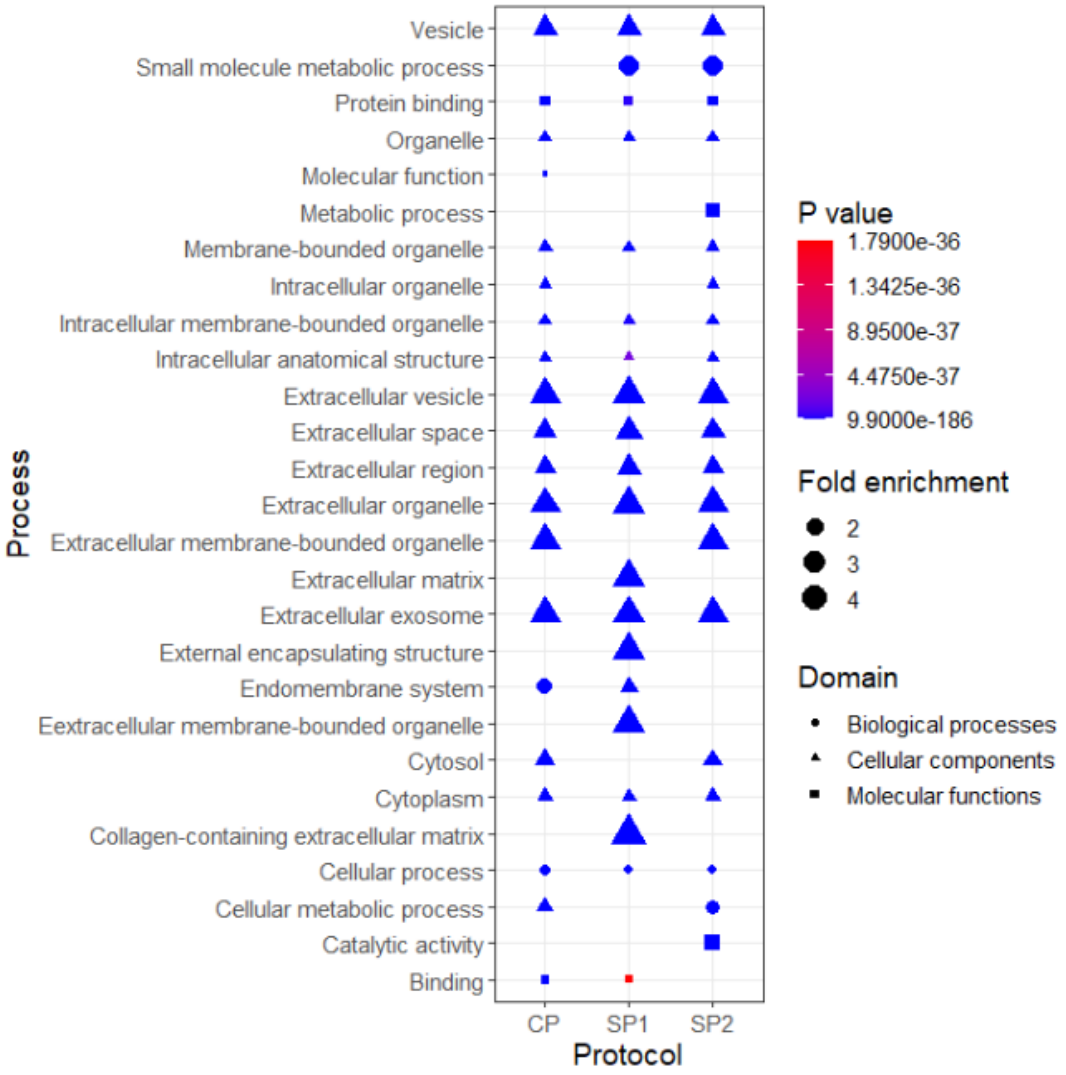

Figure 3- 6. The gene ontology processes. The plot shows the gene ontology processes being **(A)** retained **(B)** and removed. n = 3.

Firstly, looking at the significant GO categories retained in dBrM (**Figure 3- 6 A**), These findings were supported by statistically significant p-values, ranging from $3.45x10^{-15}$ to $8.38x10^{-101}$. The analysis revealed significant upregulation of ECM-related GO categories, including structural organisation and focal adhesion processes in decellularisation via CP and SP2. The organisation of the ECM (BP), extracellular space (CC), region (CC), and organisation (BP), ECM structural constituent (MF) as well as the external encapsulating structure (CC) and organisation (BP), was preserved in both CP and SP2, supporting the structural scaffold maintenance. Furthermore, the processes successfully preserved in both CP and SP2 were ECM structural constituents, such as collagen (CC) and basement membrane

(CC) supported the organisation of the ECM. Decellularisation via SP1 showed no significant retention of any processes.

CP demonstrated significant retention of molecules involved in system development (BP), suggesting the maintenance of structural and functional elements essential for cellular differentiation and tissue formation. Key activities, including binding sulfur (MF) compounds and heparin (MF), were maintained in CP, while glycosaminoglycan binding (MF) was maintained in both CP and SP2. These processes maintain molecular interactions essential for structural stability and biochemical signalling.

Furthermore, cytokine (MF) activity was retained in CP, indicating the preservation of signaling molecules involved in intercellular communication and inflammatory responses. Components of the endomembrane system (CC) was preserved in SP2 and the endoplasmic reticulum lumen (CC) were preserved in CP and SP2 , highlighting the ability of these processes to retain structures essential for protein synthesis, trafficking, and cellular stress responses.

Interestingly, extracellular exosomes (CC) and organelles (CC), extracellular vesicle (CC) including membrane-bound organelles (MF), were retained in SP2. This retention could compromise the goal of creating an acellular scaffold. Structural molecular activity (MF) was also retained in SP2 suggesting retention of protein complexes. Signalling receptor regulator activity (MF), signalling receptor activator activity (MF), and receptor-ligand interactions (MF) were retained in CP with the latter retained in SP2. The signalling receptor binding (MF) was preserved in both CP and SP2. These processes are crucial for maintaining the functional integrity of cellular communication.

Next, the significant GO categories removed in dBrM, as shown in **Figure 3- 6 B**, were supported statistically by significant p-values ranging from $1.79x10^{-36}$ to $9.9x10^{-186}$. The analysis revealed processes such as vesicle (CC), protein binding (MF), organelle (CC), membrane-bound organelle (CC), intracellular membrane-bound organelle (CC), intracellular anatomical structure (CC), extracellular vesicle (CC), extracellular space (CC), extracellular region (CC), extracellular organelle (CC), cytoplasm (CC), extracellular exosome (CC) and cellular processes (CC) were broadly reduced across CP, SP1, and SP2, reflecting the loss of cellular and extracellular structures as well as their functional interactions.

In SP1 and SP2 specifically, small molecule metabolic processes (BP) were significantly removed, suggesting a loss of metabolic activity linked to cellular components. In CP, the notable reduction in molecular function (MF) indicates a broader impact on cellular and biochemical activities. SP2 alone showed significant removal of metabolic processes (MF) and

catalytic activity (MF), further emphasising the disruption of enzymatic and metabolic pathways in this subgroup. SP1 exhibited a distinct loss of structural elements, such as extracellular matrix (CC), extracellular membrane-bound organelle (CC), external encapsulating structure (CC), and collagen-containing extracellular matrix (CC), indicating a marked alteration in the supportive and structural framework.

Additionally, categories such as intracellular organelle (CC), extracellular membrane-bound organelle (CC), cytosol (CC), and cellular metabolic processes (BP) were removed in both CP and SP2, highlighting shared effects in these subgroups. Similarly, both CP and SP1 experienced a significant reduction in the endomembrane system (BP or CC) and binding processes (MF), signifying a loss in intracellular transport and molecular interaction capabilities.

Collectively, the results demonstrate that CP and SP2 are effective in retaining critical molecular and structural features, including ECM components and functional molecules essential for extracellular organisation, signalling, and system development. However, these subgroups also showed the removal of key intracellular and metabolic processes, such as intracellular organelles, cytosol, and catalytic activity, indicating a targeted decellularisation effect. In contrast, SP1 showed retention of ECM and cellular material, indicating minimal decellularisation of BrM.

3.4 Discussion

In this chapter, we investigated the decellularisation of BrM using CP, SP1, and SP2 methods, each showing varying degrees of ECM retention and cellular component removal as summarised in **Table 3- 3**. CP was the most effective in preserving the ECM while removing the majority of cellular material. SP2 and SP1 followed in effectiveness. Brightfield imaging confirmed that SP1 retained more pigmentation compared to CP and SP2, which could indicate incomplete removal of melanin from the melanocytes. Immunofluorescence further supported these findings, showing the absence of nuclear staining in CP and SP2 and the preservation of Collagen IV and laminin while SP1 displayed detectable nuclear staining.

	CP	**SP1**	**SP2**
Brightfield and immunofluorescence imaging	• No pigmentation • Detection of COLIV and laminin	• Some pigmentation • Detection of COLIV, laminin and nuclear stain	• Some pigmentation • Detection of COLIV and laminin
DNA concentration as mean ± SEM (ng/µl)	0.63±0.37	4.34±0.61	0.72±0.37
Proteomic analysis when compared to native BrM	Good removal of cellular material and retention of ECM	Poor removal of cellular material and poor retention of ECM	Partial removal of cellular material and retention of ECM

Table 3- 3. Summary table. The bright field, immunofluorescence, DNA concentration and proteomic summary for BrM decellularised via CP, SP1 and SP2.

Furthermore, DNA quantification was used to measure cellular material, as DNA is a key cellular component, and its concentration directly correlates with the presence of cellular material (Chirco et al., 2017). The lowest DNA concentration after decellularisation was found in CP, followed by SP2 and SP1, suggesting that CP was the most effective at removing cellular components.

The proteomic analysis demonstrated that ECM retention was best preserved in CP, with significant cellular material removal, while SP2 showed some residual cellular components, as indicated by the GO processes related to ECM and cellular content. When comparing SP1 and SP2, the inclusion of DNase in SP2 enhances the removal of cellular material compared to SP1. This highlights the beneficial role of DNase in the decellularisation process. In the proteomic analysis, laminin, fibronectin and collagen IV were used as markers for ECM retention, while histones and nucleoporins were used as markers for cellular removal. Laminin and integrin

interaction, as discussed previously, are crucial for RPE cell attachment to BrM (Aisenbrey et al., 2006). RPE cells synthesis synthesises laminin 1 (α1ß1γ1), 5 (α3ß3γ2), and 10/11 (α5ß1/2γ1), to facilitate its adhesion to BrM via the integrin-mediated mechanism (Aisenbrey et al., 2006). Besides that, collagen, laminin and fibronectin play a crucial role in the ECM interaction pathway for RPE cell adhesion (Booij et al., 2009). Hence, the retention of fibronectin, collagen and laminin provides promising results for potential RPE attachment. Histones and nucleoporins provided the markers used to identify the completeness of cellular material removal. Histones are proteins that provides structural support to chromosomes and are also involved in regulation of gene expression (Bannister & Kouzarides, 2011). While nucleoporins are the main components of the nuclear pore, which regulate molecular transit through the nuclear membrane (Mariño-Ramírez et al., 2005; Chatel & Fahrenkrog, 2011). The removal of these proteins provides promising results in the removal of cellular materials.

Comparing the results of this chapter to the previous studies looking at human BrM decellularisation, such as by Tazel T *et al* (Tezel et al., 1999, 2004) research, where their primary objectives were to observe the ability of RPE reattachment, the rate of apoptosis, and proliferation. However, the culture surface was not investigated regarding the preservation of ECM, removal of DNA, and maintenance of the BrM structure. This is crucial for the culture of RPE cells, as discussed in previous studies the culture surfaces influence the ability of RPE cells to bind (Benedicto et al., 2017; Gullapalli et al., 2005).

An interesting conclusion by Cai H *et al* (Cai et al., 2018) shows that as BrM age increases, the number of genes expressed by RPE cells cultured on dBrM also varies. This was reflected in significantly lower RPE attachment rates and phagocytosis activity when cultured on older BrM compared to younger BrM. Besides that, in their study, BrM were solidified in agarose gel to ensure they stayed in place prior to culturing primary RPE cells. However, the impact of the added agarose layer on these outcomes, particularly its effect on RPE attachment rates with and without the gel, was not considered.

The study by Chirco K *et a*l (Chirco et al., 2017) conducted an analysis of dBrM using four distinct protocols, with CP identified as the most effective for decellularisation. Their findings, showing 1.2% residual DNA after CP treatment, align with our results that CP removed the most cellular material. They also observed the presence of collagen and laminin, alongside the absence of CD31 and nuclear staining, which was consistent with our observations. However, our proteomic analysis extends beyond these findings. While Chirco K *et al* (Chirco et al., 2017) only noted the detected proteins, they did not compare their presence to that in native BrM, a comparison that would provide valuable insight into how closely the decellularised BrM

mimics native tissue. This direct comparison is crucial as it helps assess the extent to which the decellularisation process preserves ECM integrity.

In summary, we demonstrated that decellularisation of BrM using CP effectively removes cellular content while preserving the ECM compared to native BrM. SP2 showed good preservation of the ECM, though to a lesser extent than CP. Both SP1 and SP2 resulted in some removal of cellular content, with CP achieving the most complete cellular removal. It is crucial to ensure that decellularisation is performed in a way that maintains the structural integrity of the tissue, as this is essential for its use in further modeling applications.

Chapter 4 Modelling the outer retina

4.1 Introduction

A representative and validated model of the outer retina would enable researchers to investigate disease mechanisms and evaluate potential therapies. Ensuring that the model closely resembles the native state, both functionally and morphologically, is crucial. To accurately model the outer retina 3 fundamental components are required: The RPE monolayer, the choroidal endothelium and a semipermeable membrane with the biomechanical and transmission properties of BrM separating these two cellular components.

No model has yet faithfully represented all three layers. The most similar is the 3D model by Song M *et al* (Song et al., 2023), as discussed earlier; however, it does not utilise BrM. Instead, it relies on a biodegradable scaffold in place of BrM, where the diffusion properties have not been tested against the native state (Song et al., 2023). Other studies utilise the culture of primary cells instead (Castellarin et al., 1998; Tsukahara et al., 2002; Gullapalli et al., 2005; Sugino et al., 2011; Gullapalli et al., 2008; Palanisamy et al., 2019), or cells from monkey origin on dBrM (Chirco et al., 2017). Hence, there is still a gap in creating an outer retinal model that accurately reflects its native state, including its diffusion characteristics.

4.1.1 Retinal pigment epithelium cells

One promising approach to recapitulate the RPE monolayer is using iPSC-RPE cells. Many studies have already utilised patient-specific iPSC-RPE cells to model AMD (Gong et al., 2020; Fisher et al., 2022; Hallam et al., 2017), particularly for investigating complement activation and evaluating new complement-targeted therapies (Hallam et al., 2017). A key factor in developing a reliable model is ensuring that iPSC-RPE cells exhibit the functional and anatomical characteristics of cells in the native tissue. Several established assays can assess this, including evaluating cellular morphology, TEER measurements for cellular and junctional integrity, secretory profiles (VEGF and PEDF), PG genes as RPE markers and phagocytic activity.

RPE cells are pigmented and hexagonally shaped with a high melanin content. Recently, it was shown that the intensity of pigmentation is a temporal condition and does not correlate with

the functional characteristics of RPE cells (Nakai-Futatsugi et al., 2024). Understanding the cellular morphology of RPE cells provides insights into cellular polarity, which is determined by the localisation of intracellular structures such as cilia, microvilli, melanosomes, and basal infoldings. Cilia located apically are essential for ciliary signalling, with signalling mediated by WNT and PKC delta occurring through the cilia (May-Simera et al., 2018). These signalling pathways are crucial for the formation of tight junctions (TEER values are typically above 200Ωcm²) and the establishment of apical-basal polarity (May-Simera et al., 2018). Microvilli are specialised, elongated projections that extend from the apical RPE cells and communicate with the photoreceptor cells (Bonilha et al., 2006). They play a crucial role in exchange of nutrients with photoreceptors and removing shed POS (Bonilha et al., 2006). Melanin, stored in melanosomes, plays a vital role in the eye by reducing light backscatter and neutralising free radicals (D'Alba & Shawkey, 2019). In the retina, melanosomes are present apically in RPE cells and choroidal melanocytes, where they protect photoreceptors from excessive light exposure (D'Alba & Shawkey, 2019). Furthermore, basal infoldings, which are found towards the basal side, play a significant role in the exchange between RPE and the choroid, particularly in the foveal region (Hayes et al., 2019). The greater density and increased surface area of basal infoldings in the fovea, compared to the parafovea, indicate an optimised structure for metabolite and ion exchange, aligning with the high metabolic demands of the fovea (Hayes et al., 2019). Additionally, RPE cells regulate angiogenesis through the secretion of VEGF towards the choroid and PEDF towards the apical side, inhibiting unwanted angiogenesis near the photoreceptors while PEDF promoting cell survival (Dawson et al., 1999; Polato & Becerra, 2016; Zhu et al., 2011). Phagocytosis of POS, shed daily, is another essential RPE function that can be assessed through phagocytosis assays (Westenskow et al., 2012).

Proteomic analysis showing the PG genes detected in iPSC-RPE cultures aids in identifying certain functional aspects, such as proteins involved in the visual cycle, lipid metabolism and cellular adhesion (Senabouth et al., 2022). Firstly, the visual cycle involves photoreceptors converting light energy into electrical signals via phototransduction. Besides that, RPE cells rely heavily on lipid metabolism as an alternative energy source, rather than glycolysis. However, they actively transport glucose from the choroid to the photoreceptors, which primarily depend on glycolysis for ATP production. Through beta-oxidation, fatty acids are broken down into acetyl-CoA , which then enters the Krebs cycle to generate ATP. This process is essential for preventing toxic accumulation of excess fatty acids while meeting the high energy demands of the RPE (Mitchell, 2001). Additionally, lipid metabolism enhances

antioxidant levels, protecting the RPE from long-term oxidative stress (Mitchell, 2001). ATP release also plays a significant role in fluid transport and modulating phagocytosis. Lastly, RPE cells are adherent-dependent, meaning they cannot survive without attachment to a culture surface (Aisenbrey et al., 2006; Bertolotti et al., 2014). When examining the ability of RPE cells to adhere to the culture surface, a previous study demonstrates that ARPE-19 synthesise laminin chains α3, α5, β1, β3, and γ2, along with heterotrimeric laminin 5 (Aisenbrey et al., 2006). Laminin is a crucial ECM that facilitates the adhesion of these RPE cells to BrM via the integrin–laminin interaction (Aisenbrey et al., 2006). Therefore, proteomic analysis showing the presence of ITGA6, ITGB4, ITGB1, and ITGA5 would indicate cellular adhesion. Additionally, immunofluorescence staining for laminin and collagen IV serves as a useful marker for the ECM, while ZO-1 represents a tight junction marker for RPE cells, indicating maturation. TEER measurements, which assess membrane integrity, also serve as a test for RPE cell maturation.

4.1.2 Bruch's membrane

BrM is a unique ECM that acts as a barrier between the retina and the choroid. The composition of BrM, allows it to be rich in ECM giving it its semi-permeability structure. The composition of BrM based on the different BrM layers is summarised in **Table 4- 1**.

Layers	Thickness (μm)	Composition
RPE basement layer	0.15	• Chondroitin sulphate • Collagen IV α1–5 • Collagen V • Heparan sulphate • Laminins 1, 5, 10, and 11 • Nidogen-1
Inner collagenous layer	1.4	• Apolipoprotein E • Chondroitin sulphate • Clusterin • Collagen I, III, and V • Dermatan sulphate • Fibronectin • Haem • Lipoproteins • Vitronectin
Central elastic layer	0.8	• Elastin

Outer collagenous layer	1 to 5	• Apolipoprotein E • Chondroitin sulphate • Clusterin • Collagen I, III, and V • Dermatan sulphate • Fibronectin • Fibulin-5 • Lipoproteins
Choroidal EC basement layer	0.07	• Chondroitin sulphate • Collagen IV, α1, α2 • Collagen V • Collagen VI • Endostatin • Heparan sulphate • Laminin

Table 4- 1. The layers, thickness and composition of human BrM.

One aspect to consider when modelling the outer retina is the diffusion properties. BrM has unique transmission properties which play a central role in the pathogenesis of AMD particularly with respect to complement proteins which are key contributors to disease initiation and progression. Understanding the diffusion properties of complement proteins across a representative BrM in any model would be important in validating its representativeness. Studies have shown that FHL-1, FD, and C5a can diffuse across dBrM (RPE and choroid physically scraped off) (10). These previous studies have demonstrated the diffusion of complement proteins using Western blotting; however, these results are semi-quantitative, and Western blotting lacks sensitivity. Using an alternative approach, such as MSD, would provide more accurate and quantitative results.

4.1.3 Choroidal endothelial cells

The model fully incorporating the three-layer RPE, BrM-like mimic, and EC by song *et al* (Song et al., 2023) cultured fibroblasts and pericytes alongside the iPSC-EC to create the suitable microenvironment. The iPSC-RPE was on the apical side as they secrete VEGF, which would contribute to the EC proliferation and migration to the ghost vessels.

In addition, Chiro K *et al* (Chirco et al., 2017) demonstrated success in monkey CEC and primary human renal glomerular EC migration towards dBrM separately. The dBrM was placed in the centre of a culture dish, with the ECs added around it. After 10 days in culture, the monkey CEC and primary human renal glomerular EC were found to be viable in co-culture with the dBrM, indicating no observable effects from the decellularisation treatments. The cells

were present within the dbrM, residing in ghost vessels. These two studies demonstrate the importance of EC concerning their ability to migrate towards the ghost vessel for potential vascularisation functions. Both studies also detect ECs through immunofluorescence staining of CD31, which highlights the cell adhesion molecule that is highly expressed on the surface of ECs.

In this chapter, we aim to bridge the gap in the three-component system to enable modeling of the outer retina by culturing iPSC-RPE cells apically on dBrM and EC or iPSC-EC basally. In particular, we investigate the ability of ECFCs and iPSC-EC to proliferate and migrate toward ghost vessels in dBrM. Additionally, we examine the diffusion of truncated sCR1 through dBrM, which is especially relevant for **Chapter 5**, where we explore the delivery of gene therapy carrying this soluble complement protein. Understanding its diffusion properties will help determine the optimal direction (apical or basal) for administering the therapy.

4.2 Aims

This chapter focused on the creation and validation of an outer retina model using dBrM via CP, with recellularisation incorporating iPSC-RPE cells and ECFCs or iPSC-EC. The key objectives include:

1. Assessing the diffusion properties of with CFI, FHL-1, C5a, FD,C3a, truncated sCR1, IgG, and glucose, through dBrM (via SP1 and CP) in an Ussing chamber.
2. Constructing a two-chamber culture system with dBrM as a barrier and evaluating chamber independence based on its known diffusion properties.
3. Culturing iPSC-derived RPE cells on the apical side of dBrM.
4. Culturing ECFCs or iPSC-derived ECs on the basal side.

Imaging, proteomic analysis, and functional analysis are conducted to support the study. Diffusion rate were investigated using MSD analysis and JESS western blotting.

Figure 4- 1 summarises the experimental aims of this chapter.

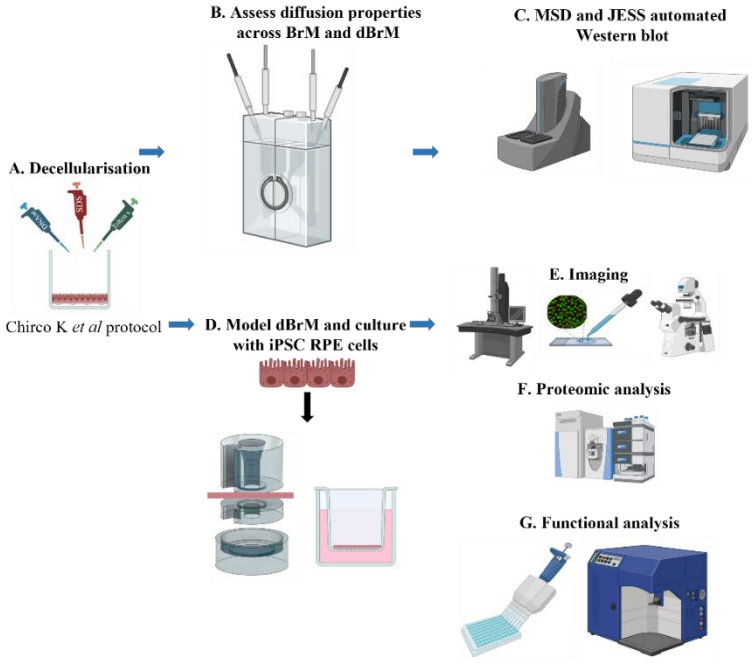

Figure 4- 1. Graphical overview of the chapter. (A) BrM decellularised via CP was tested for **(B)** diffusion and compared to native BrM via **(C)** MSD and JESS automated Western blot analysis. **(D)** Modelling the outer retina with dBrM in a two-chamber system with iPSC-RPE cells cultured on the apical side followed by **(E)** imaging via TEM, immunofluorescence and brightfield. **(F)** Proteomic analysis and **(G)** functional analysis by ELISA and flow cytometry.

4.3 Results

4.3.1 Diffusion across native Bruch's membrane and Bruch's membrane decellularised via shortened protocol 1

This section will discuss the diffusion of complement protein across BrM decellularised via SP1 in Ussing Chamber. These experiments were performed by Scott Sharp from Gyroscope Therapeutics, a Novartis company. These experiments were made to replicate the study by Clark S *et al* (Clark et al., 2017). The sample chamber contained complement proteins at 10 µg/ml was left for 24 hours. Some samples were set aside as the "pre-chamber" group. Protein diffusion was assessed by measuring the amount of protein that passed through to the diffusate chamber. To determine the percentage of proteins captured by dBrM, total recovery was calculated. This was prepared by comparing the protein concentrations in the sample and diffusate chambers against the original protein concentration.

To evaluate the diffusion of complement proteins from the RPE to the choroid across BrM, Scott compared the diffusion of CFI, FHL-1, C5a, FD, and C3a between native BrM and dBrM which was decellularised using SP1 (**Table 4- 2 - Table 4- 5**). As shown in **Table 4- 2**, the diffusion percentages of these proteins were comparable between native and dBrM. Specifically, the diffusion percentages were as follows: CFI (native: 0.54%, dBrM: 0.91%), FHL-1 (native: 0.12%, dBrM: 0.07%), C5a (native: 2.70%, dBrM: 2.60%), FD (native: 1.67%, dBrM: 2.21%), and C3a (native: 2.47%, dBrM: 0.96%). The percentage of total recovery was calculated to confirm that the proteins were accounted for in the sample, diffusate, or retained on BrM. This value was determined using the pre-chamber content as a reference. The formula was as follows:

$$\frac{(\text{Concentration of proteins in sample chamber} + \text{in diffusate chamber})}{\text{Concentration of proteins in pre-chamber}} \text{ X } 100$$

Values close to 100% indicate full recovery of the proteins. Recoveries greater than 100% occurred due to the combined amounts measured in the sample and diffusate chambers were slightly higher than the initial amount in the pre-chamber, likely due to minor experimental

variability. Values below 100% indicate protein loss during the experiment, which could be attached to dBrM. The percentage of total protein recovery for CFI (native: 74.4%, dBrM: 65.6%), FHL-1 (native: 69.1%, dBrM: 30%), C5a (native: 92.5%, dBrM: 92.4%), FD (native: 29.6%, dBrM: 27.6%), and C3a (native: 72.8%, dBrM: 52.1%) (**Table 4- 3**).

Next, Scott evaluated whether the direction of complement protein diffusion - from the RPE to the choroid or vice versa - affected diffusion percentages. **Table 4- 4** show that the diffusion direction did not markedly affect the results for AMD-dBrM or non-AMD dBrM tissues. In AMD-dBrM (**Table 4- 4**), the diffusion percentages were as follows: CFI (RPE to choroid: 1.1%, choroid to RPE: 0.8%), FHL-1 (RPE to choroid: 0.4%, choroid to RPE: 0.5%), C5a (RPE to choroid: 6.0%, choroid to RPE: 7.1%), FD (RPE to choroid: 4.1%, choroid to RPE: 4.5%), and C3a (RPE to choroid: 5.0%, choroid to RPE: 5.8%). The percentage of protein recovery were as follows: CFI (RPE to choroid: 154%, choroid to RPE: 132%), FHL-1 (RPE to choroid: 131%, choroid to RPE: 117%), C5a (RPE to choroid: 141%, choroid to RPE: 118%), FD (RPE to choroid: 136%, choroid to RPE: 123%), and C3a (RPE to choroid: 101%, choroid to RPE: 63%) (**Table 4- 5**).

A similar trend was observed in non-AMD dBrM tissues (**Table 4- 4**). Diffusion percentages for non-AMD dBrM were as follows: CFI (RPE to choroid: 3.6%, choroid to RPE: 4.6%), FHL-1 (RPE to choroid: 1.9%, choroid to RPE: 3.5%), C5a (RPE to choroid: 9.4%, choroid to RPE: 8.5%), FD (RPE to choroid: 6.3%, choroid to RPE: 6.4%), and C3a (RPE to choroid: 9.2%, choroid to RPE: 7.9%) (n = 1). The percentage of protein recovery were as follows: CFI (RPE to choroid: 68.9%, choroid to RPE: 64.6%), FHL-1 (RPE to choroid: 62.9%, choroid to RPE: 61.4%), C5a (RPE to choroid: 123.9%, choroid to RPE: 105.4%), FD (RPE to choroid: 61.5%, choroid to RPE: 78.9%), and C3a (RPE to choroid: 125%, choroid to RPE: 132.7%) (**Table 4- 5**).

It is important to note, the donor tissues used across the experiments differed in pathology and age. As Scott utilised tissues from an 85-year-old AMD donor, a 64-year-old AMD donor and a 47-year-old non-AMD donor. This further highlights differences in donor characteristics across experiments. These experiments were also performed once due to the limited availability of complement proteins.

These results show that the diffusion of complement proteins across BrM was generally comparable between native and dBrM with only minor variations observed. This suggests that the presence of remaining cellular components in native BrM has little impact on protein permeability. Similarly, diffusion rates remained consistent regardless of the diffusion direction, indicating no differences in protein movement. Additionally, total protein recovery varied among proteins, with some losses potentially due to retention on BrM or dBrM.

	Percentage of diffusion (%)	
	85 years old, AMD	
	Native	**dBrM**
CFI	0.54	0.91
FHL-1	0.12	0.07
C5a	2.7	2.6
FD	1.67	2.21
C3a	2.47	0.96

Table 4- 2. Complement protein diffusion experiment. The diffusion of CFI, FHL-1, C5a, FD and C3a between native and dBrM. n=1.

	Percentage of total protein recovery (%)	
	85 years old, AMD	
	Native	**dBrM**
CFI	74.4	65.6
FHL-1	69.1	30
C5a	92.5	92.4
FD	29.6	27.6
C3a	72.8	52.1

Table 4- 3. Total protein recovery. The total protein recovery of CFI, FHL-1, C5a, FD and C3a between native and dBrM. n=1.

	Percentage of diffusion (%)			
	64 years old, AMD		47 years old, non-AMD	
	RPE-Choroid	**Choroid-RPE**	**RPE-Choroid**	**Choroid-RPE**
CFI	1.1	0.8	3.6	4.6
FHL-1	0.4	0.5	1.9	3.5
C5a	6	7.1	9.4	8.5
FD	4.1	4.5	6.3	6.4
C3a	5	5.8	9.2	7.9

Table 4- 4. Complement protein diffusion experiment. The diffusion of CFI, FHL-1, C5a, FD and C3a from RPE to choroid or choroid to RPE in AMD and non-AMD dBrM. n=1.

	Percentage of total protein recovery (%)			
	64 years old, AMD		47 years old, non-AMD	
	RPE-Choroid	**Choroid-RPE**	**RPE-Choroid**	**Choroid-RPE**
CFI	154	132	68.9	64.6
FHL-1	131	117	62.9	61.4
C5a	141	118	123.9	105.5
FD	136	123	61.5	78.9
C3a	101	63	125	132.7

Table 4- 5. Total protein recovery. The total protein recovery of CFI, FHL-1, C5a, FD and C3a from RPE to choroid or choroid to RPE in AMD and non-AMD dBrM. n=1.

4.3.2 Diffusion across Bruch's membrane decellularised via Chirco K *et al* protocol

Scott's previous diffusion experiments (**Section 4.3.1**), did not include truncated sCR1. This complement protein is particularly relevant as it will be explored as a potential gene therapy delivery mechanism in **Chapter 5** and hence was included for these experiments. The rate of its diffusion of CFI, C5a, FD, C3a, truncated sCR1, FITC IgG and glucose after 24 hours was examined in the RPE- to choroid direction on dBrM via CP in an Ussing chamber. The sample chamber contained the molecules at 10 µg/ml, except for FH at 5 µg/ml and was left for 24 hours. Diffusion rates for CFI, C5a, FD, C3a, and truncated sCR1 were 5.3%, 13.2%, 9.9%, 9.7%, and 0.30%, respectively. For the negative control, IgG was used, demonstrating a diffusion rate of 2%, whereas glucose, acting as a positive control, diffused at 44% (n=1)

(**Figure 4- 2**). The percentage of total recovery for CFI were 100%, 96% for C5a, 100% for FD, 6.2% for C3a, 100% for sCR1 CCP1-11 Flag His tag, 100% for FITC IgG and 88% for glucose (**Figure 4- 2**). These results show that truncated sCR1 diffuses through dBrM at the lowest rate, while C3a has a low percentage of total recovery, indicating it could be trapped on the dBrM. Compared to Scott's experiment, the percentage of diffusion overall appear slightly higher. The total recovery of C3a appears the lowest, which was not previously seen in Scott's experiments.

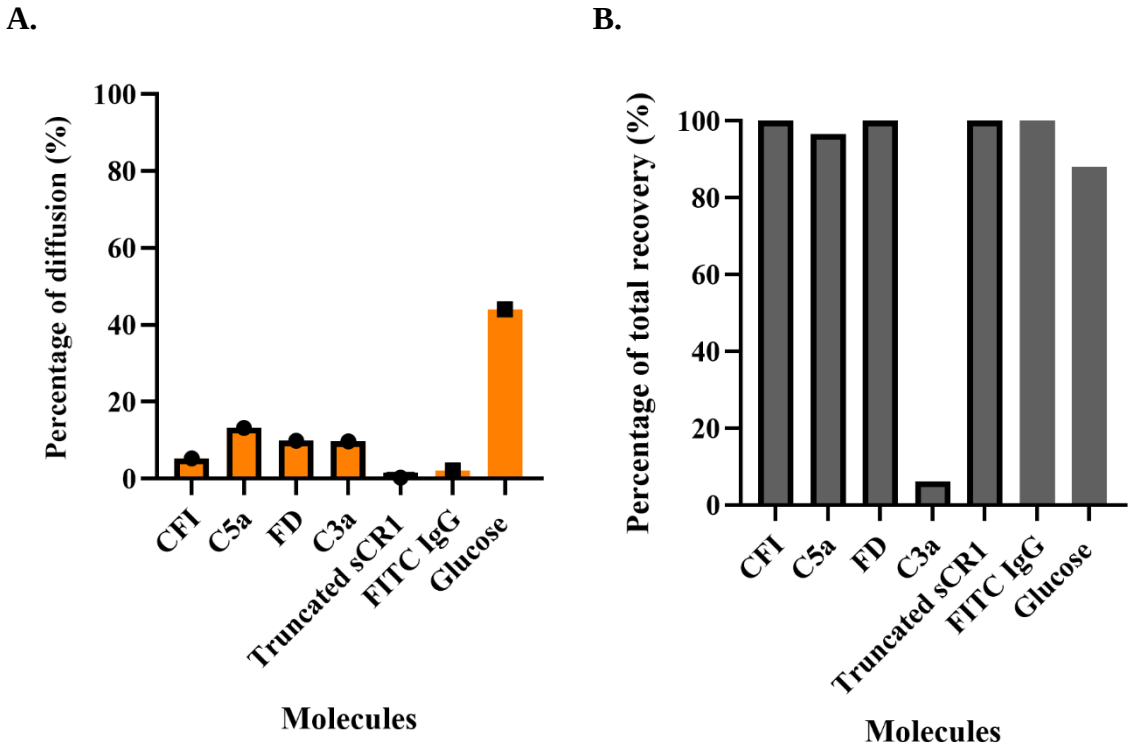

Figure 4- 2. Percentage of diffusion. The bar chart shows the **(A)** percentage of diffusion of CFI, C5a, FD, C3a, and truncated sCR1, IgG and glucose and their **(B)** percentage of total recovery. BrM was from a donor with no AMD and 54 years old.

4.3.3 Design and testing of two chamber systems

Initially, cell crowns were tested for their ability to hold dBrM in a two-chamber system. However, the 24, 48 and 96 well cell crowns were unable to hold dBrM as it caused dBrM to tear (**Figure 4- 3 A-C**).

A. **B.** **C.**

Figure 4- 3. Images of dBrM attached in cell crowm. **(A)** the 24 **(B)** 48 and **(C)** 96 wel cell crowns with dBrM attached showing a tear at the red arrow.

Based on the lack of availability of a two-chamber culture system that met our absolute requirement to separate the two chambers other than by diffusion through the dBrM, we explored various options and proceeded to design several potential solutions. They were assessed based on comparative diffusion with IgG (which does not diffuse through dBrM) and glucose (with free diffusion expected). We set a target of less than 0.5% IgG diffusion and above 50% glucose (assuming equilibrium is reached) over 24 hours. They are described sequentially based on the experimental progression. The results are shown as mean ± SEM.

Model 1

Model 1 incorporated a 12-well transwell with a nitrile rubber O-ring placed ontop of dBrM to secure it and minimise edge leakage with basal volume of 2 ml and apical volume 0.5ml. (**Figure 4- 4 A**). Over 24 hours, 56.3% ± 2.42% glucose and 9.8% ± 0.47% IgG diffused (n=3) (**Figure 4- 4 A**).

Model 2

Model 2 addressed sealing issues observed in Model 1 with similar basal and apical volumes, as the O-ring was tighter in the transwell. After 24 hours, the diffusion rates improved slightly, with 57% ± 0.41% of glucose diffused across BrM, while IgG diffusion was limited to 3.9% ± 0.18% (n=3) (**Figure 4- 4 B**).

Model 3

A modified approach was taken in Model 3, which used a Corning 12-well transwell without its membrane, combined with a layered O-ring system with basal volume of 2 ml and apical volume of 0.15 ml. This design placed one O-ring above the BrM and two below. Under these conditions, glucose diffusion reached 91% ± 0.423%, while IgG diffusion was higher at 34% ± 6.42% (n=2) (**Figure 4- 4 C**).

Model 5

Based on the failures of simple transwell and O ring designs we designed a bespoke system with the engineering department to fabricate this. Model 5 was thus custom-machined from clear acrylic by technician, Michael Wilkes at Newcastle University's School of Engineering (**Figure 4- 4 D**). It featured a two-piece membrane holder, secured by an O-ring within a rigid acrylic base with 2.5ml basal and 0.15ml apical volume. Glucose diffusion was measured at 94% ± 0.06% and IgG diffusion at 76% ± 3.38% after 24 hours (n=2) (**Figure 4- 4 D**).

Model 6

A 3D-printed version, Model 6, created from clear resin, offered another iteration of the design with reduced basal and apical volume to 0.4 ml and 0.3 ml respectively. It achieved diffusion rates with 86% glucose diffusion and only 20% IgG diffusion. Both model 5 and 6 was hindered by inadequate sealing and low apical and basal chamber volumes, rendering them unsuitable for further experimentation (n=1). (**Figure 4- 4 E**).

Model 7

Model 7, a refined version of Model 5, was also machined from clear acrylic with the basal volume of 1 ml and an apical of 0.25 ml. This design achieved the best results, with glucose diffusion at 73% ± 1.49% and IgG diffusion reduced to just 0.3% ± 0.17% after 24 hours (n=2), demonstrating its superior sealing and chamber separation (**Figure 4- 4 F**). This was thus used in subsequent experiments that required the two chambers to be separated other than by dBrM.

A.

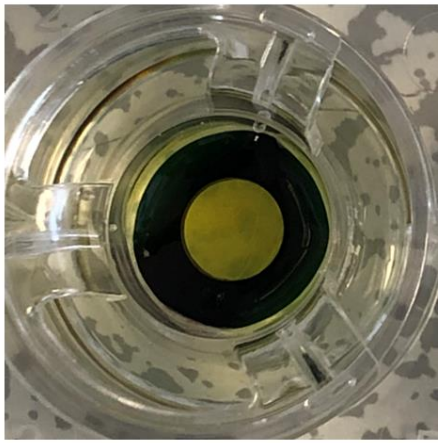

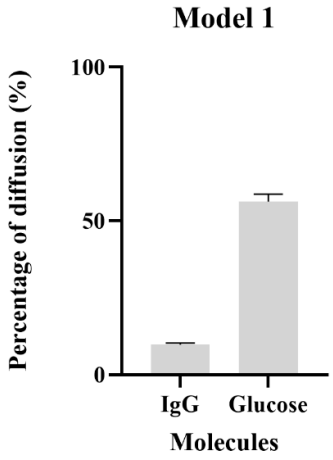
Model 1
Percentage of diffusion (%)
100
50
0
IgG
Glucose
Molecules

B.

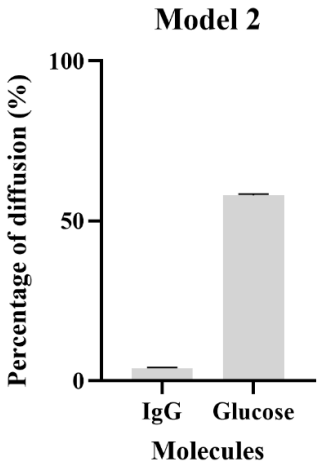
Model 2
Percentage of diffusion (%)
100
50
0
IgG
Glucose
Molecules

C.

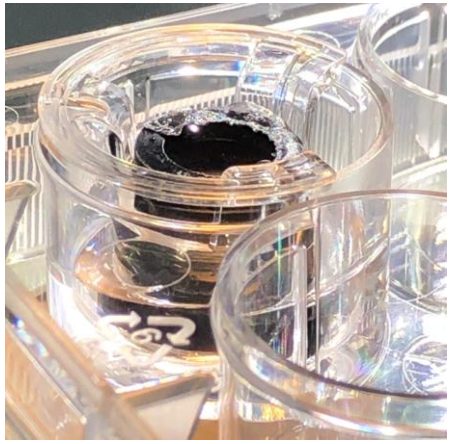

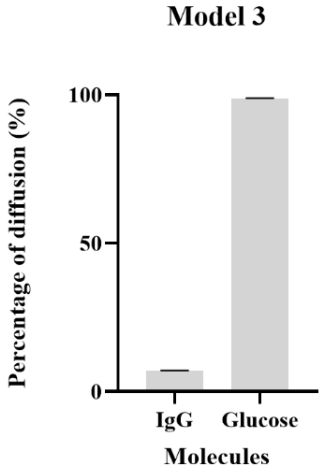
Model 3
Percentage of diffusion (%)
100
50
0
IgG
Glucose
Molecules

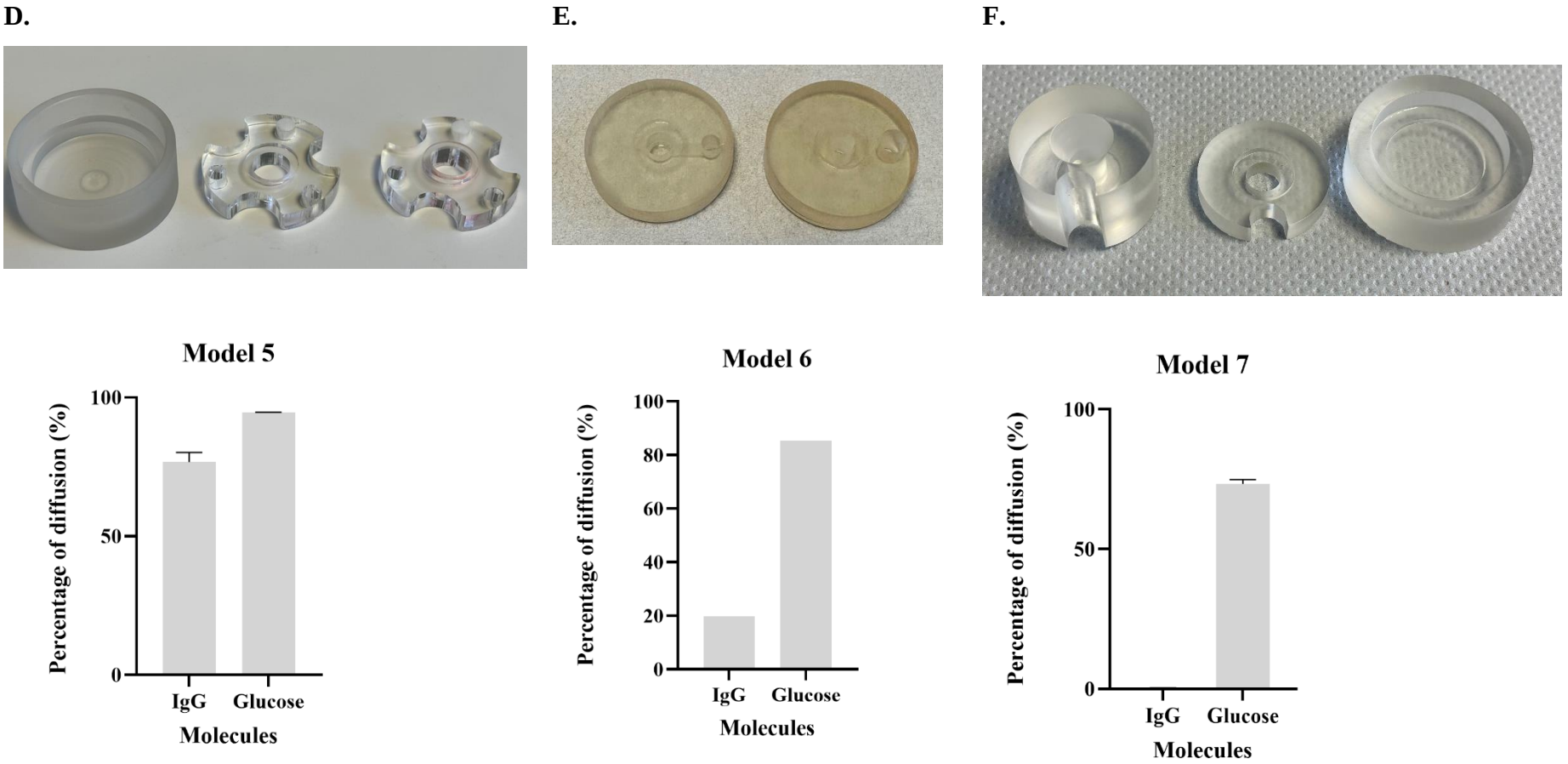

Figure 4- 4. Diffusion of IgG and glucose across the models. The diffusion of IgG and glucose measured after 24 hours, from the RPE to choroid direction through dBrM in **(A)** model 1, **(B)** model 2, **(C)** model 3, **(D)** model 5, **(E)** model 6, and **(F)** model 7.

4.3.4 iPSC-RPE cells cultured on Matrigel mature by day 21

The time required for the iPSC-RPE cells obtained commercially to mature was assessed when cultured on Matrigel in transwells with TEER measurements obtained at day 7, 14, 21 and 28. Besides that, immunofluorescence staining against ZO1 were performed at day 23. The iPSC-RPE were seeded at 154, 867 cells/ cm^2. The TEER, which provides information about the integrity and permeability of cells, was measured as mean ± SEM (n = 4). The measurements revealed significantly different values: 21 ± 0.5 Ωcm² on day 7, 62 ± 1.3 Ωcm² on day 14, 308 ± 11.4 Ωcm² on day 21, and 520 ± 13.9 Ωcm² on day 28 (**Figure 4- 5 A**). These data show significant increase in TEER values over time (**Figure 4- 5 A**). At day 23, iPSC-RPE cells were positive for ZO1 (tight junction marker) (**Figure 4- 5 B)**. These results indicate that the iPSC-RPE cells reach maturity by day 21.

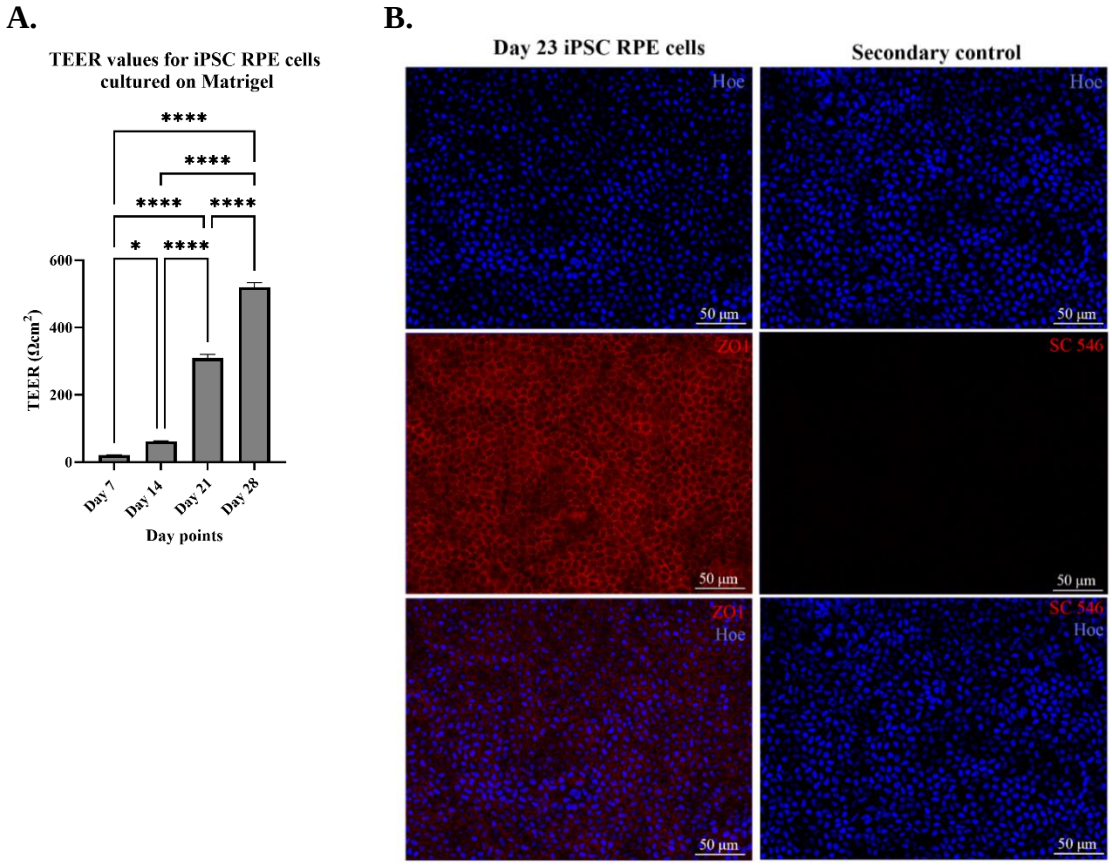

Figure 4- 5. Culture of iPSC-RPE cells. (A) The TEER measurement (Ωcm²) at day 7, 14, 21 and 28. Data shows mean ± SEM (n = 4). **(B)** Immunohistochemistry staining showing ZO1 (red) in tight junction alongside nuclear stain, Hoechst (Hoe) (blue) for day 23 iPSC-RPE and the secondary control (no primary antibody One-way ANOVA with Tukey's multiple comparisons test was conducted to determine significance. Values with $p \leq 0.05$ were considered statistically significant (*p = 0.03 and ****$p \leq 0.01$).

4.3.5 The co-culture model exhibits characteristic cell morphology and expression of key markers for iPSC-RPE

To assess whether iPSC-RPE cells could adhere and grow on the dBrM, bright-field images were captured. Bright-field imaging was feasible only in model 2, as the design of model 7 did not permit this type of imaging. On days 12, 16, and 21, tight clusters of cells were observed on dBrM (**Figure 4- 6**). These clusters were more distinctly visible in specific areas of the dBrM (for example within the red box regions of the images in **figure 4-6**), as the uneven surface of dBrM made it challenging to focus sharply on the cell clusters. When comparing iPSC-RPE cells on dBrM to those on Matrigel, the cells similarly appeared tightly packed with a hexagonal shape; however, it was challenging to assess their pigmentation because of the pigmented background in the dBrM (melanosomes from previous cells) (**Supplementary figure- 1**).

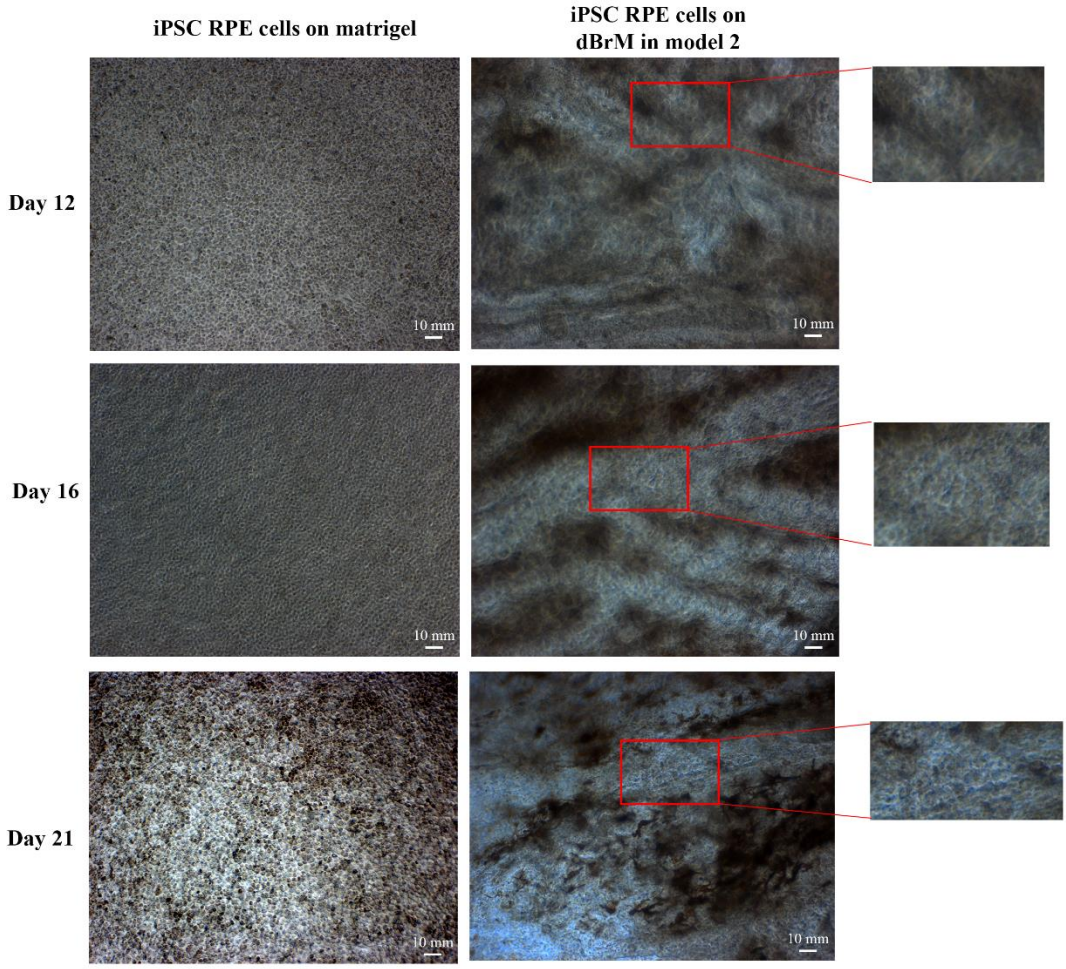

Figure 4- 6. Bright field imaging of iPSC-RPE cells. Day 12, 16 and 21 of iPSC-RPE cells cultured on Matrigel and on dBrM in model 2. The red boxes highlight areas of maximum visibility.

Next, we compared the cellular morphology at day 28 of iPSC-RPE cells cultured on Matrigel-coated dBrM versus uncoated dBrM to determine whether Matrigel coating allows cell growth. TEM images provided insights into the cells' culture orientation and intracellular structural details. Cells demonstrated organised structures on the apical side (Ap), while the basal side (Ba) showed no significant cell attachment (**Figure 4- 7 A I-III**). Image artefacts caused by sectioning were marked with black arrow (**Figure 4- 7 A I**).

Specific structures were highlighted in the magnified regions. The basal section, represented in the purple box, contained a ghost vessel (indicated by a white asterisk) (**Figure 4- 7 A I-III**). **Figure 4- 7 A IV-VI** focused on the apical region (blue box), which showed intracellular details. Key features included microvilli (blue arrow), the nucleus (black asterisk) surrounded by mitochondria (purple arrow), melanin (green arrow), and basal infoldings (red arrow) (**Figure 4- 7 A IV-VI**).

The TEM images for iPSC-RPE cells cultured on Matrigel-coated dBrM, and analysis of the basal side (Ba) in **Figure 4- 7 B I** revealed ghost vessels (white asterisk). On the apical side (Ap), the blue box displayed structures including microvilli (blue arrow), the nucleus (black asterisk), mitochondria (purple arrow), melanin (green arrow), and basal infoldings (red arrow) (**Figure 4- 7 B I-IV**).

These findings were compared to iPSC-RPE cells cultured on Matrigel which displayed clear intracellular features, such as microvilli (blue arrow), nucleus (black asterisk), mitochondria (purple arrow), melanin (green arrow), and basal infoldings (red arrow) (**Figure 4- 7 C I-III**). The ghost vessels were consistent with the ones in dBrM alone (as a control) with no visible cells (**Figure 4- 7 D**). These results show the cellular morphology of iPSC-RPE cells remained consistent whether cultured on uncoated dBrM or Matrigel-coated dBrM when compared to iPSC-RPE cells on Matrigel. These results show the ability of iPSC-RPE cells on dBrM to grow and exhibit the expected intracellular morphology without the need for Matrigel layer.

A.

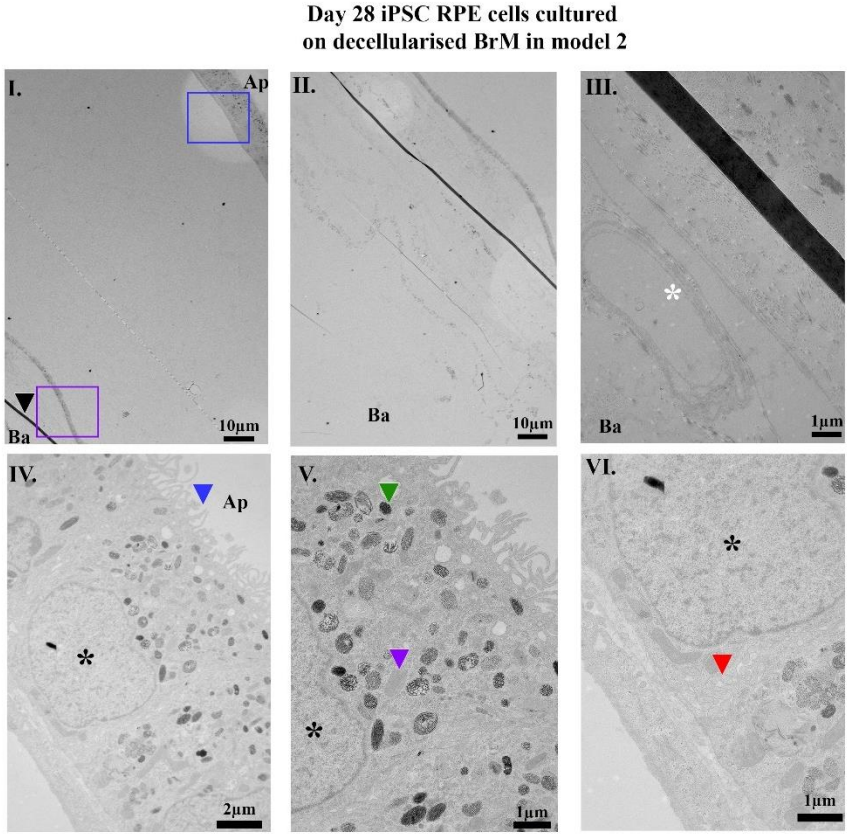

B.

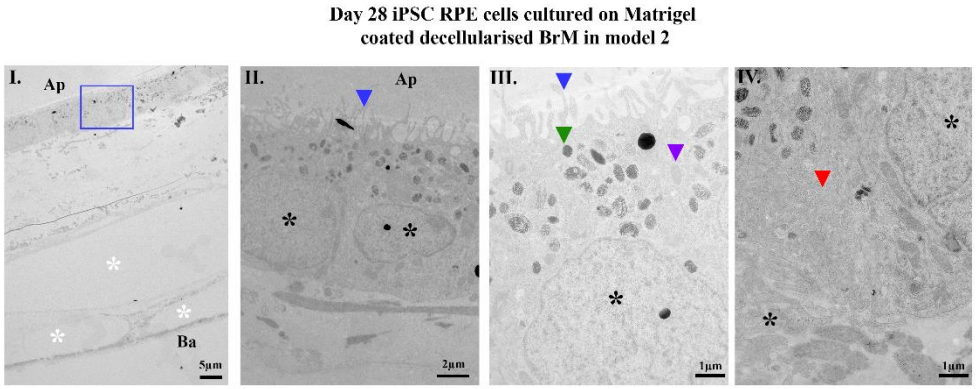

C.

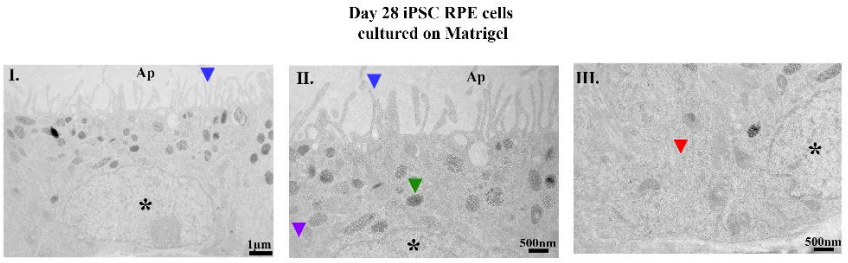

D.

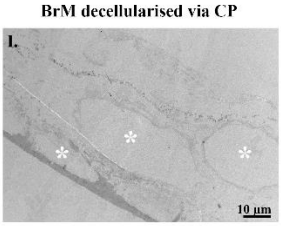

Figure 4- 7. TEM images. Day 28 iPSC-RPE cells on **(A)** dBrM, **(B)** Matrigel coated dBrM, **(C)** Matrigel, **(D)** dBrM. Features include, microvilli (blue arrow), the nucleus (black asterisk) surrounded by mitochondria (purple arrow), melanin (green arrow), basal infoldings (red arrow) and ghost vessel (white asterisk). Ap: apical; Ba: basal.

Immunofluorescence images were analysed at day 28 of culture to examine pan-laminin (hereafter referred to as laminin) as an ECM marker and ZO1 as an iPSC-RPE tight junction marker. These analyses were conducted on iPS- RPE cells cultured on Matrigel-coated dBrM, as well as on dBrM in model 2 and model 7 to ensure that the culture set up did not effect RPE maturation. As controls, dBrM was used as a negative control, while Native BrM and side section of iPSC-RPE cell cultured on Matrigel in transwells served as positive controls (**Figure 4- 8 A-F**). The secondary controls are in **Figure 4- 9**.

Laminin staining (green), visible beneath iPSC-RPE cells was positive in iPSC-RPE cells cultured on Matrigel-coated dBrM, as well as on dBrM in model 2 and model 7, consistent with observations in the dBrM control, Native BrM, and iPSC-RPE cell sections (**Figure 4- 8 A-F**). The ZO1 expression (Red) was also detected on iPSC-RPE cells alongside Hoechst (Hoe) (blue) nuclear stain, confirming that iPSC-RPE cells successfully formed tight junctions and grew on both Matrigel-coated and uncoated dBrM, regardless of the model (model 2 or 7) (**Figure 4- 8**).

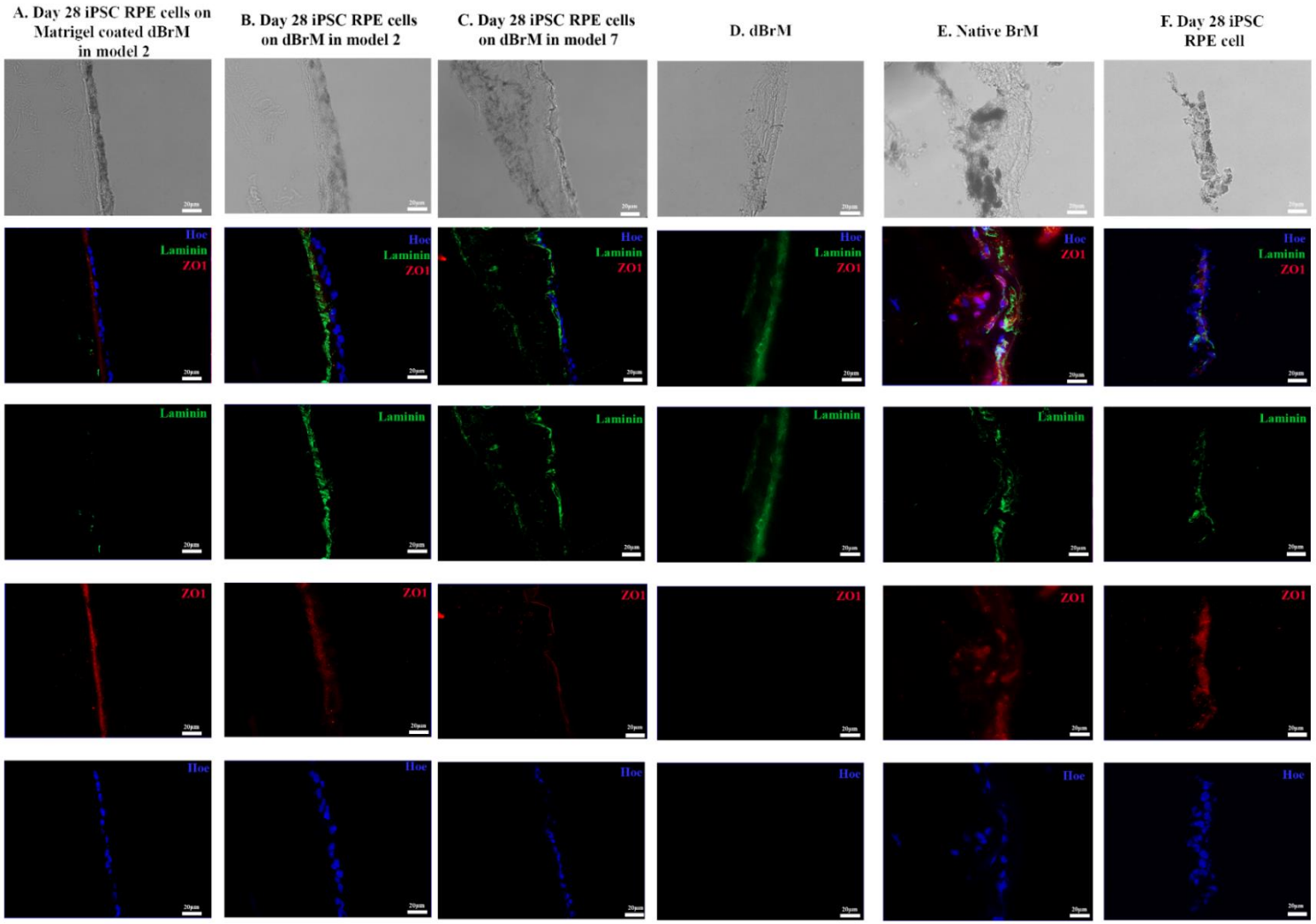

Figure 4- 8. Immunofluorescence images of iPSC-RPE cells culture. The brightfield images, laminin (green), ZO1 (red) and Hoechst (Hoe) (blue) immunofluorescence of day 28 iPSC-RPE cells cultured on **(A)** Matrigel coated dBrM in model 2, **(B)** dBrM in model 2, **(C)** dBrM in model 7, **(D)** dBrM alone, **(E)** native BrM and **(F)** side sectioned iPSC-RPE cells cultured on Matrigel in transwell.

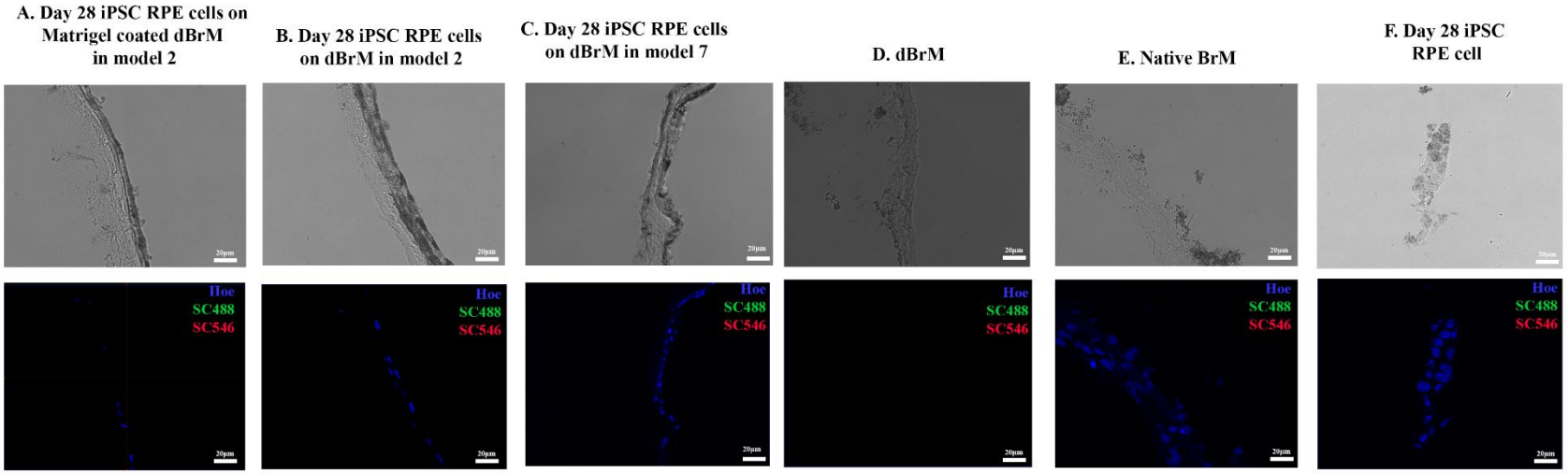

Figure 4- 9. Secondary control immunofluorescence images of iPSC-RPE cells culture. The brightfield images, secondary control (No primary antibody added) and Hoechst (Hoe) (blue) immunofluorescence of day 28 iPSC-RPE cells cultured on **(A)** Matrigel coated dBrM in model 2, **(B)** dBrM in model 2, **(C)** dBrM in model 7, **(D)** dBrM alone, **(E)** native BrM and **(F)** side sectioned iPSC-RPE cells cultured on Matrigel in transwell.

4.3.6 Proteomic analysis of co-culture model reveals key RPE markers

The proteomic analysis was performed to assess the RPE PG genes in the co-culture models (iPSC-RPE cells on Matrigel coated dBrM and iPSC-RPE cells on dBrM) in model 2 compared to native BrM and dBrM alone. We focused on proteins associated with key biological processes, including the visual cycle (RBP1, DCT), lipid biosynthesis (PTGDS), melanin biosynthesis (ENPP2, PMEL, TTR, TYRP1), phagocytosis (GULP1), secretion (SERPINF1), and adhesion (ITGA6, ITGB4, ITGB1, ITGA5), due to their critical roles in maintaining cellular function and homeostasis (**Figure 4- 10 A-D) (Supplementary table- 1).** The volcano plot analysis was performed to visualise the RPE proteins that were differentially expressed in the co-culture models compared to Native BrM or dBrM alone (n=3). In this analysis, native BrM serves as the positive control, while dBrM acts as the negative control. Since Native BrM retains attached RPE cells, the presence of RPE protein markers is expected. In contrast, dBrM, having undergone decellularisation, should show no RPE markers. Given this, the co-culture model is expected to exhibit higher RPE marker expression compared to dBrM alone, as the reintroduction of RPE cells restores marker expression. This suggests that the co-culture system more closely mimics physiological conditions than dBrM. **Supplementary table- 2 - Supplementary table- 9** shows the top 50 most differentially expressed proteins that are significantly higher or lower in the co-culture models compared to native BrM or dBrM.

The volcano plot visualised -Log10 P (y-axis) against Z score (Fold change co-culture/Native BrM) (x-axis) (**Figure 4- 10 A and C**) and -Log10 P (y-axis) against Z score (Fold change co-culture/dBrM) (x-axis) (**Figure 4- 10 B and D**) revealing significance based on a p-value of -Log10 P greater than 1.3, with Z score values less than -2 or greater than 2 considered significant (red plots) (**Figure 4- 10 A-D**). Values that fall within the Z score range are represented as green plots, p-value ranges as blue dots, and non-significant values as grey dots (**Figure 4- 10 A-D).** The z-scores represent effect sizes, with higher values (farther from zero) indicating stronger deviations from the reference. A Z-score above 2 suggests higher protein detected in the culture model than native BrM or dBrM, while a Z-score below -2 indicates lower protein detection. The direction (positive or negative) reflects whether the change is an increase or a decrease relative to the baseline.

A total of 7700 PG genes were detected in the analysis. Comparing iPSC-RPE cells cultured on Matrigel-coated dBrM to native BrM, no significant differences were observed for RBP1, PTGDS, GULP1, SERPINF1, ITGA6, ITGB4, ITGB1, ENPP2 and ITGA5 (grey plots). However, DCT, TYRP1, and PMEL were expressed at higher levels in the co-culture model (green plots on the right), with TTR showing a significant lower (red plots on the left). SOD1 was within the p-value significance range but did not meet the Z-score significance threshold (blue plots (**Figure 4- 10 A**). To further demonstrate protein levels in the Matrigel co-culture model compared to dBrM alone, we identified that ITGB1, ITGB4, and ENPP2 were significantly expressed at higher levels in Matrigel-coculture (red plots on the right). RBP1, SERPINF1, PMEL, GULP1, and ITGA6 were within the Z-score significance range, but not the p-value range (green plots on the right) (**Figure 4- 10 B**). No significant differences were observed for TTR, TYRP1, PTGDS, ITGA5, or DCT (**Figure 4- 10 B**).

When comparing iPSC-RPE cells cultured on dBrM to native BrM, no significant differences were found for CRYAB, SERPINF1, ITGB1, ITGA6, ITGA5, ITGB4, ENPP2, TYRP1, SOD1, PTGDS, RBP1, and GULP1 (grey plots) (**Figure 4- 10 C**). PMEL showed significantly higher expression in the co-culture model (red plots on the right), while TTR was significantly lower (green plots on the left) (**Figure 4- 10 C**). To assess protein levels in the non-Matrigel co-culture model compared to dBrM, significantly higher expression was observed for ITGB1, ITGB4, SERPINF1, and GULP1 (red plots on the right) (**Figure 4- 10 D**). RBP1, SERPINF1, ENPP2, ITGA5, and ITGA6 were within the Z-score significance range but not the p-value range (green plots on the right) (**Figure 4- 10 D**). No significant differences were found for TTR, TYRP1, PTGDS, or DCT (grey plots). PMEL fell within the p-value significance range, but not the Z-score significance range (blue plots) (**Figure 4- 10 D**). Overall, these results show that in both co-culture models (iPSC-RPE on dBrM or on Matrigel coated dBrM) contain the RPE markers similarly seen to native BrM.

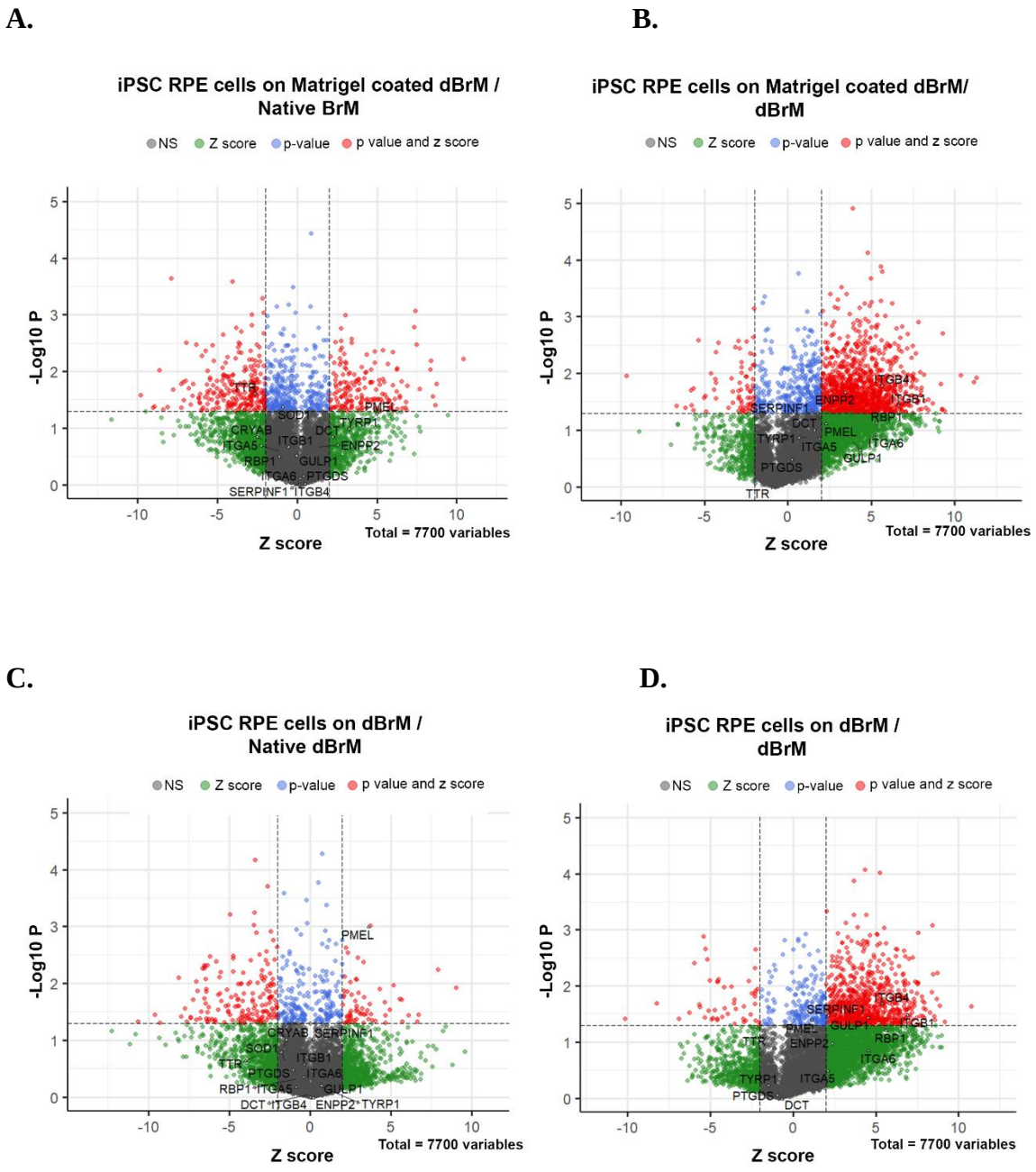

Figure 4- 10. Proteomic analysis of RPE cell markers. The volcano plots of **(A)** iPSC-RPE cells on Matrigel coated dBrM/Native BrM, **(B)** iPSC-RPE cells on Matrigel coated dBrM/dBrM, **(C)** iPSC-RPE cells on dBrM/Native BrM and **(D)** iPSC-RPE cells on dBrM/dBrM. n=3.

4.3.7 Proteomic analysis of the two co-culture models reveals similar RPE and laminin retention

The levels of RPE PG genes and laminin PG genes in the co-culture models (iPSC-RPE cells on Matrigel coated dBrM and iPSC-RPE cells on dBrM) in model 2 compared to each other were performed (**Supplementary table- 10**) (**Figure 4- 11 A-B**). This was to observe the differences in the level of these protein-coding genes, to understand if the addition of Matrigel enhances the model. Similar analysis as **Section 4.3.6** was performed, with similar thresholds. **Supplementary table- 11** and **Supplementary table- 12** shows the top 50 most differentially expressed proteins that are significantly higher or lower in two co-culture models respectively.

The RPE markers as in **section 4.3.6** were compared between iPSC-RPE cells on Matrigel coated dBrM and iPSC-RPE cells on dBrM. There was no significant difference in ITGB1, ITGB4, ITGA5, ITGA6, RBP1, PMEL, SERPINF1, GULP1, TTR, PTGDS and ENPP2 (grey plots) (**Figure 4- 11 A**). The RPE markers that were higher in iPSC-RPE cells on Matrigel compared to iPSC-RPE cells on dBrM, within the Z score threshold, was TYRP1 and DCT (green plots on the right) (**Figure 4- 11 A**).

When comparing laminin, the markers labelled in the volcano plot were LAMA1, LAMA2, LAMA3, LAMA4, LAMA5 LAMB1, LAMB2, LAMB3, LAMC1 and LAMC2 and LAMC3 (**Figure 4- 11 B**). These proteins were not significantly differentially expressed in iPSC-RPE cells on Matrigel coated dBrM compared to iPSC-RPE on dbrM (**Figure 4- 11 B**). There is no significant difference in the LAMA2, LAMA3, LAMA4, LAMB1, LAMB2, LAMC1 and LAMC3 between Matrigel coated dBrM and iPSC-RPE on dBrM (grey plots) (**Figure 4- 11 B)**. Both LAMA1 and LAMA5 were higher in iPSC-RPE cells on Matrigel coated dBrM, although not significant only within the Z score threshold (green plots on the right) (**Figure 4- 11 B**). While LAMB3 and LAMC2 were lower in iPSC-RPE cells on Matrigel coated dBrM compared to iPSC-RPE on dBrM, within Z score threshold (green plots on the left) (**Figure 4- 11 B**). These results show that there are no differences in the RPE and laminin RPE-coding genes between the two different culture methods.

A. **B.**

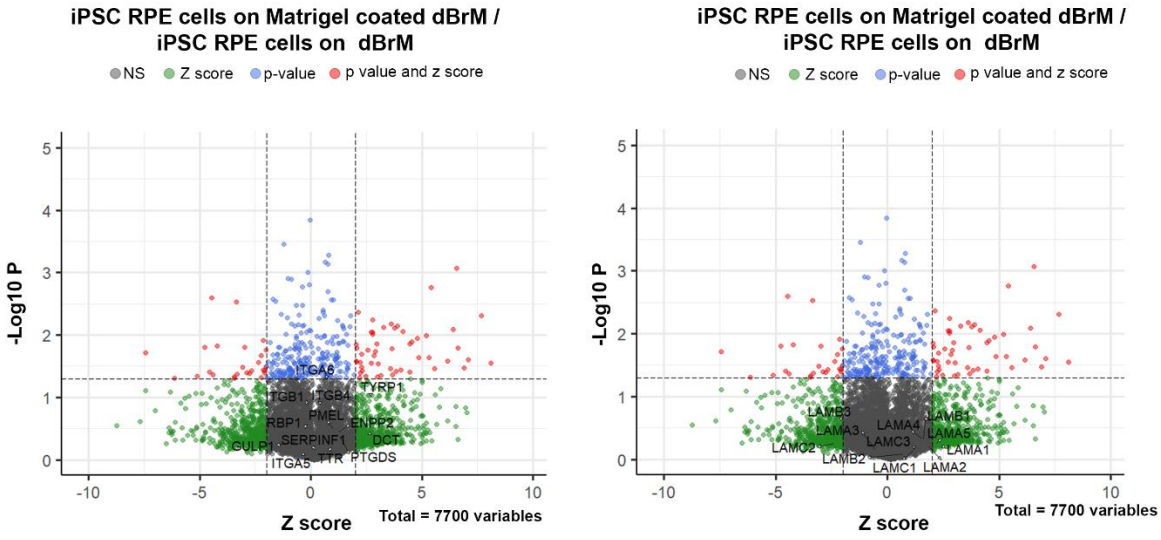

Figure 4- 11. Proteomic analysis of laminin markers. The volcano plot of iPSC-RPE cells on Martigel coated dBrM against iPSC-RPE cells on dBrM analysing **(A)** RPE markers and **(B)** laminin markers. The laminin markers were LAMA1, LAMA2, LAMA3, LAMA4, LAMA5 LAMB1, LAMB2, LAMB3, LAMC1 and LAMC2 and LAMC3. n=3.

4.3.8 Similar intracellular structure and composition observed in iPSC-RPE cells cultured on dBrM in Models 2 and 7

As iPSC-RPE cells successfully grew on dBrM without the need for Matrigel, and were positive for ZO1 in model 2 and model 7, TEM image sections were captured on day 28 of iPSC-RPE cells on dBrM in model 2 and 7 to observe the cellular structure and composition for comparing the growth in both models (**Figure 4- 12**). The overall structure of iPSC-RPE was consistent in both models, with microvilli (blue arrow) appearing as slender projections extending from the apical surface of the cell (**Figure 4- 12**). The nucleus (black asterisk) is located centrally, surrounded by melanin (green arrow) and mitochondria (purple arrow) (**Figure 4- 12**). Towards the basal side, basal infoldings (red arrow) are observed (**Figure 4- 12**). The correct positioning and orientation of the cellular components, as evidenced in the TEM images, highlight the RPE cells' well-maintained polarity. This organisation is crucial for the cells' specialised functions.

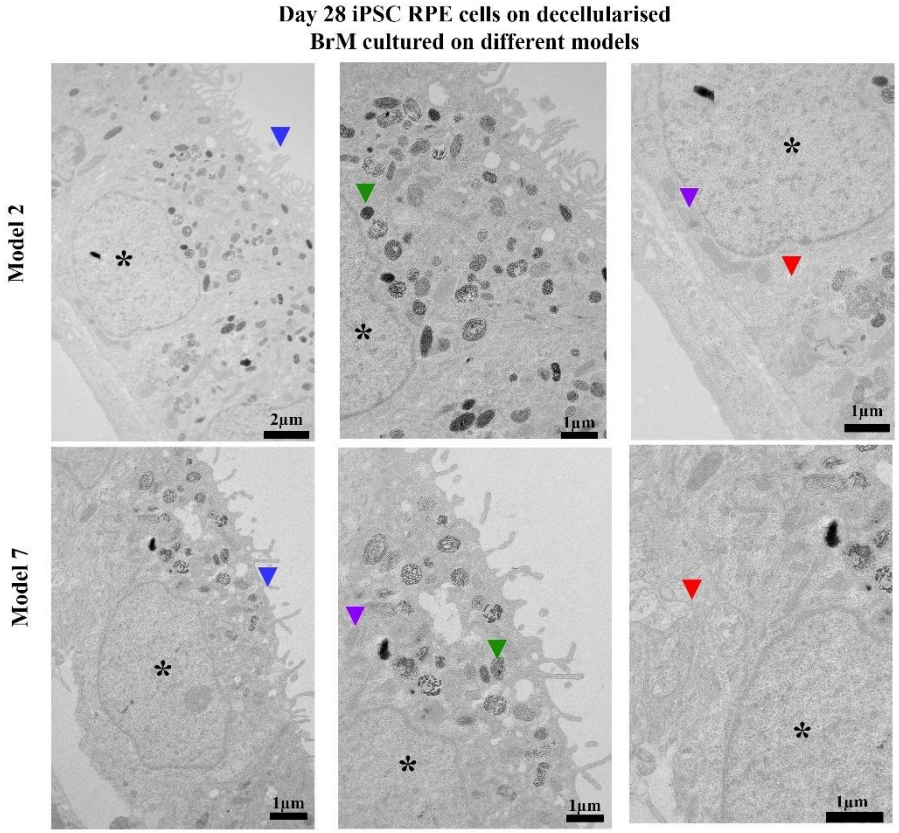

Figure 4- 12. TEM images. Day 28 iPSC-RPE cells on dBrM cultured in model 2 vs model 7. Featured include microvilli (blue arrow), the nucleus (black asterisk) surrounded by mitochondria (purple arrow), melanin (green arrow), basal infoldings (red arrow) and ghost vessel (white asterisk).

4.3.9 Secretion of VEGF and PEDF by iPSC-RPE cells cultured on decellularised Bruch's membrane

Secretion of VEGF and PEDF by RPE cells is essential for their function and serves as a marker for polarisation, with higher VEGF expected basally and higher PEDF apically. The total VEGF (ng) and PEDF (µg) were measured in iPSC-RPE cells cultured on dBrM in Model 2 and Model 7, with iPSC-RPE cells on Matrigel serving as a control reference, presented as mean±SEM percentage with n=3 These were performed to observe the differences in VEGF and PEDF release in the different models.

In Model 2, VEGF secretion was higher apically at day 7 (0.28±0.02 ng) compared to basally (0.14±0.05 ng, p=0.237) (**Figure 4- 13 A**). However, at days 14 and 21, basal VEGF levels became significantly higher than apical levels, reaching 1.01±0.11 ng and 1.47±0.02 ng, respectively, while apical levels were 0.21±0.03 ng and 0.26±0.02 ng ($p<0.0001$ for both time points) (**Figure 4- 13 A**). In Model 7, basal VEGF secretion consistently significantly exceeded apical levels at days 14 and 21 ($p<0.0001$), while day 7 showed no significant difference

(p=0.577) (**Figure 4- 13 B**). Basal VEGF levels were 0.17±0.01 ng, 0.74±0.01 ng, and 1.32±0.01 ng at days 7, 14, and 21, respectively, compared to apical levels of 0.10±0.01 ng, 0.10±0.06 ng, and 0.13±0.07 ng (**Figure 4- 13 B**). Similarly, iPSC-RPE cells on Matrigel exhibited higher basal VEGF secretion at days 7 ,14, and 21 (day 7;$p = 0.406$, day 14 and 21;$p < 0.003$) (**Figure 4- 13 C**). Basal levels were 0.063±0.01 ng, 0.20±0.02 ng, and 0.24±0.02 ng at days 7, 14, and 21, respectively, compared to apical levels of 0.034±0.01 ng, 0.10±0.01 ng, and 0.047±0.01 ng (**Figure 4- 13 C**).

Since prior findings identified day 21 as the time point for iPSC-RPE cell maturation, it was chosen as the key time point despite TEER being higher at day 28 (See **Section 4.3.4**). This selection was based on the earlier maturation of the cells at day 21. VEGF secretion across models was further analysed at this stage. Apical VEGF levels showed no significant differences between Model 2 and Model 7 ($p = 0.554$) or between Model 7 and iPSC-RPE cells on Matrigel ($p = 0.923$), but there was a significant difference between Model 2 and iPSC-RPE cells on Matrigel ($p = 0.770$) (**Figure 4- 13 D**). Basal VEGF levels were significantly higher in Model 2 compared to Matrigel ($p < 0.0001$) and in Model 7 compared to Matrigel ($p < 0.0001$), with no significant difference between Model 2 and Model 7 ($p = 0.117$) (**Figure 4- 13 E**).

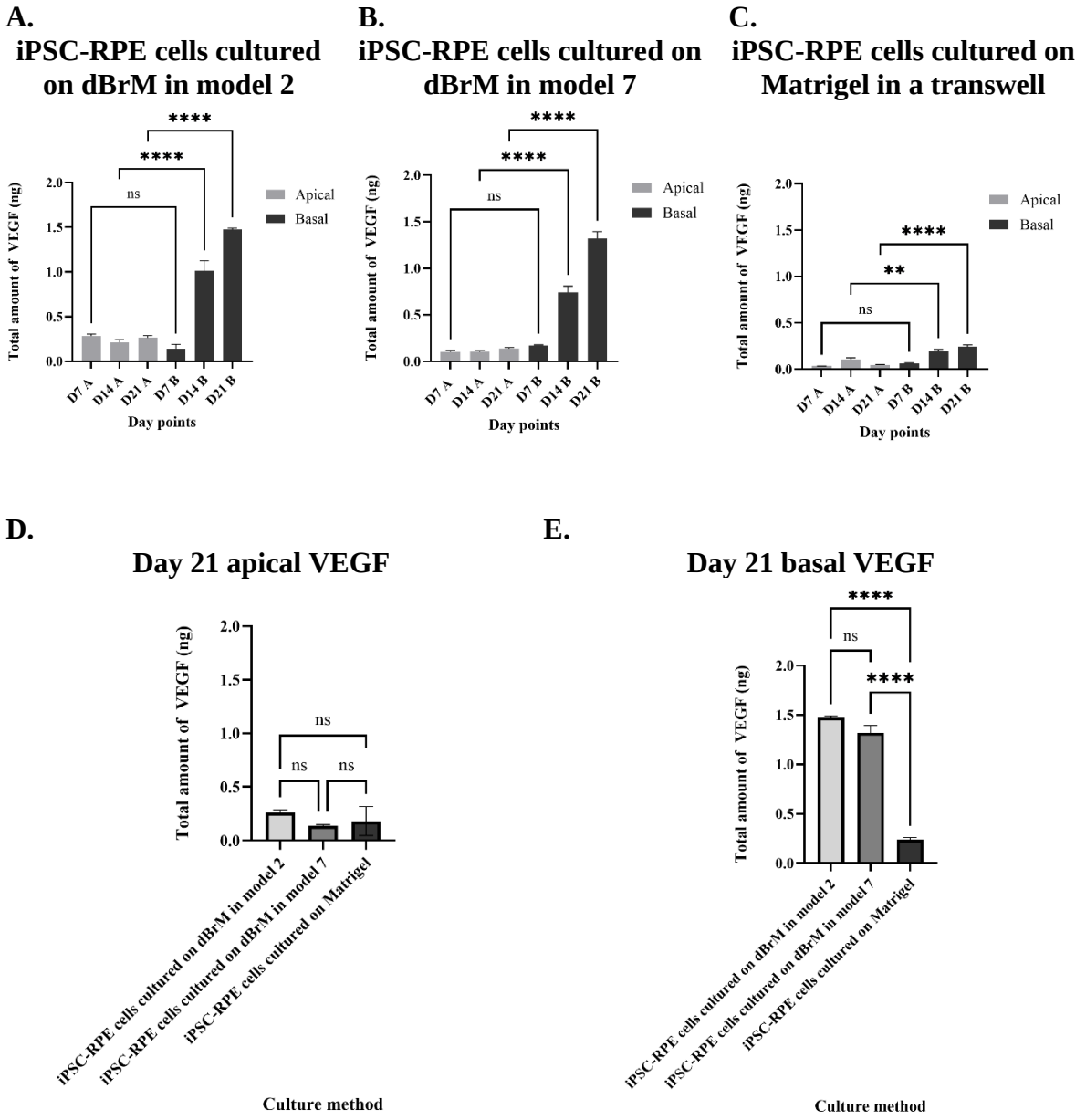

Figure 4- 13. Total amount of VEGF. The amount of VEGF secreted in the apical and basal chambers at days 7, 14 and 21 for **(A)** iPSC-RPE-cells cultured on dBrM in model 2, **(B)** iPSC-RPE cells cultured on dBrM in model 7 and **(C)** iPSC-RPE cells cultured on Matrigel. The **(D)** apical and **(E)** basal VEGF at day 21 of iPSC-RPE cells cultured on dBrM in model 2, iPSC-RPE cells cultured on dBrM in model 7 and iPSC-RPE cells cultured on Matrigel. Data shows mean (n = 3). One-way ANOVA with Tukey's multiple comparisons test was conducted to determine significance. Values with $p \leq 0.05$ were considered statistically significant.

The total PEDF levels were measured as mean±SEM percentage, n=3. Model 2 showed no significant differences between apical and basal measurements across the different time points (day 7, day 14, and day 21) (**Figure 4- 14 A**). At day 7, the apical and basal PEDF levels were 0 µg ($p > 0.99$). At day 14, the apical levels were 2.92±0.22 µg and basal levels were 2.59±0.47

µg (p = 0.65) (**Figure 4- 14 A**). By day 21, apical levels were 0.30±0.04 µg, and basal levels were 0.22±0.07 µg (p = 0.99) (**Figure 4- 14 A**). In contrast, Model 7 showed no significant differences at day 7, with apical levels at 0.33±0.17 µg and basal levels at 0 µg (p = 0.25) (**Figure 4- 14 B**). However, at day 14, apical PEDF levels were significantly higher at 3.01±0.25 µg compared to basal levels of 2.06±0.01 µg (p < 0.01) (**Figure 4- 14 B**). At day 21, no significant difference was observed, with apical levels at 0.47±0.05 µg and basal levels at 0 µg (p = 0.07) (**Figure 4- 14 B**). When iPSC-RPE cells were cultured on Matrigel, a trend similar to Model 2 was observed, as no significant differences were detected between apical and basal measurements. At day 7, apical levels were 0.07±0.01 µg and basal levels were 0.002±0.01 µg (p = 0.72) (**Figure 4- 14 C**). At day 14, apical PEDF levels were 0.95±0.05 µg and basal levels were 0.83±0.12 µg (p = 0.29) (**Figure 4- 14 C**). By day 21, apical levels were 0.18±0.07 µg and basal levels were 0.13±0.08 µg (p = 0.89) (**Figure 4- 14 C**).

Apical PEDF levels at day 21 were not significantly different between the three culture methods (**Figure 4- 14 D**). Comparing PEDF levels apically, no significant differences were observed between iPSC-RPE cultured on dBrM in Model 2 vs. Model 7 (p = 0.16) and Model 2 vs. iPSC-RPE on Matrigel (p = 0.44). However, there were significant differences between iPSC-RPE on dBrM in Model 7 vs. iPSC-RPE on Matrigel (p = 0.02) (**Figure 4- 14 D**). Besides that, comparing PEDF levels basally, no significant differences were observed between iPSC-RPE cultured on dBrM in Model 2 vs. Model 7 (p = 0.10), Model 2 vs. iPSC-RPE on Matrigel (p = 0.62), and iPSC-RPE on dBrM in Model 7 vs. iPSC-RPE on Matrigel (p = 0.34) (**Figure 4- 14 E**).

These results show that VEGF secretion patterns in iPSC-RPE cells vary across different culture models, with a significant shift toward higher basal secretion at later time points, particularly by day 21. Model 2 and Model 7 both demonstrated significantly greater basal VEGF levels compared to Matrigel, highlighting the influence of culture surface composition on RPE polarisation and function. In contrast, PEDF secretion remained relatively stable across models, with no significant differences between apical and basal levels at most time points.

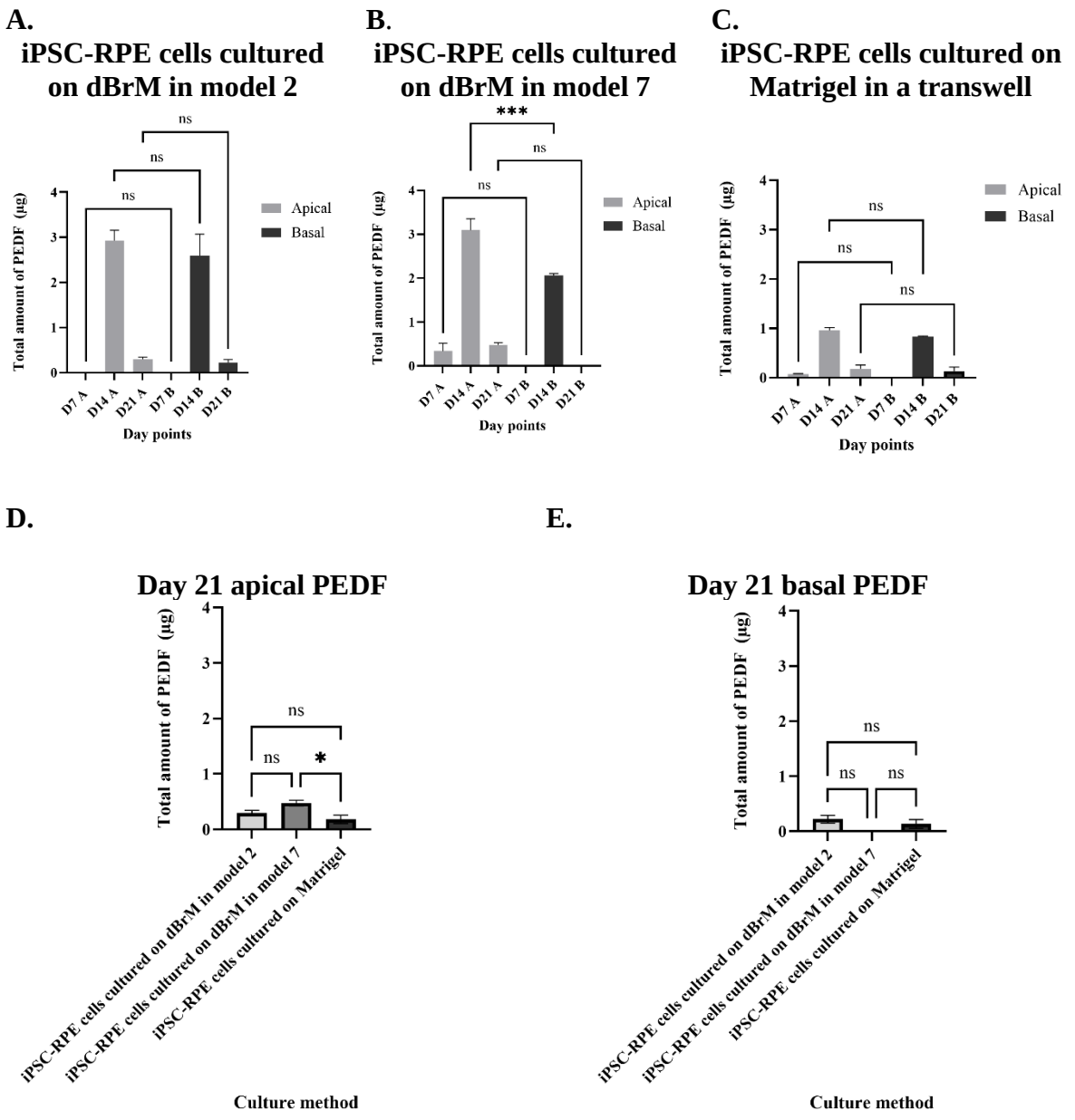

Figure 4- 14.Total amount of secreted PEDF. The amount of PEDF secreted in the apical and basal chambers at days 7, 14 and 21 for **(A)** iPSC- RPE cells cultured on dBrM in model 2, **(B)** iPSC-RPE cells cultured on dBrM in model 7 and **(C)** iPSC-RPE cells cultured on Matrigel. The **(D)** apical and **(E)** basal PEDF at day 21 of iPSC-RPE cells cultured on dBrM in model 2, iPSC-RPE cells cultured on dBrM in model 7 and iPSC-RPE cells cultured on Matrigel. Data shows mean (n = 3). One-way ANOVA with Tukey's multiple comparisons test was conducted to determine significance. Values with $p \leq 0.05$ were considered statistically significant.

4.3.10 Phagocytosis by iPSC-RPE cells cultured on decellularised Bruch's membrane

Phagocytosis of POS is one of the key RPE functions *in vivo*. Hence, we performed phagocytosis on day 21 iPSC-RPE cells cultured on dBrM in model 2 vs on Matrigel. Model 2 was used instead of model 7 as it was easier to visualise the cells when dissociating them. To identify the level of FITC fluorescence caused by phagocytosis of POS, two control experiments were performed. In the first control, FITC labelled POS were added to iPSC-RPE cells at 4^{o}C; this could identify any background fluorescence not caused by phagocytosis of FITC, such as FITC that just passively entered the cells, which is the background signal and is represented by **Figure 4- 15 A**. DRAQ5 staining was performed to label live cells to distinguish just capturing FITC. Next, was adding unlabelled POS to iPSC-RPE cells at 37^{o}C to determine if the FITC labelling caused the fluorescence (**Figure 4- 15 B**). **Figure 4- 15 C and D** represent FITC and DRAQ5 positive, which captured FITC labelled cells on dBrM in Model 2 and Matrigel respectively. The percentage of cells POS fluorescent was represented in the bar chart as a mean with n=2 (**Figure 4- 15 E).** An Average 67% of the iPSC-RPE cell population cultured on dBrM in model 2 were fluorescent for POS, and 68% of iPSC-RPE cells cultured on Matrigel were fluorescent for POS (**Figure 4- 15 E**). Meanwhile, mean fluorescence intensity (MFI) measures the average fluorescence per cell, reflecting the relative level of FITC-POS uptake within the population. The plot comparing fluorescence intensity (488 530/30-A) between the control and two sample groups shows overlapping populations, with the control group shifted to the left, indicating lower fluorescence intensity (**Figure 4- 15 F**). This suggests that the control cells have a relatively lower amount of FITC-POS. Both sample groups exhibit a similar fluorescence distribution, with no significant shift to the right, implying that there is no differences in fluorescence intensity (**Figure 4- 15 F**). Overall, these results show that iPSC-RPE cells cultured on dBrM have similar phagocytosis function as iPSC-RPE cultured on Matrigel.

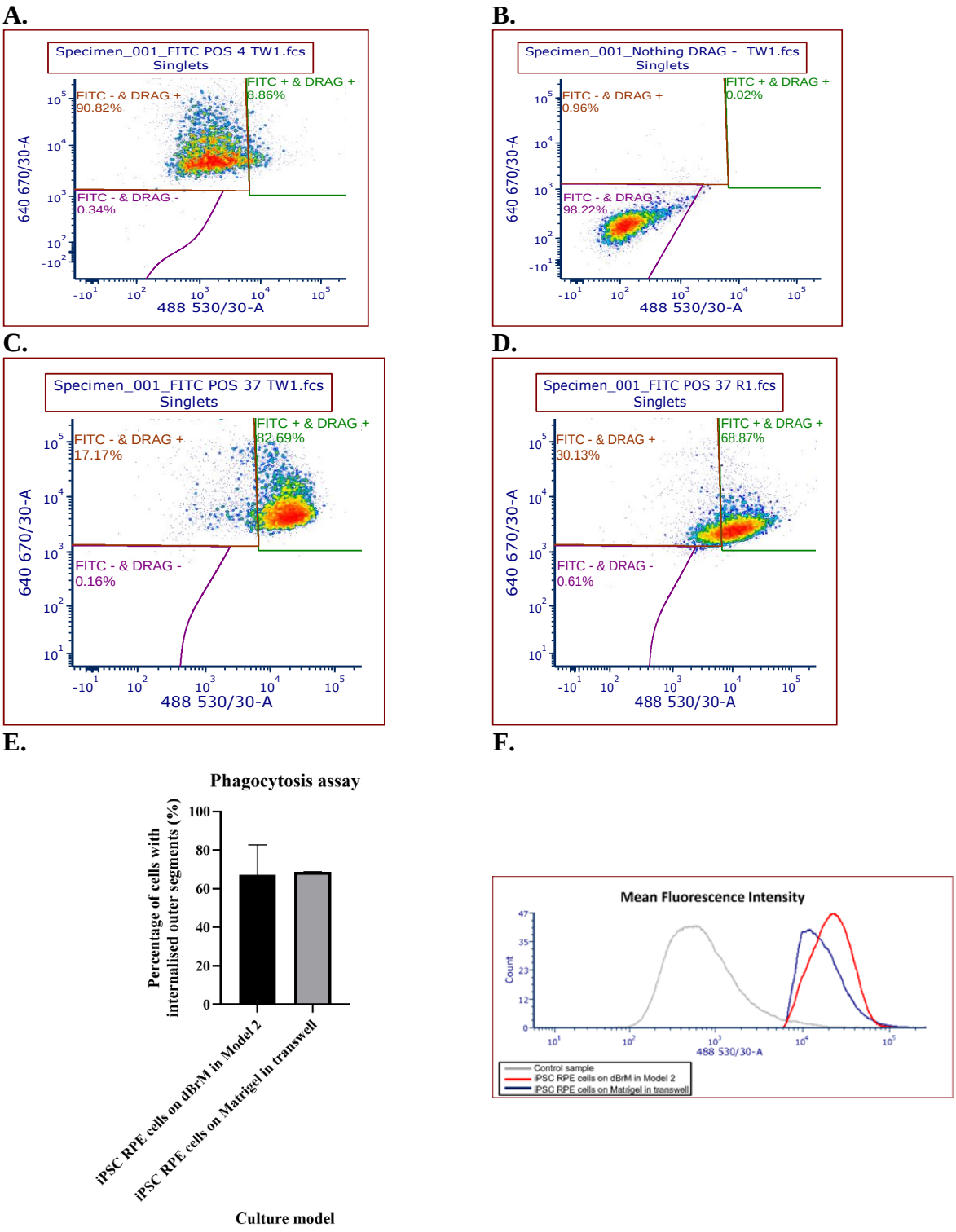

Figure 4- 15. Phagocytosis of FITC labelled POS by iPSC-RPE cells. Flow cytometry scatter plot showing the side scatter (SSC-A; cell granularity) of **(A)** labelled POS incubated at 4ºC, **(B)** unlabelled POS with unlabelled DRAQ5 at 37ºC. iPSC-RPE cells incubated with labelled POS at 37ºC with labelled DRAQ5 cultured on **(C)** dBrM in Model 2 and **(D)** Marrigel in a transwell. **(E)** Bar chart showing the percentage of cells with an internalised outer segment for iPSC-RPE cells cultured on dBrM in model 2 and on Matrigel. **(F)** The mean fluorescence intensity. Results are shown in mean, n = 2. A minimum of 10 000 events were recorded per flow cytometry experiment.

4.3.11 Culture of ECFC and iPSC-EC on decellularised Bruch's membrane

To complete the outer retina model, having EC would be ideal. We hypothesised that added ECFCs could adhere and migrate into the choroidal ghost vessels remaining after decellularisation. ECFCs were tested due to their high proliferation rate and abilities to promote vascularisation (Reid et al., 2018; Hookham et al., 2016). ECFCs at passage 15 were seeded on collagen I and iPSC-EC were seeded on Matrigel, at day 7 these cells were CD31 positive (**Figure 4- 16**). Next, the ECFCs at passage 15 were seeded and cultured basally on collagen I or Matrigel-coated dBrM in model 2 at 5 000 cells for 5 days; however, this was unsuccessful with immunofluorescent imaging negative for both CD31 and Hoechst (**Figure 4- 17**). Next, we looked at culturing iPSC-EC instead, due to their ability to proliferate and migrate to ghost vessels (Song et al., 2023). Hence, iPSC-ECs at passage 1 were co-cultured on the basal at 7 500 cells with day 21 iPSC-RPE cells on the apical. As the hypothesis was that prior culture of iPSC-RPE cells on the apical side of dBrM would enhance the potential for iPSC-EC survival and migration by trophic factor secretion particularly their basal VEGF production. However, this again was unsuccessful with CD31 negative (**Figure 4- 17**). The nuclear stain was towards the apical side, staining the iPSC-RPE cell nuclei. The IHC was also compared to dBrM where it is CD31 and Hoechst negative and to native BrM, where CD31 was detected (white arrow) (**Figure 4- 17**). In conclusion, under the experimental conditions we evaluated, we were unsuccessful in culturing ECFC or iPSC-derived EC on collagen I or Matrigel-coated dBrM.

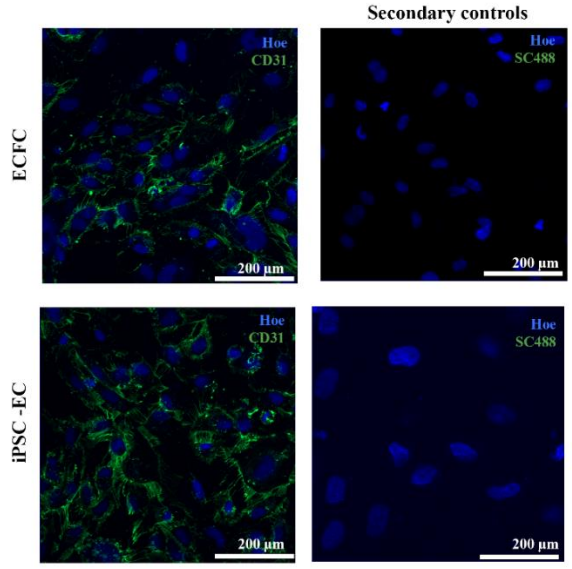

Figure 4- 16. Immunofluorescence images of ECFC and iPSC-EC cultures. The Immunofluorescence images of day 7 ECFC and iPSC-EC cultured on collagen I and Matrigel respectively.

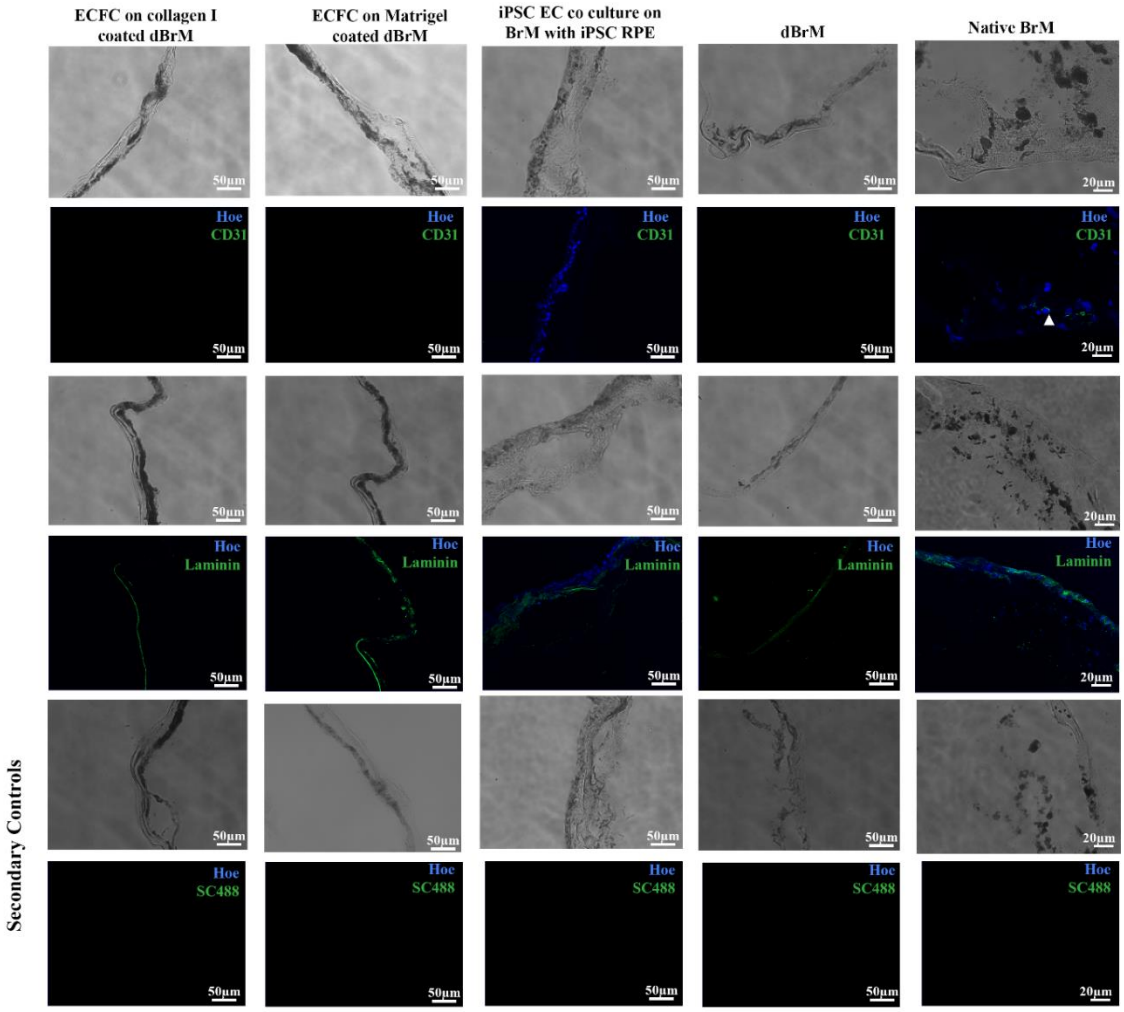

Figure 4- 17. Immunofluorescence images of iPSC-RPE cells culture. The brightfield images, CD31 (green), laminin (green) and Hoechst (Hoe) (blue) immunofluorescence of day 7 ECFC on collagen I coated dBrM, Matrigel coated dBrM, day 7 iPSC-EC on dBrM with iPSC-RPE, dBrM and native BrM with their secondary controls (No primary antibody).

4.4 Discussion

The unique diffusion properties of BrM are crucial for understanding outer retinal disease pathogenesis and potential therapeutic interventions. We therefore wanted to assess that decellularisation did not alter its unique diffusion properties of complement proteins. Besides that, dBrM supported cell adhesion and growth for forming an *in vitro* model. The results here showed that iPSC-RPE cells cultured on dBrM exhibit key characteristics of native RPE, including polarisation, tight junction formation, and phagocytic activity. However, there was no success in culturing ECFC or iPSC-EC to complete the culture model. These findings suggest that dBrM is a suitable culture surface for iPSC-RPE cell growth, as it better represents the native state due to its appropriate diffusion properties.

Examining the diffusion properties of BrM, previous studies identified FHL-1, Factor D, and C5a as complement proteins capable of passing through dBrM (RPE and choroid scraped) (Clark et al., 2017). Here, our results demonstrate a diffusion hierarchy, from the lowest to the highest rate: truncated sCR1, FI, FHL-1, C3a, FD, and C5a. This diffusion occurred through dBrM, regardless of dBrM type (SP1 or CP) or diffusion direction (RPE to choroid or vice versa). Our study found that our complement protein of interest, truncated sCR1, exhibited the lowest rate of diffusion of the complement proteins tested. Additionally, we observed an unexpectedly low percentage of total recovery for C3a with dBrM via CP, a result not seen in preliminary experiments by Scott with dBrM via SP1. This discrepancy may be attributed to differences in the decellularisation protocols used, which could have allowed C3a to become trapped within dBrM. Another possible explanation is variation in the region of dBrM examined, as diffusion may differ between peripheral and central sections. In our experiments, including Scott's experiments we were not able to distinguish the sections used in the diffusion experiment. However, in Clark S *et al* experiments, the macula region was used (Clark et al., 2017). Besides that, other key differences exist between our experiment and Clark S *et al* prior research. Firstly, the concentration of tested molecules varied: Clark S *et al* used 100 µg/ml, whereas we used 10 µg/ml—except for FH at 5 µg/ml and glucose at 400 µg/ml. The choice of 10 µg/ml was made to reflect physiological conditions better and maintain consistency with our previous experiments. Additionally, the detection methods differed as Clark S *et al* relied on Western blotting, we utilised MSD assays and JESS-quantified Western blots to obtain more precise, quantifiable results. Decellularisation protocol of BrM also differed, as we utilised either SP1 or CP for the diffusion experiments, while Clark S *et al* looked at scraping the RPE

and choroid (McHarg et al., 2015; Clark et al., 2017). Nevertheless, a limitation of our study was that each experiment was conducted only once due to the limited availability of complement proteins. The diffusion of complement proteins through dBrM is key in modelling their natural movement and interactions within the outer retina. Ensuring these diffusion patterns in outer retinal models closely replicate physiological conditions is essential for drawing reliable conclusions about complement activity. A summary of molecular diffusion findings from our experiments and Clark S *et al* (Clark et al., 2017) is presented in **Table 4- 6**.

Molecules	**Percentage of diffusion (%)**	
	Our findings, dBrM via CP	**Clark S *et al***
FHL-1	Not tested	50
CFI	5.3	No detectable
C5a	13.2	32
FD	9.9	42
C3a	9.7	No detectable
Truncated sCR1	0.30	Not tested
IgG	2	No detectable
Glucose	44	Not tested

Table 4- 6. Summary of the percentage of diffusion of complement proteins, FITC IgG and glucose through non-AMD dBrM.

When trying to identify which model is the most suitable for iPSC-RPE cells culture on dBrM, Model 2 and Model 7 were identified as the most suitable. This is as they allow the least IgG diffusion indication of a proper seal. Model 4 was excluded from diffusion rate testing due to the lack of basal access. However, when moving to the culture of iPSC-RPE on dBM, model 2 was preferred for bright-field imaging and proteomic analysis, as it offered a more straightforward setup and ease of use during the culture process. In the bright field of iPSC-RPE on dBrM compared to Matrigel, the pigmentation was harder to observe. However, as stated previously, the pigmentation of iPSC-RPE cells does not correlate with the functional characteristics of RPE cells (Nakai-Futatsugi et al., 2024).

In this chapter, we looked at the ability of iPSC-RPE cells to proliferate and mature on dBrM with and without adding Matrigel. Next, once we concluded that iPSC-RPE cells successfully grew on dBrM without Matrigel, we looked at their morphology and secretion of VEGF and PEDF between Model 2 and Model 7.

Firstly, the key contributions of this chapter are investigating iPSC-derived RPE culture on dBrM and its successful culture without requiring an added ECM layer to support its adhesion. This is novel, as previous studies either modeled BrM without using actual BrM or relied on

primary RPE cells instead (Tezel et al., 2004, 1999; Cai et al., 2018; Song et al., 2023). **Table 4-7** summarises the functional properties of the iPSC-RPE cells when cultured on dBrM, Matrigel-coated dBrM and Matrigel only in model 2 vs model 7.

Using the commercially bought iPSC-RPE, we first determined the time point at which after seeding on a polyester transwell membrane the TEER values rose above 200 Ωcm^2 and positive ZO-1 immunofluorescence appeared based on these well-known markers of RPE maturity and confluence. Following this, we examined iPSC-RPE cell growth on dBrM at day 21 using bright field imaging. Once these cells were confirmed on dBrM, immunofluorescence, TEM, and proteomic analyses were performed on day 28 of co-culture, comparing iPSC-RPE on dBrM and iPSC-RPE on Matrigel coated dBrM. The measurement of TEER was not possible due to the culture model not being suitable for electrodes. We then compared RPE cell growth directly on dBrM against culture on Matrigel-coated dBrM using IHC where both culture methods showed visible staining for ZO1 and laminin. A previous study demonstrated that ARPE-19 cells synthesise laminin chains α3, α5, β1, β3, and γ2, along with heterotrimeric laminin 5 (Aisenbrey et al., 2006). Laminin is a crucial ECM component that facilitates RPE cell adhesion to BrM via integrin–laminin interactions (Aisenbrey et al., 2006). While ECM is absent in the side section of iPSC-RPE cells (as they are cultured on Matrigel which does not contain laminin), they do secrete laminin, and its presence was detected via immunofluorescence. This suggests that iPSC-RPE cells release laminin onto their culture surface to facilitate adhesion, which has enabled them to adhere to dBrM without the need for an additional ECM layer. At the same time, they maintain their ability to produce laminin, which is crucial for RPE attachment and function.

Examining the intracellular structure of iPSC-RPE cells cultured on dBrM vs Matrigel coated dBrM reveals promising signs of key cellular morphology. TEM images highlight the presence of microvilli essential for cellular signalling, alongside melanin accumulation, which plays a key role in light absorption and oxidative stress protection (D'Alba & Shawkey, 2019; May-Simera et al., 2018). The well-defined basal infoldings also indicate an optimised metabolite and ion exchange interface (Hayes et al., 2019). These features collectively support the suitability of dBrM as culture surfaces for iPSC-RPE maturation.

Furthermore, the proteomic analysis provided valuable insight into RPE markers in Matrigel coated dBrM and non Matrigel coated dBrM models, comparing them to native and dBrM conditions. Notably, the co-culture models retained RPE markers similarly to native BrM,

highlighting their similarities. Ensuring that iPSC-RPE cells cultured on dBrM, with or without Matrigel, closely resemble their native state is crucial. From our proteomic analysis, the laminin and RPE marker levels between these two culture models are similar, showing that Matrigel as an added layer does not enhance the model. This suggests that the low laminin staining observed in iPSC-RPE cells on Matrigel-coated dBrM may be due to the specific section analyzed rather than an overall reduction in laminin levels. Detecting proteomic markers related to the visual cycle, lipid biosynthesis, melanin biosynthesis, phagocytosis, secretion, and adhesion further confirmed that iPSC-RPE cells on dBrM, regardless of Matrigel coating, exhibit mature RPE state. These proteomic markers were previously used to characterise patient-derived iPSC-RPE (Senabouth et al., 2022).

All approaches confirmed the successful culture of iPSC-RPE cells on dBrM without the need for Matrigel. Next, we compared iPSC-RPE cells on dBrM using two different models, Model 2 and Model 7, to determine their suitability for culture. Proteomic analysis of the intracellular structure in iPSC-RPE cells on dBrM in both models revealed similar expected intracellular organelles as discussed above. Besides that, the polarity of iPSC-RPE cells varied depending on the culture surface. The increased secretion of VEGF and PEDF by iPSC-RPE cells cultured on dBrM in Model 2 or Model 7, compared to those cultured on Matrigel alone, may be attributed to the higher polarity of the cells. The culture surface of dBrM closely resembles the native state, allowing the iPSC-RPE cells to grow confluent with elevated polarity. Previous studies have shown that polarity influences the total secretion of VEGF-A and PEDF (apical and basal summed) (Sonoda et al., 2009). The secretion of VEGF was 5.7-fold higher, while PEDF was 33.6-fold higher when compared to non-polarised cells (Sonoda et al., 2009). The level of PEDF secreted into the apical and basal supernatants was over 1800 times and over 300 times greater than that of VEGF-A, respectively (Sonoda et al., 2009). This supports our finding that PEDF secretion (measured in µg) exceeds VEGF secretion (measured in ng). Our results indicate higher overall VEGF and PEDF secretion compared to the previous study, except for PEDF levels in iPSC-RPE on dBrM in Model 7, where basal secretion was lower than previously reported. Additionally, on day 21, when iPSC-RPE cells are mature, PEDF secretion is not significantly different apically compared to basally, whereas VEGF is significantly higher basally, with a TEER value exceeding 200 Ωcm^2, as illustrated in our results under the different culture conditions.

Structural and functional characteristics	iPSC-RPE cells on dBrM		iPSC-RPE cells on Matrigel coated dBrM	iPSC-RPE cells on a Matrigel coated polyester membrane
	Model 2	**Model 7**	**Model 2**	
Tight junction	• ZO1 positive • TEER: NA	• ZO1 positive • TEER: NA	• ZO1 positive • TEER: NA	• ZO1 positive • TEER: > 200Ωcm²
Cellular morphology	• Pigmented hexagonal cells • Microvilli • Melanin • Basal infoldings • Nucleus • Mitochondria	• Pigmented hexagonal cells • Microvilli • Melanin • Basal infoldings • Nucleus • Mitochondria	• Pigmented hexagonal cells • Microvilli • Melanin • Basal infoldings • Nucleus • Mitochondria	• Pigmented hexagonal cells • Microvilli • Melanin • Basal infoldings • Nucleus • Mitochondria
VEGF secretion at day 21	• Apical: 0.26±0.02ng • Basal: 1.47±0.02ng	• Apical: 0.13±0.07 ng • Basal: 1.32±0.01 ng	NA	• Apical: 0.047±0.01ng • Basal: 0.24±0.02ng
PEDF VEGF secretion at day 21	• Apical: 0.30±0.04µg • Basal: 0.22±0.07µg	• Apical: 0.47±0.05 µg • Basal: 0µg	NA	• Apical: 0.18±0.07µg • Basal: 0.13±0.08µg
Phagocytosis of POS at day 21	67%	NA	NA	68%

Table 4- 7. Summary of the structural and functional characteristics of the different culture conditions.

An ideal model would incorporate EC on the basal side; however, it was unsuccessful when culturing ECFC or iPSC-EC on dBrM or in a co-culture with iPSC-RPE cells. In previous instances, success was achieved by incorporating pericytes and fibroblasts alongside the ECs, which regulated endothelial proliferation and promoted vascularisation, and this is an approach that could be tried in future work (Song et al., 2023).

Some limitations of this study include the absence of an in-depth analysis of how AMD-affected BrM influences diffusion properties. AMD alters BrM through lipid deposition,

increased ECM thickness, and other structural changes, which may impact molecular diffusion and the ability of iPSC-RPE cells to grow on its surface. This raises the question of whether decellularised AMD BrM remains a suitable ECM model based on these properties. Scott's diffusion experiment observed lower diffusion rate in AMD tissues when compared to non-AMD. However, these experiments were performed once, indicating low sample size. Hence, future studies should explore whether diffusion dynamics differ significantly in AMD dBrM versus healthy dBrM and assess the implications for disease modelling.

Additionally, BrM characteristics can vary between donors due to factors such as age and anatomical location. In humans, peripheral BrM is typically twice as thick as central BrM, with a more pronounced elastic layer (Volland et al., 2015b). A central section, particularly from the macular region, would be ideal for modelling the outer retina. However, obtaining intact central BrM can be challenging due to the risk of tears during sectioning. Obtaining age-matched sections and observing the diffusion across the younger vs older (>65 years old) would be useful in observing diffusion changes with age. In our diffusion experiments, the ages ranged from 47-85 years old. Clark S *et al* observed the diffusion across the two age groups, <35 years old and > 70 years old and observed no differences in diffusion, which could be due to the low sample size (n=5) (Clark et al., 2017). As with aging, the rate of diffusion is expected to decrease (Starita et al., 1997; Hussain et al., 2010; Lee et al., 2015). Future studies comparing diffusion properties between central and peripheral dBrM and investigating age-related differences would provide valuable insights into dBrM function across different physiological states.

Another consideration is that our study examined complement proteins individually, without accounting for the complex interactions that occur *in vivo*. In a physiological setting, complement components exist within a dynamic system influenced by enzymatic activity, regulatory proteins, and molecular interactions that may alter diffusion patterns. Understanding how these factors affect complement movement across BrM is crucial, particularly in diseases such as AMD, where complement dysregulation plays a role.

Lastly, variations in decellularisation methods may have influenced diffusion outcomes as Scott utilised SP1 compared while the remaining experiments were performed utilising CP. Differences in collagen cross-linking, lipid retention, and ECM integrity could alter BrM permeability, potentially explaining inconsistencies such as the unexpected retention of C3a.

Standardising decellularisation protocols and further characterising regional differences in BrM permeability will be essential for refining diffusion models.

Despite these limitations, our findings provide valuable insights into how complement proteins and other molecules interact with BrM. Improving our understanding of diffusion properties can enhance the accuracy of *in vitro* models, advancing retinal disease research and therapeutic development.

Chapter 5 Evaluating the potential for complement gene therapy

5.1 Introduction

Gene therapy by delivering a wild-type gene of interest carried into host cells by viral vectors to correct a variety of health conditions is the subject of much interest and therapeutic hope. AAVs are widely used for this purpose based on their safety, long-term expression, non-integrating episomal location, low immunogenicity, and wide tropism (Carter & Samulski, 2000; Mezzina & Merten, 2011). The production of AAVs for gene therapy requires a specific set of plasmids. Understanding the fundamental components of AAV vectors is crucial for designing effective gene delivery systems. AAVs are small and non-enveloped with an icosahedral protein capsid of about 25nm (Carter & Samulski, 2000; Mezzina & Merten, 2011). They have a linear single-stranded DNA (ssDNA) of approximately 4.8kb packaged within (Carter & Samulski, 2000; Mezzina & Merten, 2011). When used in gene therapy, AAVs remain episomal, as their DNA forms a circular structure that remains in the nucleus and does not integrate with the host genome (Carter & Samulski, 2000; Mezzina & Merten, 2011).

5.1.1 Components of adeno-associated viruses

One of the key elements in AAV design is the AAV transfer plasmid, which contains the viral genome that will be packaged into the vector. At the core of this plasmid are inverted terminal repeats (ITRs), which define the boundaries of the viral genome packaging (Naso et al., 2017) (**Figure 5- 1 A**). Between the ITRs is the transgene, or the gene of interest that will be delivered (Naso et al., 2017) (**Figure 5- 1 A**).

A promoter, located upstream of the transgene, controls its expression, ensuring proper regulation in the target cells (Naso et al., 2017) (**Figure 5- 1 A)**. Common promoters include the CMV (cytomegalovirus), chicken β-actin, CASI (a combination of CMV and chicken β-actin), and CAG (a combination of CMV, chicken β-actin, and rabbit β-globin). In addition to these key elements, other regulatory sequences can enhance plasmid functionality (Naso et al., 2017). For example, the WPRE (Woodchuck Hepatitis Virus Posttranscriptional Regulatory Element) boosts transgene expression (Naso et al., 2017). A terminator, such as the polyA signal, functions to ensure efficient mRNA processing and stability (Naso et al., 2017) **(Figure**

5- 1 A). Understanding these components is essential for designing successful AAV-based gene delivery experiments.

There are 13 AAV serotypes (AAV1–AAV13), each differing in tropism due to their use of different cellular receptors (Issa et al., 2023). This chapter explores AAV2 and AAV8, each carrying one of the following: enhanced green fluorescent protein (mEGFP), a random stuffer sequence (hereafter referred to as "null"), or truncated sCR1 (**Figure 5- 1 B-D**) The Flag tag peptide is DYKDDDDK, and His is 6 histidine (H); the added tag was to enable easy detection of the gene of interest. All vectors contain the CMV promoter, followed by the cytomegalovirus beta-actin promoter (CβAP) in GFP and null constructs to enhance gene expression, and a signalling peptide (SP) in truncated sCR1 to allow the protein to be directed to the endoplasmic reticulum (ER) for secretion (**Figure 5- 1 B-D**). This is then followed by the transgene of interest, and WPRE in the GFP and null constructs (**Figure 5- 1 B-D**). Lastly, the construct ends with bovine growth hormone with poly-A tail (bGH pA) which serves as the terminator for all AAV to ensure mRNA from the transgene is properly processed (**Figure 5- 1 B-D**).

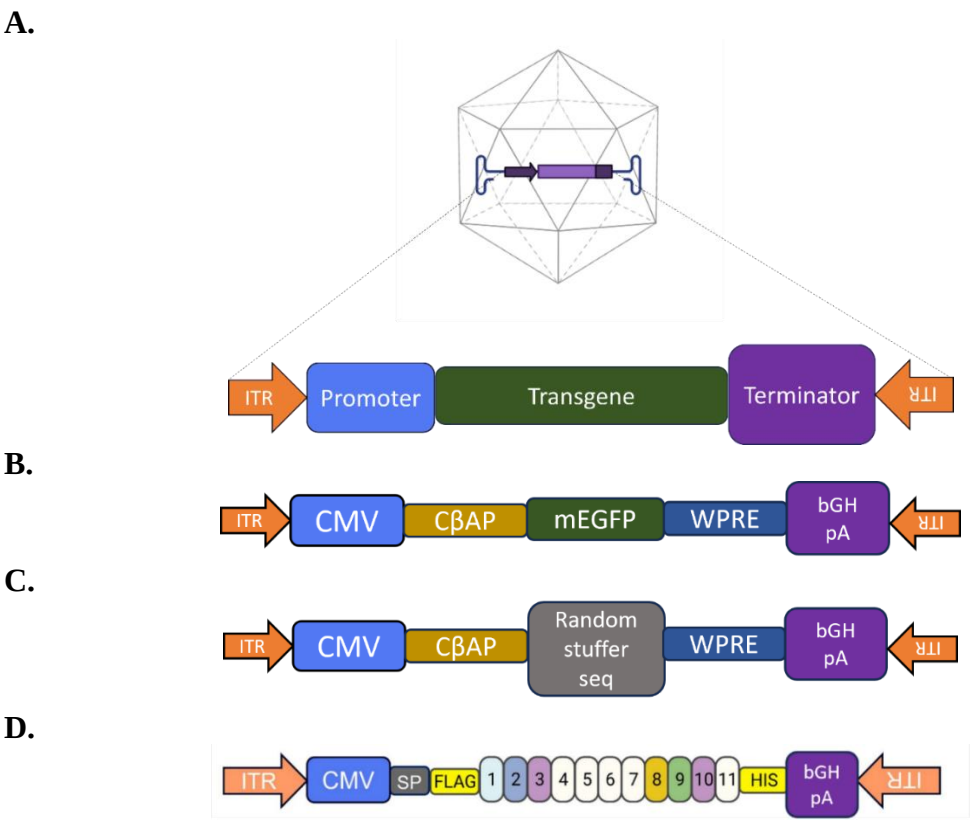

Figure 5- 1. Schematic of AAVs. (A) Shows an example of an AAV vector with ITRs with the promoter, transgene, and terminator in between. **(B)** The AAV schematic with mEGFP as the transgene **(C)** random stuffer as the transgene, allowing it to be the null AAV as a control, and **(D)** the AAV carrying truncated sCR1.

5.1.2 AAV entry into the cell

The cell entry and tracking of AAVs begin with the binding of AAV to the cell, mediated by interactions with receptors and co-receptors (Lopez-Gordo et al., 2024) (**Figure 5- 2**). The AAV enters via endocytosis and travels within endosome encapsulation (Lopez-Gordo et al., 2024) (**Figure 5- 2**). The acidification of the endosome and other triggers cause structural changes within the capsid, exposing the phospholipase A2 (PLA2) catalytic domain, which allows the virion to escape into the cytosol (Lopez-Gordo et al., 2024). The AAV virion is then imported into the nucleus through the nuclear pore complex, where it accumulates in the nucleolus and is subsequently released as ssDNA (Lopez-Gordo et al., 2024) (**Figure 5- 2**). The ssDNA is incorporated into the episomal DNA and is transcribed into mRNA, which then exits the nucleus and undergoes translation into the transgenic protein of interest (Lopez-Gordo et al., 2024) (**Figure 5- 2**).

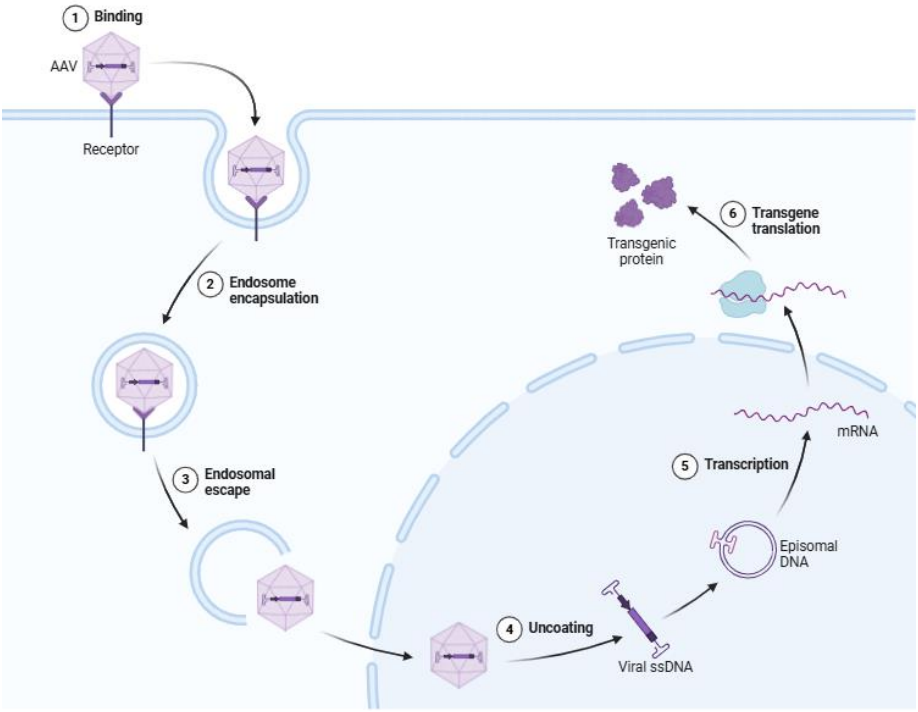

Figure 5- 2. Cell entry and trafficking of AAV. The AAV enters the cell via receptor-mediated endocytosis (1), followed by encapsulation within an endosome (2). It then escapes the endosome (3) and translocates to the nucleus, where it uncoats (4). Once uncoated, the viral genome undergoes transcription (5) into mRNA, which is subsequently translated (6) into the transgenic protein. Image created using BioRender.

5.1.3 Transduction efficiency

When transducing RPE cells, several key factors must be considered to achieve optimal transduction efficiency, including the AAV serotype, multiplicity of infection (MOI) (i.e., the number of viral particles delivered per target cell), promoter selection, and cytotoxicity assessment. Selecting the appropriate serotype is critical, as different serotypes exhibit varying specificity and efficiency in different cell types. Studies have shown that AAV2 is highly specific and ideal for RPE cells, while AAV2-7m8 is more suited for photoreceptors in retinal organoids (Cereso et al., 2014; Gonzalez-Cordero et al., 2018; Brydon et al., 2019; Garita-Hernandez et al., 2020).

MOI optimisation is another crucial factor, as it determines the number of viral particles per cell. Multiple studies on human iPSC-RPE cells cultured on Matrigel have investigated transduction efficiency using various AAV2 variants, reporting GFP-positive cell percentages ranging from 12% to 80%, depending on the MOI (Cereso et al., 2014; Gonzalez-Cordero et al., 2018; Brydon et al., 2019; Garita-Hernandez et al., 2020) (**Table 5- 1**). These findings highlight the importance of choosing the correct AAV serotype for the specific cell type and optimising MOI to achieve efficient gene delivery. Before introducing the gene of interest, it is essential first to optimise transduction conditions using reporter AAV, ensuring the experimental setup is effective.

Promoter selection plays a significant role in regulating transgene expression, with CAG, CMV, and CSI being commonly used for their ability to drive robust and sustained gene expression. By optimising these parameters, researchers can enhance transduction efficiency while minimising potential toxicity, ensuring successful gene delivery in RPE cells.

Besides that, the media used during transduction have shown to play a role in the transduction efficiency. However, previous studies have shown contradictory results, with some indicating that the presence of FBS during transduction had a negligible effect on transduction efficiency (Rambhai et al., 2020; Rogers et al., 2021; Wang et al., 2016) or enhanced efficiency (Wang et al., 2017). This, however, could be due to different cell lines and AAV serotypes used, which shows the need to optimise the media used.

Finally, while a higher MOI may improve transduction efficiency, excessive viral load can lead to cytotoxic effects, which must be carefully monitored. In the case of RPE cell transduction cytotoxicity can be assessed using TEER measurements to evaluate cell integrity and barrier

formation or LDH assays to detect plasma membrane damage. LDH is released when the plasma membrane is damaged, serving as a marker of cell injury. LDH catalyses the conversion of lactate to pyruvate, simultaneously reducing nicotinamide adenine dinucleotide (NAD^+) to NADH. INT (2-(4-iodophenyl)-3-(4-nitrophenyl)-5-phenyl-2H-tetrazolium chloride) is a chemical compound commonly used in biochemical assays to detect enzyme activity, including LDH. In the presence of NADH, INT is reduced to form formazan, a red-coloured product. The intensity of this colour is measured to quantify LDH release, providing an indicator of cell damage.

Articles	**Tissue**	**Optimal serotype(s)**	**Optimal promoter**	**Target gene**	**Optimal MOI**	**AAV incubation period**	**Percentage GFP positive cells**
Cereso N et al 2014	iPSC-RPE cells	AAV2/5	CAG	GFP & *CHM*	5×10^9	2, 4 & 6 weeks	Up to 60%
Gonzalez-Cordero A *et al* 2018	Human iPSC-RPE	• AAV2/5 • AAV2/ShH10	CMV	GFP	6,000	1 week	Up to 71%
Brydon E et al 2019	Human iPSC-RPE	AAV2/Anc80	CASI	GFP & *PRPF31*	50,000-100,000	2, 4 & 8 weeks	Up to 80%
Garita-Hernandez 2020	Human iPSC-RPE	AAV2-7m8	CAG	GFP	200,000	4 weeks	Up to 12%

Table 5- 1. Details for previous AAV transduction experiments. The tissue, optimal serotype(s), optimal promoter, target gene, optimal MOI, AAV incubation time and percentage of GFP positive cells post transduction.

There is a gap in knowledge of optimum conditions for the transduction of iPSC-RPE cells on dBrM *in vitro*. Hence, this chapter focuses on transducing iPSC-RPE cells on dBrM in model 2 or 7 and iPSC-RPE cells grown on Matrigel in a transwell. Since **Chapter 4** has demonstrated that iPSC-RPE cells cultured on dBrM are functional (releasing VEGF, PEDF, and able to phagocytose POS), it would be beneficial to investigate transduction efficiency on these iPSC-RPE cells with viral vectors. Previous studies have shown mini-CR1 expression in murine eyes following subretinal injection of a viral vector. MAC formation following laser-induced CNV was reduced by 65% and 69% relative to the null vector at $5x10^8$ and $5x10^9$ vg, respectively

(Keefe D et al., 2023). Hence, this chapter investigates the delivery of AAV 2 truncated sCR1. We hypothesised that this should reduce complement overactivation by release of the truncated sCR1, with control of complement induced inflammation.

5.2 Aims

This chapter aimed to evaluate the transduction efficiency of AAV2 and AAV8 in iPSC-RPE cell**s** cultured under different conditions: Matrigel (standard culture conditions) and dBrM (representing Models 2 and 7 from **Chapter 4**). **Figure 5- 3** represents the graphical overview of the chapter. The AAVs were added apically, directly on iPSC-RPE cells in all the conditions. The key objectives include:

1. Compare AAV2 and AAV8 transduction efficiency after 24 hours
    - Evaluate transduction at five different MOI (0, 1 000, 10 000, 100 000 and 1 000 000 MOI) in iPSC-RPE cells cultured on Matrigel at Day 3 and Day 23.
    - Compare MEM (with FBS) vs. Opti-MEM (no FBS) media during transduction.
2. Assess AAV2 transduction efficiency at 500,000 MOI on iPSC-RPE cells cultured on Matrigel
    - Investigate three different concentrations by having varying apical volume: 5.63E+10 vg/ml, 9.00E+10 vg/ml and 2.25E+11 vg/ml.
3. Assess AAV2 transduction efficiency at 500,000 MOI in iPSC-RPE cells cultured on dBrM in model 2 and 7 at 1.56E+11 vg/ml.
4. Evaluate AAV2 truncated sCR1 transduction efficiency at 500,000 MOI in iPSC-RPE cells cultured on Matrigel (4.50E+10 vg/ml) and dBrM in Models 2 (4.88E+10 vg/ml) and 7 (4.50E+10 vg/ml).

A. Transduction of AAV2 and AAV8 GFP in iPSC-RPE cells on Matrigel at day 3, measuring after 21 and 28 days

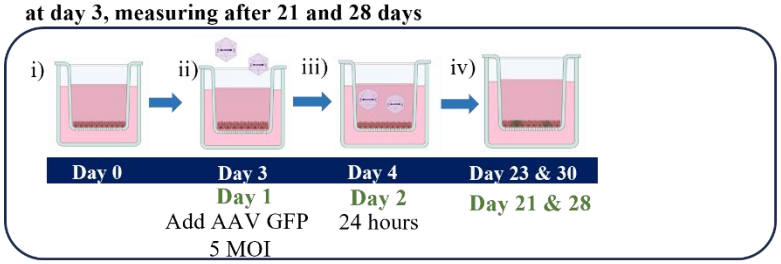

B. Transduction of AAV2 and AAV8 GFP in iPSC-RPE cells on Matrigel at day 23, measuring after 7 days

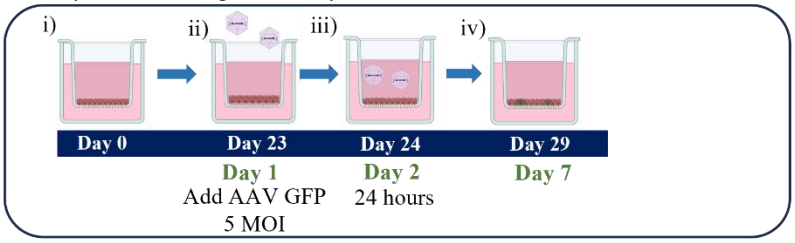

C. Transduction of AAV2 and AAV8 GFP in iPSC-RPE cells on Matrigel at day 23, measuring after 7 , 21 and 28 days

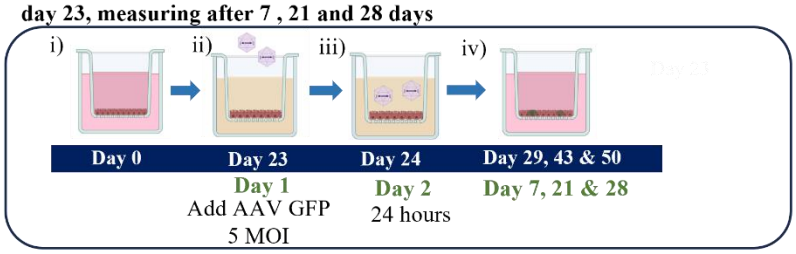

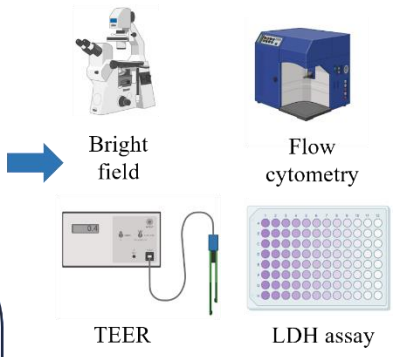

D. Transduction of AAV2 GFP on iPSC-RPE cells in Matrigel at day 23, measuring after 21 days

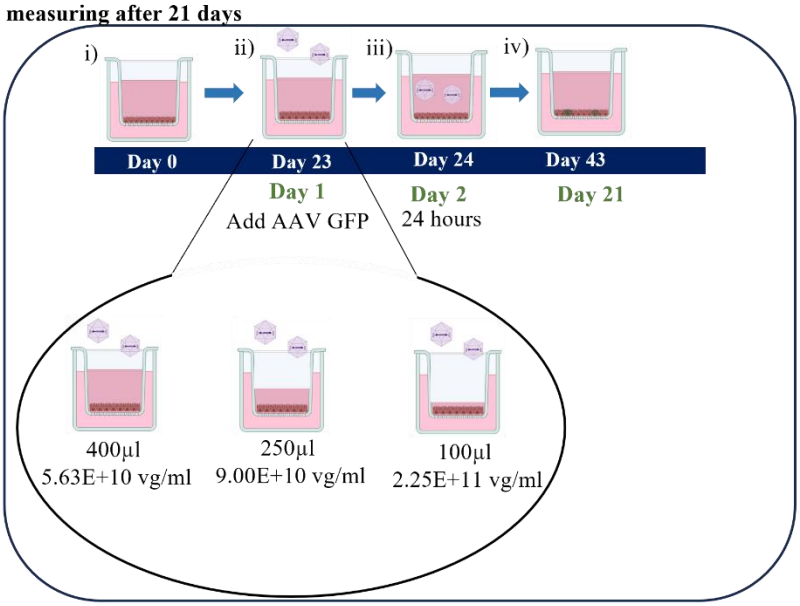

E. Transduction of AAV2 GFP in iPSC-RPE cells on dBrM at day 23, measuring after 21 days

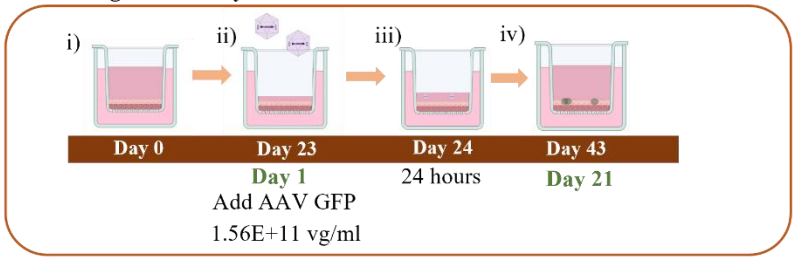

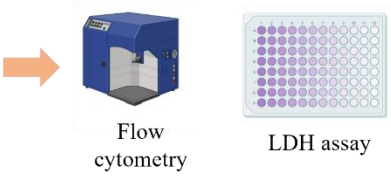

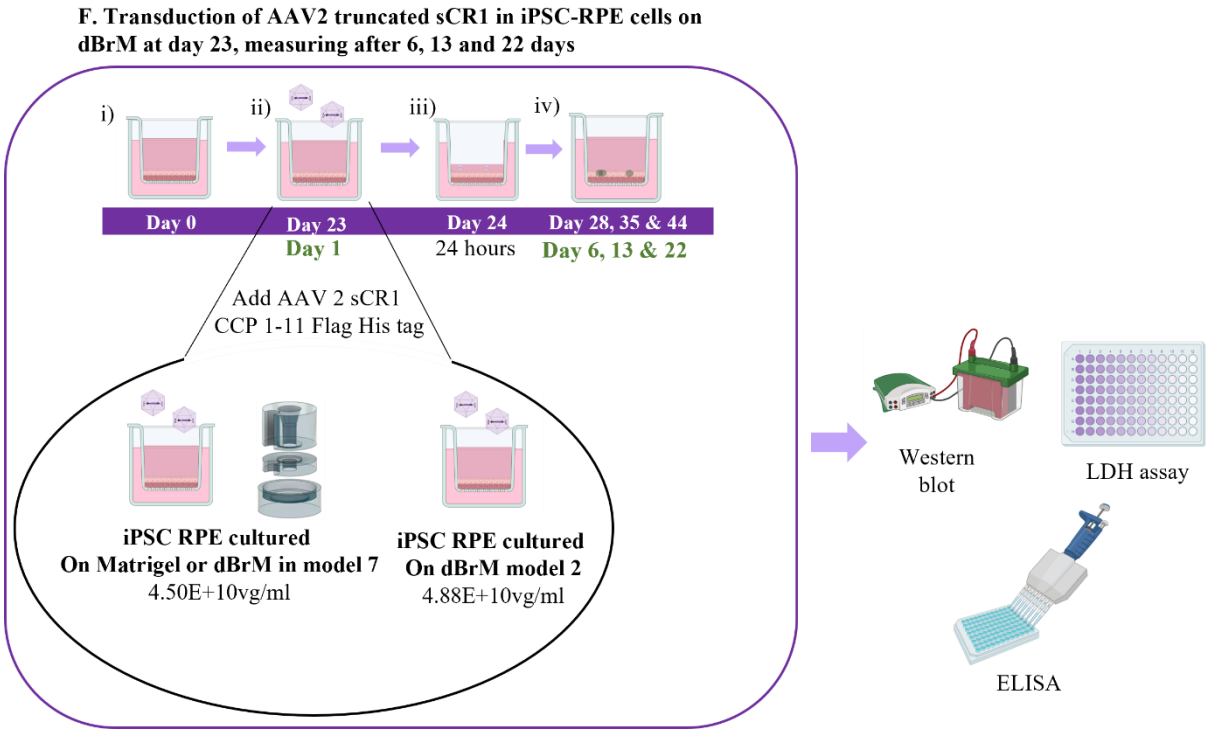

Figure 5- 3. Graphical overview of Chapter 5. Transduction was performed for 24 hours, measuring the efficacy of AAV2 compared to AAV8 GFP in iPSC-RPE cells cultured on Matrigel with **(A-B)** MEM media and **(C)** Opti-MEM media during transduction**. (D)** Transduction using MEM media were performed in iPSC-RPE cells on Matrigel. **(E)** Transduction using MEM media in iPSC-RPE cells cultured on dBrM. **(F)** Transduction using MEM media with AAV2 truncated sCR1 on iPSC-RPE cells cultured on Matrigel and dBrM in model 7 and model 2.

5.3 Results

5.3.1 Transduction of iPSC-RPE cells on Matrigel at day 3 with AAV2 and AAV 8-GFP using media containing serum (MEM media)

iPSC-RPE cells cultured on Matrigel were transduced at day 3 using either AAV2 GFP, AAV8 GFP, or their respective null vectors as controls (n=1). The AAV vectors were applied at five different MOIs: 0, 1,000, 10,000, 100,000, and 1,000,000. The null vector control (only applied at 1,000,000 MOI) is to assess that any observed GFP expression is due to the transgene carried by the AAV vector, not simply a result of the viral transduction process itself. Brightfield imaging and GFP measurements via flow cytometry were performed to assess the transduction efficiency by detecting GFP-positive cells. Additionally, TEER measurements were taken to evaluate cell cytotoxicity, with a low TEER value indicating potential damage to the cellular membrane. During transduction, MEM media was used and after transduction, the cells were incubated for 24 hours before a media change. Measurements were then taken at 21- and 28-days post-transduction, corresponding to day 23 and day 30 of culture, when the cells had reached full maturity.

The brightfield imaging of AAV2 GFP showed increased green fluorescence with higher MOIs, observed at both day 21 and day 28 post-transduction (**Figure 5- 4**). A similar trend was seen for AAV8 GFP, though AAV2 exhibited more fluorescence at all MOIs compared to AAV8 (**Figure 5- 4** and **Figure 5- 5**). The percentage of GFP-positive cells corresponded to this trend. For AAV2, at 21 days post-transduction, the percentage of GFP-positive cells was higher across all MOIs when compared to AAV8 GFP (**Figure 5- 6 A**). Specifically, for AAV2 at MOIs of 0, 1,000, 10,000, 100,000, and 1,000,000, the percentages of GFP-positive cells were 0.05%, 2.89%, 14.55%, 30.34%, and 42.95%, respectively (**Figure 5- 6 A**). In comparison, for AAV8 at the same MOIs, the percentages of GFP-positive cells were 0.2%, 0.04%, 0.24%, 0.26%, and 5.38%, respectively (**Figure 5- 6 A**). Similar results were observed at 28 days post-transduction, with AAV2 showing percentages of GFP-positive cells at 0.01%, 1.62%, 7.8%, 20.84%, and 60.62% for the MOIs of 0, 1,000, 10,000, 100,000, and 1,000,000, respectively (**Figure 5- 6 B**). In comparison, for AAV8 at the same time point, the percentages were 0.23%, 0.1%, 0.06%, 1.23%, and 7.21%, respectively (**Figure 5- 6 B**). When comparing AAV2 at day 21 and day 28 post-transduction, a consistent increase in GFP expression was observed, particularly at higher MOIs. Similarly, AAV8 showed a modest increase in GFP-

positive cells from day 21 to day 28, though the overall percentage remained lower than AAV2 at both time points.

The TEER values for AAV2 and AAV8 were measured at both day 21 and day 28 post-transduction to assess cell membrane integrity. For AAV2 at day 21, the TEER values for the null vector and GFP at MOIs of 0, 1,000, 10,000, 100,000, and 1,000,000 were 113Ωcm², 239Ωcm², 302Ωcm², 201Ωcm², 170Ωcm², and 125Ωcm², respectively (**Figure 5- 6 C**). By day 28, the TEER values for these MOIs had changed to 132Ωcm², 510Ωcm², 365Ωcm², 442Ωcm², 341Ωcm², and 173 Ωcm², showing an overall increase over time, except for the highest MOI and AAV 2 null, which remained relatively low (**Figure 5- 6 E**).

For AAV8 at day 21 post-transduction, the TEER values for the null vector and GFP at MOIs of 0, 1,000, 10,000, 100,000, and 1,000,000 were 205Ωcm², 264Ωcm², 303Ωcm², 298Ωcm², 272Ωcm², and 255Ωcm², respectively (**Figure 5- 6 D**). By day 28, the TEER values increased across all MOIs, measuring 364Ωcm², 416Ωcm², 546Ωcm², 601Ωcm², 504Ωcm², and 450 Ωcm² (**Figure 5- 6 F**).

These results suggest that AAV2 transduction leads to a higher percentage of GFP-positive cells, indicating greater transduction efficiency. However, AAV8 maintained higher TEER values, particularly at higher MOIs (AAV2 GFP and null), suggesting better preservation of cell membrane integrity over time. In contrast, AAV2 showed more fluctuations in TEER, with a noticeable drop at the highest MOI, indicating potential cytotoxic effects at higher MOIs.

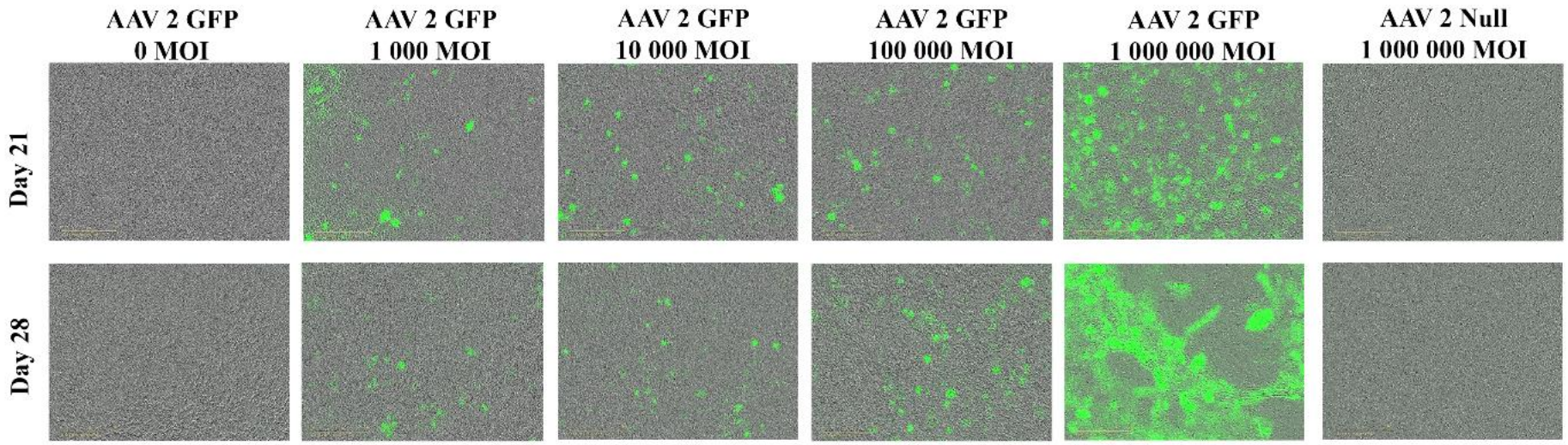

Figure 5- 4. Bright field and fluorescent images of iPSC-RPE cells on Matrigel 21- and 28-days post transduction with AAV2 GFP. Images were captured at five different MOIs: 0, 1,000, 10,000, 100,000, and 1,000,000, using AAV2 GFP. Additionally, AAV2 null was imaged at an MOI of 1,000,000. These images were taken at 21- and 28-days post-transduction.

Figure 5- 5.Bright field and fluorescent images of iPSC-RPE cells on Matrigel 21- and 28-days post transduction with AAV8 GFP. Brightfield images were captured at five different MOIs: 0, 1,000, 10,000, 100,000, and 1,000,000, using AAV8 GFP. Additionally, AAV8 null was imaged at an MOI of 1,000,000. These images were taken at 21- and 28-days post-transduction.

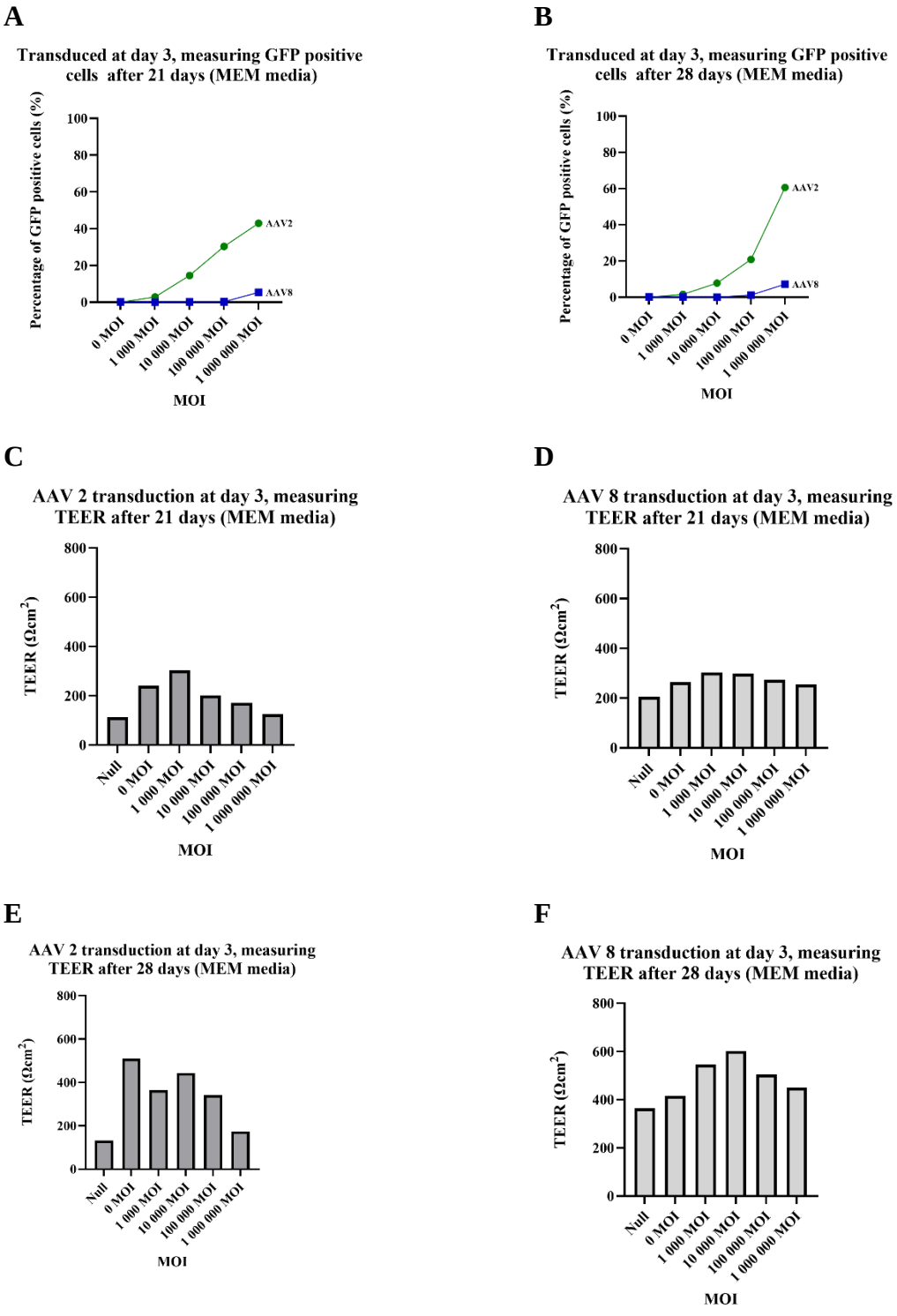

Figure 5- 6. Transduction efficiency and cytotoxicity assessment post-AAV transduction. (A) Percentage of GFP-positive iPSC-RPE cells cultured on Matrigel and transduced on day 3 with AAV2 and AAV8 GFP, assessed 21 days post-transduction. **(B)** Percentage of GFP-positive iPSC-RPE cells under the same conditions, assessed 28 days post-transduction. The TEER values of iPSC-RPE cells transduced with **(C)** AAV2 after 21 days, **(D)** AAV8 after 21 days, **(E)** AAV2 after 28 days and **(F)** AAV8 after 28 days. Transduction was performed at five different MOIs: 0, 1,000, 10,000, 100,000, and 1,000,000, with a null vector control at 1,000,000 MOI. n = 1.

5.3.2 Transduction of iPSC-RPE cells on Matrigel at day 23 with AAV2 and AAV 8-GFP using media containing serum (MEM media)

To optimise transduction efficiency while minimising TEER reduction, transduction was performed on day 23 of iPSC-RPE cell on Matrigel, when they were mature using five different MOIs (0, 1,000, 10,000, 100,000, and 1,000,000 MOI) (n=1). The AAV null were at 1,000,000 MOI. MEM media was used during transduction, and the media was changed after 24 hours. Transduction efficiency was assessed seven days later, on day 29 of culture. Bright-field imaging confirmed that the morphology of iPSC-RPE cells remained intact after transduction. GFP fluorescence indicated that AAV2 resulted in more GFP expression than AAV8 across increasing MOIs (**Figure 5- 7**). Flow cytometry showed a higher percentage of GFP-positive cells in AAV2-transduced samples, with values of 0.07%, 2.24%, 3.19%, 8.87%, and 22.21% for MOIs of 0, 1,000, 10,000, 100,000, and 1,000,000, respectively (**Figure 5- 8 A**). In contrast, AAV8 exhibited lower GFP expression, with percentages of 0.01%, 0.02%, 0.01%, 0.19%, and 2.58% for the corresponding MOIs (**Figure 5- 8 A**). TEER measurements remained stable across all conditions after seven days, indicating that neither AAV2 nor AAV8 transduction impacted monolayer integrity. TEER values for AAV2 were 709Ωcm², 625Ωcm², 694Ωcm², 677Ωcm², 722Ωcm², and 732Ωcm² for MOIs of Null, 0, 1,000, 10,000, 100,000, and 1,000,000 respectively (**Figure 5- 8 B**). Similarly, TEER values for AAV8 were 634Ωcm², 593Ωcm², 589Ωcm², 608Ωcm², 609Ωcm², and 601Ωcm² across the same MOIs (**Figure 5- 8 C**). These results demonstrate that transduction at day 23 better preserved TEER stability than day 3 transduction, with AAV2 showing better transduction efficiency compared to AAV8.

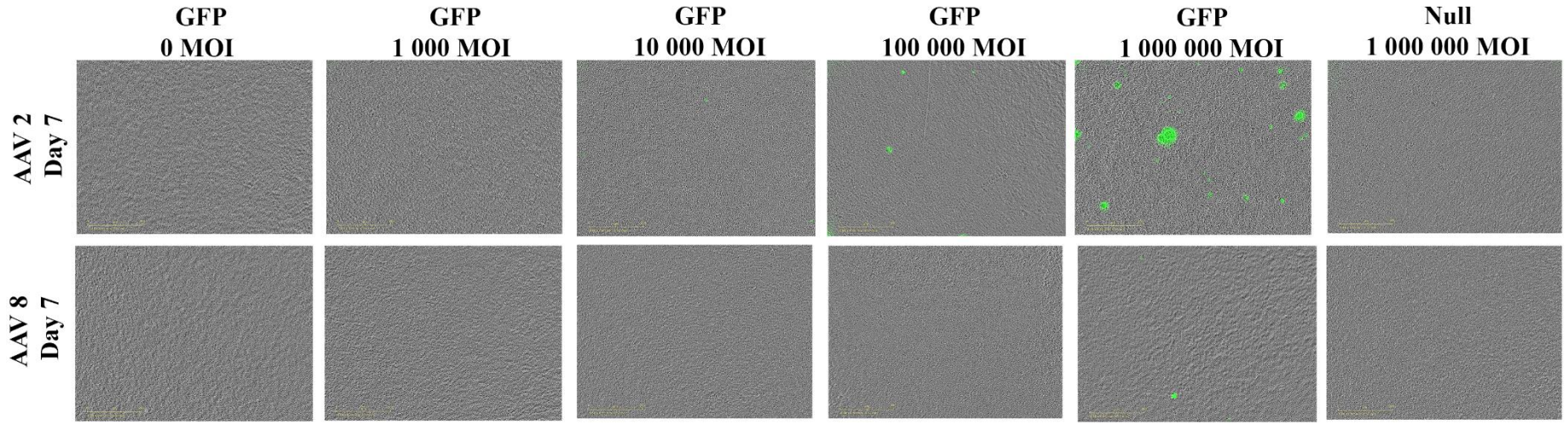

Figure 5- 7.Bright field and fluorescence images of iPSC-RPE cells on Matrigel 7 days post transduction with AAV2 and 8 GFP. Brightfield images were captured at five different MOIs: 0, 1,000, 10,000, 100,000, and 1,000,000, using AAV2 and 8 GFP. Additionally, AAV2 and 8 null were imaged at an MOI of 1,000,000. These images were taken at 7 days post-transduction.

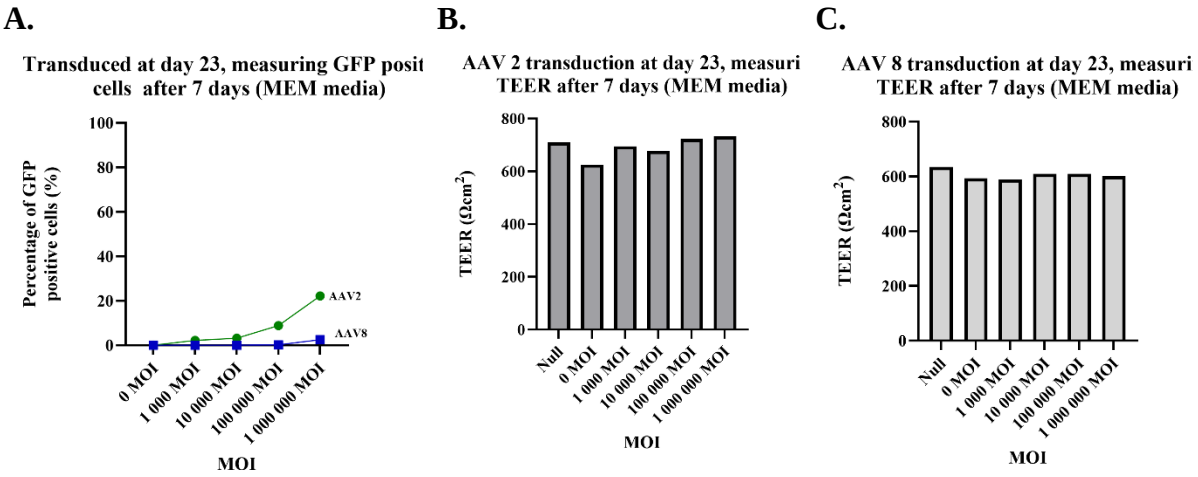

Figure 5- 8. Transduction efficiency and TEER assessment post-AAV transduction. (A) Percentage of GFP-positive iPSC-RPE cells cultured on Matrigel and transduced on day 23 with AAV2 and AAV8 GFP, assessed 7 days post-transduction. TEER measurements 7 days post **(B)** AAV2 and **(C)** AAV8 transduction. Transduction was performed at five different MOIs: 0, 1,000, 10,000, 100,000, and 1,000,000, with a null vector control at 1,000,000 MOI. n = 1.

5.3.3 Transduction of iPSC-RPE cells on Matrigel at day 23 with AAV2 and AAV 8-GFP using serum free media (Opti-MEM media)

To assess if the presence of FBS in MEM media influenced transduction efficiency based on previous studies, we performed transduction experiments using AAV2 and AAV8 GFP at the same 5 MOI (0, 1,000, 10,000, 100,000 and 1,000,000 MOI) on day 23 using Opti-MEM which is a serum free medium, followed by a return to MEM after 24 hours. Transduction was measured at 7, 21 and 28 days post-transduction , corresponding to culture day 29, 43 and 50. The AAV null was delivered at 1,000,000 MOI.

The bright field imaging revealed increased GFP expression over time in AAV2 and AAV8, with a higher intensity observed with increasing MOI (**Figure 5- 9** and **Figure 5- 10**).

At day 7 post-transduction, the percentage of GFP-positive cells for AAV2 at 0, 1000, 10,000, 100,000, and 1,000,000 MOI was 0%, 0.53%, 1.78%, 7.94%, and 30.47%, respectively (**Figure 5- 11 A**). At day 21, these values increased to 0.02%, 0.62%, 2.89%, 15.29%, and 68.17%, while at day 28, they were 0.35%, 1.83%, 5.63%, 36.77%, and 47.8% (**Figure 5- 11 A**). For AAV8, transduction efficiency was lower across all MOIs, with GFP-positive percentages at day 7 of 0.02%, 0.01%, 0.04%, 0.49%, and 4.61% (**Figure 5- 11 B**). By day 21, these values

were 0.06%, 0.12%, 0.13%, 2.05%, and 25.78%, and at day 28, 0.53%, 0.96%, 0.47%, 6%, and 33.79%, respectively (**Figure 5- 11 B**).

Next, the TEER measurements which indicated stable barrier was constant with AAV2 and AAV8 with the increasing MOI. For AAV2, TEER values at day 7 were 621Ωcm² ,610Ωcm² ,622Ωcm² ,647Ωcm² , 654Ωcm² , 673Ωcm² for null, 0, 1000, 10,000, 100,000, and 1,000,000 MOI, respectively (**Figure 5- 11 C**). At day 21, these values were 642Ωcm² , 593Ωcm² , 685Ωcm² , 719Ωcm² , 694Ωcm² , and 757 Ωcm² ,while at day 28, they were 672Ωcm² , 561Ωcm² , 641Ωcm² , 650Ωcm² , 669Ωcm² , and 639 Ωcm² (**Figure 5- 11 C**). AAV8 showed similar trends, with TEER values at day 7 of 611Ωcm² , 600Ωcm² , 652Ωcm² , 642Ωcm² , 671Ωcm² , and 682 Ωcm² , at day 21 of 646Ωcm² , 598Ωcm² , 669Ωcm² , 659Ωcm² , 695Ωcm² , and 654 Ωcm² , and at day 28 of 567Ωcm² , 561Ωcm² , 673Ωcm² , 640Ωcm² , 645Ωcm² , and 635 Ωcm² (**Figure 5- 11 D**).

The LDH release, which is an indictive of cytotoxicity remained low throughout the study. AAV2-exposed cells exhibited minimal LDH release, with percentages at day 7 of 0.25%, 1.01%, 0.76%, 0.69%, 0.27% and 0%, for 0, 1000, 10,000, 100,000, and 1,000,000 MOI, and null, respectively (**Figure 5- 11 E**). At day 21, these values were 0%, 1.3%, 0.1%, 0%, 0%, and 0%, while at day 28, LDH release was 0% across all conditions (**Figure 5- 11 E**). AAV8 showed slightly higher cytotoxicity, with LDH release at day 7 of 0.67%, 0.98%, 1.39%, 0.84%, 0%, and 1.36% (**Figure 5- 11 F**). At day 21, these values were 4.07%, 4.65%, 1.96%, 2.24%, 0.36%, and 0%, while at day 28, they were 0.03%, 0%, 0%, 9%, 0%, and 0% (**Figure 5- 11 F**).

These findings indicate that transduction efficiency, as evidenced by increased GFP expression over time, was notably higher in AAV2 compared to AAV8 across all time points and MOIs. AAV2 demonstrated superior transduction efficiency, particularly at higher MOIs. TEER measurements showed that barrier integrity was well-maintained, suggesting minimal disruption to cellular function. Additionally, LDH release remained low, signifying limited cytotoxicity. Overall, AAV2 was more efficient at transducing cells, especially at elevated MOIs, while AAV8 exhibited lower transduction efficiency.

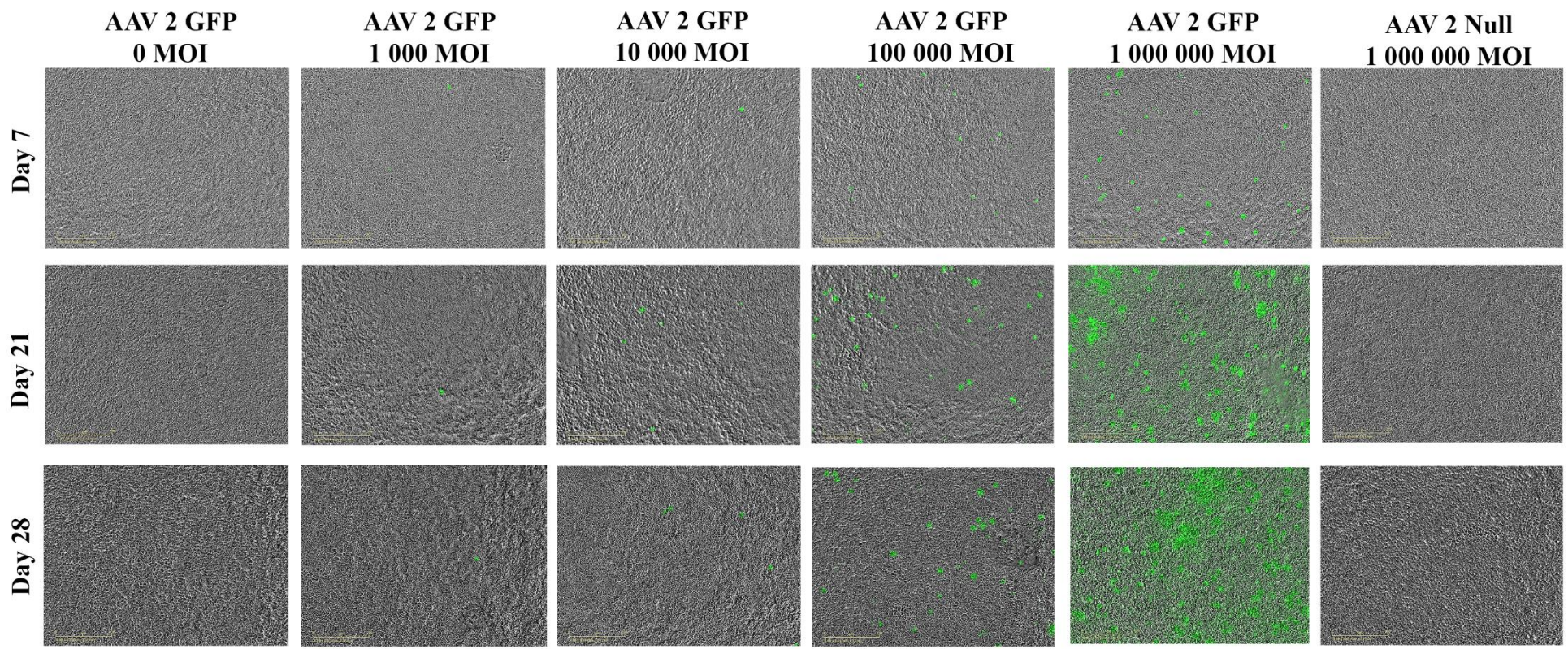

Figure 5- 9. Bright field and fluorescence images of iPSC-RPE cells on Matrigel 7, 21- and 28-days post transduction with AAV2 GFP. Brightfield images were captured at five different MOIs: 0, 1,000, 10,000, 100,000, and 1,000,000, using AAV2 GFP. Additionally, AAV2 null was imaged at an MOI of 1,000,000. These images were taken at 7-, 21- and 28-days post-transduction.

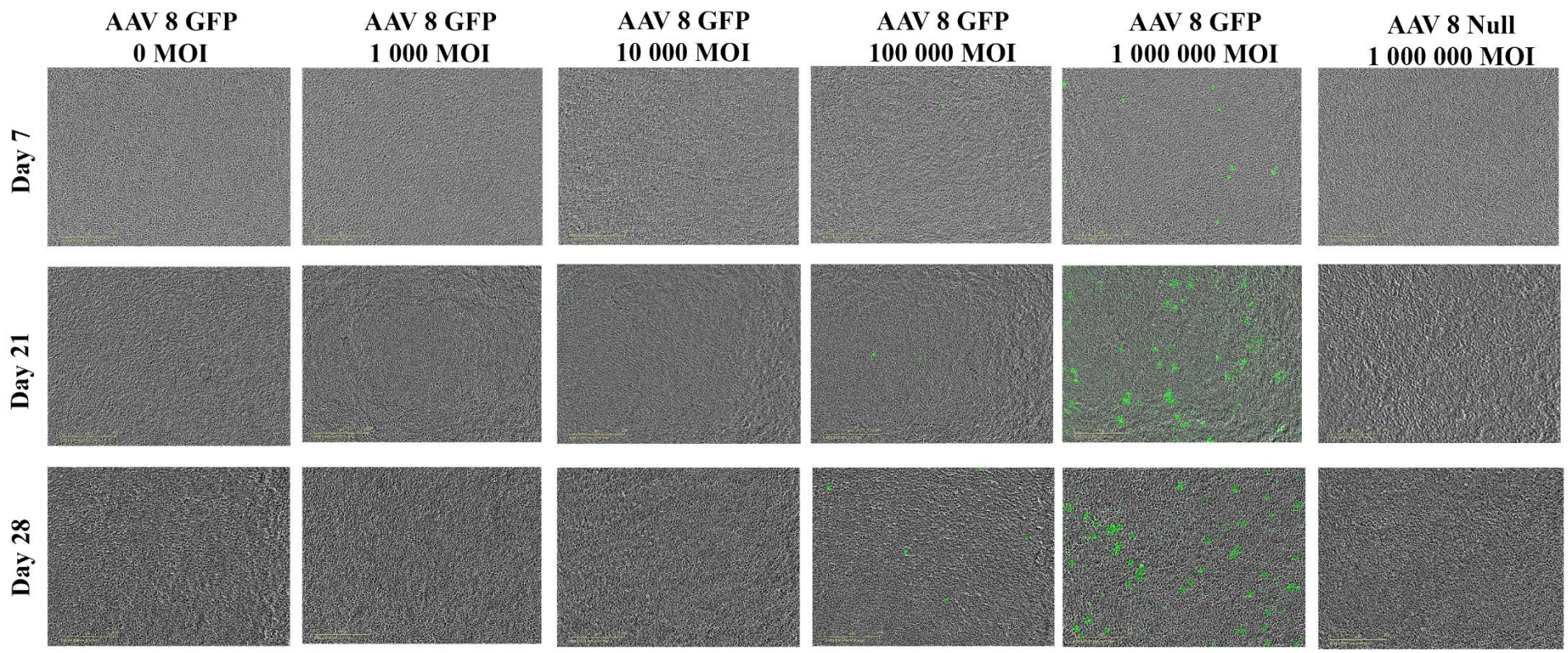

Figure 5- 10.Bright field and fluorescence images of iPSC-RPE cells on Matrigel 7, 21- and 28-days post transduction with AAV8 GFP. Brightfield images were captured at five different MOIs: 0, 1,000, 10,000, 100,000, and 1,000,000, using AAV8 GFP. Additionally, AAV8 null was imaged at an MOI of 1,000,000. These images were taken at 7-, 21- and 28-days post-transduction.

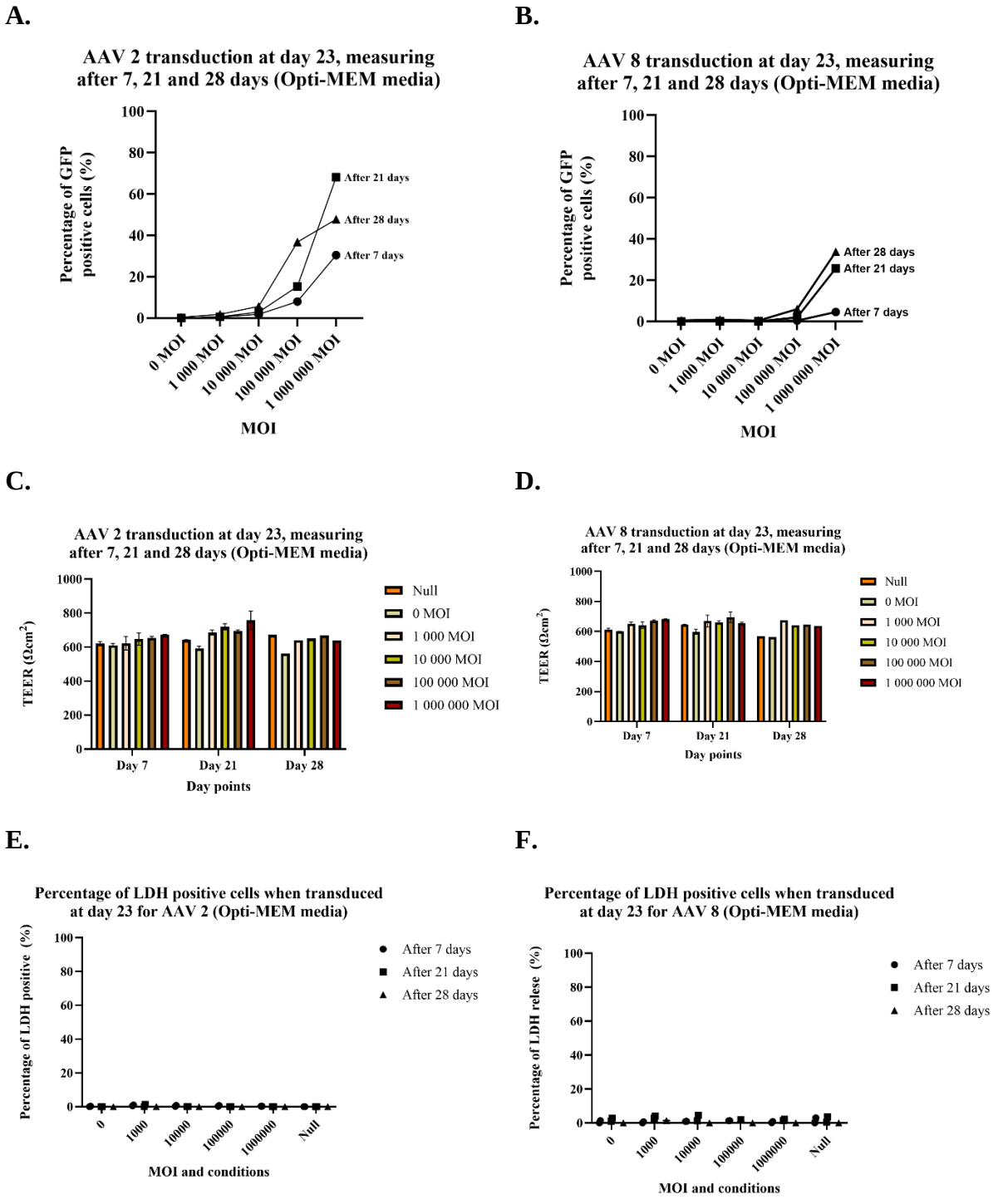

Figure 5- 11. Transduction efficiency, TEER and LDH assessment post-AAV transduction. (A) Percentage of GFP-positive iPSC-RPE cells cultured on Matrigel and transduced on day 23 with AAV2, 7-, 21 and 28-days post-transduction. **(B)** Percentage of GFP-positive iPSC-RPE cells cultured on Matrigel and transduced on day 23 with AAV8, 7, 21and 28 days post-transduction. The TEER measurements 7-, 21 and 28-days post transduction with **(C)** AAV 2 and **(D)** AAV8. Measurements for day 7 and 21 were as mean n=2 and for day 28 n=1, The percentage of LDH release 7-, 21 and 28-days post transduction with **(E)** AAV2 and **(F)** AAV8. Transduction was performed at five different MOIs: 0, 1,000, 10,000, 100,000, and 1,000,000, with a null vector control at 1,000,000 MOI. n = 1.

5.3.4 Comparing transduction at day 23 iPSC-RPE cells on Matrigel using media containing serum and serum free media

The transduction efficiency of AAV2 and AAV8 in iPSC-RPE cultured on Matrigel was assessed in both Opti-MEM and MEM media at various MOIs. For AAV2 in Opti-MEM, the transduction efficiencies at 0, 1,000, 10,000, 100,000 and 1,000,000 MOI were 0.07%, 0.53%,1.78%,7.94% and 34.47%, respectively (**Figure 5- 12 A**). In contrast, AAV2 in MEM media values were 0.18%, 2.24%, 3.19%,8.87% and 22.21%, respectively (**Figure 5- 12 A**). Overall, AAV2 in Opti-MEM consistently exhibited higher transduction efficiency than MEM media, particularly at higher MOIs.

For AAV8, transduction efficiency was lower across all MOIs compared to AAV2. In Opti-MEM, the transduction efficiencies at 0, 1,000, 10,000, 100,000 and 1,000,000 MOI were 0.02%, 0.02%,0.04%,0.50% and 4.61%, respectively (**Figure 5- 12 B**). In MEM media, the values were 0.06%, 0.02%, 0.01%, 0.19% and 2.58%, respectively (**Figure 5- 12 B**). Overall, AAV2 demonstrated higher transduction efficiency than AAV8, and Opti-MEM media provided enhanced transduction results than MEM media for both AAV serotypes.

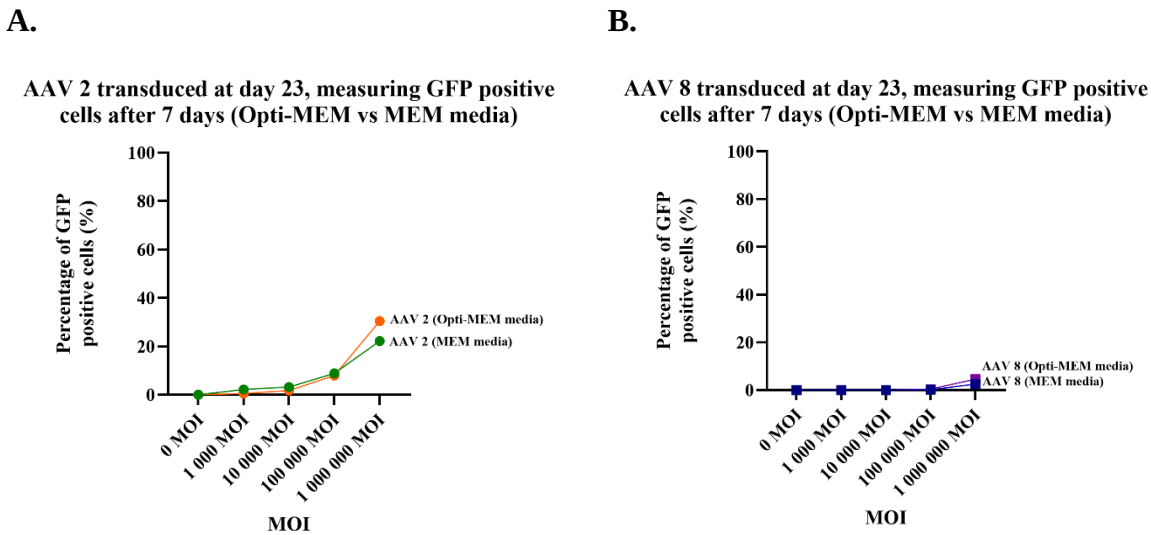

Figure 5- 12. Transduction efficiency assessment post-AAV transduction with MEM vs Opti-MEM during transduction. (A) Percentage of GFP-positive iPSC-RPE cells cultured on Matrigel and transduced on day 23 with AAV2, 7 days post-transduction with MEM vs Opti-MEM. **(B)** Percentage of GFP-positive iPSC-RPE cells cultured on Matrigel and transduced on day 23 with AAV8, 7 days post-transduction with MEM vs Opti-MEM. Transduction was performed at five different MOIs: 0, 1,000, 10,000, 100,000, and 1,000,000, with a null vector control at 1,000,000 MOI. n = 1.

5.3.5 Transduction of iPSC-RPE cells on Matrigel at the same MOI but different concentration

As previous results demonstrated that AAV2 outperforms AAV8 when transduction is performed on day 23, with measurements taken after 21 days, we conducted transduction on day 23 in iPSC-RPE cells cultured on Matrigel using AAV2-GFP with MEM media. Measurements were taken 21 days post-transduction. Additionally, we aimed to test the same MOI at different concentrations, ensuring the virus-to-cell ratio remained constant while varying the total volume of the viral solution. For this experiment, an MOI of 500,000 was tested at three different concentrations: 5.63E+10 vg/ml, 9.00E+10 vg/ml, and 2.25E+11 vg/ml. After 24 hours, the media was changed. The brightfield images show increasing green fluorescence with the increasing AAV concentration over 7, 14 and 21 days post-transduction (**Figure 5- 13**). The percentage of GFP-positive cells, measured as the mean (n=2), was as follow, 71% for 5.63E+10 vg/ml, 71% for 9.00E+10 vg/ml, and 82% for 2.25E+11 vg/ml (**Figure 5- 14 A**).

TEER values remained stable, the values for AAV2 GFP at 5.63E+10 vg/ml was 674 Ωcm², for 9.00E+10 vg/ml was 669 Ωcm², and 2.25E+11 vg/ml was 661 Ωcm² (**Figure 5- 14 B**). Similarly, for AAV2 Null, values were 631 Ωcm² for 5.63E+10 vg/ml , 660 Ωcm² for 9.00E+10 vg/ml and 612 Ωcm²) for 2.25E+11 vg/ml (**Figure 5- 14 B).**

The percentage of LDH release after 24 hours post-transduction for AAV 2 GFP at 5.63E+10 vg/ml, 9.00E+10 vg/ml, and 2.25E+11 vg/ml was 0%, 0.06%, and 0.19% respectively (**Figure 5- 14 C**). After 21 days, it was 0%, 0.11%, and 0% respectively **(Figure 5- 14 C**). For AAV2 null at 5.63E+10 vg/ml, 9.00E+10 vg/ml, and 2.25E+11 vg/ml, the percentages were 0.04%, 0.16%, and 0.38% respectively **(Figure 5- 14 C**). After 21 days, it was 0%, 0%, and 0% respectively (**Figure 5- 14 C**).

These findings suggest that within the tested range, variations in viral concentration do not substantially impact transduction efficiency or barrier integrity. However, it demonstrated the use of a lower MOI of 500 000 MOI with higher concentration to obtain a higher transduction efficiency, as previously, an MOI of 1 000 000 showed the best transduction efficiency (**Section 5.3.1-5.3.4**).

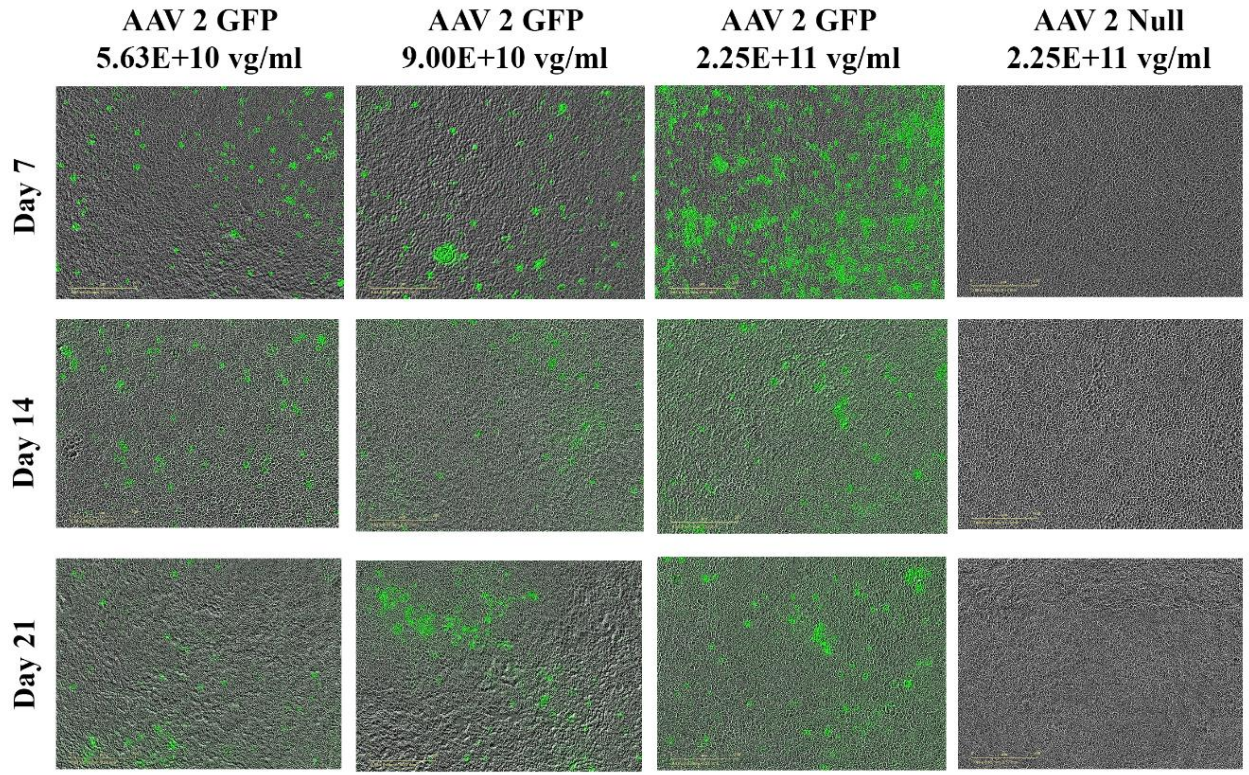

Figure 5- 13. Bright field and fluorescence images of iPSC-RPE cells on Matrigel 7-, 14- and 21-days post transduction with AAV2 GFP. Brightfield images were captured at three different concentrations using AAV2 GFP and null. These images were taken at 7-, 14- and 21-days post-transduction.

A.

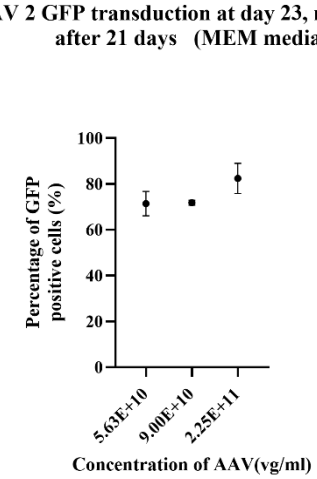

B.

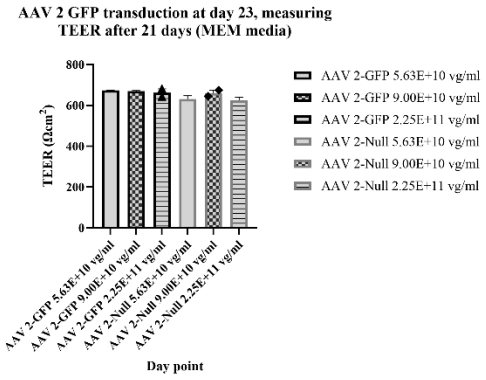

C.

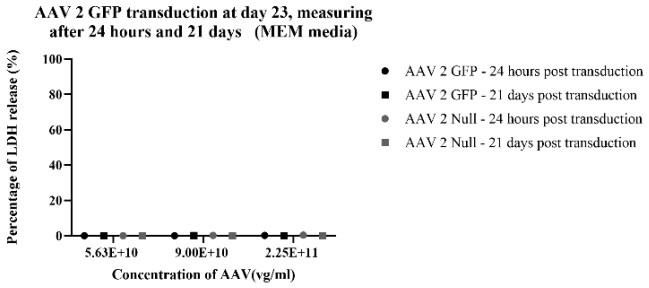

Figure 5- 14. Transduction efficiency assessment post-AAV transduction with AAV2. (A) Percentage of GFP-positive iPSC-RPE cells cultured on Matrigel and transduced on day 23 with AAV 2, 21 days post-transduction. **(B)** TEER measurements of iPSC-RPE cells cultured on Matrigel 24 hours and 21 days post transduction. **(C)** Percentage of LDH releases 24 hours and 21 days post-transduction. n = 2.

5.3.6 Transduction of iPSC-RPE cells on dBrM

The previous experiments demonstrated that iPSC-RPE cells on Matrigel could be successfully transduced with AAV vectors, particularly when transduced at a 500,000 MOI and 2.25E+11 vg/ml concentration using MEM media, and the results were measured after 21 days. In this section, transduction was performed on iPSC-RPE cultured on dBrM. Transduction efficiency with AAV2 GFP at 500 000 MOI and 1.56E+11 vg/ml was measured in iPSC-RPE cells

cultured on dBrM in Model 2. MEM media was used during transduction at day 23 of culture, and the media was changed after 24 hours. Transduction efficiency was assessed 21 days later, on day 43 of culture.. The percentage of GFP-positive cells, measured as mean, was 56% (**Figure 5- 15 A**). Cytotoxicity, measured by LDH release, was 0% for both AAV2 GFP and AAV2 Null, both 24 hours post-transduction and 21 days post-transduction (**Figure 5- 15 B**). These findings suggest that AAV2 GFP is an efficient vector for transducing iPSC-RPE cells on dBrM with no cytotoxic effect.

A.

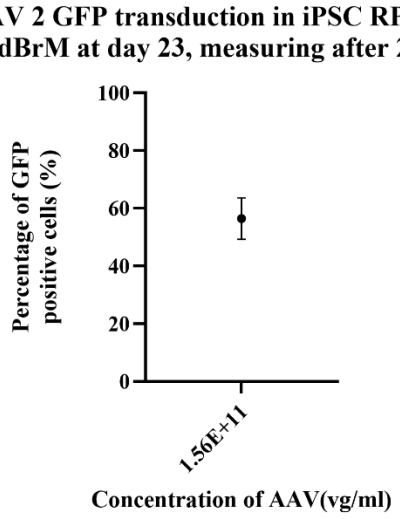

B.

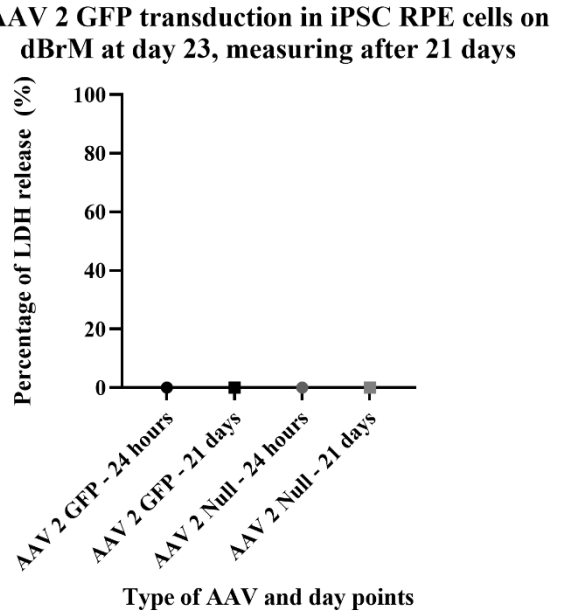

Figure 5- 15. Transduction efficiency assessment post-AAV transduction with AAV2. (A) Percentage of GFP-positive cells quantified from iPSC-RPE cells cultured on dBrM and transduced with AAV2 on day 23, evaluated 21 days post-transduction. **(B)** Percentage of LDH release 24 hours and 21 days post transduction. Transduction was performed at 1.56E+11vg/ml. n = 2.

5.3.7 Absence of complement activity in media alone

As the initial optimisation showed success, including the transduction of iPSC-RPE on dBrM, we then wanted to assess transduction of iPSC-RPE cells on dBrM with AAV2 truncated sCR1. However, when culturing iPSC-RPE cells, the MEM media contains heat-inactivated FBS. It has been shown that heat inactivation halts complement activity due to the denaturation of complement proteins (Soltis et al., 1979; Shen et al., 1997). The ability of truncated sCR1 to function as a co-factor for FI-mediated cleavage of C3b was detailed in **Chapter 2 Section**

2.14.6. To ensure that the media alone did not contain complement proteins which could lead to the breakdown of C3b to iC3b, it was incubated with FI and truncated sCR1 to demonstrate no C3b activity in the media, with C3b and FI to show no co-factor activity in the media, and finally with C3b and truncated sCR1 to indicate no FI activity in the media. The amount of FI was 100 ng, C3b was 1 µg and truncated sCR1 was 130 µg. These incubations were conducted at 37°C for one hour, followed by analysis for C3b cleavage by SDS-PAGE under reducing conditions. Subsequently, the samples were transferred to a blot and stained with primary antibody, polyclonal rabbit anti-human C3d, to visualise the alpha chain of C3b into downstream fragments and C3d. These steps are consistent for all the experiments for **Section 5.3.7-5.3.11**.

In the blots, the positive control (+) contained C3b, FI, and truncated sCR1 to show the bands at α' C3b (105 kDa), α'1 iC3b (68 kDa), and C3d (37 kDa) (**Figure 5- 16**). The negative control (-) contained C3b and FI to demonstrate α' C3b (105 kDa) with no C3b breakdown activity, as it was negative for the bands α'1 iC3b (68 kDa) and C3d (37 kDa) (**Figure 5- 16**). In the lanes with FI and truncated sCR1, no bands for α' C3b (105 kDa), α'1 iC3b (68 kDa), and C3d (37 kDa) were detected, indicating no C3b in the media (**Figure 5- 16**). In the lanes with C3b and FI, only α' C3b (105 kDa) was detected, and in the lanes with C3b and truncated sCR1, only α' C3b (105 kDa) was also detected (**Figure 5- 16**). These results indicate no complement breakdown activity in the media, as no C3b and co-factor activities are observed in the media without the addition of complement proteins.

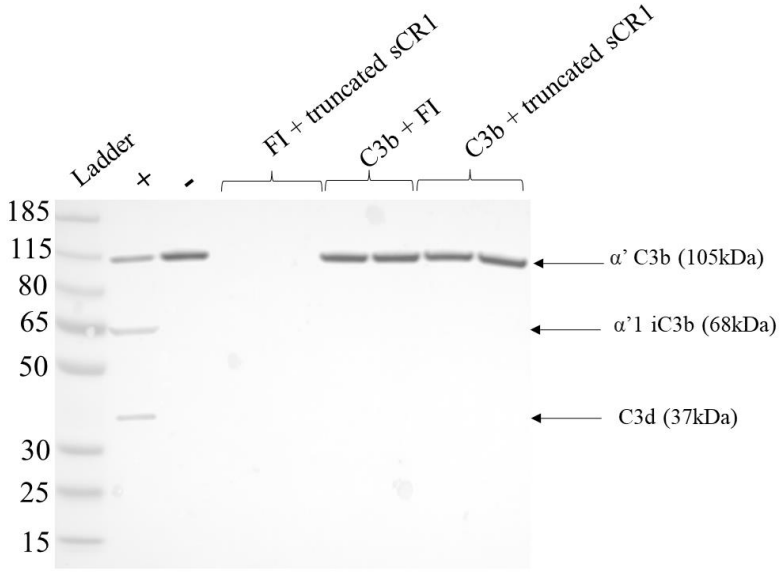

Figure 5- 16. No complement activity in MEM media alone. No C3b cleavage was detected in the lanes with FI + truncated sCR1, C3b + FI and C3b + truncated sCR1.

5.3.8 Effect of low truncated sCR1 levels on C3b cleavage into C3d

As no complement activity was detected in media alone, the next step was to determine whether the breakdown of C3b into C3d (37 kDa) could be observed at lower concentrations of truncated sCR1, as previous analysis had used 130 µg. This was as we were unsure how much of truncated sCR1 will be released from transduced cells, hence, we wanted to determine the lowest amount of truncated sCR1 that will still allow the breakdown to C3d. The samples were handled by incubating the media at 37°C for 1 hour with FI (100 ng), C3b (1 µg), and varying concentrations of truncated sCR1 (1.3 µg, 0.65 µg, and 0.1 µg). The negative control consisted of only C3b (1 µg) and FI (100 ng) to confirm the absence of C3d formation without truncated sCR1, ensuring the specificity of the reaction. The C3d band was faintly observed at 37 kDa for the 1.3 µg and 0.65 µg concentrations, but no bands were visible for 0.1 µg (**Figure 5- 17**). These results suggest that C3b breakdown into C3d occurs at higher truncated sCR1 concentrations but is not detectable at the lowest concentration tested.

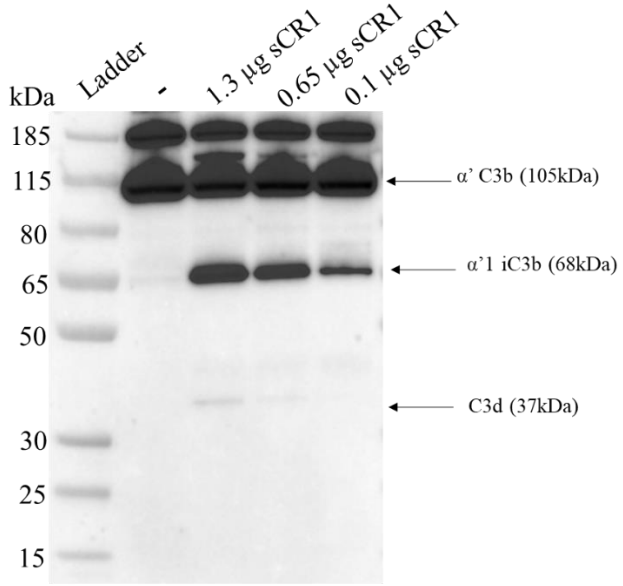

Figure 5- 17. Determining the lowest concentration of truncated sCR1 require to breakdown C3b. When C3b (1 µg), FI (100 ng), and truncated sCR1 at 1.3 µg, 0.65 µg, and 0.1 µg were incubated, C3b breakdown was confirmed by the presence of a C3d band at 37 kDa for the 1.3 µg and 0.65 µg conditions. However, incomplete C3b cleavage was observed with 0.1 µg of truncated sCR1, as indicated by the presence of a smaller α'1 iC3b band at 68 kDa compared to the higher concentrations (1.3 µg and 0.65 µg).

5.3.9 Breakdown of C3b by truncated sCR1 from iPSC-RPE supernatant at day 21 with and without added FI

Since iPSC-RPE cells release FI and FH (Luo et al., 2013; Hallam et al., 2017), the breakdown of C3b was tested with and without the addition of FI, this experiment was to demonstrate that the supernatant from iPSC-RPE cells cultured on Matrigel and dBrM in model 2 can degrade C3b in the presence of low truncated sCR1, with and without the addition of FI. Supernatants from iPSC-RPE cultured on Matrigel and dBrM in model 2 at day 21 were obtained and incubated at 37ºC for 1 hour with added FI (1 µg C3b, 100ng FI, and 1.3 µg truncated sCR1) or without added FI (1 µg C3b and 1.3 µg truncated sCR1). The negative control contained supernatant with 1 µg C3b and 100ng FI. The C3d band at 37kDa was visible in the reaction with and without added FI, with weaker bands in no added FI lane in supernatant from iPSC-RPE cells on Matrigel or iPSC-RPE on dBrM (**Figure 5- 18 and Figure 5- 19**). These results show that the FI produced by the iPSC-RPE cells cultured on Matrigel and dBrM are sufficient for the breakdown of C3b.

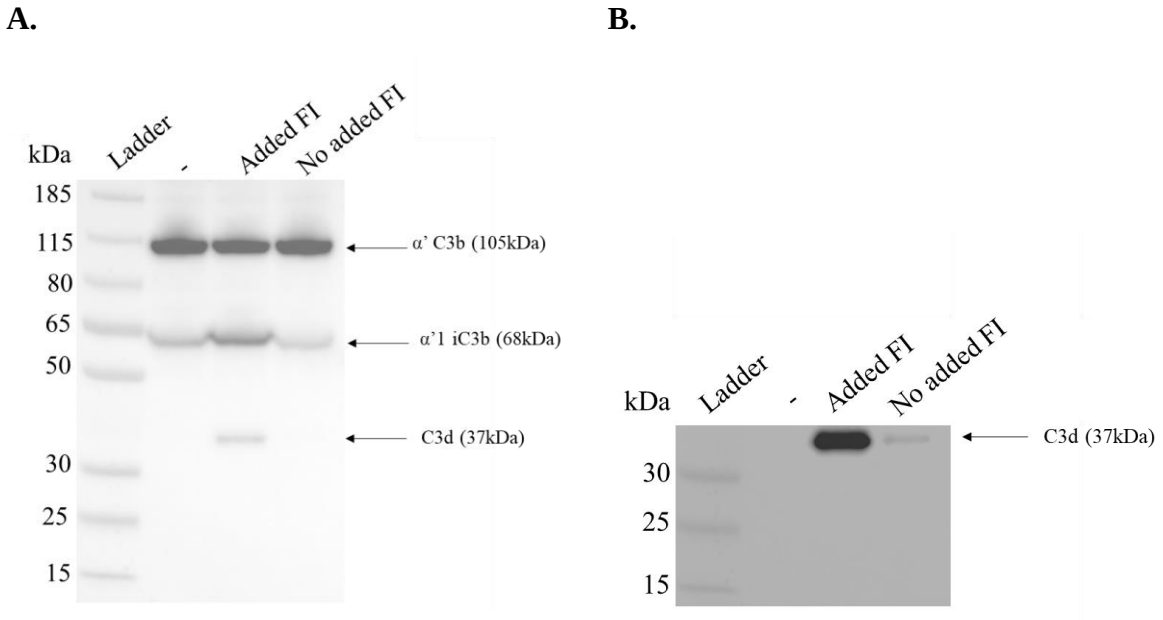

Figure 5- 18.Supernatant from iPSC-RPE cells cultured on Matrigel releases FI. When day 21 supernatant from iPSC-RPE cells cultured on Matrigel were incubated with C3b (1µg) and truncated sCR1 (1.3 µg) with or without added FI (100ng). Breakdown of C3b was detected by the stronger band at C3d (37kDa) with added FI, compared to a fainter band without added FI. The band at 68kDa in the negative control (supernatant, 1µg C3b and 100ng FI) shows the incomplete breakdown of C3b into iC3b as FH in supernatant aids the breakdown from C3b into iC3b but not from iC3b to C3d.

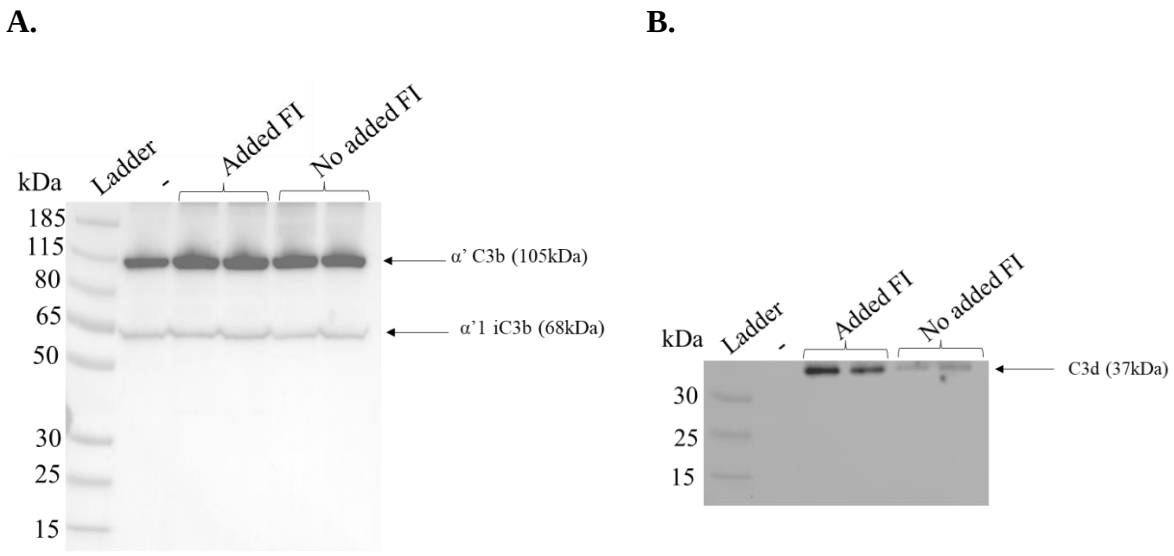

Figure 5- 19. Supernatant from iPSC-RPE cells cultured on dBrM releases FI. When day 21 supernatant from iPSC-RPE cells cultured on dBrM were incubated with C3b (1µg) and truncated sCR1 (1.3 µg) with or without added FI (100ng). Breakdown of C3b was detected by the stronger band at C3d (37kDa) with added FI, compared to a fainter band without added FI. The band at 68kDa in the negative control (supernatant, 1µg C3b and 100ng FI) shows the incomplete breakdown of C3b into iC3b as FH in supernatant aids the breakdown from C3b into iC3b but not from iC3b to C3d.

5.3.10 Breakdown of C3b by truncated sCR1 from iPSC-RPE supernatant at different day points with and without added FI

For the transduction experiment, iPSC-RPE cells cultured on Matrigel (4.50E+10vg/ml) and dBrM in Models 2 (4.88E+10vg/ml) and 7 (4.50E+10vg/ml) were transduced with AAV2 truncated sCR1 on day 21. Supernatants were collected on days 6, 13, and 22 post-transduction and incubated at 37°C for 1 hour with or without added FI (1 µg C3b and 100 ng FI for the FI-added condition; 1 µg C3b for the non-FI condition). For the FI-added condition, the negative control consisted of supernatant with 1 µg C3b and 100 ng FI, while the positive control contained 1 µg C3b, 100 ng FI, and 1.3 µg truncated sCR1. In the non-FI condition, the negative control included supernatant with 1 µg C3b, whereas the positive control contained 1 µg C3b and 1.3 µg truncated sCR1. No additional truncated sCR1 was introduced to the experimental samples, as the objective was to assess C3b breakdown mediated by truncated sCR1 secreted by the transduced cells. As early as day 6, followed by day 13 and 22 post transduction, C3d bands were detected in supernatant from all three models, indicating truncated sCR1 in the supernatant were functional in breakdown C3b, with and without the added FI (**Figure 5- 20**, **Figure 5- 21** and **Figure 5- 22**). The bands for C3d were weaker without added FI compared

with added FI (**Figure 5- 20**, **Figure 5- 21** and **Figure 5- 22**). However, the lanes for added FI and no added FI were on separate blots, making it difficult to compare band intensity. Overall, both conditions—with and without added FI—enabled the inactivation of C3b into iC3b, along with the release of truncated sCR1 at days 6, 13, and 22 post-transduction.

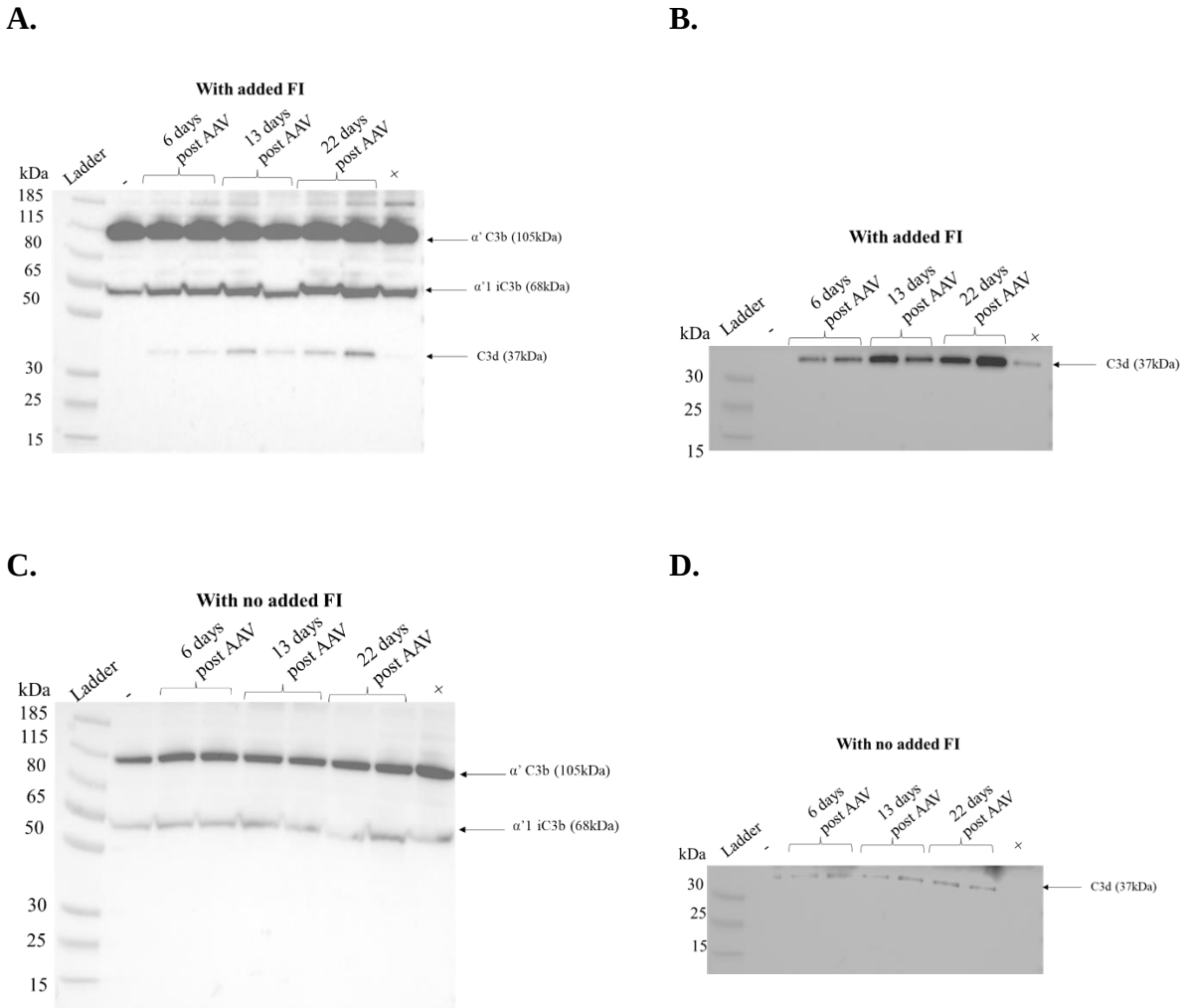

Figure 5- 20. Post transduction supernatant from iPSC-RPE cells cultured on Matrigel releases truncated sCR1. Supernatant collected on days 6, 13, and 22 post-AAV2 truncated sCR1 transduction from iPSC-RPE cells cultured on Matrigel was incubated with C3b (1 µg). **(A-B)** with or **(C-D)** without added FI (100ng). Breakdown of C3b at day 6, 13 and 21 detected by the band at C3d (37kDa) with and without added FI. The band at 68kDa in the negative control (supernatant, 1µg C3b and 100ng FI) shows the incomplete breakdown of C3b into iC3b as FH in supernatant aids the breakdown from C3b into iC3b but not from iC3b to C3d.

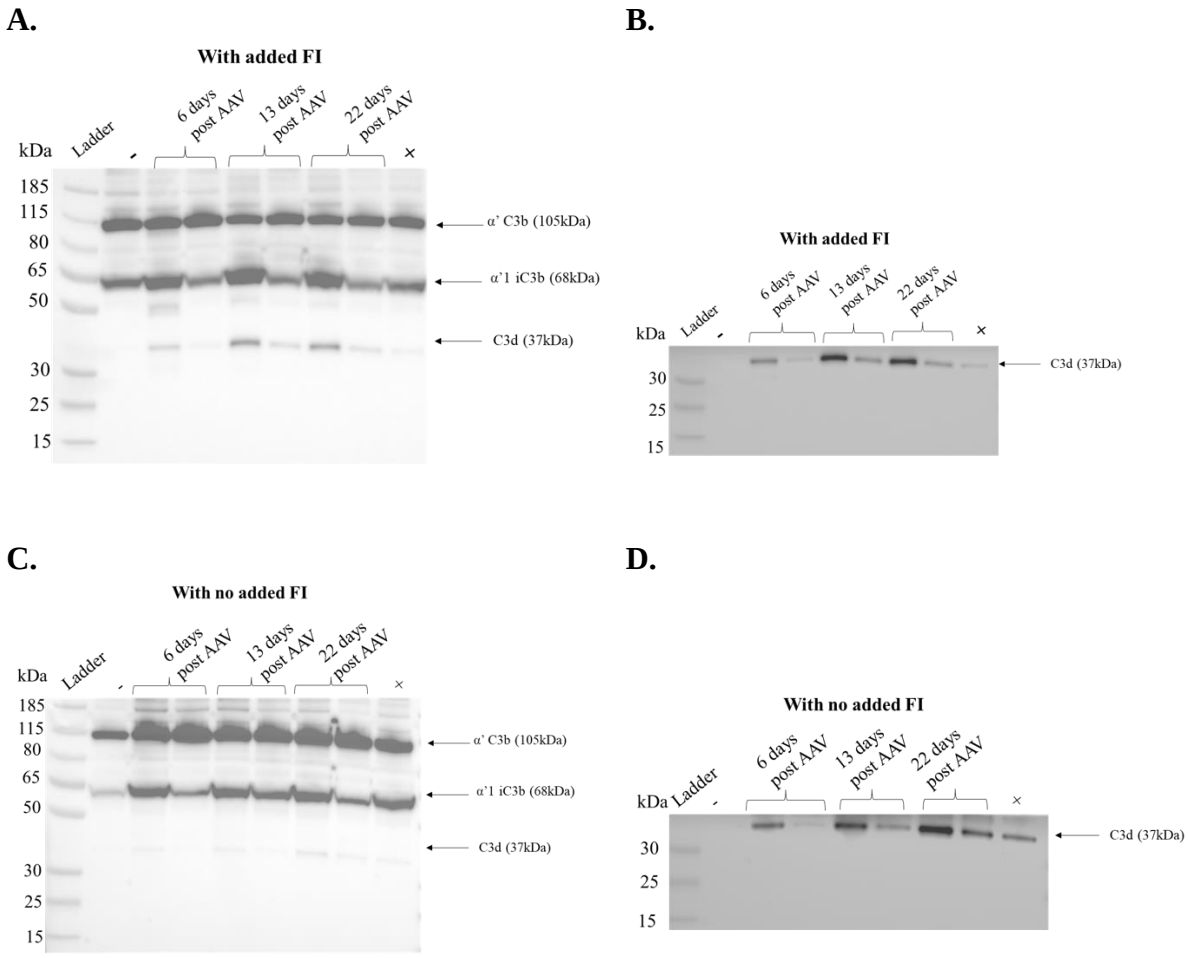

Figure 5- 21. Post transduction supernatant from iPSC-RPE cells cultured on dBrM in model 2 releases truncated sCR1. Supernatant collected on days 6, 13, and 22 post-AAV2 ttruncated sCR1 transduction from iPSC-RPE cells cultured on Matrigel was incubated with C3b (1 µg). **(A-B)** with or **(C-D)** without added FI (100ng). Breakdown of C3b at day 6, 13 and 21 detected by the band at C3d (37kDa) with and without added FI. The band at 68kDa in the negative control (supernatant, 1µg C3b and 100ng FI) shows the incomplete breakdown of C3b into iC3b as FH in supernatant aids the breakdown from C3b into iC3b but not from iC3b to C3d.

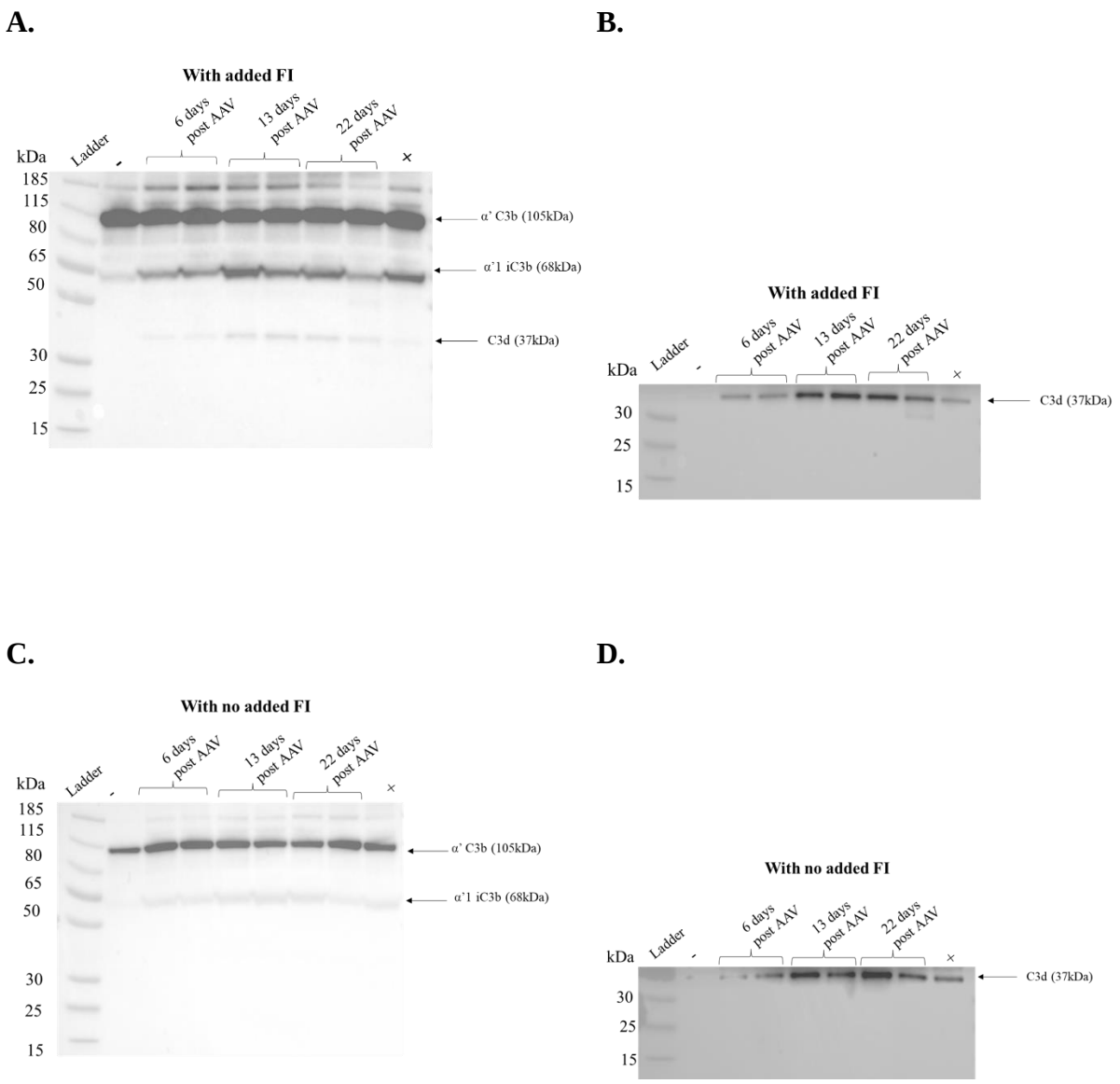

Figure 5- 22. Post transduction supernatant from iPSC-RPE cells cultured on dBrM in model 7 releases truncated sCR1. Supernatant collected on days 6, 13, and 22 post-AAV2 truncated sCR1 transduction from iPSC-RPE cells cultured on Matrigel was incubated with C3b (1 µg). **(A-B)** with or **(C-D)** without added FI (100ng). Breakdown of C3b at day 6, 13 and 21 detected by the band at C3d (37kDa) with and without added FI. The band at 68kDa in the negative control (supernatant, 1µg C3b and 100ng FI) shows the incomplete breakdown of C3b into iC3b as FH in supernatant aids the breakdown from C3b into iC3b but not from iC3b to C3d.

5.3.11 Breakdown of C3b by truncated sCR1 from iPSC-RPE supernatant at day 22 with and without added FI

Since **section 5.3.3** showed that 21 days post-transduction yielded the highest percentage of GFP-positive cells, the breakdown of C3b into C3d at day 22 post-transduction was analysed in supernatants from iPSC-RPE cells cultured on Matrigel and dBrM in model 2 and model 7. Supernatants were incubated with added FI (1 µg C3b and 100 ng FI) and without added FI (1 µg C3b) for 1 hour at 37°C. The negative control contained 1 µg C3b and 100 ng FI, while the positive control was with added FI (1 µg C3b, 100 ng FI, and 1.3 µg truncated sCR1) or without added FI (1 µg C3b and 1.3 µg truncated sCR1). However as opposed to **Section 5.3.10**, these were on the same blots, to visually compare the intensities of the bands with and without added FI. Overall, a consistent trend was observed, with less intense C3d bands detected without added FI compared to those with added FI, indicating that less C3d is detected when no extra FI is added (**Figure 5- 23**).

A. iPSC RPE cells cultured on Matrigel

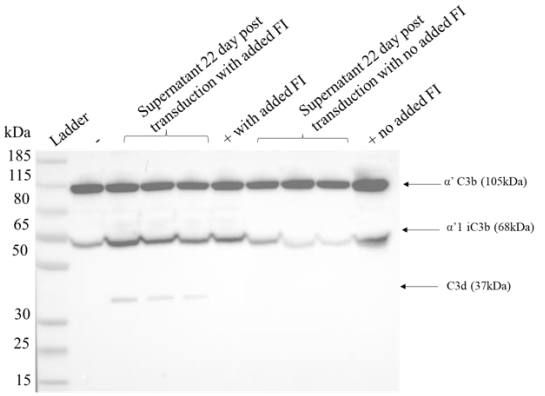

B. iPSC RPE cells cultured on Matrigel

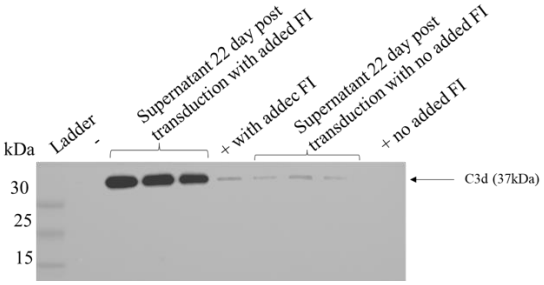

C. iPSC RPE cells cultured on dBrM in Model 2

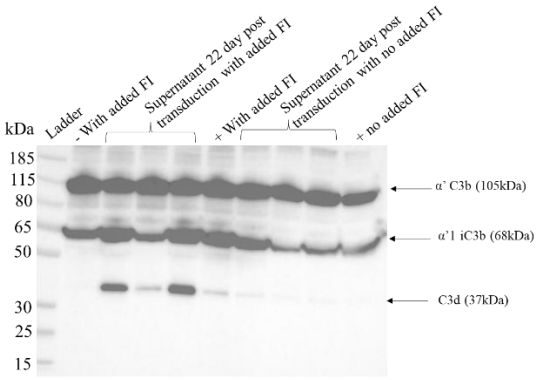

D. iPSC RPE cells cultured on dBrM in Model 2

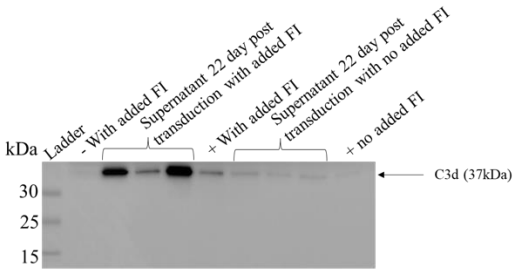

E. iPSC RPE cells cultured on dBrM in Model 7

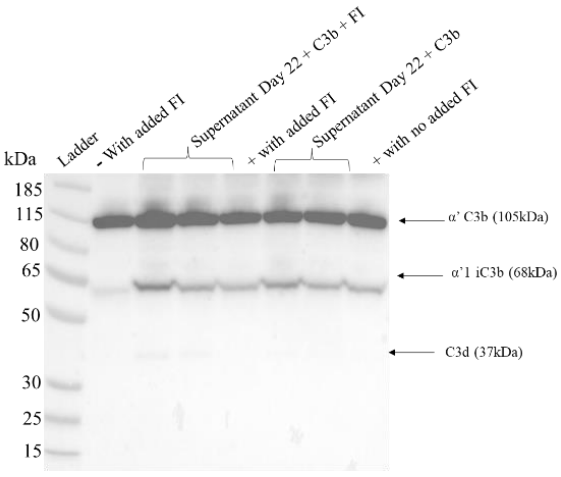

F. iPSC RPE cells cultured on dBrM in Model 7

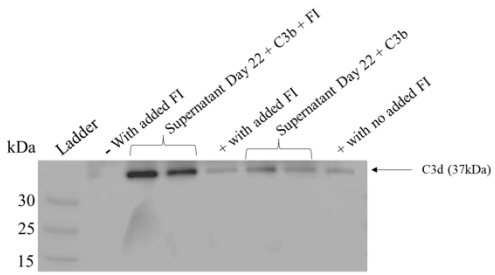

Figure 5- 23. Day 22 post transduction supernatant from iPSC-RPE cells cultured on Matrigel and dBrM in model 2 and 7 releases truncated sCR1. Supernatant collected on day 22 post-AAV2 truncated sCR1 transduction from iPSC-RPE cells cultured on **(A-B)** Matrigel **(C-D)** dBrM in model 2 and **(E-F)** dBrM in model 7 were incubated with C3b (1 µg) with or without added FI (100 ng) on the same blot. The band at 68kDa in the negative control (supernatant, 1µg C3b and 100ng FI) shows the incomplete breakdown of C3b into iC3b as FH in supernatant aids the breakdown from C3b into iC3b but not from iC3b to C3d.

5.3.12 Cytotoxicity and quantified results with AAV2 truncated sCR1 transduction

Cytotoxicity was measured in the supernatant 24 hours and 22 days post-transduction for iPSC-RPE cells cultured on Matrigel and dBrM in Model 2 with AAV2 truncated sCR1. The results were compared to transduction with AAV2 null and within the three conditions. Measurements, presented as mean ± SEM (n = 3), were taken at 24 hours and 21 days post-transduction. The percentage of LDH release, which is an indication of cytotoxicity, revealed no signs if cytotoxicity. Values were ranging from 4% - 0% when transduction was performed with AAV 2 truncated sCR1 or null on iPSC-RPE on Matrigel or dBrM in model 2 (**Figure 5- 24 A-B**). The amount of truncated sCR1 was also measured in the supernatant, with comparisons made between iPSC-RPE cells cultured on Matrigel and those cultured on dBrM in Model 2. At days 6, 17, and 22, no significant differences were observed (**Figure 5- 24 C**). At day 6, iPSC-RPE on Matrigel had 0 µg, and iPSC-RPE on dBrM in Model 2 had 0 µg ($p > 0.999$) (**Figure 5- 24 C**). At day 17, iPSC-RPE on Matrigel had 0.04 ± 0.35 µg, and iPSC-RPE on dBrM in Model 2 had 0.11 ± 0.07 µg ($p = 0.280$) (**Figure 5- 24 C**). At day 22, iPSC-RPE on Matrigel had 0.10 ± 0.02 µg, and iPSC-RPE on dBrM in Model 2 had 0.17 ± 0.04 µg ($p = 0.242$) (**Figure 5- 24 C**). These findings indicate that transduction and culture conditions did not significantly affect cytotoxicity and the secretion of truncated sCR1 increases with time.

A.

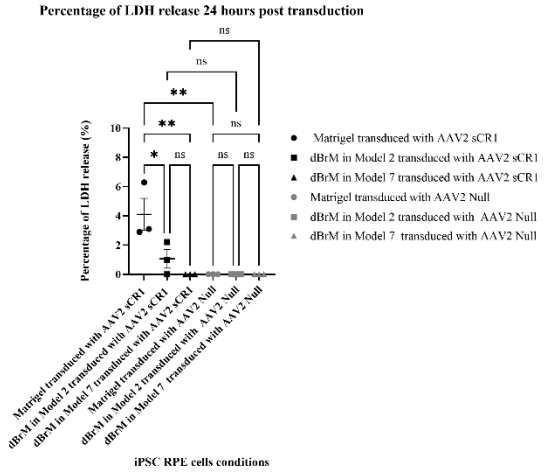

B.

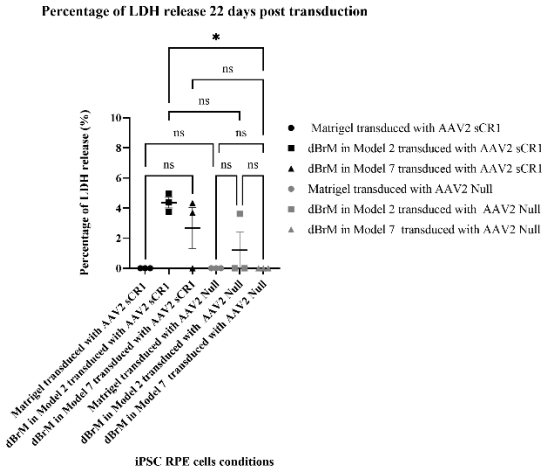

C.

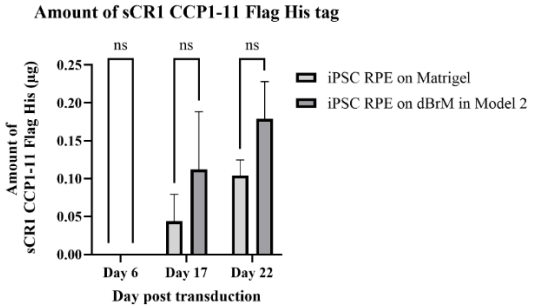

Figure 5- 24. Data for amount of released truncated sCR1 and cytotoxicity assay. The percentage of LDH release **(A)** 24 hours and **(B)** 21 days post transduction with AAV2 truncated sCR1. **(B)** The amount of truncated sCR1 6-, 17 and 22 days post transduction in the supernatant of iPSC-RPE cells cultured on Matrigel and dBrM in model 2. For the LDH statistical analysis, one-way ANOVA with Sidaks multiple comparison test were performed to determine significance while for the amount of truncated sCR1 analysis, two way ANOVA was performed. Significance was determined with $P < 0.05$. * = 0.01, ** = 0.001. n = 3.

5.4 Discussion

This chapter primarily focuses on optimising the delivery of AAV2 and AAV8-GFP to iPSC-RPE on Matrigel, as well as AAV2 GFP and AAV2 truncated sCR1 to iPSC-RPE on dBrM in Model 2 and 7. The optimisations include refining the timing of delivery, MOI, AAV concentration, and assessing transduction efficiency at various time points. These optimisations are essential for identifying the most effective methods for treating these cells. Understanding these parameters will not only improve gene delivery strategies, but also provide valuable insights into how different surfaces influence transduction efficiency, ultimately aiding in the development of more effective gene therapies for retinal diseases.

The initial transduction optimisation experiments with AAV2 or 8 GFP transduction were performed on iPSC-RPE cells cultured on Matrigel. We compared AAV2 and AAV8 across five different MOIs and demonstrated that at the highest MOI (1,000,000 MOI), AAV2 was more effective than AAV8. This was particularly evident when transduction was performed on day 23 instead of day 3 with measurement of transduction efficiency 21 days post-transduction. Additionally, these results indicated a lower cytotoxic effect when transduction was performed on day 23 compared to day 3. This may be because at day 3, iPSC-RPE cells were still proliferating, and the addition of AAV could potentially damage cell membrane formation. By day 23, as the iPSC-RPE cells matured and formed tight junctions, they were less vulnerable to cytotoxic effects. As with any gene therapy aiming for clinical trials, it is crucial that the AAV can transduce mature iPSC-RPE cells. Previous studies also align with our results, where AAVs were added to mature cells with varying optimal MOI from 6,000 to 500,000,000 MOI (Cereso et al., 2014; Gonzalez-Cordero et al., 2018; Brydon et al., 2019; Garita-Hernandez et al., 2020).

When investigating transduction efficiency, we did not observe any differences with or without FBS. However, previous studies have shown contradictory results, with some indicating that the presence of FBS during transduction had a negligible effect on transduction efficiency (Rambhai et al., 2020; Rogers et al., 2021; Wang et al., 2016) or enhanced efficiency (Wang et al., 2017). We performed all the experiments with FBS in the media (MEM), to maximise the viability of the iPSC-RPE cells.

Once it was established that AAV2 showed the highest efficiency, we aimed to further optimise transduction while reducing AAV usage to lower costs. This was achieved by reducing the

MOI, increasing viral concentration, and decreasing the apical volume during culture. Looking at the day 23 transduction on iPSC-RPE on Matrigel using AAV2 GFP, as the AAV concentration was higher, the transduction efficiency increased from 68% at 1,000,000 MOI (9.0E+10vg/ml) to 82% at 500,000 MOI (2.25E+11 vg/ml). This shows that despite the lower MOI, the higher AAV concentration enhanced transduction efficiency by at least 14%. Our results are consistent with previous transduction experiments on iPSC-RPE cells, where efficiencies of 12-60% have been found based on different AAV stereotypes, with AAV2 having the highest transfection efficiency for RPE cells (Brydon et al., 2019; Cereso et al., 2014; Gonzalez-Cordero et al., 2018; Garita-Hernandez et al., 2020).

Once the transduction of iPSC-RPE cells grown on Matrigel was optimised, we transduced iPSC-RPE on dBrM in Model 2 on day 23 at an MOI of 500,000 with a concentration of 1.56E+11 vg/ml, yielding 56% GFP-positive cells. However, this percentage was lower than the 82% observed when transducing iPSC-RPE on Matrigel at a similar MOI and a concentration of 2.25E+11 vg/ml. This discrepancy may be attributed to the higher AAV concentration in iPSC-RPE cells on Matrigel compared to iPSC-RPE on dBrM in Model 2. However, transduction on iPSC-RPE on dBrM likely represents the native state more faithfully.

The key experiment in this chapter involved the transduction of AAV2 truncated sCR1 into iPSC-RPE in dBrM in model 2 and model 7. These were compared to iPSC-RPE grown on Matrigel, representing the standard culture conditions. Transduction was performed on day 23, and the supernatant was measured at 6, 13, and 22 days post-transduction for the ability of C3b to break down into iC3b with and without added FI as RPE cells release FI (Hallam et al., 2017; Luo et al., 2013). This shows the functionality of released truncated sCR1 from iPSC-RPE cell. We consistently demonstrate, as early as day 6, that transduced iPSC-RPE cells on dBrM in model 2 or 7 release functional truncated sCR1, and the breakdown of C3b to iC3b was successful with or without added FI. However, we found that the intensity of the iC3b band (37kDa) increased with added FI compared to samples without added FI, where the bands appeared less intense. This suggest that the amount of FI can be rate limiting for the reaction.

As stated previously, a similar study utilising CTx001, which consisted of mini-CR1, showed that MAC formation following laser-induced CNV in murine eyes was reduced by 65% and 69% relative to the null vector at 5.00E+8 and 5.00E+9 vg/eye (Keefe D et al., 2023). Their study showed that the mini-CR1 functions similarly to truncated sCR1 by regulating

complement activation, however, no information has been made publicly available regarding the size or structure of mini-CR1, preventing direct comparison with truncated sCR1.

A limitation of our study was that the bands were not quantifiable, as there were no reference bands, such as the β chain band at 75 kDa, which would have allowed for normalisation to the negative control and semi-quantification. The FLAG ELISA did permit quantitative results on the supernatant from treated iPSC-RPE on dBrM in model 2, compared to the supernatant from treated iPSC-RPE on Matrigel. This showed an increase from day 6 to day 22 post-transduction.

The delivery of AAV2 truncated sCR1 has not yet been tested on disease models, but this would be an interesting next step. The AAV carried the complement protein with Flag His tag to allow for easy detection of the secreted complement protein. However, the delivery of truncated sCR1 should be analysed without the Flag His tag, as the final delivery should not contain any unwanted protein constructs. This would mean that an ELISA specific to truncated sCR1 would need to be developed, which would require optimisation to ensure specificity.

Overall, this chapter demonstrates the successful transduction of iPSC-RPE cells on dBrM with AAV2 GFP or truncated sCR1. Optimal conditions were explored, and functionally active expression of CR1 was demonstrated in preparation for future studies using representative disease models of outer retinal disease and in particular AMD.

Chapter 6 General discussion and future work

AMD is estimated to affect 1 in 8 people 60 years of age or older with a rising prevalence as the population ages (Vyawahare & Shinde, 2022). It is predicted that by the year 2040, 300 million people worldwide will develop AMD (Wong et al., 2014). Both the late stages of the disease, wet and dry AMD lead to irreversible blindness. The current therapy approach, anti-VEGF for wet AMD and pegcetacoplan and avacinacaptad pegol for dry AMD slow down the progression of the disease. This leads to a gap in developing a therapeutic target to stop the progression and reverse the disease.

In order to allow the development of effective therapy, a suitable experimental model must be available. Animal models, such as rodents (mice and rats) and non-human primates (mainly macaques) have been used to evaluate potential therapies for AMD (Pennesi et al., 2012). Rodent models allow disease progression in a short time scale and offer the ability to easily perform genetic manipulation. However, they do not faithfully mimic the disease as they lack the anatomical macula. On the other hand, non-human primates offer the closest anatomy to humans as they have a macula but remain costly and harder to manipulate genetically (Pennesi et al., 2012). Instead, the use of human iPSC-RPE cells on BrM mimics have been shown to be suitable to model the outer retina as they mimic mature RPE characteristics (Cai et al., 2018; Manian et al., 2021; Song et al., 2023), can be made patient specific (Cerniauskas et al., 2020; Hallam et al., 2017) and are able to mimic the hallmarks of the disease (Manian et al., 2021).

The retina has been thought to be the ideal target for gene therapy as it is immune privileged and protected from the systemic circulation by the blood-retina barrier (Ladha et al., 2022). AAVs, especially AAV2, are thought to have high transduction rates in the retina, allowing observable therapeutic effects (Cereso et al., 2014; Gonzalez-Cordero et al., 2018; Brydon et al., 2019; Garita-Hernandez et al., 2020). After the success of the subretinal delivery of Luxturna, the first approved gene therapy in the retina, it paves the way for the future direction of the use of gene therapy in the retina (Novartis Pharmaceuticals Canada Inc., 2021). This has allowed the investigation of many gene therapies to treat AMD, including RGX-314 which uses a AAV8 vector to express an anti-VEGF-A antigen binding fragment to treat wet AMD (AbbVie, 2025, 2024a; Campochiaro et al., 2024).

The complement system is crucial in the body's defence against pathogens. Complement overactivation in AMD results in inflammation, exacerbating the disease's pathogenesis. Hence, targeting complement has been a direction of high interest in AMD gene therapy approaches (NGM Biopharmaceuticals, 2020, 2023; Innovent Biologics (Suzhou) Co. Ltd., 2024; Innovent Biologics (Suzhou) Co. Ltd, 2024, 2025; Innovent Biologics (Suzhou) Co. Ltd., 2021; Philip J. Rosenfeld, 2017; Novartis Pharmaceuticals, 2021; Annexon, 2024; Novartis Pharmaceuticals, 2024; Ionis Pharmaceuticals, 2025; Hoffmann-La Roche, 2019a, 2019b; Alexion Pharmaceuticals, 2025; Alcon Research, 2019; Gyroscope Therapeutics, 2024a, 2024b; Perceive Biotherapeutics, 2024; Gemini Therapeutics, 2021; Janssen Research & Development, 2025; L. Janssen Research & Development, 2025b). It is crucial to understand how early or late in the complement pathway should be optimally targeted. Agents acting on C3 could lead to a complete loss in complement activity while targeting C5 allows the inhibition of MAC. It is important to also understand the need for a degree of complement activation, and that the removal of complement activity completely may worsen the pathogenesis of AMD. Trials that attempted to modulate complement overactivation by over expression of FI, were terminated early due to lack of effect and it was hypothesied that they resulted in insufficient complement inhibition as compared to C3 blockade (Hallam et al., 2024a). However, studies have not investigated the delivery of more than one complement protein. For instance, delivering FI with a co-factor such as FH or CR1 could potentially show more effective complement inhibition.

This thesis highlights the gap in the research, where we successfully modelled the outer retina by utilising iPSC-RPE cells cultured on dBrM, with its unique properties in a two-chamber system and observed the transduction of these iPSC-RPE cells with the delivery of AAV2 truncated sCR1. In our model, iPSC-RPE cells successfully grew and proliferated on dBrM, with the morphology, proteomic markers, phagocytosis function, VEGF and PEDF secretion in keeping with adult human RPE. This is novel, as no study has shown successful culture of iPSC-RPE cells on dBrM. Besides that, iPSC-RPE in our model was successfully transduced with AAV2 truncated sCR1, with the release of functional truncated sCR1 that was able to inactivate C3b, with and without the addition of FI. The breakdown of C3b highlights success in complement control, which is key in targeting AMD.

The future direction of this research is in disease modelling as opposed to healthy outer retinal modelling. This could be performed by culturing disease patient specific iPSC-RPE cells lines

on dBrM in our model which have previously been conducted on Matrigel coated substrates (Cerniauskas et al., 2020; Hallam et al., 2017). The disease model could then be treated with AAV2 truncated sCR1 to observe if the disease phenotype could be reversed, with control of complement activation and reversal of thecellular morphology.

Another approach could be the delivery of truncated sCR1 in addition to FI, as used in the GT005 trials. As we showed in our results, C3b inactivation is enhanced with added FI, suggesting its rate-limiting nature and the GT005 study showed that FI alone did not lead to disease inhibition. The studies using GT005 showed the delivery of FI subretinally increased FI by two-fold, however it was not enough to increase iC3b, indicating the complement breakdown was limited (Hallam et al., 2024b). We could potentially look at dual supplementation, as some AMD patients with factor I rare variants have been reported as having low FI (Hallam et al., 2020), so supplementation with GT005 and AAV2 truncated sCR1, as we have shown to be functional, could potentially increase the breakdown product, iC3b. However, we should take into consideration if the delivery of two gene therapy simultaneously or one bicistronic vector carrying two genes would be better, as the latter has shown to be more effective (Moradian et al., 2022). Additionally, as we have shown that truncated sCR1 does not diffuse through dBrM, subretinal delivery will be the appropriate administration route to ensure successful transduction of RPE cells. If an alternative delivery route is considered, using a version of truncated sCR1 with fewer CCP domains may help reduce its size and facilitate diffusion through BrM.

A recent study by Gyroscope therapeutics, a Novartis company developed an AAV8 bicistronic gene therapy vector co-expressing aflibercept and FHL-1 (Tam et al., 2024). They performed the subretinal delivery of this vector into mouse models and the co-expression was detected up to 4 weeks after delivery (Tam et al., 2024). In the mouse with laser induced CNV, the delivery of this bicistronic vector significantly reduce CNV leakage and lesion (Tam et al., 2024). However, the development of bicistronic AAV comes with some challenges due to the limited packaging capacity of AAVs (< 5kb), making the expression of two genes difficult (Hutson et al., 2014).

Additionally, a more precise approach to modelling the diseased outer retina would involve culturing patient-derived iPSC-RPE cells onto the macular region of dBrM, as this has not yet been demonstrated. However, this will come with a challenge to ensure no tear of the macula

occurs during dissection, which will require gentle removal from the sclera. It would also be valuable to examine the growth rate and behaviour of iPSC-RPE cells on older (> 70 years old) versus younger (< 70 years old) dBrM to better understand age-related changes and their impact on cell culture. As stated previously, the findings by M Zarbin *et al* showed some challenges when culturing RPE cells on aged BrM, due to the surface which could be due to the lack of ECM proteins or the expression of age-related proteins such as tenascin-C ,which has been shown to inhibit adhesion of RPE cells *in vitro* (Gullapalli et al., 2005; Tsukahara et al., 2002; Sugino et al., 2011; Kobayashi et al., 2016)

Exploring different cell culture methods, cell lines, and experimental approaches could provide further insights regarding the culture of EC on the dBrM. For example, Chirco K *et al* study showed EC migration, suggesting that modifying dBrM culture conditions might enhance this process (Chirco et al., 2017). One potential approach could involve allowing EC migration before introducing a two-chamber system to culture iPSC-RPE cells. Alternatively, Song M *et al* work explored the addition of and co-culture with fibroblasts, which could be another avenue worth investigating (Song et al., 2023).

Our study investigated a process mimicking subretinal delivery of AAV2 truncated sCR1, with success in transducing iPSC-RPE cells to release functional sCR1. However, we showed that truncated sCR1 does not diffuse efficiently. Hence, exploring delivery via the choroidal side (mimicking suprachoroidal delivery) and observing if AAV2 could either cross BrM and transduce RPE or transduce CEC (in a future model containing these cells) with prolonged CR1 expression would be of interest.

Overall, the results obtained through this research provides valuable insight into having an outer retina model, that closely resembles the native state. The success in the culture of iPSC-RPE on dBrM allow further research to explore methods on culturing EC on the choroidal side, to complete and improve the model. The success in transducing iPSC-RPE cells on dBrM, provides novel information, which will pave the way for the future of gene therapy deliveries in the outer retina. Ultimately, the research performed provides the basis for a novel biomimetic laboratory model of the outer retina to allow the investigation of disease pathogenesis and experimental therapies.

Appendices

Appendix A: Supplementary results

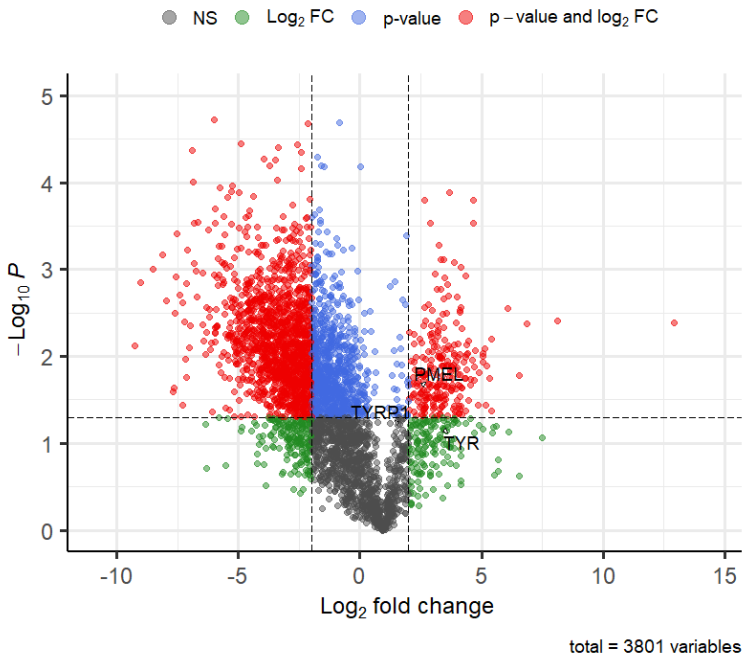

Supplementary figure- 1. Proteomic analysis of melanosome protein marker. Showing melanosome protein marker retention in dBrM via CP when compared to native BrM.

Z score iPSC-RPE cells on Matrigel coated dBrM/ Native BrM	Z score iPSC-RPE cells on dBrM / Native BrM	Z score iPSC-RPE cells on Matrigel coated dBrM/ dBrM	Z score iPSC-RPE cells on dBrM / dBrM	P value (iPSC-RPE cells on Matrigel coated dBrM/ Native BrM)	P value (iPSC-RPE cells on dBrM / Native BrM)	P value (iPSC-RPE cells on Matrigel coated dBrM/ dBrM)	P value (iPSC-RPE cells on dBrM/ dBrM)	Accession	PG Genes	Description
0.350	0.182	5.218	5.094	0.795	0.874	0.063	0.054	Q9P2E9	RRBP1	Ribosome-binding protein 1
2.468	-0.072	1.732	-0.764	0.159	0.911	0.104	0.973	P40126	DCT	L-dopachrome tautomerase
0.367	-0.953	0.370	-0.906	0.720	0.326	0.316	0.889	P41222	PTGDS	Prostaglandin-H2 D-isomerase
1.297	0.115	3.560	2.422	0.217	0.972	0.021	0.107	Q13822	ENPP2	Ectonucleotide pyrophosphatase/phosphodiesterase family member 2
4.690	3.720	2.188	1.262	0.067	0.001	0.073	0.039	P40967	PMEL	Melanocyte protein PMEL
-2.538	-3.357	-0.845	-1.619	0.026	0.191	0.963	0.066	P02766	TTR	Transthyretin
3.201	0.605	1.185	-1.367	0.106	0.648	0.131	0.624	P17643	TYRP1	5,6-dihydroxyindole-2-carboxylic acid oxidase
-0.116	0.594	3.898	4.653	0.300	0.602	0.158	0.035	Q9UBP9	GULP1	PTB domain-containing engulfment adapter protein 1
0.208	0.163	2.021	2.020	0.894	0.104	0.069	0.036	P36955	SERPINF1	Pigment epithelium-derived factor
0.313	-0.460	5.175	4.447	0.807	0.454	0.115	0.135	P23229	ITGA6	Integrin alpha-6
0.354	0.061	5.511	5.263	0.899	0.996	0.018	0.022	P16144	ITGB4	Integrin beta-4
-0.647	-0.446	6.547	6.792	0.225	0.279	0.039	0.031	P05556	ITGB1	Integrin beta-1
-1.140	-0.868	1.894	2.211	0.252	0.666	0.130	0.309	P08648	ITGA5	Integrin alpha-5

Supplementary table- 1. The PG genes of interest. The PG genes involved in the visual cycle (RBP1, DCT), lipid biosynthesis (PTGDS), melanin biosynthesis (ENPP2, PMEL, TTR, TYRP1), phagocytosis (GULP1), secretion (SERPINF1), and adhesion (ITGA6, ITGB4, ITGB1, ITGA5).

Num	Z score iPSC-RPE cells on Matrigel coated dBrM/ Native BrM	P value (iPSC-RPE cells on Matrigel coated dBrM/ Native BrM	Accession	PG Genes	Description
1	7.399	0.00085	A6NHL2;P68366;Q9BQE3	TUBA1C;TUBA4A;TUBAL3	Tubulin alpha chain-like 3
2	3.00	0.0010	O95319	CELF2	CUGBP Elav-like family member 2
3	7.323	0.0016	Q8TAV3	CYP2W1	Cytochrome P450 2W1
4	2.757	0.0017	A0A0B4J2H0;P01742;P01743	IGHV1-46;IGHV1-69;IGHV1-69D	Immunoglobulin heavy variable 1-69D
5	3.407	0.0026	P50453	SERPINB9	Serpin B9
6	2.760	0.0029	Q86T65	DAAM2	Disheveled-associated activator of morphogenesis 2
7	2.398	0.0030	Q15397	PUM3	Pumilio homolog 3
8	3.427	0.0031	P04350;P07437;P68371;Q13885;Q9BVA1	TUBB;TUBB2A;TUBB2B;TUBB4A;TUBB4B	Tubulin beta-4A chain
9	7.487	0.0033	O00425;Q9NZI8;Q9Y6M1	IGF2BP1;IGF2BP2;IGF2BP3	Insulin-like growth factor 2 mRNA-binding protein 3
10	2.771	0.0037	P09544	WNT2	Protein Wnt-2
11	2.702	0.0041	P48509	CD151	CD151 antigen
12	5.382	0.0042	Q03591;Q9BXR6	CFHR1;CFHR5	Complement factor H-related protein 1

13	4.863	0.0044	Q9NRP0	OSTC	Oligosaccharyltransferase complex subunit OSTC
14	6.011	0.0045	A8MV23	SERPINE3	Serpin E3
15	2.940	0.0049	Q01955	COL4A3	Collagen alpha-3(IV) chain
16	4.332	0.0050	Q5T4F7	SFRP5	Secreted frizzled-related protein 5
17	2.088	0.0054	Q9H2V7	SPNS1	Protein spinster homolog 1
18	2.683	0.0058	Q9Y2Y8	PRG3	Proteoglycan 3
19	10.425	0.0059	Q9H336	CRISPLD1	Cysteine-rich secretory protein LCCL domain-containing 1
20	8.370	0.0065	P08729	KRT7	Keratin, type II cytoskeletal 7
21	3.033	0.0068	P15586	GNS	N-acetylglucosamine-6-sulfatase
22	2.760	0.0068	P15692	VEGFA	Vascular endothelial growth factor A, long form
23	4.857	0.0069	P00338;P07195	LDHA;LDHB	L-lactate dehydrogenase A chain
24	2.332	0.0069	A0A3B3IRU6;M0QZD4	PEG3	Paternally expressed 3
25	3.048	0.0074	P08729;P19013	KRT4;KRT7	Keratin, type II cytoskeletal 7
26	5.699	0.0074	P23443;Q9UBS0	RPS6KB1;RPS6KB2	Ribosomal protein S6 kinase beta-1
27	2.658	0.0076	P51688	SGSH	N-sulphoglucosamine sulphohydrolase
28	4.039	0.0084	O00425;Q9NZI8	IGF2BP1;IGF2BP3	Insulin-like growth factor 2 mRNA-binding protein 3
29	2.991	0.0084	P35052	GPC1	Glypican-1

30	6.250	0.0087	P04899;P08754;P63096	GNAI1;GNAI2;GNAI3	Guanine nucleotide-binding protein G(i) subunit alpha-2
31	3.048	0.0090	Q14520	HABP2	Hyaluronan-binding protein 2
32	8.333	0.0091	P15153;P60763;P60953;P63000;P84095	CDC42;RAC1;RAC2;RAC3;RHOG	Ras-related C3 botulinum toxin substrate 2
33	4.614	0.0091	P02788	LTF	Lactotransferrin
34	6.221	0.0091	Q9BQB6	VKORC1	Vitamin K epoxide reductase complex subunit 1
35	4.326	0.010	O76076	CCN5	CCN family member 5
36	3.301	0.010	Q9BXY4	RSPO3	R-spondin-3
37	4.268	0.010	O95989;Q9NZJ9	NUDT3;NUDT4	Diphosphoinositol polyphosphate phosphohydrolase 1
38	2.279	0.010	Q5XUX1	FBXW9	F-box/WD repeat-containing protein 9
39	3.209	0.011	Q8TBR7	TLCD3A	TLC domain-containing protein 3A
40	2.876	0.011	Q6ZMG9	CERS6	Ceramide synthase 6
41	3.561	0.011	O00462	MANBA	Beta-mannosidase
42	2.434	0.011	Q16890	TPD52L1	Tumor protein D53
43	4.204	0.013	O00754	MAN2B1	Lysosomal alpha-mannosidase
44	5.3780	0.013	P03973	SLPI	Antileukoproteinase
45	3.855	0.013	P22090	RPS4Y1	Small ribosomal subunit protein eS4, Y isoform 1
46	3.833	0.013	X5CMH5	TAP2	ABC-type antigen peptide transporter
47	5.134	0.014	P29972	AQP1	Aquaporin-1

48	2.402	0.014	P10915	HAPLN1	Hyaluronan and proteoglycan link protein 1
49	3.700	0.014	P08727	KRT19	Keratin, type I cytoskeletal 19
50	6.548	0.015	O75531	BANF1	Barrier-to-autointegration factor

Supplementary table- 2. **PG genes significantly overexpressed in iPSC-RPE on Matrigel coated dBrM compared to native.** In order of the most significant based on p value, smallest to largest. Within Z score > 2.

Num	Z score iPSC-RPE cells on Matrigel coated dBrM/ Native BrM	P value(iPSC-RPE cells on Matrigel coated dBrM/ Native BrM)	Accession	PG Genes	Description
1	-7.903	0.00022	P04216	THY1	Thy-1 membrane glycoprotein
2	-4.068	0.00025	Q9Y4K1	CRYBG1	Beta/gamma crystallin domain-containing protein 1
3	-2.190	0.00051	Q9Y2I8	WDR37	WD repeat-containing protein 37
4	-2.104	0.00091	Q9P0J0	NDUFA13	NADH dehydrogenase [ubiquinone] 1 alpha subcomplex subunit 13
5	-2.832	0.00098	P04424	ASL	Argininosuccinate lyase
6	-2.858	0.00152	Q9H223;Q9NZN3;Q9NZN4	EHD2;EHD3;EHD4	EH domain-containing protein 4
7	-3.833	0.00169	P06213	INSR	Insulin receptor
8	-3.518	0.00194	F8WE43;F8WF23	SYNPR	Synaptoporin
9	-2.094	0.00211	P55290	CDH13	Cadherin-13
10	-4.641	0.00222	Q15599	NHERF2	Na(+)/H(+) exchange regulatory cofactor NHE-RF2
11	-6.959	0.00308	Q9ULC5	ACSL5	Long-chain-fatty-acid--CoA ligase 5
12	-3.686	0.00311	P37235	HPCAL1	Hippocalcin-like protein 1
13	-3.574	0.00327	P49593	PPM1F	Protein phosphatase 1F
14	-6.322	0.00332	P78363	ABCA4	Retinal-specific phospholipid-transporting ATPase ABCA4
15	-2.527	0.00336	Q9Y6M9	NDUFB9	NADH dehydrogenase [ubiquinone] 1 beta subcomplex subunit 9
16	-5.308	0.00344	Q9Y2D0	CA5B	Carbonic anhydrase 5B, mitochondrial
17	-2.397	0.00368	P01834	IGKC	Immunoglobulin kappa constant

18	-3.704	0.0036	P07196	NEFL	Neurofilament light polypeptide
19	-5.756	0.00428	Q687X5	STEAP4	Metalloreductase STEAP4
20	-2.912	0.00429	P46527	CDKN1B	Cyclin-dependent kinase inhibitor 1B
21	-3.675	0.00457	Q5NDL2	EOGT	EGF domain-specific O-linked N-acetylglucosamine transferase
22	-3.531	0.00467	Q8TBG9	SYNPR	Synaptoporin
23	-2.362	0.00526	O60478	GPR137B	Integral membrane protein GPR137B
24	-5.984	0.00529	P52566	ARHGDIB	Rho GDP-dissociation inhibitor 2
25	-4.387	0.00557	Q9BW30	TPPP3	Tubulin polymerization-promoting protein family member 3
26	-3.851	0.00579	P03923	MT-ND6	NADH-ubiquinone oxidoreductase chain 6
27	-2.808	0.00620	Q9UBW8	COPS7A	COP9 signalosome complex subunit 7a
28	-3.001	0.00623	Q8N8L6	ARL10	ADP-ribosylation factor-like protein 10
29	-2.630	0.00645	Q9NP92	MRPS30	Large ribosomal subunit protein mL65
30	-5.219	0.00652	O95810	CAVIN2	Caveolae-associated protein 2
31	-2.337	0.00665	P12277	CKB	Creatine kinase B-type
32	-4.500	0.00696	P23470	PTPRG	Receptor-type tyrosine-protein phosphatase gamma
33	-2.687	0.00771	P61018	RAB4B	Ras-related protein Rab-4B
34	-2.126	0.00795	P05771;P17252	PRKCA;PRKCB	Protein kinase C beta type
35	-2.442	0.00801	F8WD96	CTSD	Cathepsin D
36	-2.915	0.00809	Q9C0D6	FHDC1	FH2 domain-containing protein 1
37	-3.293	0.00839	Q9NS86	LANCL2	LanC-like protein 2
38	-4.704	0.00852	P48681	NES	Nestin

39	-3.220	0.00921	P35443	THBS4	Thrombospondin-4
40	-2.792	0.00932	P55789	GFER	FAD-linked sulfhydryl oxidase ALR
41	-8.648	0.00947	P15090	FABP4	Fatty acid-binding protein, adipocyte
42	-5.640	0.00966	P16452	EPB42	Protein 4.2
43	-2.671	0.00972	P13716	ALAD	Delta-aminolevulinic acid dehydratase
44	-3.321	0.00979	P25686	DNAJB2	DnaJ homolog subfamily B member 2
45	-2.653	0.0109	Q8TD55	PLEKHO2	Pleckstrin homology domain-containing family O member 2
46	-2.298	0.0109	O43676	NDUFB3	NADH dehydrogenase [ubiquinone] 1 beta subcomplex subunit 3
47	-4.603	0.0112	Q9BX66	SORBS1	Sorbin and SH3 domain-containing protein 1
48	-4.006	0.0112	O14558	HSPB6	Heat shock protein beta-6
49	-4.055	0.0115	Q9UKV8	AGO2	Protein argonaute-2
50	-4.670	0.0116	Q13432	UNC119	Protein unc-119 homolog A

Supplementary table- 3. PG genes significantly underexpressed in iPSC-RPE on Matrigel coated dBrM compared to native BrM. In order of the most significant based on p-value, smallest to largest. Within Z score > 2.

Num	Z score iPSC-RPE cells on Matrigel coated dBrM/ dBrM	P value (iPSC-RPE cells on Matrigel coated dBrM/ dBrM)	Accession	PG Genes	Description
1	3.890	1.23E-05	O43657	TSPAN6	Tetraspanin-6
2	4.795	7.54E-05	O00754	MAN2B1	Lysosomal alpha-mannosidase
3	5.585	0.000131	Q92945;Q96AE4	FUBP1;KHSRP	Far upstream element-binding protein 2
4	5.646	0.000159	F8WCM5;P01308	INS;INS-IGF2	Insulin, isoform 2
5	4.964	0.000210	P07686	HEXB	Beta-hexosaminidase subunit beta
6	3.192	0.000302	P49321	NASP	Nuclear autoantigenic sperm protein
7	3.495	0.000394	P04792	HSPB1	Heat shock protein beta-1
8	2.519	0.000400	P56192	MARS1	Methionine--tRNA ligase, cytoplasmic
9	2.982	0.000501	Q9BVG9	PTDSS2	Phosphatidylserine synthase 2
10	5.569	0.000527	O94788;P47895	ALDH1A2;ALDH1A3	Retinal dehydrogenase 2
11	5.015	0.000553	O95758;P26599	PTBP1;PTBP3	Polypyrimidine tract-binding protein 3
12	4.604	0.000577	P30533	LRPAP1	Alpha-2-macroglobulin receptor-associated protein
13	6.229	0.000578	Q9BR76	CORO1B	Coronin-1B
14	4.901	0.000645	O43488	AKR7A2	Aflatoxin B1 aldehyde reductase member 2
15	2.809	0.000670	Q70J99	UNC13D	Protein unc-13 homolog D
16	4.291	0.000693	Q9NZ01	TECR	Very-long-chain enoyl-CoA reductase

17	2.974	0.000709	Q5T6V5	QNG1	Queuosine 5'-phosphate N-glycosylase/hydrolase
18	2.104	0.000797	Q9Y237	PIN4	Peptidyl-prolyl cis-trans isomerase NIMA-interacting 4
19	3.691	0.000889	P51790	CLCN3	H(+)/Cl(-) exchange transporter 3
20	5.352	0.000936	P53985	SLC16A1	Monocarboxylate transporter 1
21	5.846	0.000973	P60842	EIF4A1	Eukaryotic initiation factor 4A-I
22	4.643	0.00109	O96005	CLPTM1	Putative lipid scramblase CLPTM1
23	4.155	0.00115	P22695	UQCRC2	Cytochrome b-c1 complex subunit 2, mitochondrial
24	4.839	0.00120	P00533	EGFR	Epidermal growth factor receptor
25	4.335	0.00121	P26012	ITGB8	Integrin beta-8
26	7.823	0.00123	Q6ZVX7	NCCRP1	F-box only protein 50
27	2.776	0.00125	Q6DD88	ATL3	Atlastin-3
28	3.937	0.00129	Q8TEM1	NUP210	Nuclear pore membrane glycoprotein 210
29	2.278	0.00134	Q13098	GPS1	COP9 signalosome complex subunit 1
30	5.387	0.00138	P47895	ALDH1A3	Retinaldehyde dehydrogenase 3
31	4.305	0.00141	P19367	HK1	Hexokinase-1
32	2.631	0.00145	Q8N4L2	PIP4P2	Type 2 phosphatidylinositol 4,5-bisphosphate 4-phosphatase
33	5.28	0.00145	Q04446	GBE1	1,4-alpha-glucan-branching enzyme

34	6.85	0.00147	P00403	MT-CO2	Cytochrome c oxidase subunit 2
35	4.99	0.00153	O75352	MPDU1	Mannose-P-dolichol utilization defect 1 protein
36	5.305	0.00158	Q8WXF1	PSPC1	Paraspeckle component 1
37	3.939	0.00158	Q9UG01	IFT172	Intraflagellar transport protein 172 homolog
38	6.508	0.00160	Q13162	PRDX4	Peroxiredoxin-4
39	4.081	0.00174	O95373	IPO7	Importin-7
40	4.675	0.00182	Q9Y230	RUVBL2	RuvB-like 2
41	4.272	0.00182	P28482	MAPK1	Mitogen-activated protein kinase 1
42	9.274	0.00197	P60174	TPI1	Triosephosphate isomerase
43	7.197	0.00201	P40926	MDH2	Malate dehydrogenase, mitochondrial
44	2.718	0.00202	Q9H082	RAB33B	Ras-related protein Rab-33B
45	4.615	0.00210	Q7L1Q6	BZW1	eIF5-mimic protein 2
46	2.620	0.00210	Q14678	KANK1	KN motif and ankyrin repeat domain-containing protein 1
47	5.259	0.00219	P49755	TMED10	Transmembrane emp24 domain-containing protein 10
48	3.597	0.00225	Q01968	OCRL	Inositol polyphosphate 5-phosphatase OCRL
49	4.341	0.00226	P62633	CNBP	CCHC-type zinc finger nucleic acid binding protein
50	6.742	0.00233	Q9BRX8	PRXL2A	Peroxiredoxin-like 2A

Supplementary table- 4. PG genes significantly overexpressed in iPSC-RPE on Matrigel coated dBrM compared to dBrM. In order of the most significant based on p-value smallest to largest. Within Z score > 2.

Num	Z score iPSC-RPE cells on Matrigel coated dBrM/ dBrM	P value (iPSC-RPE cells on Matrigel coated dBrM/ dBrM)	Accession	PG Genes	Description
1	-2.028	0.000711	Q7Z4F1	LRP10	Low-density lipoprotein receptor-related protein 10
2	-2.079	0.00227	Q13496	MTM1	Myotubularin
3	-5.350	0.00263	Q9UK61	TASOR	Protein TASOR
4	-2.966	0.00269	P51608	MECP2	Methyl-CpG-binding protein 2
5	-2.479	0.00274	P98160	HSPG2	Basement membrane-specific heparan sulfate proteoglycan core protein
6	-4.171	0.00284	P12645	BMP3	Bone morphogenetic protein 3
7	-3.173	0.00344	Q6UX46	ALKAL2	ALK and LTK ligand 2
8	-2.894	0.00360	P26022	PTX3	Pentraxin-related protein PTX3
9	-4.330	0.00419	O95631	NTN1	Netrin-1
10	-2.241	0.00444	P06731	CEACAM5	Carcinoembryonic antigen-related cell adhesion molecule 5
11	-2.050	0.00468	Q9UBU2	DKK2	Dickkopf-related protein 2
12	-2.778	0.00633	H0YAC5	REEP2	Receptor expression-enhancing protein (Fragment)
13	-2.023	0.00700	Q8NDC0	MAPK1IP1L	MAPK-interacting and spindle-stabilizing protein-like
14	-2.119	0.00725	P56182	RRP1	Ribosomal RNA processing protein 1 homolog A
15	-2.768	0.00771	Q14515	SPARCL1	SPARC-like protein 1
16	-2.264	0.00840	Q14185	DOCK1	Dedicator of cytokinesis protein 1
17	-2.789	0.00968	Q9Y6K5	OAS3	2'-5'-oligoadenylate synthase 3
18	-4.622	0.00987	H0Y9Y3	SYNPO2	Synaptopodin 2 (Fragment)

19	-9.683	0.01109	Q14114	LRP8	Low-density lipoprotein receptor-related protein 8
20	-2.539	0.0112	Q07817	BCL2L1	Bcl-2-like protein 1
21	-2.483	0.0112	Q8IWU5	SULF2	Extracellular sulfatase Sulf-2
22	-3.381	0.0121	Q5JRA6	MIA3	Transport and Golgi organization protein 1 homolog
23	-2.117	0.0124	Q16787	LAMA3	Laminin subunit alpha-3
24	-4.374	0.0125	Q9NPH5	NOX4	NADPH oxidase 4
25	-4.304	0.0144	P17213	BPI	Bactericidal permeability-increasing protein
26	-2.900	0.0146	P29973	CNGA1	cGMP-gated cation channel alpha-1
27	-2.098	0.0160	Q6UWY5	OLFML1	Olfactomedin-like protein 1
28	-2.446	0.0166	P52655	GTF2A1	Transcription initiation factor IIA subunit 1
29	-2.094	0.0181	Q9NQZ2	UTP3	Something about silencing protein 10
30	-5.685	0.0184	P14222	PRF1	Perforin-1
31	-2.423	0.0190	Q6UXB8	PI16	Peptidase inhibitor 16
32	-2.804	0.0191	P57721	PCBP3	Poly(rC)-binding protein 3
33	-4.419	0.0191	P09038	FGF2	Fibroblast growth factor 2
34	-5.814	0.0197	Q9H6Z9	EGLN3	Prolyl hydroxylase EGLN3
35	-2.963	0.0202	O00339	MATN2	Matrilin-2
36	-2.246	0.0206	P35913	PDE6B	Rod cGMP-specific 3',5'-cyclic phosphodiesterase subunit beta
37	-2.273	0.0208	P26583	HMGB2	High mobility group protein B2
38	-3.320	0.0210	P21781	FGF7	Fibroblast growth factor 7
39	-2.012	0.0248	Q9BQ50	TREX2	Three prime repair exonuclease 2
40	-4.946	0.0249	P05164	MPO	Myeloperoxidase

41	-2.918	0.0252	P12109	COL6A1	Collagen alpha-1(VI) chain
42	-2.400	0.0269	Q6ICL7	SLC35E4	Solute carrier family 35 member E4
43	-2.269	0.0270	P42892	ECE1	Endothelin-converting enzyme 1
44	-5.013	0.0271	Q6UXI7	VIT	Vitrin
45	-2.978	0.0272	P08048;P17010	ZFX;ZFY	Zinc finger Y-chromosomal protein
46	-2.059	0.0274	A8MQ03	CYSRT1	Cysteine-rich tail protein 1
47	-4.312	0.0275	P11678	EPX	Eosinophil peroxidase
48	-2.839	0.0297	Q9H8L6	MMRN2	Multimerin-2
49	-2.081	0.0317	Q14161	GIT2	ARF GTPase-activating protein GIT2
50	-2.769	0.0329	Q3B8N2;Q6DKI2	LGALS9B;LGALS9C	Galectin-9B

Supplementary table- 5. PG genes significantly underexpressed in iPSC-RPE on Matrigel coated dBrM compared to dBrM. In order of the most significant based on p-value smallest to largest. Within Z score > 2.

Num	Z score iPSC-RPE cells on dBrM/ Native BrM N	P value (iPSC-RPE cells on dBrM/ Native BrM)	Accession	PG Genes	Description
1	3.719	0.000958	P40967	PMEL	Melanocyte protein PMEL
2	2.226	0.00236	A0A590UJ24	BRCA2	BRCA2 DNA repair associated (Fragment)
3	2.331	0.00287	Q9UH62	ARMCX3	Armadillo repeat-containing X-linked protein 3
4	2.967	0.00354	Q8IVL6	P3H3	Prolyl 3-hydroxylase 3
5	3.290	0.00424	P10619	CTSA	Lysosomal protective protein
6	7.925	0.00564	Q5T5S1	CCDC183	Coiled-coil domain-containing protein 183
7	2.156	0.00762	P07996;P35442	THBS1;THBS2	Thrombospondin-1
8	2.846	0.00836	Q9Y6Y0	IVNS1ABP	Influenza virus NS1A-binding protein
9	2.860	0.00851	Q8N8R3	SLC25A29	Mitochondrial basic amino acids transporter

10	2.496	0.00942	Q8N6L1	KRTCAP2	Keratinocyte-associated protein 2
11	5.150	0.0107	O00425	IGF2BP3	Insulin-like growth factor 2 mRNA-binding protein 3
12	9.056	0.0119	O00204	SULT2B1	Sulfotransferase 2B1
13	4.311	0.0123	Q15392	DHCR24	Delta(24)-sterol reductase
14	2.091	0.0135	Q8IWT6;Q8TDW0	LRRC8A;LRRC8C	Volume-regulated anion channel subunit LRRC8A
15	2.302	0.0139	Q14315	FLNC	Filamin-C
16	3.006	0.0144	P41227	NAA10	N-alpha-acetyltransferase 10
17	2.554	0.0159	O00541	PES1	Pescadillo homolog
18	2.094	0.0162	Q9UGI8	TES	Testin
19	2.049	0.0173	P42785	PRCP	Lysosomal Pro-X carboxypeptidase
20	3.350	0.0176	Q24JP5	TMEM132A	Transmembrane protein 132A
21	5.541	0.0188	Q16790	CA9	Carbonic anhydrase 9
22	5.651	0.0195	P08729;Q14CN4	KRT7;KRT72	Keratin, type II cytoskeletal 7
23	2.798	0.0205	Q9H813	PACC1	Proton-activated chloride channel

24	4.620	0.0214	Q9NRX3	NDUFA4L2	NADH dehydrogenase [ubiquinone] 1 alpha subcomplex subunit 4-like 2
25	3.682	0.0229	P10620	MGST1	Microsomal glutathione S-transferase 1
26	2.031	0.0235	Q14CN4;Q3SY84;Q7RTS7;Q86Y46	KRT71;KRT72;KRT73;KRT74	Keratin, type II cytoskeletal 72
27	2.879	0.0249	Q9P2X0	DPM3	Dolichol-phosphate mannosyltransferase subunit 3
28	3.236	0.0275	O43657	TSPAN6	Tetraspanin-6
29	2.894	0.0285	Q9BQP9	BPIFA3	BPI fold-containing family A member 3
30	4.943	0.0292	Q4KMQ1	TPRN	Taperin
31	3.519	0.0297	O00469	PLOD2	Procollagen-lysine,2-oxoglutarate 5-dioxygenase 2
32	2.847	0.0302	Q9H2H8	PPIL3	Peptidyl-prolyl cis-trans isomerase-like 3
33	2.534	0.0304	Q96S52	PIGS	GPI transamidase component PIG-S
34	3.018	0.0322	A0A8I5KXG8	MYLK	Myosin light chain kinase (Fragment)

35	2.441	0.0333	P51610	HCFC1	Host cell factor 1
36	3.241	0.0336	Q8TBR7	TLCD3A	TLC domain-containing protein 3A
37	3.454	0.0347	P24593	IGFBP5	Insulin-like growth factor-binding protein 5
38	3.093	0.0347	Q8NFF5	FLAD1	FAD synthase
39	3.754	0.0349	Q9C0H2	TTYH3	Protein tweety homolog 3
40	6.714	0.0352	Q8TAV3	CYP2W1	Cytochrome P450 2W1
41	3.348	0.0356	Q7Z3E5	ARMC9	LisH domain-containing protein ARMC9
42	2.471	0.0362	Q9BRJ7	NUDT16L1	Tudor-interacting repair regulator protein
43	6.101	0.0363	A0A0G2JPD3;A0A140T8Y4;A0A1W2PR61;Q5SPM2	HLA-A	HLA class I histocompatibility antigen, A alpha chain
44	4.675	0.0366	Q86V35	CABP7	Calcium-binding protein 7
45	2.306	0.0369	Q9H853	TUBA4B	Putative tubulin-like protein alpha-4B
46	2.496	0.0374	Q9NRR5	UBQLN4	Ubiquilin-4
47	2.280	0.0394	Q6ZRS2	SRCAP	Helicase SRCAP

48	2.526	0.0408	Q8IZF6	ADGRG4	Adhesion G-protein coupled receptor G4
49	2.864	0.0420	O75718	CRTAP	Cartilage-associated protein
50	3.624	0.0422	A0A087X2C4;A0A8Q3SI70;A0A8V8TM73	PCDH7	Protocadherin 7

Supplementary table- 6. **PG genes significantly overexpressed in iPSC-RPE on dBrM compared to Native.** In order of the most significant based on p value smallest to largest. Within Z score > 2

Num	Z score iPSC-RPE cells on dBrM/ Native BrM	P value (iPSC-RPE cells on dBrM/ Native BrM)	Accession	PG Genes	Description
1	-3.393	6.75E-05	Q9UPI3	FLVCR2	Heme transporter FLVCR2
2	-2.607	0.000198	Q9HD33	MRPL47	Large ribosomal subunit protein uL29m
3	-3.432	0.000574	P43003	SLC1A3	Excitatory amino acid transporter 1
4	-4.956	0.000618	P00918	CA2	Carbonic anhydrase 2
5	-3.480	0.000935	Q9UL12	SARDH	Sarcosine dehydrogenase, mitochondrial
6	-2.438	0.00121	Q8N3Z0	PRSS35	Inactive serine protease 35
7	-3.305	0.00127	O14786	NRP1	Neuropilin-1
8	-2.266	0.00174	Q9Y276	BCS1L	Mitochondrial chaperone BCS1
9	-2.036	0.00227	Q96C45	ULK4	Serine/threonine-protein kinase ULK4
10	-2.691	0.00274	Q9HBJ8	CLTRN	Collectrin
11	-3.129	0.00309	A0A0S2Z4L3	PROS1	Protein S (Fragment)
12	-4.767	0.00329	O95428	PAPLN	Papilin
13	-6.174	0.00335	P20231;Q15661	TPSAB1;TPSB2	Tryptase beta-2
14	-4.764	0.00358	Q86VB7	CD163	Scavenger receptor cysteine-rich type 1 protein M130
15	-2.204	0.00381	O15481	MAGEB4	Melanoma-associated antigen B4
16	-3.673	0.00385	Q9BPU6	DPYSL5	Dihydropyrimidinase-related protein 5
17	-2.729	0.00386	O00478	BTN3A3	Butyrophilin subfamily 3 member A3

18	-5.816	0.00409	P19087	GNAT2	Guanine nucleotide-binding protein G(t) subunit alpha-2
19	-2.608	0.00453	P27169	PON1	Serum paraoxonase/arylesterase 1
20	-6.546	0.00475	O43301	HSPA12A	Heat shock 70 kDa protein 12A
21	-6.344	0.00482	Q9P241	ATP10D	Phospholipid-transporting ATPase VD
22	-6.500	0.00500	P60201	PLP1	Myelin proteolipid protein
23	-6.673	0.00536	P50135	HNMT	Histamine N-methyltransferase
24	-6.549	0.00544	P14415	ATP1B2	Sodium/potassium-transporting ATPase subunit beta-2
25	-2.988	0.00578	Q86UU1	PHLDB1	Pleckstrin homology-like domain family B member 1
26	-4.756	0.00611	Q9UBP4	DKK3	Dickkopf-related protein 3
27	-5.523	0.00635	O75891	ALDH1L1	Cytosolic 10-formyltetrahydrofolate dehydrogenase
28	-4.149	0.00648	Q86UX7	FERMT3	Fermitin family homolog 3
29	-2.470	0.00658	O15484	CAPN5	Calpain-5
30	-2.997	0.00720	Q9BT40	INPP5K	Inositol polyphosphate 5-phosphatase K
31	-5.611	0.00771	Q9NSD5	SLC6A13	Sodium- and chloride-dependent GABA transporter 2
32	-2.776	0.00779	Q7Z2X4	PID1	PTB-containing, cubilin and LRP1-interacting protein
33	-8.137	0.00801	P15090	FABP4	Fatty acid-binding protein, adipocyte
34	-2.975	0.00824	Q6PIU2	NCEH1	Neutral cholesterol ester hydrolase 1

35	-2.321	0.00829	Q15119	PDK2	[Pyruvate dehydrogenase (acetyl-transferring)] kinase isozyme 2, mitochondrial
36	-6.478	0.00831	O14495	PLPP3	Phospholipid phosphatase 3
37	-2.860	0.00868	O60641	SNAP91	Clathrin coat assembly protein AP180
38	-7.035	0.00935	Q9UNN8	PROCR	Endothelial protein C receptor
39	-3.720	0.00942	P19320	VCAM1	Vascular cell adhesion protein 1
40	-3.248	0.00984	Q9NSB2	KRT84	Keratin, type II cuticular Hb4
41	-4.263	0.00992	Q9NU02	ANKEF1	Ankyrin repeat and EF-hand domain-containing protein 1
42	-2.361	0.0100	P05023;P13637	ATP1A1;ATP1A3	Sodium/potassium-transporting ATPase subunit alpha-1
43	-2.452	0.0101	Q9NZM3	ITSN2	Intersectin-2
44	-4.274	0.0101	Q14031	COL4A6	Collagen alpha-6(IV) chain
45	-3.842	0.0102	P49961	ENTPD1	Ectonucleoside triphosphate diphosphohydrolase 1
46	-4.465	0.0102	A0A140TA21	HLA-B	HLA class I histocompatibility antigen, B alpha chain
47	-2.228	0.0104	Q8TE56	ADAMTS17	A disintegrin and metalloproteinase with thrombospondin motifs 17
48	-2.414	0.0109	Q9NRG1	PRTFDC1	Phosphoribosyltransferase domain-containing protein 1
49	-2.610	0.0111	Q96AP7	ESAM	Endothelial cell-selective adhesion molecule
50	-6.432	0.0125	Q9H254	SPTBN4	Spectrin beta chain, non-erythrocytic 4

Supplementary table- 7. PG genes significantly underexpressed in iPSC-RPE on dBrM compared to Native. In order of the most significant based on p value, smallest to largest. Within Z score > 2.

Num	Z score iPSC-RPE cells on dBrM / dBrM	P value (iPSC-RPE cells on dBrM/ dBrM)	Accession	PG Genes	Description
1	4.358	8.54E-05	Q15370	ELOB	Elongin-B
2	5.236	9.69E-05	Q9H008	LHPP	Phospholysine phosphohistidine inorganic pyrophosphate phosphatase
3	3.661	0.000133	Q99569	PKP4	Plakophilin-4
4	2.030	0.000460	Q6IA86	ELP2	Elongator complex protein 2
5	4.401	0.000535	O75439	PMPCB	Mitochondrial-processing peptidase subunit beta
6	3.674	0.000535	P40616	ARL1	ADP-ribosylation factor-like protein 1
7	3.167	0.000743	Q01082	SPTBN1	Spectrin beta chain, non-erythrocytic 1
8	8.410	0.000836	P27797	CALR	Calreticulin

9	3.881	0.000899	Q6EMK4	VASN	Vasorin
10	5.484	0.000926	P68366;Q9BQE3;Q9NY65	TUBA1C;TUBA4A;TUBA8	Tubulin alpha-4A chain
11	7.544	0.00113	Q6ZVX7	NCCRP1	F-box only protein 50
12	2.696	0.00114	Q9Y6A9	SPCS1	Signal peptidase complex subunit 1
13	5.041	0.00118	Q13630	GFUS	GDP-L-fucose synthase
14	5.082	0.00120	Q8WXF1	PSPC1	Paraspeckle component 1
15	4.648	0.00124	Q13740	ALCAM	CD166 antigen
16	3.309	0.00135	Q9HDC9	APMAP	Adipocyte plasma membrane-associated protein
17	4.245	0.00154	Q8NBX0	SCCPDH	Saccharopine dehydrogenase-like oxidoreductase
18	3.502	0.00158	Q9H1Z9	TSPAN10	Tetraspanin-10
19	4.420	0.00160	P00918	CA2	Carbonic anhydrase 2
20	4.491	0.00163	P04350;P07437;P68371;Q13509;Q13885;Q9BVA1	TUBB;TUBB2A;TUBB2B;TUBB3;TUBB4A;TUBB4B	Tubulin beta-4A chain
21	2.966	0.00169	Q9H0H0	INTS2	Integrator complex subunit 2
22	3.910	0.00170	P30876	POLR2B	DNA-directed RNA polymerase II subunit RPB2
23	2.968	0.00170	Q9UN37	VPS4A	Vacuolar protein sorting-associated protein 4A
24	5.601	0.00172	O15258	RER1	Protein RER1

25	5.220	0.00174	Q969H8	MYDGF	Myeloid-derived growth factor
26	4.066	0.00180	P15170	GSPT1	Eukaryotic peptide chain release factor GTP-binding subunit ERF3A
27	4.508	0.00182	Q92900	UPF1	Regulator of nonsense transcripts 1
28	4.212	0.00183	Q9BVC6	TMEM109	Transmembrane protein 109
29	5.102	0.00188	O43865	AHCYL1	S-adenosylhomocysteine hydrolase-like protein 1
30	3.216	0.00205	P18031	PTPN1	Tyrosine-protein phosphatase non-receptor type 1
31	4.295	0.00212	Q86UP0	CDH24	Cadherin-24
32	6.221	0.00218	O60361;P15531	NME1;NME2P1	Putative nucleoside diphosphate kinase
33	6.276	0.00222	Q9BRX8	PRXL2A	Peroxiredoxin-like 2A
34	6.706	0.00234	P20618	PSMB1	Proteasome subunit beta type-1
35	2.773	0.00241	Q8TEM1	NUP210	Nuclear pore membrane glycoprotein 210
36	4.225	0.00241	Q9UBQ7	GRHPR	Glyoxylate reductase/hydroxypyruvate reductase
37	3.306	0.00256	Q13308	PTK7	Inactive tyrosine-protein kinase 7

38	5.413	0.00273	Q9NY33	DPP3	Dipeptidyl peptidase 3
39	4.881	0.00282	P20020;P23634;Q01814;Q16720	ATP2B1;ATP2B2;ATP2B3;ATP2B4	Plasma membrane calcium-transporting ATPase 1
40	2.369	0.00292	P61353	RPL27	Large ribosomal subunit protein eL27
41	6.214	0.00293	P61204;P84077	ARF1;ARF3	ADP-ribosylation factor 3
42	6.757	0.00296	P00387	CYB5R3	NADH-cytochrome b5 reductase 3
43	2.663	0.00303	Q9NRR5;Q9UMX0	UBQLN1;UBQLN4	Ubiquilin-4
44	4.890	0.00310	P13861	PRKAR2A	cAMP-dependent protein kinase type II-alpha regulatory subunit
45	3.462	0.00313	Q9BRF8	CPPED1	Serine/threonine-protein phosphatase CPPED1
46	7.234	0.00313	Q6BCY4	CYB5R2	NADH-cytochrome b5 reductase 2
47	2.925	0.00319	Q9BUN8	DERL1	Derlin-1
48	7.009	0.00327	O43707;P12814	ACTN1;ACTN4	Alpha-actinin-4
49	5.764	0.00332	P11586	MTHFD1	C-1-tetrahydrofolate synthase, cytoplasmic
50	3.307	0.00342	P48426;P78356	PIP4K2A;PIP4K2B	Phosphatidylinositol 5-phosphate 4-kinase type-2 alpha

Supplementary table- 8. **PG genes significantly overexpressed in iPSC-RPE on dBrM compared to dBrM.** In order of the most significant based on p value smallest to largest. Within Z score > 2.

Num	Z score iPSC-RPE cells on dBrM/ dBrM	P value (iPSC-RPE cells on dBrM/ dBrM)	Accession	PG Genes	Description
1	-5.414	0.00130	P12544	GZMA	Granzyme A
2	-5.300	0.00219	Q9Y240	CLEC11A	C-type lectin domain family 11 member A
3	-2.284	0.00221	P07320	CRYGD	Gamma-crystallin D
4	-5.178	0.00339	Q9BXJ1	C1QTNF1	Complement C1q tumor necrosis factor-related protein 1
5	-5.985	0.00394	Q00604	NDP	Norrin
6	-2.326	0.00477	Q7Z6L1	TECPR1	Tectonin beta-propeller repeat-containing protein 1
7	-4.513	0.00759	O43184	ADAM12	Disintegrin and metalloproteinase domain-containing protein 12
8	-5.036	0.00794	Q8IX30	SCUBE3	Signal peptide, CUB and EGF-like domain-containing protein 3
9	-2.700	0.00818	P35443	THBS4	Thrombospondin-4
10	-4.579	0.00827	Q92777	SYN2	Synapsin-2
11	-4.567	0.00830	Q13201	MMRN1	Multimerin-1
12	-3.723	0.0101	P08294	SOD3	Extracellular superoxide dismutase [Cu-Zn]
13	-4.180	0.0104	O15525;O60675;Q9ULX9	MAFF;MAFG;MAFK	Transcription factor MafG
14	-2.146	0.0114	Q9NZB8	MOCS1	Molybdenum cofactor biosynthesis protein 1
15	-2.271	0.0122	Q9UBS5	GABBR1	Gamma-aminobutyric acid type B receptor subunit 1

16	-2.501	0.0133	Q9UFW8	CGGBP1	CGG triplet repeat-binding protein 1
17	-2.297	0.0134	P29622	SERPINA4	Kallistatin
18	-2.326	0.0155	Q9NS98	SEMA3G	Semaphorin-3G
19	-3.542	0.0173	P49863	GZMK	Granzyme K
20	-3.588	0.0202	O95996	APC2	Adenomatous polyposis coli protein 2
21	-8.263	0.0203	C9JKG1	BGN	Biglycan (Fragment)
22	-2.301	0.0207	P20648	ATP4A	Potassium-transporting ATPase alpha chain 1
23	-5.662	0.0215	P09237	MMP7	Matrilysin
24	-3.000	0.0229	Q16394	EXT1	Exostosin-1
25	-5.630	0.0236	Q96JE9	MAP6	Microtubule-associated protein 6
26	-4.146	0.0251	Q9HCB6	SPON1	Spondin-1
27	-3.471	0.0254	P05164	MPO	Myeloperoxidase
28	-4.749	0.0271	Q9NPH5	NOX4	NADPH oxidase 4
29	-5.122	0.0278	H0Y9Y3	SYNPO2	Synaptopodin 2 (Fragment)
30	-6.267	0.0300	A0A087WYX9	COL5A2	Collagen type V alpha 2 chain
31	-3.968	0.0312	Q70IA8	MOB3C	MOB kinase activator 3C
32	-2.587	0.0322	A8K968	EPB41L3	Erythrocyte membrane protein band 4.1 like 3
33	-4.288	0.0351	Q5JRA6	MIA3	Transport and Golgi organization protein 1 homolog
34	-5.331	0.0360	A0A3B3ISX9	TNXB	Tenascin XB
35	-4.853	0.0374	O94769	ECM2	Extracellular matrix protein 2
36	-10.163	0.0378	Q14114	LRP8	Low-density lipoprotein receptor-related protein 8
37	-6.907	0.0379	Q9H254	SPTBN4	Spectrin beta chain, non-erythrocytic 4
38	-3.020	0.0382	P52943	CRIP2	Cysteine-rich protein 2

39	-4.587	0.0385	O15335	CHAD	Chondroadherin
40	-4.942	0.0394	Q14314	FGL2	Fibroleukin
41	-4.596	0.0402	P57721	PCBP3	Poly(rC)-binding protein 3
42	-2.869	0.0408	O75582	RPS6KA5	Ribosomal protein S6 kinase alpha-5
43	-2.265	0.0410	Q13356	PPIL2	RING-type E3 ubiquitin-protein ligase PPIL2
44	-2.064	0.0429	O60488	ACSL4	Long-chain-fatty-acid--CoA ligase 4
45	-2.975	0.0431	P35243	RCVRN	Recoverin
46	-3.528	0.0465	Q4LDE5	SVEP1	Sushi, von Willebrand factor type A, EGF and pentraxin domain-containing protein 1
47	-2.049	0.048865	Q7L1I2	SV2B	Synaptic vesicle glycoprotein 2B

Supplementary table- 9. PG genes significantly underexpressed in iPSC-RPE on dBrM compared to dBrM. In order of the most significant based on p value, smallest to largest. Within Z score > 2.

Z score iPSC-RPE cells on Matrigel coated dBrM/ iPSC-RPE cells on dBrM	Z score iPSC-RPE cells on dBrM/iPSC-RPE cells on Matrigel coated dBrM	P value (iPSC-RPE cells on Matrigel coated dBrM/ iPSC-RPE cells on dBrM)	P value (iPSC-RPE cells on dBrM/iPSC-RPE cells on Matrigel coated dBrM)	Accession	PG Genes	Description
0.201	-0.201	0.663	0.663	Q9P2E9	RRBP1	Ribosome-binding protein 1
2.574	-2.574	0.366	0.366	P40126	DCT	L-dopachrome tautomerase
1.354	-1.354	0.428	0.428	P41222	PTGDS	Prostaglandin-H2 D-isomerase
1.216	-1.216	0.369	0.369	Q13822	ENPP2	Ectonucleotide pyrophosphatase/phosphodiesterase family member 2
1.004	-1.004	0.321	0.321	P40967	PMEL	Melanocyte protein PMEL
0.853	-0.853	0.657	0.657	P02766	TTR	Transthyretin
2.630	-2.630	0.094	0.094	P17643	TYRP1	5,6-dihydroxyindole-2-carboxylic acid oxidase
-0.676	0.676	0.520	0.520	Q9UBP9	GULP1	PTB domain-containing engulfment adapter protein 1
0.079	-0.079	0.699	0.699	P36955	SERPINF1	Pigment epithelium-derived factor
0.806	-0.806	0.050	0.050	P23229	ITGA6	Integrin alpha-6
0.327	-0.327	0.127	0.127	P16144	ITGB4	Integrin beta-4
-0.166	0.166	0.132	0.132	P05556	ITGB1	Integrin beta-1
-0.238	0.238	0.775	0.775	P08648	ITGA5	Integrin alpha-5
2.387	-2.387	0.601	0.601	P25391	LAMA1	Laminin subunit alpha-1

1.847	-1.847	0.622	0.622	P24043	LAMA2	Laminin subunit alpha-2
1.604	-1.604	0.554	0.554	O15230;Q16787	LAMA3;LAMA5	Laminin subunit alpha-5
1.552	-1.552	0.468	0.468	Q16363	LAMA4	Laminin subunit alpha-4
2.145	-2.145	0.563	0.563	O15230	LAMA5	Laminin subunit alpha-5
1.614	-1.614	0.476	0.476	P07942	LAMB1	Laminin subunit beta-1
0.712	-0.712	0.819	0.819	P55268	LAMB2	Laminin subunit beta-2
-1.982	1.982	0.236	0.236	Q13751	LAMB3	Laminin subunit beta-3
1.176	-1.176	0.713	0.713	P11047	LAMC1	Laminin subunit gamma-1
-2.355	2.355	0.555	0.555	Q13753	LAMC2	Laminin subunit gamma-2
1.259	-1.259	0.668	0.668	Q9Y6N6	LAMC3	Laminin subunit gamma-3

Supplementary table- 10. **The PG genes of interest.** The PG genes involved in the visual cycle (RBP1, DCT), lipid biosynthesis (PTGDS), melanin biosynthesis (ENPP2, PMEL, TTR, TYRP1), phagocytosis (GULP1), secretion (SERPINF1), and adhesion (ITGA6, ITGB4, ITGB1, ITGA5.

Num	Z score iPSC-RPE cells on Matrigel coated dBrM/ iPSC-RPE cells on dBrM	P value (iPSC-RPE cells on Matrigel coated dBrM/ iPSC-RPE cells on dBrM)	Accession	PG Genes	Description
1	6.565	0.000847	Q9BQB6	VKORC1	Vitamin K epoxide reductase complex subunit 1
2	5.422	0.00172	O60565;Q9H772	GREM1;GREM2	Gremlin-1
3	2.126	0.00427	P29317;P29323;P54753;P54760;P54764	EPHA2;EPHA4;EPHB2;EPHB3;EPHB4	Ephrin type-A receptor 2
4	7.665	0.00491	Q496H8	NRN1L	Neuritin-like protein
5	2.770	0.00574	Q9H0W9	C11orf54	Ester hydrolase C11orf54
6	3.619	0.00660	Q96B54	ZNF428	Zinc finger protein 428
7	3.896	0.00724	Q9UBF2;Q9Y678	COPG1;COPG2	Coatomer subunit gamma-2
8	3.274	0.00751	Q12840	KIF5A	Kinesin heavy chain isoform 5A
9	3.777	0.00770	P60510;P62714;P67775	PPP2CA;PPP2CB;PPP4C	Serine/threonine-protein phosphatase 4 catalytic subunit

10	6.415	0.00809	Q9H254	SPTBN4	Spectrin beta chain, non-erythrocytic 4
11	4.144	0.00880	P35556	FBN2	Fibrillin-2
12	2.718	0.00894	Q7L311	ARMCX2	Armadillo repeat-containing X-linked protein 2
13	2.766	0.00894	O15247	CLIC2	Chloride intracellular channel protein 2
14	2.773	0.00964	P09651	HNRNPA1	Heterogeneous nuclear ribonucleoprotein A1
15	5.206	0.0103	A0A0S2Z4L3	PROS1	Protein S (Fragment)
16	4.798	0.0112	O00399	DCTN6	Dynactin subunit 6
17	4.535	0.0129	P36980	CFHR2	Complement factor H-related protein 2
18	2.970	0.0138	P09471	GNAO1	Guanine nucleotide-binding protein G(o) subunit alpha
19	4.458	0.0140	P12036	NEFH	Neurofilament heavy polypeptide
20	2.025	0.0141	Q15041	ARL6IP1	ADP-ribosylation factor-like protein 6-interacting protein 1

21	2.076	0.0163	Q59EK9	RUNDC3A	RUN domain-containing protein 3A
22	6.618	0.0163	Q8TD08	MAPK15	Mitogen-activated protein kinase 15
23	3.647	0.0167	P10109	FDX1	Adrenodoxin, mitochondrial
24	2.569	0.0175	P57087	JAM2	Junctional adhesion molecule B
25	2.907	0.0185	A0A087WSY4	IGHV4-30-2	Immunoglobulin heavy variable 4-30-2
26	2.294	0.0203	Q8IYS1	PM20D2	Xaa-Arg dipeptidase
27	2.842	0.0216	O43184	ADAM12	Disintegrin and metalloproteinase domain-containing protein 12
28	5.331	0.0228	P03973	SLPI	Antileukoproteinase
29	4.867	0.0230	O00585	CCL21	C-C motif chemokine 21
30	7.079	0.0247	P48307	TFPI2	Tissue factor pathway inhibitor 2
31	6.143	0.0259	P02462;P29400	COL4A1;COL4A5	Collagen alpha-1(IV) chain
32	2.044	0.0263	P30046	DDT	D-dopachrome decarboxylase
33	2.058	0.0266	Q01484	ANK2	Ankyrin-2

34	2.214	0.0275	P11532	DMD	Dystrophin
35	2.708	0.0282	Q0IIM8	TBC1D8B	TBC1 domain family member 8B
36	8.108	0.0285	A0A087WTP0	PGAP3	Post-GPI attachment to proteins phospholipase 3
37	3.027	0.0287	Q9BYZ2	LDHAL6B	L-lactate dehydrogenase A-like 6B
38	2.299	0.0329	Q96SW2	CRBN	Protein cereblon
39	6.909	0.0336	P00747;P08519	LPA;PLG	Plasminogen
40	3.573	0.0344	P48595	SERPINB10	Serpin B10
41	5.560	0.0345	A0A1B0GXB6	GSTT1	Glutathione S-transferase theta-1 (Fragment)
42	4.039	0.0368	P41221	WNT5A	Protein Wnt-5a
43	2.316	0.0369	P13929	ENO3	Beta-enolase
44	3.829	0.0382	Q9NVV0	TMEM38B	Trimeric intracellular cation channel type B
45	4.453	0.0394	P02655	APOC2	Apolipoprotein C-II
46	2.209	0.0407	Q9UBP4	DKK3	Dickkopf-related protein 3
47	3.672	0.0431	Q13362;Q14738;Q16537	PPP2R5C;PPP2R5D;PPP2R5E	Serine/threonine-protein phosphatase 2A 56 kDa regulatory

					subunit gamma isoform
48	3.146	0.0447	Q9UBN4;Q9UL62	TRPC4;TRPC5	Short transient receptor potential channel 4
49	2.474	0.0460	P63261	ACTG1	Actin, cytoplasmic 2
50	2.999	0.0467	Q9BQB4	SOST	Sclerostin

Supplementary table- 11. **PG genes significantly overexpressed in iPSC-RPE on Matrigel coated dBrM compared to iPSC-RPE on dBrM and underexpressed in iPSC-RPE on dBrM compared to iPSC-RPE on Matrigel coated dBrM.** In the order of the most significant based on p value smallest to largest. Within Z score > 2.

Num	Z score iPSC-RPE cells on Matrigel coated dBrM/ iPSC-RPE cells on dBrM	P value (iPSC-RPE cells on Matrigel coated dBrM/ iPSC-RPE cells on dBrM)	Accession	PG Genes	Description
1	6.565	0.000847	Q9BQB6	VKORC1	Vitamin K epoxide reductase complex subunit 1
2	5.422	0.00172	O60565;Q9H772	GREM1;GREM2	Gremlin-1
3	2.126	0.00427	P29317;P29323;P54753;P54760;P54764	EPHA2;EPHA4;EPHB2;EPHB3;EPHB4	Ephrin type-A receptor 2
4	7.665	0.00491	Q496H8	NRN1L	Neuritin-like protein
5	2.770	0.00574	Q9H0W9	C11orf54	Ester hydrolase C11orf54
6	3.619	0.00660	Q96B54	ZNF428	Zinc finger protein 428
7	3.896	0.00724	Q9UBF2;Q9Y678	COPG1;COPG2	Coatomer subunit gamma-2
8	3.274	0.00751	Q12840	KIF5A	Kinesin heavy chain isoform 5A
9	3.777	0.00770	P60510;P62714;P67775	PPP2CA;PPP2CB;PPP4C	Serine/threonine-protein phosphatase 4 catalytic subunit
10	6.415	0.00809	Q9H254	SPTBN4	Spectrin beta chain, non-erythrocytic 4
11	4.144	0.00880	P35556	FBN2	Fibrillin-2

12	2.718	0.00894	Q7L311	ARMCX2	Armadillo repeat-containing X-linked protein 2
13	2.766	0.00894	O15247	CLIC2	Chloride intracellular channel protein 2
14	2.773	0.00964	P09651	HNRNPA1	Heterogeneous nuclear ribonucleoprotein A1
15	5.206	0.0103	A0A0S2Z4L3	PROS1	Protein S (Fragment)
16	4.798	0.0112	O00399	DCTN6	Dynactin subunit 6
17	4.535	0.0129	P36980	CFHR2	Complement factor H-related protein 2
18	2.970	0.0138	P09471	GNAO1	Guanine nucleotide-binding protein G(o) subunit alpha
19	4.458	0.0140	P12036	NEFH	Neurofilament heavy polypeptide
20	2.025	0.0141	Q15041	ARL6IP1	ADP-ribosylation factor-like protein 6-interacting protein 1
21	2.076	0.0163	Q59EK9	RUNDC3A	RUN domain-containing protein 3A

22	6.618	0.0163	Q8TD08	MAPK15	Mitogen-activated protein kinase 15
23	3.647	0.0167	P10109	FDX1	Adrenodoxin, mitochondrial
24	2.569	0.0175	P57087	JAM2	Junctional adhesion molecule B
25	2.907	0.0185	A0A087WSY4	IGHV4-30-2	Immunoglobulin heavy variable 4-30-2
26	2.294	0.0203	Q8IYS1	PM20D2	Xaa-Arg dipeptidase
27	2.842	0.0216	O43184	ADAM12	Disintegrin and metalloproteinase domain-containing protein 12
28	5.331	0.0228	P03973	SLPI	Antileukoproteinase
29	4.867	0.0230	O00585	CCL21	C-C motif chemokine 21
30	7.079	0.0247	P48307	TFPI2	Tissue factor pathway inhibitor 2
31	6.143	0.0259	P02462;P29400	COL4A1;COL4A5	Collagen alpha-1(IV) chain
32	2.044	0.0263	P30046	DDT	D-dopachrome decarboxylase
33	2.058	0.0266	Q01484	ANK2	Ankyrin-2
34	2.214	0.0275	P11532	DMD	Dystrophin

35	2.708	0.0282	Q0IIM8	TBC1D8B	TBC1 domain family member 8B
36	8.108	0.0285	A0A087WTP0	PGAP3	Post-GPI attachment to proteins phospholipase 3
37	3.027	0.0287	Q9BYZ2	LDHAL6B	L-lactate dehydrogenase A-like 6B
38	2.299	0.0329	Q96SW2	CRBN	Protein cereblon
39	6.909	0.0336	P00747;P08519	LPA;PLG	Plasminogen
40	3.573	0.0344	P48595	SERPINB10	Serpin B10
41	5.560	0.0345	A0A1B0GXB6	GSTT1	Glutathione S-transferase theta-1 (Fragment)
42	4.039	0.0368	P41221	WNT5A	Protein Wnt-5a
43	2.316	0.0369	P13929	ENO3	Beta-enolase
44	3.829	0.0382	Q9NVV0	TMEM38B	Trimeric intracellular cation channel type B
45	4.453	0.0394	P02655	APOC2	Apolipoprotein C-II
46	2.209	0.0407	Q9UBP4	DKK3	Dickkopf-related protein 3
47	3.672	0.0431	Q13362;Q14738;Q16537	PPP2R5C;PPP2R5D;PPP2R5E	Serine/threonine-protein phosphatase 2A 56 kDa regulatory

					subunit gamma isoform
48	3.146	0.0447	Q9UBN4;Q9UL62	TRPC4;TRPC5	Short transient receptor potential channel 4
49	2.474	0.0460	P63261	ACTG1	Actin, cytoplasmic 2
50	2.999	0.0467	Q9BQB4	SOST	Sclerostin

Supplementary table- 12. **Significantly underexpressed in iPSC-RPE on Matrigel coated dBrM compared to iPSC-RPE on dBrM and overexpressed in iPSC-RPE on dBrM compared to iPSC-RPE on Matrigel coated dBrM.** In the order of the most significant based on p value smallest to largest. Within Z score > 2.

Appendix B: List of publications

1. **Hammadi S**, Tzoumas N, Ferrara M., Meschede IP, Lo K, Harris C, Lako M, Steel DH. (2023). Bruch's membrane: A key consideration with complement-based therapies for age-related macular degeneration. *Journal of Clinical Medicine, 12*(8), 2870.
Available from: https://doi.org/10.3390/jcm12082870

2. Collin J, Hasoon M, Zerti D, **Hammadi S**, Dorgau B, Clarke L, Steel D, Hussain R, Coxhead J, Lisgo S, Queen R, Lako M. Single-cell RNA sequencing reveals transcriptional changes of human choroidal and retinal pigment epithelium cells during fetal development, in healthy adult and intermediate age-related macular degeneration, *Human Molecular Genetics*, 32(10), 1698–1710. Available from: https://doi.org/10.1093/hmg/ddad007

References

4D Molecular Therapeutics (2024) *Clinical trial: 4D-150 in Patients with Neovascular (Wet) Age-Related Macular Degeneration. Available from: https://clinicaltrials.gov/study/NCT05197270?cond=nct05197270&rank=1*. [Online]

AbbVie (2024a) *Clinical trial: Pivotal 2 Study of RGX-314 Gene Therapy in Participants With nAMD (ASCENT). Available from: https://clinicaltrials.gov/study/NCT05407636*. [Online]

AbbVie (2024b) *Clinical trial: RGX-314 Gene Therapy Administered in the Suprachoroidal Space for Participants With Neovascular Age-Related Macular Degeneration (nAMD) (AAVIATE). Available from: https://clinicaltrials.gov/study/NCT04514653*. [Online]

AbbVie (2024c) *Clinical trial: RGX-314 Gene Therapy Pharmacodynamic Study for Neovascular Age-related Macular Degeneration (nAMD). Available from: https://clinicaltrials.gov/study/NCT04832724*. [Online]

AbbVie (2025) *Clinicla trial: Pivotal 1 Study of RGX-314 Gene Therapy in Participants With nAMD (ATMOSPHERE). Available from: https://clinicaltrials.gov/study/NCT04704921?a=2*. [Online]

Abrahamson, D.R. & Fearon, D.T. (1983) 'Endocytosis of the C3b receptor of complement within coated pits in human polymorphonuclear leukocytes and monocytes.', *Laboratory investigation; a journal of technical methods and pathology*, 48(2), pp. 162–8.

Acar, İ.E., Lores-Motta, L., Colijn, J.M., Meester-Smoor, M.A., Verzijden, T., Cougnard-Gregoire, A., Ajana, S., Merle, B.M.J., de Breuk, A., Heesterbeek, T.J., van den Akker, E., Daha, M.R., Claes, B., Pauleikhoff, D., Hense, H.-W., van Duijn, C.M., Fauser, S., Hoyng, C.B., Delcourt, C., et al. (2020) 'Integrating Metabolomics, Genomics, and Disease Pathways in Age-Related Macular Degeneration', *Ophthalmology*, 127(12), pp. 1693–1709.

Adverum Biotechnologies, I. (2025) *Clinical trial: Safety and Efficacy of ADVM-022 in Treatment-Experienced Patients With Neovascular Age-related Macular Degeneration [LUNA]. Available from: https://clinicaltrials.gov/study/NCT05536973*. [Online]

Adverum Biotechnologies, I. (2023) *Clinical Trials : ADVM-022 Intravitreal Gene Therapy for Wet AMD (OPTIC). Available from: https://clinicaltrials.gov/study/NCT03748784*. [Online]

Ahearn, J.M. & Fearon, D.T. (1989) *Structure and Function of the Complement Receptors, CR1 (CD35) and CR2 (CD21)*, in [Online]. pp. 183–219.

Aisenbrey, S., Zhang, M., Bacher, D., Yee, J., Brunken, W.J. & Hunter, D.D. (2006) 'Retinal Pigment Epithelial Cells Synthesize Laminins, Including Laminin 5, and Adhere to Them through α3- and α6-Containing Integrins', *Investigative Opthalmology & Visual Science*, 47(12), p. 5537.

Alcon Research (2019) *Clinical trials: CLG561 Proof-of-Concept Study as a Monotherapy and in Combination With LFG316 in Subjects With Geographic Atrophy (GA). Available from: https://clinicaltrials.gov/study/NCT02515942*. [Online]

Alexion Pharmaceuticals, Inc. (2025) *Clinical trials: A Study of Danicopan in Participants With Geographic Atrophy Secondary to Age-Related Macular Degeneration. Available from: https://clinicaltrials.gov/study/NCT05019521?cond=NCT05019521&rank=1*. [Online]

Anderson, D.H., Ozaki, S., Nealon, M., Neitz, J., Mullins, R.F., Hageman, G.S. & Johnson, L. V (2001) 'Local cellular sources of apolipoprotein E in the human retina and retinal pigmented epithelium: implications for the process of drusen formation', *American Journal of Ophthalmology*, 131(6), pp. 767–781.

Annexon, I. (2024) *Clinical trials: A Study Investigating the Efficacy and Safety of Intravitreal Injections of ANX007 in Patients With Geographic Atrophy (ARCHER). Available from: https://clinicaltrials.gov/study/NCT04656561*. [Online]

Armento, A., Ueffing, M. & Clark, S.J. (2021) 'The complement system in age-related macular degeneration', *Cellular and Molecular Life Sciences*, 78(10), pp. 4487–4505.

Auguste, P., Javerzat, S. & Bikfalvi, A. (2003) 'Regulation of vascular development by fibroblast growth factors', *Cell and Tissue Research*, 314(1), pp. 157–166.

Bajic, G., Degn, S.E., Thiel, S. & Andersen, G.R. (2015) 'Complement activation, regulation, and molecular basis for complement-related diseases', *The EMBO Journal*, 34(22), pp. 2735–2757.

Bakri, S.J., Bektas, M., Sharp, D., Luo, R., Sarda, S.P. & Khan, S. (2023) 'Geographic atrophy: Mechanism of disease, pathophysiology, and role of the complement system', *Journal of Managed Care & Specialty Pharmacy*, 29(5-a Suppl), pp. S2–S11.

Bannister, A.J. & Kouzarides, T. (2011) 'Regulation of chromatin by histone modifications', *Cell Research*, 21(3), pp. 381–395.

Beattie, J.R., Pawlak, A.M., Boulton, M.E., Zhang, J., Monnier, V.M., McGarvey, J.J. & Stitt, A.W. (2010) 'Multiplex analysis of age-related protein and lipid modifications in human Bruch's membrane', *The FASEB Journal*, 24(12), pp. 4816–4824.

Benedicto, I., Lehmann, G.L., Ginsberg, M., Nolan, D.J., Bareja, R., Elemento, O., Salfati, Z., Alam, N.M., Prusky, G.T., Llanos, P., Rabbany, S.Y., Maminishkis, A., Miller, S.S., Rafii, S. & Rodriguez-Boulan, E. (2017) 'Concerted regulation of retinal pigment epithelium basement membrane and barrier function by angiocrine factors', *Nature Communications*, 8(1), p. 15374.

Bertolotti, E., Neri, A., Camparini, M., Macaluso, C. & Marigo, V. (2014) 'Stem cells as source for retinal pigment epithelium transplantation', *Progress in Retinal and Eye Research*, 42pp. 130–144.

Bhutto, I. & Lutty, G. (2012) 'Understanding age-related macular degeneration (AMD): Relationships between the photoreceptor/retinal pigment epithelium/Bruch's membrane/choriocapillaris complex', *Molecular Aspects of Medicine*, 33(4), pp. 295–317.

Bhutto, I.A. (2004) ‘Localization of Collagen XVIII and the Endostatin Portion of Collagen XVIII in Aged Human Control Eyes and Eyes with Age-Related Macular Degeneration’, *Investigative Ophthalmology & Visual Science*, 45(5), pp. 1544–1552.

Bhutto, I.A., Baba, T., Merges, C., Juriasinghani, V., McLeod, D.S. & Lutty, G.A. (2011) ‘C-reactive protein and complement factor H in aged human eyes and eyes with age-related macular degeneration’, *British Journal of Ophthalmology*, 95(9), pp. 1323–1330.

Bindu A, H. & B, S. (2011) ‘Potency of Various Types of Stem Cells and their Transplantation’, *Journal of Stem Cell Research & Therapy*, 01(03), .

Bio-techne. (2025) *Available from: https://www.bio-techne.com/resources/protocols-troubleshooting/elisa-direct-sandwich-protocol*. [Online]

Bird, A.C., Bressler, N.M., Bressler, S.B., Chisholm, I.H., Coscas, G., Davis, M.D., de Jong, P.T.V.M., Klaver, C.C.W., Klein, B.E.K., Klein, R., Mitchell, P., Sarks, J.P., Sarks, S.H., Soubrane, G., Taylor, H.R. & Vingerling, J.R. (1995) ‘An international classification and grading system for age-related maculopathy and age-related macular degeneration’, *Survey of Ophthalmology*, 39(5), pp. 367–374.

Blaauwgeers, H.G.T., Holtkamp, G.M., Rutten, H., Witmer, A.N., Koolwijk, P., Partanen, T.A., Alitalo, K., Kroon, M.E., Kijlstra, A., van Hinsbergh, V.W.M. & Schlingemann, R.O. (1999) ‘Polarized Vascular Endothelial Growth Factor Secretion by Human Retinal Pigment Epithelium and Localization of Vascular Endothelial Growth Factor Receptors on the Inner Choriocapillaris’, *The American Journal of Pathology*, 155(2), pp. 421–428.

Bok, D. (1993) ‘The retinal pigment epithelium: a versatile partner in vision’, *Journal of Cell Science*, 1993(Supplement_17), pp. 189–195.

Bonilha, V.L., Rayborn, M.E., Bhattacharya, S.K., Gu, X., Crabb, J.S., Crabb, J.W. & Hollyfield, J.G. (2006) ‘The Retinal Pigment Epithelium Apical Microvilli and Retinal Function’, in *Retinal Degenerative Diseases*. [Online]. Boston, MA: Springer US. pp. 519–524.

Booij, J.C., Baas, D.C., Beisekeeva, J., Gorgels, T.G.M.F. & Bergen, A.A.B. (2010) ‘The dynamic nature of Bruch’s membrane’, *Progress in Retinal and Eye Research*, 29(1), pp. 1–18.

Booij, J.C., van Soest, S., Swagemakers, S.M., Essing, A.H., Verkerk, A.J., van der Spek, P.J., Gorgels, T.G. & Bergen, A.A. (2009) ‘Functional annotation of the human retinal pigment epithelium transcriptome’, *BMC Genomics*, 10(1), p. 164.

Borrelli, E., Sarraf, D., Freund, K.B. & Sadda, S.R. (2018) ‘OCT angiography and evaluation of the choroid and choroidal vascular disorders’, *Progress in Retinal and Eye Research*, 67pp. 30–55.

Branchini, L.A., Adhi, M., Regatieri, C. V., Nandakumar, N., Liu, J.J., Laver, N., Fujimoto, J.G. & Duker, J.S. (2013) ‘Analysis of Choroidal Morphologic Features and Vasculature in Healthy Eyes Using Spectral-Domain Optical Coherence Tomography’, *Ophthalmology*, 120(9), pp. 1901–1908.

de Breuk, A., Acar, I.E., Kersten, E., Schijvenaars, M.M.V.A.P., Colijn, J.M., Haer-Wigman, L., Bakker, B., de Jong, S., Meester-Smoor, M.A., Verzijden, T., Missotten, T.O.A.R.,

Monés, J., Biarnés, M., Pauleikhoff, D., Hense, H.W., Silva, R., Nunes, S., Melo, J.B., Fauser, S., et al. (2021) 'Development of a Genotype Assay for Age-Related Macular Degeneration', *Ophthalmology*, 128(11), pp. 1604–1617.

Brinks, J., van Dijk, E.H.C., Klaassen, I., Schlingemann, R.O., Kielbasa, S.M., Emri, E., Quax, P.H.A., Bergen, A.A., Meijer, O.C. & Boon, C.J.F. (2022) 'Exploring the choroidal vascular labyrinth and its molecular and structural roles in health and disease', *Progress in Retinal and Eye Research*, 87p. 100994.

Brydon, E.M., Bronstein, R., Buskin, A., Lako, M., Pierce, E.A. & Fernandez-Godino, R. (2019) 'AAV-Mediated Gene Augmentation Therapy Restores Critical Functions in Mutant PRPF31+/− iPSC-Derived RPE Cells', *Molecular Therapy - Methods & Clinical Development*, 15pp. 392–402.

Cabral-Pacheco, G.A., Garza-Veloz, I., Castruita-De la Rosa, C., Ramirez-Acuña, J.M., Perez-Romero, B.A., Guerrero-Rodriguez, J.F., Martinez-Avila, N. & Martinez-Fierro, M.L. (2020) 'The Roles of Matrix Metalloproteinases and Their Inhibitors in Human Diseases', *International Journal of Molecular Sciences*, 21(24), p. 9739.

Cai, H., Gong, J., Del Priore, L. V., Tezel, T.H. & Fields, M.A. (2018) 'Culturing of Retinal Pigment Epithelial Cells on an Ex Vivo Model of Aged Human Bruch's Membrane', *Journal of Visualized Experiments*, (134), .

Call, T.W. & Hollyfield, J.G. (1990) 'Sulfated proteoglycans in Bruch's membrane of the human eye: Localization and characterization using cupromeronic blue', *Experimental Eye Research*, 51(4), pp. 451–462.

Campochiaro, P.A., Avery, R., Brown, D.M., Heier, J.S., Ho, A.C., Huddleston, S.M., Jaffe, G.J., Khanani, A.M., Pakola, S., Pieramici, D.J., Wykoff, C.C. & Van Everen, S. (2024) 'Gene therapy for neovascular age-related macular degeneration by subretinal delivery of RGX-314: a phase 1/2a dose-escalation study', *The Lancet*, 403(10436), pp. 1563–1573.

Capowski, E.E., Samimi, K., Mayerl, S.J., Phillips, M.J., Pinilla, I., Howden, S.E., Saha, J., Jansen, A.D., Edwards, K.L., Jager, L.D., Barlow, K., Valiauga, R., Erlichman, Z., Hagstrom, A., Sinha, D., Sluch, V.M., Chamling, X., Zack, D.J., Skala, M.C., et al. (2018) 'Reproducibility and staging of 3D human retinal organoids across multiple pluripotent stem cell lines', *Development*,

Carter, P.J. & Samulski, R.J. (2000) 'Adeno-associated viral vectors as gene delivery vehicles.', *International Journal of Molecular Medicine*,

Castellarin, A.A., Sugio, I.K., Vargas, J.A., Parolini, B., L, G.M. & Zarbin, M.A. (1998) 'In vitro Transplantation of Fetal Human Retinal Pigment Epithelial Cells onto Human Cadaver Bruch's Membrane', *Experimental Eye Research*, 66(1), pp. 49–68.

Cayman Chemical. DYKDDDDK-Tag Detection ELISA Kit. (2025) *Available from: https://www.caymanchem.com/product/501560/dykddddk-tag-detection-elisa-kit*. [Online]

Cayman Chemical. Glucose assay. (2025) *Available from: https://cdn.caymanchem.com/cdn/seawolf/insert/10009582.pdf*. [Online]

Cereso, N., Pequignot, M.O., Robert, L., Becker, F., De Luca, V., Nabholz, N., Rigau, V., De Vos, J., Hamel, C.P. & Kalatzis, V. (2014) 'Proof of concept for AAV2/5-mediated gene therapy in iPSC-derived retinal pigment epithelium of a choroideremia patient', *Molecular Therapy - Methods & Clinical Development*, 1p. 14011.

Cerniauskas, E., Kurzawa-Akanbi, M., Xie, L., Hallam, D., Moya-Molina, M., White, K., Steel, D., Doherty, M., Whitfield, P., Al-Aama, J., Armstrong, L., Kavanagh, D., Lambris, J.D., Korolchuk, V.I., Harris, C. & Lako, M. (2020) 'Complement modulation reverses pathology in Y402H-retinal pigment epithelium cell model of age-related macular degeneration by restoring lysosomal function', *Stem Cells Translational Medicine*, 9(12), pp. 1585–1603.

Chakravarthy, U., Bailey, C.C., Johnston, R.L., McKibbin, M., Khan, R.S., Mahmood, S., Downey, L., Dhingra, N., Brand, C., Brittain, C.J., Willis, J.R., Rabhi, S., Muthutantri, A. & Cantrell, R.A. (2018) 'Characterizing Disease Burden and Progression of Geographic Atrophy Secondary to Age-Related Macular Degeneration', *Ophthalmology*, 125(6), pp. 842–849.

Chatel, G. & Fahrenkrog, B. (2011) 'Nucleoporins: Leaving the nuclear pore complex for a successful mitosis', *Cellular Signalling*, 23(10), pp. 1555–1562.

Chen, L. (2003) 'Distribution of the collagen IV isoforms in human Bruch's membrane', *British Journal of Ophthalmology*, 87(2), pp. 212–215.

Chen, L.-J., Ito, S., Kai, H., Nagamine, K., Nagai, N., Nishizawa, M., Abe, T. & Kaji, H. (2017) 'Microfluidic co-cultures of retinal pigment epithelial cells and vascular endothelial cells to investigate choroidal angiogenesis', *Scientific Reports*, 7(1), p. 3538.

Chen, Y., Bedell, M. & Zhang, K. (2010) 'Age-related Macular Degeneration: Genetic and Environmental Factors of Disease', *Molecular Interventions*, 10(5), pp. 271–281.

Chengdu Kanghong Pharmaceutical Group Co., L. (2024a) *Clinical trial: Safety and Tolerability of KH631 Gene Therapy in Participants With Neovascular Age-related Macular Degeneration. Available from: https://clinicaltrials.gov/study/NCT05657301?cond=NCT05657301&rank=1*. [Online]

Chengdu Kanghong Pharmaceutical Group Co., L. (2024b) *Clinical trials: Safety and Tolerability of KH658 Gene Therapy in Subjects With Neovascular Age-related Macular Degeneration (nAMD). Available from: https://clinicaltrials.gov/study/NCT06458595?cond=NCT06458595&rank=1*. [Online]

Chichagova, V., Dorgau, B., Felemban, M., Georgiou, M., Armstrong, L. & Lako, M. (2019) 'Differentiation of Retinal Organoids from Human Pluripotent Stem Cells', *Current Protocols in Stem Cell Biology*, 50(1), .

Chinnery, H.R., McMenamin, P.G. & Dando, S.J. (2017) 'Macrophage physiology in the eye', *Pflügers Archiv - European Journal of Physiology*, 469(3–4), pp. 501–515.

Chirco, K.R., Worthington, K.S., Flamme-Wiese, M.J., Riker, M.J., Andrade, J.D., Ueberheide, B.M., Stone, E.M., Tucker, B.A. & Mullins, R.F. (2017) 'Preparation and evaluation of human choroid extracellular matrix scaffolds for the study of cell replacement strategies', *Acta Biomaterialia*, 57pp. 293–303.

Chong, N.H.V., Keonin, J., Luthert, P.J., Frennesson, C.I., Weingeist, D.M., Wolf, R.L., Mullins, R.F. & Hageman, G.S. (2005) 'Decreased Thickness and Integrity of the Macular Elastic Layer of Bruch's Membrane Correspond to the Distribution of Lesions Associated with Age-Related Macular Degeneration', *The American Journal of Pathology*, 166(1), pp. 241–251.

Clark, S.J., Higman, V.A., Mulloy, B., Perkins, S.J., Lea, S.M., Sim, R.B. & Day, A.J. (2006) 'His-384 Allotypic Variant of Factor H Associated with Age-related Macular Degeneration Has Different Heparin Binding Properties from the Non-disease-associated Form', *Journal of Biological Chemistry*, 281(34), pp. 24713–24720.

Clark, S.J., McHarg, S., Tilakaratna, V., Brace, N. & Bishop, P.N. (2017) 'Bruch's Membrane Compartmentalizes Complement Regulation in the Eye with Implications for Therapeutic Design in Age-Related Macular Degeneration', *Frontiers in Immunology*, 8.

Clark, S.J., Perveen, R., Hakobyan, S., Morgan, B.P., Sim, R.B., Bishop, P.N. & Day, A.J. (2010) 'Impaired Binding of the Age-related Macular Degeneration-associated Complement Factor H 402H Allotype to Bruch's Membrane in Human Retina', *Journal of Biological Chemistry*, 285(39), pp. 30192–30202.

Clark, S.J., Schmidt, C.Q., White, A.M., Hakobyan, S., Morgan, B.P. & Bishop, P.N. (2014) 'Identification of Factor H–like Protein 1 as the Predominant Complement Regulator in Bruch's Membrane: Implications for Age-Related Macular Degeneration', *The Journal of Immunology*, 193(10), pp. 4962–4970.

Collin, J., Hasoon, M.S.R., Zerti, D., Hammadi, S., Dorgau, B., Clarke, L., Steel, D., Hussain, R., Coxhead, J., Lisgo, S., Queen, R. & Lako, M. (2023) 'Single-cell RNA sequencing reveals transcriptional changes of human choroidal and retinal pigment epithelium cells during fetal development, in healthy adult and intermediate age-related macular degeneration', *Human Molecular Genetics*, 32(10), pp. 1698–1710.

Complement Therapeutics (n.d.) *Investigating Geographic Atrophy Insights (i-GAIN) Natural History Study (i-GAIN)*. [Online]

Cooper, N.R. & Müller-Eberhard, H.J. (1970) 'THE REACTION MECHANISM OF HUMAN C5 IN IMMUNE HEMOLYSIS', *The Journal of Experimental Medicine*, 132(4), pp. 775–793.

Cora, V., Haderspeck, J., Antkowiak, L., Mattheus, U., Neckel, P., Mack, A., Bolz, S., Ueffing, M., Pashkovskaia, N., Achberger, K. & Liebau, S. (2019) 'A Cleared View on Retinal Organoids', *Cells*, 8(5), p. 391.

Cousins, S.W. (2004) 'Monocyte Activation in Patients With Age-Related Macular Degeneration', *Archives of Ophthalmology*, 122(7), p. 1013.

Crabb, J.W., Miyagi, M., Gu, X., Shadrach, K., West, K.A., Sakaguchi, H., Kamei, M., Hasan, A., Yan, L., Rayborn, M.E., Salomon, R.G. & Hollyfield, J.G. (2002) 'Drusen proteome analysis: An approach to the etiology of age-related macular degeneration', *Proceedings of the National Academy of Sciences*, 99(23), pp. 14682–14687.

Cunha-Vaz, J., Bernardes, R. & Lobo, C. (2011) 'Blood-Retinal Barrier', *European Journal of Ophthalmology*, 21(6_suppl), pp. 3–9.

Curcio, C.A., Kar, D., Owsley, C., Sloan, K.R. & Ach, T. (2024) 'Age-Related Macular Degeneration, a Mathematically Tractable Disease', *Investigative Opthalmology & Visual Science*, 65(3), p. 4.

Curcio, C.A., Medeiros, N.E. & Millican, C.L. (1996) 'Photoreceptor loss in age-related macular degeneration.', *Investigative ophthalmology & visual science*, 37(7), pp. 1236–49.

Curcio, C.A., Millican, C.L., Bailey, T. & Kruth, H.S. (2001) 'Accumulation of cholesterol with age in human Bruch's membrane.', *Investigative ophthalmology & visual science*, 42(1), pp. 265–74.

D'Alba, L. & Shawkey, M.D. (2019) 'Melanosomes: Biogenesis, Properties, and Evolution of an Ancient Organelle', *Physiological Reviews*, 99(1), pp. 1–19.

Darland, D.C., Massingham, L.J., Smith, S.R., Piek, E., Saint-Geniez, M. & D'Amore, P.A. (2003) 'Pericyte production of cell-associated VEGF is differentiation-dependent and is associated with endothelial survival', *Developmental Biology*, 264(1), pp. 275–288.

Das, A. (1990) 'Ultrastructural Localization of Extracellular Matrix Components in Human Retinal Vessels and Bruch's Membrane', *Archives of Ophthalmology*, 108(3), p. 421.

Davies, K.A., Schifferli, J.A. & Walport, M.J. (1994) 'Complement deficiency and immune complex disease', *Springer Seminars in Immunopathology*, 15(4), pp. 397–416.

Dawson, D.W., Volpert, O. V., Gillis, P., Crawford, S.E., Xu, H.-J., Benedict, W. & Bouck, N.P. (1999) 'Pigment Epithelium-Derived Factor: A Potent Inhibitor of Angiogenesis', *Science*, 285(5425), pp. 245–248.

Day, A.J., Willis, A.C., Ripoche, J. & Sim, R.B. (1988) 'Sequence polymorphism of human complement factor H', *Immunogenetics*, 27(3), pp. 211–214.

DeWan, A., Liu, M., Hartman, S., Zhang, S.S.-M., Liu, D.T.L., Zhao, C., Tam, P.O.S., Chan, W.M., Lam, D.S.C., Snyder, M., Barnstable, C., Pang, C.P. & Hoh, J. (2006) '*HTRA1* Promoter Polymorphism in Wet Age-Related Macular Degeneration', *Science*, 314(5801), pp. 989–992.

Dong, L., Shi, X.H., Kang, Y.K., Wei, W. Bin, Wang, Y.X., Xu, X.L., Gao, F. & Jonas, J.B. (2019) 'Bruch's Membrane Thickness and Retinal Pigment Epithelium Cell Density in Experimental Axial Elongation', *Scientific Reports*, 9(1), p. 6621.

Dorgau, B., Georgiou, M., Chaudhary, A., Moya-Molina, M., Collin, J., Queen, R., Hilgen, G., Davey, T., Hewitt, P., Schmitt, M., Kustermann, S., Pognan, F., Steel, D.H., Sernagor, E., Armstrong, L. & Lako, M. (2022) 'Human Retinal Organoids Provide a Suitable Tool for Toxicological Investigations: A Comprehensive Validation Using Drugs and Compounds Affecting the Retina', *Stem Cells Translational Medicine*, 11(2), pp. 159–177.

Dykman, T.R., Hatch, J.A., Aqua, M.S. & Atkinson, J.P. (1985) 'Polymorphism of the C3b/C4b receptor (CR1): characterization of a fourth allele.', *Journal of immunology (Baltimore, Md. : 1950)*, 134(3), pp. 1787–9.

Edwards, M. & Lutty, G.A. (2021) *Bruch's Membrane and the Choroid in Age-Related Macular Degeneration*, in [Online]. pp. 89–119.

Ehlenberger, A.G. & Nussenzweig, V. (1977) 'The role of membrane receptors for C3b and C3d in phagocytosis.', *The Journal of experimental medicine*, 145(2), pp. 357–371.

Eilken, H.M., Diéguez-Hurtado, R., Schmidt, I., Nakayama, M., Jeong, H.-W., Arf, H., Adams, S., Ferrara, N. & Adams, R.H. (2017) 'Pericytes regulate VEGF-induced endothelial sprouting through VEGFR1', *Nature Communications*, 8(1), p. 1574.

Epstein, F.H., Schifferli, J.A., Ng, Y.C. & Peters, D.K. (1986) 'The Role of Complement and Its Receptor in the Elimination of Immune Complexes', *New England Journal of Medicine*, 315(8), pp. 488–495.

Erdei, A., Prechl, J., Isaak, A. & Molnar, E. (2003) 'Regulation of B-Cell Activation by Complement Receptors CD21 and CD35', *Current Pharmaceutical Design*, 9(23), pp. 1849–1860.

Exegenesis Bio (2025) *Clinical trial: A Study of EXG102-031 in Patients With wAMD (Everest). Available from: https://clinicaltrials.gov/study/NCT05903794*. [Online]

Faber, C., Jehs, T., Juel, H.B., Singh, A., Falk, M.K., Sørensen, T.L. & Nissen, M.H. (2015) 'Early and exudative age-related macular degeneration is associated with increased plasma levels of soluble <scp>TNF</scp> receptor <scp>II</scp>', *Acta Ophthalmologica*, 93(3), pp. 242–247.

Fearon, D. (1980) 'Identification of the membrane glycoprotein that is the C3b receptor of the human erythrocyte, polymorphonuclear leukocyte, B lymphocyte, and monocyte', *The Journal of Experimental Medicine*, 152(1), pp. 20–30.

Fearon, D.T. (1979) 'Regulation of the amplification C3 convertase of human complement by an inhibitory protein isolated from human erythrocyte membrane', *Proceedings of the National Academy of Sciences*, 76(11), pp. 5867–5871.

Fearon, D.T. & Austen, K.F. (1975) 'Properdin: binding to C3b and stabilization of the C3b-dependent C3 convertase.', *The Journal of experimental medicine*, 142(4), pp. 856–863.

Fearon, D.T., Kaneko, I. & Thomson, G.G. (1981) 'Membrane distribution and adsorptive endocytosis by C3b receptors on human polymorphonuclear leukocytes.', *The Journal of experimental medicine*, 153(6), pp. 1615–1628.

Fernandez-Godino, R., Bujakowska, K.M. & Pierce, E.A. (2018) 'Changes in extracellular matrix cause RPE cells to make basal deposits and activate the alternative complement pathway', *Human Molecular Genetics*, 27(1), pp. 147–159.

Fernando, M., Lee, S., Wark, J.R., Xiao, D., Lim, B.Y., O'Hara-Wright, M., Kim, H.J., Smith, G.C., Wong, T., Teber, E.T., Ali, R.R., Yang, P., Graham, M.E. & Gonzalez-Cordero, A. (2022) 'Differentiation of brain and retinal organoids from confluent cultures of pluripotent stem cells connected by nerve-like axonal projections of optic origin', *Stem Cell Reports*, 17(6), pp. 1476–1492.

Fett, A.L., Hermann, M.M., Muether, P.S., Kirchhof, B. & Fauser, S. (2012) 'Immunohistochemical localization of complement regulatory proteins in the human retina.', *Histology and histopathology*, 27(3), pp. 357–64.

Fisher, C.R., Ebeling, M.C., Geng, Z., Kapphahn, R.J., Roehrich, H., Montezuma, S.R., Dutton, J.R. & Ferrington, D.A. (2022) 'Human iPSC- and Primary-Retinal Pigment Epithelial Cells for Modeling Age-Related Macular Degeneration.', *Antioxidants (Basel, Switzerland)*, 11(4), .

Fritsche L, C.W.S.M. and et al (2013) 'Seven new loci associated with age-related macular degeneration', *Nature Genetics*, 45(4), pp. 433–439.

Fritsche, L.G., Igl, W., Bailey, J.N.C., Grassmann, F., Sengupta, S., Bragg-Gresham, J.L., Burdon, K.P., Hebbring, S.J., Wen, C., Gorski, M., Kim, I.K., Cho, D., Zack, D., Souied, E., Scholl, H.P.N., Bala, E., Lee, K.E., Hunter, D.J., Sardell, R.J., et al. (2016) 'A large genome-wide association study of age-related macular degeneration highlights contributions of rare and common variants', *Nature Genetics*, 48(2), pp. 134–143.

Frontera Therapeutics (2023) *Clinical trials: Gene Therapy for Wet AMD. Available from: https://clinicaltrials.gov/study/NCT05611424*. [Online]

Galloway, C.A., Dalvi, S., Shadforth, A.M.A., Suzuki, S., Wilson, M., Kuai, D., Hashim, A., MacDonald, L.A., Gamm, D.M., Harkin, D.G. & Singh, R. (2018) 'Characterization of Human iPSC-RPE on a Prosthetic Bruch's Membrane Manufactured From Silk Fibroin', *Investigative Opthalmology & Visual Science*, 59(7), p. 2792.

Garita-Hernandez, M., Routet, F., Guibbal, L., Khabou, H., Toualbi, L., Riancho, L., Reichman, S., Duebel, J., Sahel, J.-A., Goureau, O. & Dalkara, D. (2020) 'AAV-Mediated Gene Delivery to 3D Retinal Organoids Derived from Human Induced Pluripotent Stem Cells', *International Journal of Molecular Sciences*, 21(3), p. 994.

Gemini Therapeutics, I. (2021) *Clinical trials: First in Human Study to Evaluate the Safety and Tolerability of GEM103 in Geographic Atrophy Secondary to Dry Age Related Macular Degeneration. Available from: https://clinicaltrials.gov/study/NCT04246866?cond=NCT04246866&rank=1*. [Online]

Geng, Z., Walsh, P.J., Truong, V., Hill, C., Ebeling, M., Kapphahn, R.J., Montezuma, S.R., Yuan, C., Roehrich, H., Ferrington, D.A. & Dutton, J.R. (2017) 'Generation of retinal pigmented epithelium from iPSCs derived from the conjunctiva of donors with and without age related macular degeneration', *PLOS ONE*, 12(3), p. e0173575.

Gerwins, P., Sköldenberg, E. & Claesson-Welsh, L. (2000) 'Function of fibroblast growth factors and vascular endothelial growth factors and their receptors in angiogenesis', *Critical Reviews in Oncology/Hematology*, 34(3), pp. 185–194.

Glenn, J. V., Mahaffy, H., Wu, K., Smith, G., Nagai, R., Simpson, D.A.C., Boulton, M.E. & Stitt, A.W. (2009) 'Advanced Glycation End Product (AGE) Accumulation on Bruch's Membrane: Links to Age-Related RPE Dysfunction', *Investigative Opthalmology & Visual Science*, 50(1), p. 441.

Gong, J., Cai, H., Noggle, S., Paull, D., Rizzolo, L.J., Del Priore, L. V. & Fields, M.A. (2020) 'Stem cell-derived retinal pigment epithelium from patients with age-related macular

degeneration exhibit reduced metabolism and matrix interactions', *Stem Cells Translational Medicine*, 9(3), pp. 364–376.

Gonzalez-Cordero, A., Goh, D., Kruczek, K., Naeem, A., Fernando, M., kleine Holthaus, S.-M., Takaaki, M., Blackford, S.J.I., Kloc, M., Agundez, L., Sampson, R.D., Borooah, S., Ovando-Roche, P., Mehat, M.S., West, E.L., Smith, A.J., Pearson, R.A. & Ali, R.R. (2018) 'Assessment of AAV Vector Tropisms for Mouse and Human Pluripotent Stem Cell–Derived RPE and Photoreceptor Cells', *Human Gene Therapy*, 29(10), pp. 1124–1139.

Gullapalli, V.K., Sugino, I.K., Van Patten, Y., Shah, S. & Zarbin, M.A. (2005) 'Impaired RPE survival on aged submacular human Bruch's membrane', *Experimental Eye Research*, 80(2), pp. 235–248.

Gullapalli, V.K., Sugino, I.K. & Zarbin, M.A. (2008) 'Culture-induced increase in alpha integrin subunit expression in retinal pigment epithelium is important for improved resurfacing of aged human Bruch's membrane', *Experimental Eye Research*, 86(2), pp. 189–200.

Guo, L., Hussain, A.A., Limb, G.A. & Marshall, J. (1999) 'Age-dependent variation in metalloproteinase activity of isolated human Bruch's membrane and choroid.', *Investigative ophthalmology & visual science*, 40(11), pp. 2676–82.

Guymer, R., Luthert, P. & Bird, A. (1999) 'Changes in Bruch's membrane and related structures with age', *Progress in Retinal and Eye Research*, 18(1), pp. 59–90.

Gyroscope Therapeutics (2024a) *Clinical trials: EXPLORE: A Phase II Study to Evaluate the Safety and Efficacy of Two Doses of GT005 (EXPLORE). Available from: https://clinicaltrials.gov/study/NCT04437368?cond=NCT04437368&rank=1*. [Online]

Gyroscope Therapeutics (2024b) *Clinical trials: FOCUS: A Phase I/II First in Human Study to Evaluate the Safety and Efficacy of GT005 Administered in Subjects With Dry AMD. Available from: https://clinicaltrials.gov/study/NCT03846193?cond=NCT03846193&rank=1*. [Online]

Hallam, D., Collin, J., Bojic, S., Chichagova, V., Buskin, A., Xu, Y., Lafage, L., Otten, Elsje.G., Anyfantis, G., Mellough, C., Przyborski, S., Alharthi, S., Korolchuk, V., Lotery, A., Saretzki, G., McKibbin, M., Armstrong, L., Steel, D., Kavanagh, D., et al. (2017) 'An Induced Pluripotent Stem Cell Patient Specific Model of Complement Factor H (Y402H) Polymorphism Displays Characteristic Features of Age-Related Macular Degeneration and Indicates a Beneficial Role for UV Light Exposure', *Stem Cells*, 35(11), pp. 2305–2320.

Hallam, D., Hilgen, G., Dorgau, B., Zhu, L., Yu, M., Bojic, S., Hewitt, P., Schmitt, M., Uteng, M., Kustermann, S., Steel, D., Nicholds, M., Thomas, R., Treumann, A., Porter, A., Sernagor, E., Armstrong, L. & Lako, M. (2018) 'Human-Induced Pluripotent Stem Cells Generate Light Responsive Retinal Organoids with Variable and Nutrient-Dependent Efficiency', *Stem Cells*, 36(10), pp. 1535–1551.

Hallam, T.M., Gardenal, E., McBlane, F., Cho, G., Ferraro, L.L., Pekle, E., Lu, D., Carney, K., Wenden, C., Beadsmoore, H., Kaiser, S., Drage, L., Haye, T., Kassem, I., Rangaswamy, N., Obeidat, M., Grosskreutz, C., Saint-Geniez, M., Steel, D.H., et al.

(2024a) *Ocular biomarker profiling after complement factor I gene therapy in geographic atrophy secondary to age-related macular degeneration*.

Hallam, T.M., Gardenal, E., McBlane, F., Cho, G., Ferraro, L.L., Pekle, E., Lu, D., Carney, K., Wenden, C., Beadsmoore, H., Kaiser, S., Drage, L., Haye, T., Kassem, I., Rangaswamy, N., Obeidat, M., Grosskreutz, C., Saint-Geniez, M., Steel, D.H., et al. (2024b) *Ocular biomarker profiling after complement factor I gene therapy in geographic atrophy secondary to age-related macular degeneration*.

Hallam, T.M., Marchbank, K.J., Harris, C.L., Osmond, C., Shuttleworth, V.G., Griffiths, H., Cree, A.J., Kavanagh, D. & Lotery, A.J. (2020) 'Rare Genetic Variants in Complement Factor I Lead to Low FI Plasma Levels Resulting in Increased Risk of Age-Related Macular Degeneration', *Investigative Opthalmology & Visual Science*, 61(6), p. 18.

HAMER, I., PACCAUD, J.-P., BELIN, D., MAEDER, C. & CARPENTIER, J.-L. (1998) 'Soluble form of complement C3b/C4b receptor (CR1) results from a proteolytic cleavage in the C-terminal region of CR1 transmembrane domain', *Biochemical Journal*, 329(1), pp. 183–190.

Hamilton, R.D., Foss, A.J. & Leach, L. (2007) 'Establishment of a human in vitro model of the outer blood-retinal barrier', *Journal of Anatomy*, 211(6), pp. 707–716.

Handa, J.T., Verzijl, N., Matsunaga, H., Aotaki-Keen, A., Lutty, G.A., te Koppele, J.M., Miyata, T. & Hjelmeland, L.M. (1999a) 'Increase in the advanced glycation end product pentosidine in Bruch's membrane with age.', *Investigative ophthalmology & visual science*, 40(3), pp. 775–9.

Handa, J.T., Verzijl, N., Matsunaga, H., Aotaki-Keen, A., Lutty, G.A., te Koppele, J.M., Miyata, T. & Hjelmeland, L.M. (1999b) 'Increase in the advanced glycation end product pentosidine in Bruch's membrane with age.', *Investigative ophthalmology & visual science*, 40(3), pp. 775–9.

Harris, T.I., Paterson, C.A., Farjood, F., Wadsworth, I.D., Caldwell, L., Lewis, R. V., Jones, J.A. & Vargis, E. (2019) 'Utilizing Recombinant Spider Silk Proteins To Develop a Synthetic Bruch's Membrane for Modeling the Retinal Pigment Epithelium', *ACS Biomaterials Science & Engineering*, 5(8), pp. 4023–4036.

Hasegawa, T., McLeod, D.S., Bhutto, I.A., Prow, T., Merges, C.A., Grebe, R. & Lutty, G.A. (2007) 'The embryonic human choriocapillaris develops by hemo-vasculogenesis', *Developmental Dynamics*, 236(8), pp. 2089–2100.

Hayes, M.J., Burgoyne, T., Wavre-Shapton, S.T., Tolmachova, T., Seabra, M.C. & Futter, C.E. (2019) 'Remodeling of the Basal Labyrinth of Retinal Pigment Epithelial Cells With Osmotic Challenge, Age, and Disease', *Investigative Opthalmology & Visual Science*, 60(7), p. 2515.

Hayreh, S.S. (2004) 'Posterior Ciliary Artery Circulation in Health and Disease The Weisenfeld Lecture', *Investigative Opthalmology & Visual Science*, 45(3), p. 749.

He, W., Han, X., Ong, J.-S., Wu, Y., Hewitt, A.W., Mackey, D.A., Gharahkhani, P. & MacGregor, S. (2024) 'Genome-Wide Meta-analysis Identifies Risk Loci and Improves Disease Prediction of Age-Related Macular Degeneration', *Ophthalmology*, 131(1), pp. 16–29.

He, X., Hahn, P., Iacovelli, J., Wong, R., King, C., Bhisitkul, R., Massaro-Giordano, M. & Dunaief, J.L. (2007) 'Iron homeostasis and toxicity in retinal degeneration', *Progress in Retinal and Eye Research*, 26(6), pp. 649–673.

Heavner, W. & Pevny, L. (2012) 'Eye Development and Retinogenesis', *Cold Spring Harbor Perspectives in Biology*, 4(12), pp. a008391–a008391.

Heesterbeek, T.J., Lechanteur, Y.T.E., Lorés-Motta, L., Schick, T., Daha, M.R., Altay, L., Liakopoulos, S., Smailhodzic, D., den Hollander, A.I., Hoyng, C.B., de Jong, E.K. & Klevering, B.J. (2020) 'Complement Activation Levels Are Related to Disease Stage in AMD', *Investigative Opthalmology & Visual Science*, 61(3), p. 18.

Heier, J.S., Lad, E.M., Holz, F.G., Rosenfeld, P.J., Guymer, R.H., Boyer, D., Grossi, F., Baumal, C.R., Korobelnik, J.-F., Slakter, J.S., Waheed, N.K., Metlapally, R., Pearce, I., Steinle, N., Francone, A.A., Hu, A., Lally, D.R., Deschatelets, P., Francois, C., et al. (2023) 'Pegcetacoplan for the treatment of geographic atrophy secondary to age-related macular degeneration (OAKS and DERBY): two multicentre, randomised, double-masked, sham-controlled, phase 3 trials', *The Lancet*, 402(10411), pp. 1434–1448.

Hillenkamp, J. (2004) 'The Influence of Path Length and Matrix Components on Ageing Characteristics of Transport between the Choroid and the Outer Retina', *Investigative Ophthalmology & Visual Science*, 45(5), pp. 1493–1498.

Ho, T.C. & Del Priore, L. V (1997) 'Reattachment of cultured human retinal pigment epithelium to extracellular matrix and human Bruch's membrane.', *Investigative ophthalmology & visual science*, 38(6), pp. 1110–8.

Hoffmann-La Roche (2019a) *Clinical trials: A Study Investigating the Safety and Efficacy of Lampalizumab Intravitreal Injections in Participants With Geographic Atrophy Secondary to Age-Related Macular Degeneration (SPECTRI). Available from: https://clinicaltrials.gov/study/NCT02247531*. [Online]

Hoffmann-La Roche (2019b) *Clinicla trials: A Study Investigating the Efficacy and Safety of Lampalizumab Intravitreal Injections in Participants With Geographic Atrophy Secondary to Age-Related Macular Degeneration (CHROMA). Available from: https://clinicaltrials.gov/study/NCT02247479*. [Online]

Hookham, M.B., Ali, I.H.A., O'Neill, C.L., Hackett, E., Lambe, M.H., Schmidt, T., Medina, R.J., Chamney, S., Rao, B., McLoone, E., Sweet, D., Stitt, A.W. & Brazil, D.P. (2016) 'Hypoxia-induced responses by endothelial colony-forming cells are modulated by placental growth factor', *Stem Cell Research & Therapy*, 7(1), p. 173.

Horai, R., Silver, P.B., Chen, J., Agarwal, R.K., Chong, W.P., Jittayasothorn, Y., Mattapallil, M.J., Nguyen, S., Natarajan, K., Villasmil, R., Wang, P., Karabekian, Z., Lytton, S.D., Chan, C.C. & Caspi, R.R. (2013) 'Breakdown of immune privilege and spontaneous autoimmunity in mice expressing a transgenic T cell receptor specific for a retinal autoantigen', *Journal of Autoimmunity*, 44pp. 21–33.

Huang, J.-D., Curcio, C.A. & Johnson, M. (2008) 'Morphometric Analysis of Lipoprotein-like Particle Accumulation in Aging Human Macular Bruch's Membrane', *Investigative Opthalmology & Visual Science*, 49(6), p. 2721.

HuidaGene Therapeutics Co., L. (2025) *Clinical trial: CRISPR/cas13-medIated RNA tarGeting tHerapy for the Treatment of Neovascular Age-related Macular Degeneration Investigator-initiated Trial (SIGHT-I). Available from: https://clinicaltrials.gov/study/NCT06031727?cond=NCT06031727&rank=1*. [Online]

Hussain, A.A., Starita, C., Hodgetts, A. & Marshall, J. (2010) 'Macromolecular diffusion characteristics of ageing human Bruch's membrane: Implications for age-related macular degeneration (AMD)', *Experimental Eye Research*, 90(6), pp. 703–710.

Hutson, T.H., Kathe, C., Menezes, S.C., Rooney, M.-C., Bueler, H. & Moon, L.D.F. (2014) *The Use of an Adeno-Associated Viral Vector for Efficient Bicistronic Expression of Two Genes in the Central Nervous System*, in [Online]. pp. 189–207.

Iida, K. & Nussenzweig, V. (1981) 'Complement receptor is an inhibitor of the complement cascade.', *The Journal of experimental medicine*, 153(5), pp. 1138–1150.

Innostellar Biotherapeutics Co., L. (2024a) *Clinical trial: LX102 in Patients With Neovascular Age-Related Macular Degeneration (nAMD). Available from: https://clinicaltrials.gov/study/NCT06198413*. [Online]

Innostellar Biotherapeutics Co., L. (2024b) *Clinical trial: Safety and Efficacy of LX102 Gene Therapy in Patients With Neovascular Age-related Macular Degeneration (nAMD) (VENUS). Available from: https://clinicaltrials.gov/study/NCT06196840*. [Online]

Innovent Biologics (Suzhou) Co. Ltd. (2024) *Clinical trials: A Study of IBI302 in Patients With nAMD. Available from: https://clinicaltrials.gov/study/NCT04820452?cond=nct04820452&rank=1*. [Online]

Innovent Biologics (Suzhou) Co. Ltd. (2021) *Clinical trials: Trial to Evaluate the Safety and Tolerability of Repeated Intravitreal Injection of IBI302 in Neovascular AMD Patients. Available from: https://clinicaltrials.gov/study/NCT04370379?cond=NCT04370379&rank=1*. [Online]

Innovent Biologics (Suzhou) Co. Ltd (2025) *Clinicla trials: A Dose Escalation Study of IBI302 in Patients With Wet Age-related Macular Degeneration. Available from: https://clinicaltrials.gov/study/NCT03814291?cond=NCT03814291&rank=1*. [Online]

Innovent Biologics (Suzhou) Co. Ltd (2024) *Clinicla trials: A Study of Longer Interval of IVT IBI302 in Subjects With nAMD. Available from: https://clinicaltrials.gov/study/NCT05403749?cond=nct05403749&rank=1*. [Online]

Invitrogen. CyQUANT™ LDH Cytotoxicity Assay Kit. (2025) *Available from: https://www.thermofisher.com/document-connect/document-connect.html?url=https://assets.thermofisher.com/TFS-Assets%2FLSG%2Fmanuals%2FMAN0018500_CyQUANT-LDH-Cytotoxicity-Assay-Kit_PI.pdf*. [Online]

Ionis Pharmaceuticals, I. (2025) *Clinical trials: GOLDEN STUDY: A Study to Assess Safety and Efficacy of Multiple Doses of IONIS-FB-LRx in Participants With Geographic Atrophy Secondary to Age-Related Macular Degeneration (AMD). Available from: https://clinicaltrials.gov/study/NCT03815825?cond=NCT03815825&rank=1*. [Online]

Issa, S.S., Shaimardanova, A.A., Solovyeva, V. V. & Rizvanov, A.A. (2023) 'Various AAV Serotypes and Their Applications in Gene Therapy: An Overview', *Cells*, 12(5), p. 785.

Iyengar, S.K., Song, D., Klein, B.E.K., Klein, R., Schick, J.H., Humphrey, J., Millard, C., Liptak, R., Russo, K., Jun, G., Lee, K.E., Fijal, B. & Elston, R.C. (2004) 'Dissection of Genomewide-Scan Data in Extended Families Reveals a Major Locus and Oligogenic Susceptibility for Age-Related Macular Degeneration', *The American Journal of Human Genetics*, 74(1), pp. 20–39.

Jaffe, G.J., Westby, K., Csaky, K.G., Monés, J., Pearlman, J.A., Patel, S.S., Joondeph, B.C., Randolph, J., Masonson, H. & Rezaei, K.A. (2021) 'C5 Inhibitor Avacincaptad Pegol for Geographic Atrophy Due to Age-Related Macular Degeneration', *Ophthalmology*, 128(4), pp. 576–586.

Janssen Research & Development (2025) *Clinical trial: A Study to Evaluate Intravitreal JNJ-81201887 (AAVCAGsCD59) Compared to Sham Procedure for the Treatment of Geographic Atrophy (GA) Secondary to Age-related Macular Degeneration (AMD). Available from: https://clinicaltrials.gov/study/NCT05811351?cond=NCT05811351&rank=1*. [Online]

Janssen Research & Development, L. (2025a) *Clinical trial: AAVCAGsCD59 for the Treatment of Wet AMD. Available from: https://clinicaltrials.gov/study/NCT03585556?cond=NCT03585556&rank=1*. [Online]

Janssen Research & Development, L. (2025b) *Clinical trials: Treatment of Advanced Dry Age Related Macular Degeneration With AAVCAGsCD59. Available from: https://clinicaltrials.gov/study/NCT03144999?cond=NCT03144999&rank=1*. [Online]

Javerzat, S., Auguste, P. & Bikfalvi, A. (2002) 'The role of fibroblast growth factors in vascular development', *Trends in Molecular Medicine*, 8(10), pp. 483–489.

Józsi, M., Prechl, J., Bajtay, Z. & Erdei, A. (2002) 'Complement Receptor Type 1 (CD35) Mediates Inhibitory Signals in Human B Lymphocytes', *The Journal of Immunology*, 168(6), pp. 2782–2788.

Kamei, M. & Hollyfield, J.G. (1999) 'TIMP-3 in Bruch's membrane: changes during aging and in age-related macular degeneration.', *Investigative ophthalmology & visual science*, 40(10), pp. 2367–75.

Karthikeyan, G., Baalasubramanian, S., Seth, S. & Das, N. (2007) 'Low levels of plasma soluble complement receptor type 1 in patients receiving thrombolytic therapy for acute myocardial infarction', *Journal of Thrombosis and Thrombolysis*, 23(2), pp. 115–120.

Ke, X., Jiang, H., Li, Q., Luo, S., Qin, Y., Li, J., Xie, Q. & Zheng, Q. (2023) 'Preclinical evaluation of KH631, a novel rAAV8 gene therapy product for neovascular age-related macular degeneration', *Molecular Therapy*, 31(11), pp. 3308–3321.

Keefe D, Munye M, Hasan R, Rathi s, Bishop P & Clark S (2023) 'CTx001, a gene therapy for the treatment of geographic atrophy in aged-related macular degeneration', *Investigative Opthalmology & Visual Science*, 64(8), p. 3852.

Keenan, T.D.L., Pickford, C.E., Holley, R.J., Clark, S.J., Lin, W., Dowsey, A.W., Merry, C.L., Day, A.J. & Bishop, P.N. (2014) 'Age-Dependent Changes in Heparan Sulfate in

Human Bruch's Membrane: Implications for Age-Related Macular Degeneration', *Investigative Opthalmology & Visual Science*, 55(8), p. 5370.

Keenan, T.D.L., Toso, M., Pappas, C., Nichols, L., Bishop, P.N. & Hageman, G.S. (2015) 'Assessment of Proteins Associated With Complement Activation and Inflammation in Maculae of Human Donors Homozygous Risk at Chromosome 1 *CFH* -to- *F13B*', *Investigative Opthalmology & Visual Science*, 56(8), p. 4870.

Kezic, J. & McMenamin, P.G. (2008) 'Differential turnover rates of monocyte-derived cells in varied ocular tissue microenvironments', *Journal of Leukocyte Biology*, 84(3), pp. 721–729.

Khanani, A.M., Patel, S.S., Staurenghi, G., Tadayoni, R., Danzig, C.J., Eichenbaum, D.A., Hsu, J., Wykoff, C.C., Heier, J.S., Lally, D.R., Monés, J., Nielsen, J.S., Sheth, V.S., Kaiser, P.K., Clark, J., Zhu, L., Patel, H., Tang, J., Desai, D., et al. (2023) 'Efficacy and safety of avacincaptad pegol in patients with geographic atrophy (GATHER2): 12-month results from a randomised, double-masked, phase 3 trial', *The Lancet*, 402(10411), pp. 1449–1458.

Khandhadia, S., Hakobyan, S., Heng, L.Z., Gibson, J., Adams, D.H., Alexander, G.J., Gibson, J.M., Martin, K.R., Menon, G., Nash, K., Sivaprasad, S., Ennis, S., Cree, A.J., Morgan, B.P. & Lotery, A.J. (2013) 'Age-related Macular Degeneration and Modification of Systemic Complement Factor H Production Through Liver Transplantation', *Ophthalmology*, 120(8), pp. 1612–1618.

Khodamoradi, M., Eskandari, M., Keshvari, H. & Zarei, R. (2021) 'An electro-conductive hybrid scaffold as an artificial Bruch's membrane', *Materials Science and Engineering: C*, 126p. 112180.

Kim, I., Moon, S.-O., Park, S.K., Chae, S.W. & Koh, G.Y. (2001) 'Angiopoietin-1 Reduces VEGF-Stimulated Leukocyte Adhesion to Endothelial Cells by Reducing ICAM-1, VCAM-1, and E-Selectin Expression', *Circulation Research*, 89(6), pp. 477–479.

Kim, J., Kong, J.S., Kim, H., Jo, Y., Cho, D. & Jang, J. (2022) 'A Bioprinted Bruch's Membrane for Modeling Smoke-Induced Retinal Pigment Epithelium Degeneration via Hybrid Membrane Printing Technology', *Advanced Healthcare Materials*, 11(24), .

Kim, J., Park, J.Y., Kong, J.S., Lee, H., Won, J.Y. & Cho, D.W. (2021) 'Development of 3D Printed Bruch's Membrane-Mimetic Substance for the Maturation of Retinal Pigment Epithelial Cells', *International Journal of Molecular Sciences*, 22(3), p. 1095.

Kisserli, A., Tabary, T., Cohen, J.H.M., Duret, V. & Mahmoudi, R. (2017) 'High-resolution Melting PCR for Complement Receptor 1 Length Polymorphism Genotyping: An Innovative Tool for Alzheimer's Disease Gene Susceptibility Assessment', *Journal of Visualized Experiments*, (125), .

Klein, R.J., Zeiss, C., Chew, E.Y., Tsai, J.-Y., Sackler, R.S., Haynes, C., Henning, A.K., SanGiovanni, J.P., Mane, S.M., Mayne, S.T., Bracken, M.B., Ferris, F.L., Ott, J., Barnstable, C. & Hoh, J. (2005) 'Complement Factor H Polymorphism in Age-Related Macular Degeneration', *Science*, 308(5720), pp. 385–389.

Klickstein, L.B., Wong, W.W., Smith, J.A., Weis, J.H., Wilson, J.G. & Fearon, D.T. (1987) 'Human C3b/C4b receptor (CR1). Demonstration of long homologous repeating domains

that are composed of the short consensus repeats characteristics of C3/C4 binding proteins.', *The Journal of experimental medicine*, 165(4), pp. 1095–1112.

Kobayashi, Y., Yoshida, S., Zhou, Y., Nakama, T., Ishikawa, K., Kubo, Y., Arima, M., Nakao, S., Hisatomi, T., Ikeda, Y., Matsuda, A., Sonoda, K.-H. & Ishibashi, T. (2016) 'Tenascin-C secreted by transdifferentiated retinal pigment epithelial cells promotes choroidal neovascularization via integrin αV', *Laboratory Investigation*, 96(11), pp. 1178–1188.

Kolb, H., Nelson, R.F., Ahnelt, P.K., Ortuño-Lizarán, I. & Cuenca, N. (1995) *The Architecture of the Human Fovea*.

Kortvely, E., Hauck, S.M., Duetsch, G., Gloeckner, C.J., Kremmer, E., Alge-Priglinger, C.S., Deeg, C.A. & Ueffing, M. (2010) 'ARMS2 Is a Constituent of the Extracellular Matrix Providing a Link between Familial and Sporadic Age-Related Macular Degenerations', *Investigative Opthalmology & Visual Science*, 51(1), p. 79.

Kremlitzka, M., Polgar, A., Fulop, L., Kiss, E., Poor, G. & Erdei, A. (2013) 'Complement receptor type 1 (CR1, CD35) is a potent inhibitor of B-cell functions in rheumatoid arthritis patients', *International Immunology*, 25(1), pp. 25–33.

Krogh Nielsen, M., Subhi, Y., Molbech, C.R., Falk, M.K., Nissen, M.H. & Sørensen, T.L. (2019) 'Systemic Levels of Interleukin-6 Correlate With Progression Rate of Geographic Atrophy Secondary to Age-Related Macular Degeneration', *Investigative Opthalmology & Visual Science*, 60(1), p. 202.

Krych-Goldberg, M. & Atkinson, J.P. (2001) 'Structure–function relationships of complement receptor type 1', *Immunological Reviews*, 180(1), pp. 112–122.

Kundu, J., Michaelson, A., Talbot, K., Baranov, P., Young, M.J. & Carrier, R.L. (2016) 'Decellularized retinal matrix: Natural platforms for human retinal progenitor cell culture', *Acta Biomaterialia*, 31pp. 61–70.

Kur, J., Newman, E.A. & Chan-Ling, T. (2012) 'Cellular and physiological mechanisms underlying blood flow regulation in the retina and choroid in health and disease', *Progress in Retinal and Eye Research*, 31(5), pp. 377–406.

Kurzawa-Akanbi, M., Tzoumas, N., Corral-Serrano, J.C., Guarascio, R., Steel, D.H., Cheetham, M.E., Armstrong, L. & Lako, M. (2024) 'Pluripotent stem cell-derived models of retinal disease: Elucidating pathogenesis, evaluating novel treatments, and estimating toxicity', *Progress in Retinal and Eye Research*, 100p. 101248.

Lachmann, P.J. (2019) 'The story of complement factor I', *Immunobiology*, 224(4), pp. 511–517.

Lachmann, P.J., Lay, E. & Seilly, D.J. (2018) 'A novel and sensitive functional assay for complement Factor I based on the third proteolytic clip of C3b', *Journal of Immunological Methods*, 457pp. 30–32.

Ladha, R., Caspers, L.E., Willermain, F. & de Smet, M.D. (2022) 'Subretinal Therapy: Technological Solutions to Surgical and Immunological Challenges', *Frontiers in Medicine*, 9.

Landowski, M., Kelly, U., Klingeborn, M., Groelle, M., Ding, J.-D., Grigsby, D. & Bowes Rickman, C. (2019) 'Human complement factor H Y402H polymorphism causes an age-related macular degeneration phenotype and lipoprotein dysregulation in mice', *Proceedings of the National Academy of Sciences*, 116(9), pp. 3703–3711.

Lee, Y., Hussain, A.A., Seok, J.-H., Kim, S.-H. & Marshall, J. (2015) 'Modulating the Transport Characteristics of Bruch's Membrane With Steroidal Glycosides and its Relevance to Age-Related Macular Degeneration (AMD)', *Investigative Opthalmology & Visual Science*, 56(13), p. 8403.

Lejoyeux, R., Benillouche, J., Ong, J., Errera, M.-H., Rossi, E.A., Singh, S.R., Dansingani, K.K., da Silva, S., Sinha, D., Sahel, J.-A., Freund, K.B., Sadda, S.R., Lutty, G.A. & Chhablani, J. (2022) 'Choriocapillaris: Fundamentals and advancements', *Progress in Retinal and Eye Research*, 87p. 100997.

Lin, W.L., Essner, E., McCarthy, K.J. & Couchman, J.R. (1992) 'Ultrastructural immunocytochemical localization of chondroitin sulfate proteoglycan in Bruch's membrane of the rat.', *Investigative ophthalmology & visual science*, 33(6), pp. 2072–5.

Lions Eye Institute (2017) *Clinical trial: Safety and Efficacy Study of rAAV.sFlt-1 in Patients With Exudative Age-Related Macular Degeneration (AMD). Available from: https://clinicaltrials.gov/study/NCT01494805?cond=nct01494805&rank=1*. [Online]

Liu, B., Wei, L., Meyerle, C., Tuo, J., Sen, H.N., Li, Z., Chakrabarty, S., Agron, E., Chan, C.-C., Klein, M.L., Chew, E., Ferris, F. & Nussenblatt, R.B. (2011) 'Complement component C5a Promotes Expression of IL-22 and IL-17 from Human T cells and its Implication in Age-related Macular Degeneration', *Journal of Translational Medicine*, 9(1), p. 111.

Liu, H., Wu, F., Chen, R., Chen, Y., Yao, K., Liu, Z., Parikh, B.H., Jing, L., Liu, T., Su, X., Sun, J. & Huang, D. (2022) 'Electrohydrodynamic Jet-Printed Ultrathin Polycaprolactone Scaffolds Mimicking Bruch's Membrane for Retinal Pigment Epithelial Tissue Engineering', *International Journal of Bioprinting*, 8(3), p. 550.

Lopez-Gordo, E., Chamberlain, K., Riyad, J., Kohlbrenner, E. & Weber, T. (2024) 'Natural Adeno-Associated Virus Serotypes and Engineered Adeno-Associated Virus Capsid Variants: Tropism Differences and Mechanistic Insights', *Viruses*, 16(3), p. 442.

Lubbers, R., van Essen, M.F., van Kooten, C. & Trouw, L.A. (2017) 'Production of complement components by cells of the immune system', *Clinical and Experimental Immunology*, 188(2), pp. 183–194.

Lublin, D.M., Griffith, R.C. & Atkinson, J.P. (1986) 'Influence of glycosylation on allelic and cell-specific Mr variation, receptor processing, and ligand binding of the human complement C3b/C4b receptor.', *The Journal of biological chemistry*, 261(13), pp. 5736–44.

Luo, C., Zhao, J., Madden, A., Chen, M. & Xu, H. (2013) 'Complement expression in retinal pigment epithelial cells is modulated by activated macrophages', *Experimental Eye Research*, 112pp. 93–101.

Luo H, L.H.W.Y. & Zhang M, J.Y. (2013) ‘Construction of tissue-engineered cornea composed of amniotic epithelial cells and acellular porcine cornea for treating corneal alkali burn’, *Biomaterials*, 34(28), pp. 6748–6759.

Majidnia, E., Ahmadian, M., Salehi, H. & Amirpour, N. (2022) ‘Development of an electrospun poly(ε-caprolactone)/collagen-based human amniotic membrane powder scaffold for culturing retinal pigment epithelial cells’, *Scientific Reports*, 12(1), p. 6469.

Manian, K. V., Galloway, C.A., Dalvi, S., Emanuel, A.A., Mereness, J.A., Black, W., Winschel, L., Soto, C., Li, Y., Song, Y., DeMaria, W., Kumar, A., Slukvin, I., Schwartz, M.P., Murphy, W.L., Anand-Apte, B., Chung, M., Benoit, D.S.W. & Singh, R. (2021) ‘3D iPSC modeling of the retinal pigment epithelium-choriocapillaris complex identifies factors involved in the pathology of macular degeneration’, *Cell Stem Cell*, 28(5), pp. 846-862.e8.

Maqueda, M., Mosquera, J.L., García-Arumí, J., Veiga, A. & Duarri, A. (2021) ‘Repopulation of decellularized retinas with hiPSC-derived retinal pigment epithelial and ocular progenitor cells shows cell engraftment, organization and differentiation’, *Biomaterials*, 276p. 121049.

Mariño-Ramírez, L., Kann, M.G., Shoemaker, B.A. & Landsman, D. (2005) ‘Histone structure and nucleosome stability.’, *Expert review of proteomics*, 2(5), pp. 719–29.

May-Simera, H.L., Wan, Q., Jha, B.S., Hartford, J., Khristov, V., Dejene, R., Chang, J., Patnaik, S., Lu, Q., Banerjee, P., Silver, J., Insinna-Kettenhofen, C., Patel, D., Lotfi, M., Malicdan, M., Hotaling, N., Maminishkis, A., Sridharan, R., Brooks, B., et al. (2018) ‘Primary Cilium-Mediated Retinal Pigment Epithelium Maturation Is Disrupted in Ciliopathy Patient Cells’, *Cell Reports*, 22(1), pp. 189–205.

McHarg, S., Brace, N., Bishop, P.N. & Clark, S.J. (2015) ‘Enrichment of Bruch’s Membrane from Human Donor Eyes’, *Journal of Visualized Experiments*, (105), .

McMenamin, P.G. & Polla, E. (2013) ‘Mast cells are present in the choroid of the normal eye in most vertebrate classes’, *Veterinary Ophthalmology*, 16(s1), pp. 73–78.

Medicus, R.G., Götze, O. & Müller-Eberhard, H.J. (1976) ‘Alternative pathway of complement: recruitment of precursor properdin by the labile C3/C5 convertase and the potentiation of the pathway.’, *The Journal of experimental medicine*, 144(4), pp. 1076–1093.

Mellough, C.B., Collin, J., Queen, R., Hilgen, G., Dorgau, B., Zerti, D., Felemban, M., White, K., Sernagor, E. & Lako, M. (2019) ‘Systematic Comparison of Retinal Organoid Differentiation from Human Pluripotent Stem Cells Reveals Stage Specific, Cell Line, and Methodological Differences’, *Stem Cells Translational Medicine*, 8(7), pp. 694–706.

Mevorach, D., Mascarenhas, J.O., Gershov, D. & Elkon, K.B. (1998) ‘Complement-dependent Clearance of Apoptotic Cells by Human Macrophages’, *The Journal of Experimental Medicine*, 188(12), pp. 2313–2320.

Mezzina, M. & Merten, O.-W. (2011) *Adeno-Associated Viruses*, in [Online]. pp. 211–234.

Mitchell, C.H. (2001) ‘Release of ATP by a human retinal pigment epithelial cell line: potential for autocrine stimulation through subretinal space’, *The Journal of Physiology*, 534(1), pp. 193–202.

Miyagishima, K.J., Wan, Q., Miller, S.S. & Bharti, K. (2017) ‘A basis for comparison: sensitive authentication of stem cell derived RPE using physiological responses of intact RPE monolayers.’, *Stem cell and translational investigation*, 4.

Moffat, D., Ye, K. & Jin, S. (2022) ‘Decellularization for the retention of tissue niches’, *Journal of Tissue Engineering*, 13.

Moore, D.J. & Clover, G.M. (2001) ‘The effect of age on the macromolecular permeability of human Bruch’s membrane.’, *Investigative ophthalmology & visual science*, 42(12), pp. 2970–5.

Moore, D.J., Hussain, A.A. & Marshall, J. (1995) ‘Age-related variation in the hydraulic conductivity of Bruch’s membrane.’, *Investigative ophthalmology & visual science*, 36(7), pp. 1290–7.

Moradian, H., Gossen, M. & Lendlein, A. (2022) ‘Co-delivery of genes can be confounded by bicistronic vector design’, *MRS Communications*, 12(2), pp. 145–153.

Mulfaul, K., Mullin, N.K., Giacalone, J.C., Voigt, A.P., R DeVore, M., Stone, E.M., Tucker, B.A. & Mullins, R.F. (2022) ‘Local factor H production by human choroidal endothelial cells mitigates complement deposition: implications for macular degeneration’, *The Journal of Pathology*, 257(1), pp. 29–38.

Mullins, R.F., Johnson, M.N., Faidley, E.A., Skeie, J.M. & Huang, J. (2011) ‘Choriocapillaris Vascular Dropout Related to Density of Drusen in Human Eyes with Early Age-Related Macular Degeneration’, *Investigative Opthalmology & Visual Science*, 52(3), p. 1606.

Mullins, R.F., Olvera, M.A., Clark, A.F. & Stone, E.M. (2007) ‘Fibulin-5 distribution in human eyes: Relevance to age-related macular degeneration’, *Experimental Eye Research*, 84(2), pp. 378–380.

Mullins, R.F., Russell, S.R., Anderson, D.H. & Hageman, G.S. (2000) ‘Drusen associated with aging and age-related macular degeneration contain proteins common to extracellular deposits associated with atherosclerosis, elastosis, amyloidosis, and dense deposit disease.’, *FASEB journal : official publication of the Federation of American Societies for Experimental Biology*, 14(7), pp. 835–46.

Mullins, R.F., Schoo, D.P., Sohn, E.H., Flamme-Wiese, M.J., Workamelahu, G., Johnston, R.M., Wang, K., Tucker, B.A. & Stone, E.M. (2014) ‘The Membrane Attack Complex in Aging Human Choriocapillaris’, *The American Journal of Pathology*, 184(11), pp. 3142–3153.

Nakai-Futatsugi, Y., Jin, J., Ogawa, T., Sakai, N., Maeda, A., Hironaka, K., Fukuda, M., Danno, H., Tanaka, Y., Hori, S., Shiroguchi, K. & Takahashi, M. (2024) ‘Pigmentation level of human iPSC-derived RPE does not indicate a specific gene expression profile’, *eLife*, 12.

Narsinh, K.H., Plews, J. & Wu, J.C. (2011) ‘Comparison of Human Induced Pluripotent and Embryonic Stem Cells: Fraternal or Identical Twins?’, *Molecular Therapy*, 19(4), pp. 635–638.

Naso, M.F., Tomkowicz, B., Perry, W.L. & Strohl, W.R. (2017) ‘Adeno-Associated Virus (AAV) as a Vector for Gene Therapy.’, *BioDrugs : clinical immunotherapeutics, biopharmaceuticals and gene therapy*, 31(4), pp. 317–334.

Nesargikar, P., Spiller, B. & Chavez, R. (2012) ‘The complement system: History, pathways, cascade and inhibitors’, *European Journal of Microbiology and Immunology*, 2(2), pp. 103–111.

Neuracle Genetics, I. (2025) *Clinical trials: NG101 AAV Gene Therapy in Subjects With Wet Age-Related Macular Degeneration. Available from: https://clinicaltrials.gov/study/NCT05984927?cond=NCT05984927&rank=*. [Online]

Newsome, D.A., Huh, W. & Green, W.R. (1987) ‘Bruch’s membrane age-related changes vary by region’, *Current Eye Research*, 6(10), pp. 1211–1221.

NGM Biopharmaceuticals, I. (2023) *Clinical trials: A Study of NGM621 in Participants With Geographic Atrophy (CATALINA). Available from: https://clinicaltrials.gov/study/NCT04465955*. [Online]

NGM Biopharmaceuticals, I. (2020) *Clinical trials: Study of NGM621 in Participants With Geographic Atrophy. Available from: https://clinicaltrials.gov/study/NCT04014777?cond=nct04014777&rank=1*. [Online]

Nickla, D.L. & Wallman, J. (2010) ‘The multifunctional choroid’, *Progress in Retinal and Eye Research*, 29(2), pp. 144–168.

Noris, M. & Remuzzi, G. (2013) ‘Overview of Complement Activation and Regulation’, *Seminars in Nephrology*, 33(6), pp. 479–492.

Novartis Pharmaceuticals (2024) *Clinical trials: A Masked, Placebo-controlled Study to Assess Iptacopan in Age-related Macular Degeneration. Available from: https://clinicaltrials.gov/study/NCT05230537?cond=NCT05230537&rank=1*. [Online]

Novartis Pharmaceuticals (2021) *Clinical trials: Intravitreal LFG316 in Patients With Age-related Macular Degeneration (AMD). Available from: https://clinicaltrials.gov/study/NCT01527500*. [Online]

Novartis Pharmaceuticals Canada Inc. (2021) *Clinical Review Report: Voretigene Neparvovec (Luxturna): (Novartis Pharmaceuticals Canada Inc.): Indication: Vision loss, inherited retinal dystrophy*. [Online]

O’Hara-Wright, M. & Gonzalez-Cordero, A. (2020) ‘Retinal organoids: a window into human retinal development’, *Development*, 147(24), .

Owoyomi, O., . I.J., . M.S.A., . O.O.S. & . M.K.M. (2005) ‘Interactions Between Sodium Dodecylsulphate and Triton X-100: Molecular Properties and Kinetics Investigations’, *Journal of Applied Sciences*, 5(4), pp. 729–734.

Oxford BioMedica (2017) *Clinical trials: Phase I Dose Escalation Safety Study of RetinoStat in Advanced Age-Related Macular Degeneration (AMD) (GEM). Available from: https://clinicaltrials.gov/study/NCT01301443*. [Online]

Palanisamy, K., Karunakaran, C., Raman, R. & Chidambaram, S. (2019) 'Optimization of an in vitro bilayer model for studying the functional interplay between human primary retinal pigment epithelial and choroidal endothelial cells isolated from donor eyes', *BMC Research Notes*, 12(1), p. 307.

Panos, G., Lakshmanan, A., Dadoukis, P., Ripa, M., Motta, L. & Amoaku, W. (2023) 'Faricimab: Transforming the Future of Macular Diseases Treatment - A Comprehensive Review of Clinical Studies', *Drug Design, Development and Therapy*, Volume 17pp. 2861–2873.

Patel, S.S., Lally, D.R., Hsu, J., Wykoff, C.C., Eichenbaum, D., Heier, J.S., Jaffe, G.J., Westby, K., Desai, D., Zhu, L. & Khanani, A.M. (2023) 'Avacincaptad pegol for geographic atrophy secondary to age-related macular degeneration: 18-month findings from the GATHER1 trial', *Eye*, 37(17), pp. 3551–3557.

Pauleikhoff, D., Sheraidah, G., Marshall, J., Bird, A.C. & Wessing, A. (1994) '[Biochemical and histochemical analysis of age related lipid deposits in Bruch's membrane].', *Der Ophthalmologe : Zeitschrift der Deutschen Ophthalmologischen Gesellschaft*, 91(6), pp. 730–4.

Pauly, D., Agarwal, D., Dana, N., Schäfer, N., Biber, J., Wunderlich, K.A., Jabri, Y., Straub, T., Zhang, N.R., Gautam, A.K., Weber, B.H.F., Hauck, S.M., Kim, M., Curcio, C.A., Stambolian, D., Li, M. & Grosche, A. (2019) 'Cell-Type-Specific Complement Expression in the Healthy and Diseased Retina', *Cell Reports*, 29(9), pp. 2835-2848.e4.

Peking Union Medical College Hospital (2025) *Clinical trial: A Clinical Study Evaluating the Safety and Efficacy of SKG0106 in Patients With Neovascular Age-related Macular Degeneration (nAMD). Available from: https://clinicaltrials.gov/study/NCT06213038?cond=NCT06213038&rank=1*. [Online]

Peng, S., Gan, G., Qiu, C., Zhong, M., An, H., Adelman, R.A. & Rizzolo, L.J. (2013) 'Engineering a Blood-Retinal Barrier With Human Embryonic Stem Cell-Derived Retinal Pigment Epithelium: Transcriptome and Functional Analysis', *Stem Cells Translational Medicine*, 2(7), pp. 534–544.

Pennesi, M.E., Neuringer, M. & Courtney, R.J. (2012) 'Animal models of age related macular degeneration', *Molecular Aspects of Medicine*, 33(4), pp. 487–509.

Perceive Biotherapeutics, I. (2024) *Clinical trials: Study of VOY-101 in Patients With Advanced Non-Neovascular Age-Related Macular Degeneration. Available from: https://clinicaltrials.gov/study/NCT05380492?cond=NCT05380492&rank=1*. [Online]

Philip J. Rosenfeld (2017) *Clinicla trials: Complement Inhibition With Eculizumab for the Treatment of Non-Exudative Macular Degeneration (AMD) (COMPLETE). Available from: https://clinicaltrials.gov/study/NCT00935883?cond=nct00935883&rank=1*. [Online]

Pietkiewicz, J., Seweryn, E., Bartyś, A. & Gamian, A. (2008) '[Receptors for advanced glycation end products and their physiological and clinical significance].', *Postepy higieny i medycyny doswiadczalnej (Online)*, 62pp. 511–23.

Pizzirusso, A., De Nicola, A., Sevink, G.J.A., Correa, A., Cascella, M., Kawakatsu, T., Rocco, M., Zhao, Y., Celino, M. & Milano, G. (2017) 'Biomembrane solubilization mechanism by Triton X-100: a computational study of the three stage model', *Physical Chemistry Chemical Physics*, 19(44), pp. 29780–29794.

Polato, F. & Becerra, S.P. (2016) *Pigment Epithelium-Derived Factor, a Protective Factor for Photoreceptors in Vivo*, in [Online]. pp. 699–706.

Pollreisz, A., Afonyushkin, T., Oskolkova, O. V., Gruber, F., Bochkov, V.N. & Schmidt-Erfurth, U. (2013) 'Retinal pigment epithelium cells produce VEGF in response to oxidized phospholipids through mechanisms involving ATF4 and protein kinase CK2', *Experimental Eye Research*, 116pp. 177–184.

Prosser, B.E., Johnson, S., Roversi, P., Herbert, A.P., Blaum, B.S., Tyrrell, J., Jowitt, T.A., Clark, S.J., Tarelli, E., Uhrín, D., Barlow, P.N., Sim, R.B., Day, A.J. & Lea, S.M. (2007) 'Structural basis for complement factor H–linked age-related macular degeneration', *The Journal of Experimental Medicine*, 204(10), pp. 2277–2283.

Provis, J. (2001) 'Development of the Primate Retinal Vasculature', *Progress in Retinal and Eye Research*, 20(6), pp. 799–821.

PROVIS, J.M., LEECH, J., DIAZ, C.M., PENFOLD, P.L., STONE, J. & KESHET, E. (1997) 'Development of the Human Retinal Vasculature: Cellular Relations and VEGF Expression', *Experimental Eye Research*, 65(4), pp. 555–568.

Qiagen. (2025) *Available from: https://www.qiagen.com/us/resources/resourcedetail?id=9ba22130-8278-477c-b303-8c96700f21ea&lang=en*. [Online]

Quinn, P.M.J. & Wijnholds, J. (2019) 'Retinogenesis of the Human Fetal Retina: An Apical Polarity Perspective', *Genes*, 10(12), p. 987.

Rambhai, H.K., Ashby, F.J., Qing, K. & Srivastava, A. (2020) 'Role of Essential Metal Ions in AAV Vector-Mediated Transduction', *Molecular Therapy - Methods & Clinical Development*, 18pp. 159–166.

Ramrattan, R.S., van der Schaft, T.L., Mooy, C.M., de Bruijn, W.C., Mulder, P.G. & de Jong, P.T. (1994) 'Morphometric analysis of Bruch's membrane, the choriocapillaris, and the choroid in aging.', *Investigative ophthalmology & visual science*, 35(6), pp. 2857–64.

Ramrattan, R.S., Van Der Schaft, T.L., Mooy, C.M., Wim, ^, De Bruijn, C., Mulder, P.G.H. & Dejong, P.T.V.M. (n.d.) *Morphometric Analysis of Bruch's Membrane, the Choriocapillaris, and the Choroid in Aging*.

REGENXBIO Inc. (2023) *Clinical trial: Safety and Tolerability of RGX-314 (Investigational Product) Gene Therapy for Neovascular AMD Trial. Available from: https://clinicaltrials.gov/study/NCT03066258?cond=NCT03066258&rank=1*. [Online]

Reid, E., Guduric-Fuchs, J., O'Neill, C.L., Allen, L.-D., Chambers, S.E.J., Stitt, A.W. & Medina, R.J. (2018) 'Preclinical Evaluation and Optimization of a Cell Therapy Using Human Cord Blood-Derived Endothelial Colony-Forming Cells for Ischemic Retinopathies', *Stem Cells Translational Medicine*, 7(1), pp. 59–67.

Reiner, A., Fitzgerald, M.E.C., Del Mar, N. & Li, C. (2018) 'Neural control of choroidal blood flow', *Progress in Retinal and Eye Research*, 64pp. 96–130.

Ricklin, D., Reis, E.S., Mastellos, D.C., Gros, P. & Lambris, J.D. (2016) 'Complement component C3 – The "Swiss Army Knife" of innate immunity and host defense', *Immunological Reviews*, 274(1), pp. 33–58.

Rogers, G.L., Huang, C., Clark, R.D.E., Seclén, E., Chen, H.-Y. & Cannon, P.M. (2021) 'Optimization of AAV6 transduction enhances site-specific genome editing of primary human lymphocytes', *Molecular Therapy - Methods & Clinical Development*, 23pp. 198–209.

Rosenfeld, P.J., Moshfeghi, A.A. & Puliafito, C.A. (2005) 'Optical coherence tomography findings after an intravitreal injection of bevacizumab (avastin) for neovascular age-related macular degeneration.', *Ophthalmic surgery, lasers & imaging : the official journal of the International Society for Imaging in the Eye*, 36(4), pp. 331–5.

Ross, G. & Lambris, J. (1982) 'Identification of a C3bi-specific membrane complement receptor that is expressed on lymphocytes, monocytes, neutrophils, and erythrocytes', *The Journal of Experimental Medicine*, 155(1), pp. 96–110.

Rossi, V., Bally, I., Lacroix, M., Arlaud, G.J. & Thielens, N.M. (2014) *Classical Complement Pathway Components C1r and C1s: Purification from Human Serum and in Recombinant Form and Functional Characterization*, in [Online]. pp. 43–60.

Roth, F., Bindewald, A. & Holz, F.G. (2004) 'Keypathophysiologic pathways in age-related macular disease', *Graefe's Archive for Clinical and Experimental Ophthalmology*, 242(8), pp. 710–716.

Ruberti, J.W., Curcio, C.A., Millican, C.L., Menco, B.P.M., Huang, J.-D. & Johnson, M. (2003) 'Quick-Freeze/Deep-Etch Visualization of Age-Related Lipid Accumulation in Bruch's Membrane', *Investigative Opthalmology & Visual Science*, 44(4), p. 1753.

Rudolf, M., Malek, G., Messinger, J.D., Clark, M.E., Wang, L. & Curcio, C.A. (2008) 'Sub-retinal drusenoid deposits in human retina: Organization and composition', *Experimental Eye Research*, 87(5), pp. 402–408.

Saha, A., Capowski, E., Fernandez Zepeda, M.A., Nelson, E.C., Gamm, D.M. & Sinha, R. (2022) 'Cone photoreceptors in human stem cell-derived retinal organoids demonstrate intrinsic light responses that mimic those of primate fovea', *Cell Stem Cell*, 29(3), pp. 460-471.e3.

Saint-Geniez, M., Kurihara, T., Sekiyama, E., Maldonado, A.E. & D'Amore, P.A. (2009a) 'An essential role for RPE-derived soluble VEGF in the maintenance of the choriocapillaris', *Proceedings of the National Academy of Sciences*, 106(44), pp. 18751–18756.

Saint-Geniez, M., Kurihara, T., Sekiyama, E., Maldonado, A.E. & D'Amore, P.A. (2009b) 'An essential role for RPE-derived soluble VEGF in the maintenance of the choriocapillaris', *Proceedings of the National Academy of Sciences*, 106(44), pp. 18751–18756.

Sakamoto, T. (1995) 'Vessel Formation by Choroidal Endothelial Cells In Vitro Is Modulated by Retinal Pigment Epithelial Cells', *Archives of Ophthalmology*, 113(4), p. 512.

Sándor, N., Schneider, A.E., Matola, A.T., Barbai, V.H., Bencze, D., Hammad, H.H., Papp, A., Kövesdi, D., Uzonyi, B. & Józsi, M. (2024) 'The human factor H protein family – an update', *Frontiers in Immunology*, 15.

Sanofi (2018) *Clinical trial: Safety and Tolerability Study of AAV2-sFLT01 in Patients With Neovascular Age-Related Macular Degeneration (AMD). Available from: https://clinicaltrials.gov/study/NCT01024998?cond=NCT01024998&rank=1*. [Online]

Sarks, S., Cherepanoff, S., Killingsworth, M. & Sarks, J. (2007) 'Relationship of Basal Laminar Deposit and Membranous Debris to the Clinical Presentation of Early Age-Related Macular Degeneration', *Investigative Opthalmology & Visual Science*, 48(3), p. 968.

Schäfer, N., Wolf, H.N., Enzbrenner, A., Schikora, J., Reichenthaler, M., Enzmann, V. & Pauly, D. (2020) 'Properdin Modulates Complement Component Production in Stressed Human Primary Retinal Pigment Epithelium Cells', *Antioxidants*, 9(9), p. 793.

Schorlemmer, H.U., Hofstaetter, T. & Seiler, F.R. (1984) 'Phagocytosis of immune complexes by human neutrophils and monocytes: relative importance of Fc and C3b receptors.', *Behring Institute Mitteilungen*, (76), pp. 88–97.

Scott, J.E. & Thomlison, A.M. (1998) 'The structure of interfibrillar proteoglycan bridges ("shape modules") in extracellular matrix of fibrous connective tissues and their stability in various chemical environments', *Journal of Anatomy*, 192(3), pp. 391–405.

Seddon, J.M. (2001) 'Dietary Fat and Risk for Advanced Age-Related Macular Degeneration', *Archives of Ophthalmology*, 119(8), p. 1191.

Senabouth, A., Daniszewski, M., Lidgerwood, G.E., Liang, H.H., Hernández, D., Mirzaei, M., Keenan, S.N., Zhang, R., Han, X., Neavin, D., Rooney, L., Lopez Sanchez, M.I.G., Gulluyan, L., Paulo, J.A., Clarke, L., Kearns, L.S., Gnanasambandapillai, V., Chan, C.-L., Nguyen, U., et al. (2022) 'Transcriptomic and proteomic retinal pigment epithelium signatures of age-related macular degeneration', *Nature Communications*, 13(1), p. 4233.

Shadforth, A., Suzuki, S., Alzonne, R., Edwards, G., Richardson, N., Chirila, T. & Harkin, D. (2015) 'Incorporation of Human Recombinant Tropoelastin into Silk Fibroin Membranes with the View to Repairing Bruch's Membrane', *Journal of Functional Biomaterials*, 6(3), pp. 946–962.

Shadforth, A.M.A., George, K.A., Kwan, A.S., Chirila, T. V. & Harkin, D.G. (2012) 'The cultivation of human retinal pigment epithelial cells on Bombyx mori silk fibroin', *Biomaterials*, 33(16), pp. 4110–4117.

Shanghai BDgene Co., L. (2025) *Clinical trial: VEGFA-targeting Gene Therapy to Treat Retinal and Choroidal Neovascularization Diseases. Available from: https://clinicaltrials.gov/study/NCT05099094*. [Online]

Shanghai Refreshgene Technology Co., L. (2024) *Clinical trials: Safety and Efficacy of RRG001 Gene Therapy in Subjects With Neovascular Age-related Macular Degeneration (nAMD). Available from: https://clinicaltrials.gov/study/NCT06141460*. [Online]

Shen, Y., Halperin, J.A., Benzaquen, L. & Lee, C.-M. (1997) 'Characterization of neuronal cell death induced by complement activation', *Brain Research Protocols*, 1(2), pp. 186–194.

Sicari, B.M., Londono, R., Dziki, J.L. & Badylak, S.F. (2023) 'Extracellular matrix as a bioscaffold for tissue engineering', in *Tissue Engineering*. [Online]. Elsevier. pp. 137–172.

Simmons, K.T., Mazzilli, J.L., Mueller-Ortiz, S.L., Domozhirov, A.Y., Garcia, C.A., Zsigmond, E.M. & Wetsel, R.A. (2020) 'Complement Receptor 1 (CR1/CD35)-expressing retinal pigment epithelial cells as a potential therapy for age-related macular degeneration', *Molecular Immunology*, 118pp. 91–98.

Skyline Therapeutics (2025) *Clinical trial: Phase I/II Study of SKG0106 Intravitreal Injection in Patients With Neovascular Age-related Macular Degeneration (nAMD). Available from: https://clinicaltrials.gov/study/NCT05986864?cond=NCT05986864&rank=1*. [Online]

Sohn, E.H., Flamme-Wiese, M.J., Whitmore, S.S., Workalemahu, G., Marneros, A.G., Boese, E.A., Kwon, Y.H., Wang, K., Abramoff, M.D., Tucker, B.A., Stone, E.M. & Mullins, R.F. (2019) 'Choriocapillaris Degeneration in Geographic Atrophy', *The American Journal of Pathology*, 189(7), pp. 1473–1480.

Soltis, R.D., Hasz, D., Morris, M.J. & Wilson, I.D. (1979) 'The effect of heat inactivation of serum on aggregation of immunoglobulins.', *Immunology*, 36(1), pp. 37–45.

Song, M.J., Quinn, R., Nguyen, E., Hampton, C., Sharma, R., Park, T.S., Koster, C., Voss, T., Tristan, C., Weber, C., Singh, A., Dejene, R., Bose, D., Chen, Y.-C., Derr, P., Derr, K., Michael, S., Barone, F., Chen, G., et al. (2023) 'Bioprinted 3D outer retina barrier uncovers RPE-dependent choroidal phenotype in advanced macular degeneration', *Nature Methods*, 20(1), pp. 149–161.

Sonoda, S., Sreekumar, P.G., Kase, S., Spee, C., Ryan, S.J., Kannan, R. & Hinton, D.R. (2009) 'Attainment of polarity promotes growth factor secretion by retinal pigment epithelial cells: relevance to age-related macular degeneration.', *Aging*, 2(1), pp. 28–42.

Stalmans, I., Ng, Y.-S., Rohan, R., Fruttiger, M., Bouché, A., Ÿuce, A., Fujisawa, H., Hermans, B., Shani, M., Jansen, S., Hicklin, D., Anderson, D.J., Gardiner, T., Hammes, H.-P., Moons, L., Dewerchin, M., Collen, D., Carmeliet, P. & D'Amore, P.A. (2002) 'Arteriolar and venular patterning in retinas of mice selectively expressing VEGF isoforms', *Journal of Clinical Investigation*, 109(3), pp. 327–336.

Starita, C., Hussain, A.A., Pagliarini, S. & Marshall, J. (1996) 'Hydrodynamics of ageing Bruch's membrane: implications for macular disease.', *Experimental eye research*, 62(5), pp. 565–72.

Starita, C., Hussain, A.A., Patmore, A. & Marshall, J. (1997) 'Localization of the site of major resistance to fluid transport in Bruch's membrane.', *Investigative ophthalmology & visual science*, 38(3), pp. 762–7.

Strauss, O. (2005) 'The Retinal Pigment Epithelium in Visual Function', *Physiological Reviews*, 85(3), pp. 845–881.

Sugino, I.K., Gullapalli, V.K., Sun, Q., Wang, J., Nunes, C.F., Cheewatrakoolpong, N., Johnson, A.C., Degner, B.C., Hua, J., Liu, T., Chen, W., Li, H. & Zarbin, M.A. (2011) 'Cell-Deposited Matrix Improves Retinal Pigment Epithelium Survival on Aged Submacular Human Bruch's Membrane', *Investigative Opthalmology & Visual Science*, 52(3), p. 1345.

Sugita, S., Makabe, K., Fujii, S. & Takahashi, M. (2018) 'Detection of Complement Activators in Immune Attack Eyes After iPS-Derived Retinal Pigment Epithelial Cell Transplantation', *Investigative Opthalmology & Visual Science*, 59(10), p. 4198.

Sura, A.A., Chen, L., Messinger, J.D., Swain, T.A., McGwin, G., Freund, K.B. & Curcio, C.A. (2020) 'Measuring the Contributions of Basal Laminar Deposit and Bruch's Membrane in Age-Related Macular Degeneration', *Investigative Opthalmology & Visual Science*, 61(13), p. 19.

Takahashi, K., Tanabe, K., Ohnuki, M., Narita, M., Ichisaka, T., Tomoda, K. & Yamanaka, S. (2007) 'Induction of Pluripotent Stem Cells from Adult Human Fibroblasts by Defined Factors', *Cell*, 131(5), pp. 861–872.

Takahashi, K. & Yamanaka, S. (2006a) 'Induction of Pluripotent Stem Cells from Mouse Embryonic and Adult Fibroblast Cultures by Defined Factors', *Cell*, 126(4), pp. 663–676.

Takahashi, K. & Yamanaka, S. (2006b) 'Induction of Pluripotent Stem Cells from Mouse Embryonic and Adult Fibroblast Cultures by Defined Factors', *Cell*, 126(4), pp. 663–676.

Tam, L.C., Joel, J., Stampoulis, D., Little, A., Walton, A., Atkinson-Dell, R., Devine, M., Hill, J., Esteve-Rudd, J. & Ellis, S. (2024) *Preclinical development of a dual targeting bicistronic gene therapy approach for the treatment of wet age-related macular degeneration*.

Tezel, T.H., Geng, L., Lato, E.B., Schaal, S., Liu, Y., Dean, D., Klein, J.B. & Kaplan, H.J. (2009) 'Synthesis and Secretion of Hemoglobin by Retinal Pigment Epithelium', *Investigative Opthalmology & Visual Science*, 50(4), p. 1911.

Tezel, T.H., Kaplan, H.J. & Del Priore, L. V (1999) 'Fate of human retinal pigment epithelial cells seeded onto layers of human Bruch's membrane.', *Investigative ophthalmology & visual science*, 40(2), pp. 467–76.

Tezel, T.H., Del Priore, L. V. & Kaplan, H.J. (2004) 'Reengineering of Aged Bruch's Membrane to Enhance Retinal Pigment Epithelium Repopulation', *Investigative Opthalmology & Visual Science*, 45(9), p. 3337.

ThermoFisher Schientific (2025) *ThermoFisher Scientific. Human Serpin F1.* . [Online]

ThermoFisher Scientific. Qubit. (2025) *Available from: https://www.thermofisher.com/document-connect/document-connect.html?url=https://assets.thermofisher.com/TFS-Assets%2FBID%2FTechnical-Notes%2Fqubit-1x-dsdna-assays-simplified-workflow-tech-note.pdf.* [Online]

Thumann, G., Viethen, A., Gaebler, A., Walter, P., Kaempf, S., Johnen, S. & Salz, A.K. (2009) 'The in vitro and in vivo behaviour of retinal pigment epithelial cells cultured on ultrathin collagen membranes', *Biomaterials*, 30(3), pp. 287–294.

Török, K., Dezső, B., Bencsik, A., Uzonyi, B. & Erdei, A. (2015) 'Complement receptor type 1 (CR1/CD35) expressed on activated human CD4+ T cells contributes to generation of regulatory T cells', *Immunology Letters*, 164(2), pp. 117–124.

Trakkides, T.-O., Schäfer, N., Reichenthaler, M., Kühn, K., Brandwijk, R.J.M.G.E., Toonen, E.J.M., Urban, F., Wegener, J., Enzmann, V. & Pauly, D. (2019) 'Oxidative Stress Increases Endogenous Complement-Dependent Inflammatory and Angiogenic Responses in Retinal Pigment Epithelial Cells Independently of Exogenous Complement Sources', *Antioxidants*, 8(11), p. 548.

Tsukahara, I., Ninomiya, S., Castellarin, A., Yagi, F., Sugino, I.K. & Zarbin, M.A. (2002) 'Early Attachment of Uncultured Retinal Pigment Epithelium from Aged Donors onto Bruch's Membrane Explants', *Experimental Eye Research*, 74(2), pp. 255–266.

Udsen, M., Tagmose, C., Garred, P., Nissen, M.H. & Faber, C. (2022) 'Complement activation by RPE cells preexposed to TNFα and IFNγ', *Experimental Eye Research*, 218p. 108982.

Uemura, A., Ogawa, M., Hirashima, M., Fujiwara, T., Koyama, S., Takagi, H., Honda, Y., Wiegand, S.J., Yancopoulos, G.D. & Nishikawa, S.-I. (2002) 'Recombinant angiopoietin-1 restores higher-order architecture of growing blood vessels in mice in the absence of mural cells', *Journal of Clinical Investigation*, 110(11), pp. 1619–1628.

Volker Busskamp; Kritika Sharma (2023) 'Advanced vascularized human stem cell-derived retinal organoids', *Investigative Ophthalmology & Visual Science*, 64(8), p. 1894.

Volland, S., Esteve-Rudd, J., Hoo, J., Yee, C. & Williams, D.S. (2015a) 'A Comparison of Some Organizational Characteristics of the Mouse Central Retina and the Human Macula', *PLOS ONE*, 10(4), p. e0125631.

Volland, S., Esteve-Rudd, J., Hoo, J., Yee, C. & Williams, D.S. (2015b) 'A Comparison of Some Organizational Characteristics of the Mouse Central Retina and the Human Macula', *PLOS ONE*, 10(4), p. e0125631.

Vyawahare, H. & Shinde, P. (2022) 'Age-Related Macular Degeneration: Epidemiology, Pathophysiology, Diagnosis, and Treatment', *Cureus*,

Wagner, C., Ochmann, C., Schoels, M., Giese, T., Stegmaier, S., Richter, R., Hug, F. & Hänsch, G.M. (2006) 'The complement receptor 1, CR1 (CD35), mediates inhibitory signals in human T-lymphocytes', *Molecular Immunology*, 43(6), pp. 643–651.

Wahlin, K.J., Maruotti, J.A., Sripathi, S.R., Ball, J., Angueyra, J.M., Kim, C., Grebe, R., Li, W., Jones, B.W. & Zack, D.J. (2017) 'Photoreceptor Outer Segment-like Structures in Long-Term 3D Retinas from Human Pluripotent Stem Cells', *Scientific Reports*, 7(1), p. 766.

Wang, J., DeClercq, J.J., Hayward, S.B., Li, P.W.-L., Shivak, D.A., Gregory, P.D., Lee, G. & Holmes, M.C. (2016) 'Highly efficient homology-driven genome editing in human T cells by combining zinc-finger nuclease mRNA and AAV6 donor delivery', *Nucleic Acids Research*, 44(3), pp. e30–e30.

Wang, L., Clark, M.E., Crossman, D.K., Kojima, K., Messinger, J.D., Mobley, J.A. & Curcio, C.A. (2010) 'Abundant Lipid and Protein Components of Drusen', *PLoS ONE*, 5(4), p. e10329.

Wang, L., Li, C.-M., Rudolf, M., Belyaeva, O. V., Chung, B.H., Messinger, J.D., Kedishvili, N.Y. & Curcio, C.A. (2009) 'Lipoprotein Particles of Intraocular Origin in Human Bruch Membrane: An Unusual Lipid Profile', *Investigative Opthalmology & Visual Science*, 50(2), p. 870.

Wang, M., Sun, J., Crosby, A., Woodard, K., Hirsch, M.L., Samulski, R.J. & Li, C. (2017) 'Direct interaction of human serum proteins with AAV virions to enhance AAV transduction: immediate impact on clinical applications', *Gene Therapy*, 24(1), pp. 49–59.

Wang, S., Lin, S., Xue, B., Wang, C., Yan, N., Guan, Y., Hu, Y. & Wen, X. (2022) 'Bruch's-Mimetic Nanofibrous Membranes Functionalized with the Integrin-Binding Peptides as a Promising Approach for Human Retinal Pigment Epithelium Cell Transplantation', *Molecules*, 27(4), p. 1429.

Warnke, P.H., Alamein, M., Skabo, S., Stephens, S., Bourke, R., Heiner, P. & Liu, Q. (2013) 'Primordium of an artificial Bruch's membrane made of nanofibers for engineering of retinal pigment epithelium cell monolayers', *Acta Biomaterialia*, 9(12), pp. 9414–9422.

Weis, J.H., Morton, C.C., Bruns, G.A., Weis, J.J., Klickstein, L.B., Wong, W.W. & Fearon, D.T. (1987) 'A complement receptor locus: genes encoding C3b/C4b receptor and C3d/Epstein-Barr virus receptor map to 1q32.', *Journal of immunology (Baltimore, Md. : 1950)*, 138(1), pp. 312–5.

Weisman, H.F., Bartow, T., Leppo, M.K., Marsh, H.C., Carson, G.R., Concino, M.F., Boyle, M.P., Roux, K.H., Weisfeldt, M.L. & Fearon, D.T. (1990) 'Soluble Human Complement Receptor Type 1: In Vivo Inhibitor of Complement Suppressing Post-Ischemic Myocardial Inflammation and Necrosis', *Science*, 249(4965), pp. 146–151.

Westenskow, P.D., Moreno, S.K., Krohne, T.U., Kurihara, T., Zhu, S., Zhang, Z., Zhao, T., Xu, Y., Ding, S. & Friedlander, M. (2012) 'Using Flow Cytometry to Compare the Dynamics of Photoreceptor Outer Segment Phagocytosis in iPS-Derived RPE Cells', *Investigative Opthalmology & Visual Science*, 53(10), p. 6282.

Whitmore, S.S., Sohn, E.H., Chirco, K.R., Drack, A. V., Stone, E.M., Tucker, B.A. & Mullins, R.F. (2015) 'Complement activation and choriocapillaris loss in early AMD: Implications for pathophysiology and therapy', *Progress in Retinal and Eye Research*, 45pp. 1–29.

WIMMERS, S., KARL, M. & STRAUSS, O. (2007) 'Ion channels in the RPE', *Progress in Retinal and Eye Research*, 26(3), pp. 263–301.

Witkin, A.J., Jaffe, G.J., Srivastava, S.K., Davis, J.L. & Kim, J.E. (2024) 'Retinal Vasculitis After Intravitreal Pegcetacoplan: Report From the ASRS Research and Safety in Therapeutics (ReST) Committee', *Journal of VitreoRetinal Diseases*, 8(1), pp. 9–20.

Wong, D.T., Aboobaker, S., Maberley, D., Sharma, S. & Yoganathan, P. (2025) 'Switching to faricimab from the current anti-VEGF therapy: evidence-based expert recommendations', *BMJ Open Ophthalmology*, 10(1), p. e001967.

Wong, W.L., Su, X., Li, X., Cheung, C.M.G., Klein, R., Cheng, C.-Y. & Wong, T.Y. (2014) 'Global prevalence of age-related macular degeneration and disease burden projection for 2020 and 2040: a systematic review and meta-analysis', *The Lancet Global Health*, 2(2), pp. e106–e116.

Yang, Z., Tong, Z., Chen, Y., Zeng, J., Lu, F., Sun, X., Zhao, C., Wang, K., Davey, L., Chen, H., London, N., Muramatsu, D., Salasar, F., Carmona, R., Kasuga, D., Wang, X., Bedell, M., Dixie, M., Zhao, P., et al. (2010) 'Genetic and Functional Dissection of HTRA1 and LOC387715 in Age-Related Macular Degeneration', *PLoS Genetics*, 6(2), p. e1000836.

Young, T.A., Wang, H., Munk, S., Hammoudi, D.S., Young, D.S., Mandelcorn, M.S. & Whiteside, C.I. (2005) 'Vascular endothelial growth factor expression and secretion by retinal pigment epithelial cells in high glucose and hypoxia is protein kinase C-dependent', *Experimental Eye Research*, 80(5), pp. 651–662.

Yu, J., Vodyanik, M.A., Smuga-Otto, K., Antosiewicz-Bourget, J., Frane, J.L., Tian, S., Nie, J., Jonsdottir, G.A., Ruotti, V., Stewart, R., Slukvin, I.I. & Thomson, J.A. (2007a) 'Induced Pluripotent Stem Cell Lines Derived from Human Somatic Cells', *Science*, 318(5858), pp. 1917–1920.

Yu, J., Vodyanik, M.A., Smuga-Otto, K., Antosiewicz-Bourget, J., Frane, J.L., Tian, S., Nie, J., Jonsdottir, G.A., Ruotti, V., Stewart, R., Slukvin, I.I. & Thomson, J.A. (2007b) 'Induced Pluripotent Stem Cell Lines Derived from Human Somatic Cells', *Science*, 318(5858), pp. 1917–1920.

Zarbin, M.A. (2003) 'Analysis of retinal pigment epithelium integrin expression and adhesion to aged submacular human Bruch's membrane.', *Transactions of the American Ophthalmological Society*, 101pp. 499–520.

Zauhar, R., Biber, J., Jabri, Y., Kim, M., Hu, J., Kaplan, L., Pfaller, A.M., Schäfer, N., Enzmann, V., Schlötzer-Schrehardt, U., Straub, T., Hauck, S.M., Gamlin, P.D., McFerrin, M.B., Messinger, J., Strang, C.E., Curcio, C.A., Dana, N., Pauly, D., et al. (2022) 'As in Real Estate, Location Matters: Cellular Expression of Complement Varies Between Macular and Peripheral Regions of the Retina and Supporting Tissues', *Frontiers in Immunology*, 13.

Zhang, Y., Gordon, S.M., Xi, H., Choi, S., Paz, M.A., Sun, R., Yang, W., Saredy, J., Khan, M., Remaley, A.T., Wang, J.-F., Yang, X. & Wang, H. (2019) 'HDL subclass proteomic analysis and functional implication of protein dynamic change during HDL maturation', *Redox Biology*, 24p. 101222.

Zhao, H., Qu, M., Wang, Y., Wang, Z. & Shi, W. (2014) 'Xenogeneic Acellular Conjunctiva Matrix as a Scaffold of Tissue-Engineered Corneal Epithelium', *PLoS ONE*, 9(11), p. e111846.

Zhong, X., Gutierrez, C., Xue, T., Hampton, C., Vergara, M.N., Cao, L.-H., Peters, A., Park, T.S., Zambidis, E.T., Meyer, J.S., Gamm, D.M., Yau, K.-W. & Canto-Soler, M.V. (2014) 'Generation of three-dimensional retinal tissue with functional photoreceptors from human iPSCs', *Nature Communications*, 5(1), p. 4047.

Zhou, D., Hu, Y., Qiu, Z., Liu, Z., Jiang, H., Kawasaki, R. & Liu, J. (2023) 'Retinal layers changes in patients with age-related macular degeneration treated with intravitreal anti-VEGF agents', *BMC Ophthalmology*, 23(1), p. 451.

Zhu, D., Deng, X., Spee, C., Sonoda, S., Hsieh, C.-L., Barron, E., Pera, M. & Hinton, D.R. (2011) 'Polarized Secretion of PEDF from Human Embryonic Stem Cell–Derived RPE Promotes Retinal Progenitor Cell Survival', *Investigative Opthalmology & Visual Science*, 52(3), p. 1573.

Ziemssen, F., Hammer, T., Grueb, M., Mueller, B., Berk, H., Gamulescu, M.-A., Voegeler, J., Wachtlin, J. & OCEAN Study Group (2020) 'Reporting of Safety Events during Anti-VEGF Treatment: Pharmacovigilance in a Noninterventional Trial', *Journal of Ophthalmology*, 2020pp. 1–13.

Zweifel, S.A., Spaide, R.F., Curcio, C.A., Malek, G. & Imamura, Y. (2010) 'Reticular Pseudodrusen Are Subretinal Drusenoid Deposits', *Ophthalmology*, 117(2), pp. 303-312.e1.